



TUM School of Natural Sciences

---

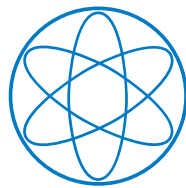
---

First measurement of the absorption of  ${}^3\overline{\text{He}}$  and  ${}^3\overline{\text{H}}$  nuclei in matter and its impact on  ${}^3\overline{\text{He}}$  propagation in the galaxy

---

---

STEPHAN KOENIGSTORFER



TECHNISCHE UNIVERSITÄT MÜNCHEN

FACHBEREICH: DENSE AND STRANGE HADRONIC MATTER (E62)

2023



TUM School of Natural Sciences  
Der Technischen Universität München

First measurement of the absorption of  ${}^3\overline{\text{He}}$  and  ${}^3\overline{\text{H}}$  nuclei in  
matter and its impact on  ${}^3\overline{\text{He}}$  propagation in the galaxy

Stephan A. Königstorfer

Vollständiger Abdruck der von der TUM School of Natural Sciences der Technischen  
Universität München zur Erlangung des akademischen Grades eines

Doktors der Naturwissenschaften (Dr. rer. nat.)

genehmigten Dissertation.

Vorsitz:

Prof. Dr. Alejandro Ibarra

Prüfer\*innen der Dissertation:

1. Prof. Dr. Laura Fabbietti

2. Prof. Dr. Susanne Mertens

Die Dissertation wurde am 31.1.2023 bei der Technischen Universität München  
eingereicht und durch die TUM School of Natural Sciences am 16.03.2023  
angenommen.

---

## Zusammenfassung

Antikerne in Kosmischen Strahlen werden seit langem als eine vielversprechende Sonde für indirekte Suchen nach WIMP dunkler Materie betrachtet, da in diesen Modellen WIMPs Antikerne durch Annihilation zu erzeugen. Sie gelten als so vielversprechende Sonde, weil das erwartete Antikernsignal von dunkler Materie bei niedrigen kinetischen Energien den Hintergrund, der von anderen astrophysikalischen Quellen erwartet wird, um mehrere Größenordnungen übersteigt. Tatsächlich wird nur eine einzige relevante Hintergrundquelle in Betracht gezogen: der Zusammenstoß von Hochenergie-Kosmischen Strahlen mit dem interstellaren Medium. Experimente der aktuellen Generation erreichen Empfindlichkeiten, die optimistische Modelle untersuchen können, und Experimente der nächsten Generation werden in der Lage sein, Signale sämtlicher Modelle vollständig aufzulösen, falls es existiert. Um aus einem solchen Signal Information zu entschlüsseln, müssen alle Wirkungen, die auf es einwirken, verstanden werden, und die Unsicherheiten jeder dieser Wirkungen bekannt sein. Die relevanten Prozesse sind die Produktion, Ausbreitung und schließlich die Annihilation dieser Antikerne. Auf der Erde werden Antikerne in hochenergetischen Teilchenkollisionen in Teilchenbeschleunigern produziert. Aufgrund ihrer Seltenheit können traditionelle "fixed-target" Experimente, die zur Messung der Annihilation-Wahrscheinlichkeiten (der sogenannten inelastischen Querschnitt) von Teilchen verwendet werden, nicht für niedrigerenergetische Antikerne verwendet werden. Die in dieser Dissertation vorgestellte Arbeit verwendete eine kürzlich entwickelte neue experimentelle Methode, um erstmals die inelastischen Querschnitte von  ${}^3\overline{\text{He}}$  und  ${}^3\overline{\text{H}}$  zu messen, und verwendete diese Messungen, um den Einfluss der Annihilation auf den erwarteten Antikernfluss in Kosmischen Strahlen zu bestimmen. Darüber hinaus wurde der gleiche Verfahren zur Bewertung des Einflusses von Antikern-Inelastischen Querschnitten auf ihre Ausbreitung auch auf Antideuteronen angewendet. Im Verlauf dieser Arbeit wurden auch die Unsicherheiten bezüglich der Propagation und Produktion von Antinukleonen neu evaluiert.

Der Inhalt meiner Dissertation ist daher die erstmalige Messung des inelastischen Wirkungsquerschnitts der  $A=3$  Antikerne  ${}^3\overline{\text{He}}$  und  ${}^3\overline{\text{H}}$ , sowie die erstmalige Bestimmung der experimentellen Unsicherheiten auf die  ${}^3\overline{\text{He}}$ - und Antideuteronflüsse auf Grund der Annihilation mit dem interstellaren Medium.

---

## Preface

Antinuclei in cosmic rays have long been considered a golden channel for indirect WIMP dark matter searches, since WIMPs are predicted to be able to annihilate to create antinuclei. They are considered such a promising probe because the expected antinuclei signal from dark matter at low kinetic energies exceeds the background expected from other astrophysical sources by several orders of magnitude. Indeed, only a single relevant background source is considered: the collision of high energy cosmic rays with the interstellar medium. Current generation experiments are reaching sensitivities which can probe optimistic models, and next generation experiments will be able to fully resolve any such signal, if it exists.

In order to decode any information from such a signal, all effects acting on it must be understood, and the uncertainties on each of these effects must be known. The relevant processes are the production, propagation, and finally annihilation of these antinuclei. On earth, antinuclei are produced in high energy particle collisions at particle colliders. Due to their rarity, traditional fixed target experiments employed to measure the annihilation probabilities (called the inelastic cross section) of particles cannot be used for low energy antinuclei. The work presented in this thesis used a recently developed new experimental method to measure the inelastic cross sections of  ${}^3\overline{\text{He}}$  and  ${}^3\overline{\text{H}}$  for the first time, and used these measurements in order to infer the effect of annihilation on the expected antinuclei flux in cosmic rays. Furthermore, the same procedure for evaluating the effect of antinuclei inelastic cross sections on their propagation has been applied to antideuterons. In the course of this work, the uncertainties concerning the propagation and production of antinuclei have also been re-evaluated.

The work carried out as part of my PhD has thus involved measuring the measurement of the inelastic cross sections of the  $A=3$  antinuclei  ${}^3\overline{\text{He}}$  and  ${}^3\overline{\text{H}}$ , as well as using them in order to determine the experimental uncertainties on  ${}^3\overline{\text{He}}$  and antideuteron fluxes due to annihilation, both for the first time.

---

## Acknowledgements

I am very happy to be able to write this section, and to thank the many people who played a part in getting me to this point. Not just this thesis, but much of my life has been a group effort, with wonderful people supporting me in different aspects. And while I hope to have helped them as much as they have helped me, it is still a pleasure to have this opportunity to specifically thank them.

Firstly, to the people without whom I would not be me at all. To my parents, Mami and Nico, go the biggest thanks I can give. Mami, not only did you push me to be my best all my life, but you supported me at every stop. This entire thesis is too short to list all the things I am grateful to you for, but fundamentally I want to say thank you for the unconditional love and the needed stern talks to keep things on track when you feel I lost my way. Nico, over the past 13 years you have never imposed your role as a stepdad. But every time I needed help or advice, or just wanted to chat, you were there. I learned so much from your calm way of discussing difficult topics, in particular to listen first and talk later (ok I'm still working on that one). I found a fantastic father figure in you, better than I could ask for. Thank you! And to my siblings, Flo, Elena, Tini and Prince Vince, thank you for all the great times we have together.

Tina – honey – loving you is my great joy, and has been for the past 5 years. Nobody else has listened to my ramblings about science, DnD, and everything else as intensely as you. I love all the times I learn from you, about fliG, and flagella and cryoEM, and about cross stitch, and dance, and the musical ideas behind the How to Train your Dragon theme. I love the geeky science conversations we have about the internal thermodynamics and chemistry of cheese melting, and I love planning our future together. Thank you for being there for me through everything.

To Benni – my very best friend – ours is a friendship which has changed me in many ways. You have been my best friend for almost 15 years, even though for 11 of these we have lived in different countries. You taught me very early on that I should not be so stuck in just my ways, but that other perspectives can have just as much value. Because our friendship is not build on mutual interest like most, but on the appreciation for the different interests we have, and on a foundation of the same base values. You are always there for me. Thank you for everything!

Now on to the people whose contribution was more directly related to my PhD. First and foremost is of course Laura, the boss. I remember the first few meetings we had, looking at plots which I had studied for the better part of the week, and you were able to pick out the critical points where something was wrong in less than

---

a minute. It took me a long time to realise that it was not just years of experience which made this possible, but the ability to ask critical questions of the information which is presented, to really try and understand the critical points. Out of all the things I learned from you over the last few years, I think this is what will stick with me the most.

Next thanks go all the people in our group, but in particular to the people I worked most closely with on the research which makes up this thesis: Ivan and Laura. Ivan, you taught me pretty much all that I know about antinuclei, and were the perfect discussion partner for all aspects of the analysis. And Laura, we worked together so closely on all the implementations in Galprop, the 100s of extra checks, the antideuteron paper, etc. We worked together through many late nights and got to know and like each other much better than I think either of us expected! We were always in the same boat whenever things were difficult, and managed to make it through together. I came to appreciate your unapologetic brand of honesty, by which you immediately get to the core of any subject. And I am very grateful that we became friends.

Finally, I want to thank my Master thesis supervisor, Prof. Paul Dauncey. You gave me another chance after I had struggled, otherwise I might not be handing in my PhD thesis today at all.

# Contents

<b>1</b>	<b>Introduction</b>	<b>1</b>
1.1	The goal of this work . . . . .	1
1.2	The standard model of particle physics . . . . .	1
1.3	Matter and antimatter in the universe . . . . .	6
1.4	Antimatter-matter annihilations . . . . .	10
1.5	Antinuclei in the cosmos . . . . .	17
1.6	Antinuclei on earth . . . . .	22
1.7	Dark matter and its connection to antinuclei . . . . .	24
<b>2</b>	<b>Experimental data and experimental method</b>	<b>35</b>
2.1	ALICE . . . . .	35
2.2	Identifying antinuclei and building the antiparticle-to-particle ratio .	43
2.3	Extracting the inelastic cross section from the antimatter-to-matter ratio . . . . .	58
<b>3</b>	<b>Measurement of the <math>{}^3\overline{\text{He}}</math> inelastic cross section</b>	<b>72</b>
3.1	Physics motivation and overview of the analysis method . . . . .	73
3.2	Secondary correction . . . . .	74
3.3	Results . . . . .	75
<b>4</b>	<b>Measurement of the antitriton inelastic cross section</b>	<b>77</b>
4.1	Physics motivation and overview of the analysis method . . . . .	77
4.2	Accessible momentum range of the measurement . . . . .	77
4.3	Secondary correction . . . . .	79
4.4	Results . . . . .	80
<b>5</b>	<b>Antinuclei in the cosmos</b>	<b>81</b>
5.1	Sources of antinuclei in the cosmos . . . . .	83
5.2	Constraining the propagation of antinuclei through the galaxy . . . . .	103
5.3	The Galprop framework . . . . .	108
5.4	Annihilations within our galaxy . . . . .	110
5.5	Antinuclei fluxes for different dark matter masses and annihilation channels . . . . .	111
5.6	Results for different dark matter profiles . . . . .	114
5.7	Discussion of the uncertainties on antinuclei fluxes and transparencies	119
5.8	Summary of propagation of antinuclei through the galaxy . . . . .	120
5.9	Experiments to detect antinuclei in the cosmos . . . . .	120

<b>6</b>	<b>Final remarks and outlook</b>	<b>126</b>
6.1	Measurements of the inelastic cross sections of antinuclei . . . . .	126
6.2	Use of these measurements . . . . .	126
6.3	Reevaluating physical and experimental effects on the cosmic anti-deuteron flux and its uncertainties . . . . .	128
6.4	Outlook . . . . .	129
<b>7</b>	<b>Appendix</b>	<b>130</b>
7.1	Current status of the evidence for and against (but mostly against) the existence of anti-stars . . . . .	130
7.2	Why the statistical hadronization model is not used for calculating (anti)nuclei yields from WIMP dark matter annihilations . . . . .	130



# 1 Introduction

## 1.1 The goal of this work

The main topic of this work is the annihilation of composite antinuclei in nuclear matter. This process – by which one or all of the antinucleons interact and annihilate with nucleons – destroys the antinucleus in the process. Because of these annihilations, antinuclei are some of the rarest stable objects in our matter dominated<sup>1</sup> universe, as once produced they tend to annihilate quickly on cosmic timescales. And only very rare processes even create antinuclei in the first place. But this rarity is why antinuclei have received increased attention in recent years [1, 2, 3, 4], since any process which gives a signal by producing antinuclei does not have to contend with large backgrounds, but can be searched for with hope for a clean signal. In particular, theories which go beyond the current standard model of physics and can produce antinuclei, often hail them as a golden channel for detection. But in order to make any inference from future antinuclei measurements from such processes, their properties must be known, including the chance by which they might annihilate before reaching our detectors. One theory in particular has a vested interest in antinuclei: the weakly-interacting-massive-particle (WIMP) dark matter model. Some versions of this model predict dark matter annihilations into antinuclei, which could enable an indirect channel into unveiling the nature of dark matter.

So this effort to aid the search for new physics thus joins two separate fields of study: high-energy physics, which allows us to produce and study the properties of antinuclei on earth, and the search for signals of dark matter in cosmic rays, in particular antinuclei. The goal of the work carried out during my PhD is the measurement of the inelastic cross sections of the  $A=3$  antinuclei, and the effect of the measured antinuclei inelastic cross sections on an antinuclei signal in cosmic rays near earth.

## 1.2 The standard model of particle physics

In this section a brief introduction to the standard model of particle physics is given, in order to introduce the terminology and concepts which will be used in this thesis. The standard model of particle physics describes the forces by which elementary particles interact with each other: the strong force, as described by quantum chromodynamics (QCD), the electromagnetic force as described by quantum electrodynamics

---

<sup>1</sup>It remains one of the biggest mysteries of physics why our universe is dominated by matter over antimatter, as the Big Bang should have produced them in equal amounts.

(QED) and the weak force as described by electroweak theory (EWT). The standard model has been incredibly successful in describing the three forces. The fourth fundamental force of nature, gravity, completes the description of nature, however, it remains unknown how to incorporate it into the standard model. Additionally, there are phenomena which are currently inexplicable within the standard model, notably dark matter and dark energy. This has prompted many searches for physics beyond the standard model (BSM), in order to complete our understanding of nature. So far however, these searches have remained without success.

In the standard model, there are 4 types of elementary particles: quarks, leptons, gauge bosons and the higgs scalar boson, which are summarized in figure 1. There are 3 generations of quarks and leptons, which differ from previous generations in their mass. Quarks are split into up-like quarks, with a  $+\frac{2}{3}$  electric charge<sup>2</sup>, and down-like quarks with a  $-\frac{1}{3}$  electric charge. Leptons are split between charged leptons with charge  $q = -1$  and neutrinos, which carry no electric or color charge, and are very light. There are 4 gauge bosons for the 3 fundamental forces which the standard model describes: the gluon ( $g$ ) for the strong force, the photon ( $\gamma$ ) for the electromagnetic force, and the W and Z bosons for the weak force. The weak bosons couple to all quarks and leptons as well as themselves, while photons couple to electrically charged particles (quarks and charged leptons), and gluons couple to quarks, since they carry a color charge<sup>3</sup>. Additionally, gluons can interact with themselves, since they also carry the color charge of the strong force. Finally, there is the scalar higgs boson, which is responsible for the mechanism which gives particles their mass. All quarks and leptons also have a corresponding antiparticle, with the same mass, spin and lifetime, but with all other quantum numbers inverted according to the charge, parity and time reversal (CPT) symmetry<sup>4</sup>.

Quarks always form composite particles made up of either three quarks (baryons) or a quark-antiquark pair (mesons). These two differ in the fact that baryons are fermions (half integer value spin) and mesons are bosons (integer value spin). The baryon number<sup>5</sup> is also conserved in all known reaction of the standard model, which means that the relative number of baryons-antibaryons remains constant. It is important to note why quarks are never found individually. Quarks carry color charge, which is the charge of the strong force. The shape of the strong force does not allow for isolated color charges to exist, a principle called color confinement. Unlike for example the electromagnetic force, which gets weaker as the distance

---

<sup>2</sup>Charges of elementary particles are given in multiples of the magnitude of the electron charge  $e$ .

<sup>3</sup>Color charge is the QCD equivalent of the electric charge.

<sup>4</sup>Further information about CPT symmetry can be found in any university level physics textbook, such as [5], and in section 1.2.1.

<sup>5</sup>The baryon number is a quantum number where baryons have 1 and antibaryons have -1.

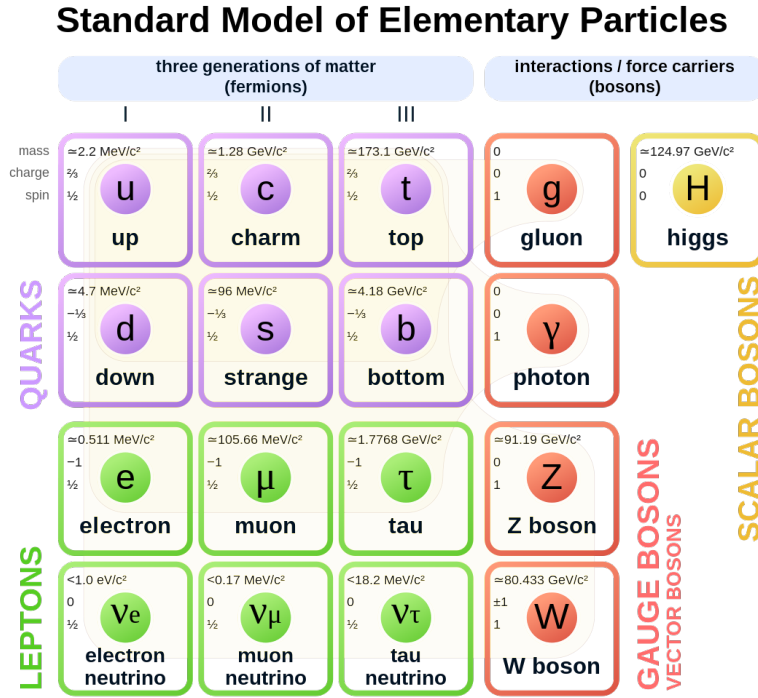


**Figure 1:** The particles of the standard model of particle physics. There are 3 generations of quarks and leptons, which differ from previous generations only in their mass. Quarks are split into up-like quarks, with a  $+\frac{2}{3}$  charge, and down-like quarks with a  $+\frac{1}{3}$  charge. Leptons are split between charged leptons with charge  $q = -1$  and neutrinos, which carry no electromagnetic or color charge, and are very light. There are 4 gauge bosons for the 3 fundamental forces which the standard model describes: the gluon ( $g$ ) for the strong force, the photon ( $\gamma$ ) for the electromagnetic force, and the  $W$  and  $Z$  bosons for the weak force. Additionally, there is the scalar higgs boson, which is responsible for the mechanism which gives other particles their mass.

between two particles grows, the strong force remains constant. The potential of the strong force can thus be phenomenologically described by the Cornell potential [6], as given in equation 1:

$$V(r) = -\frac{4}{3} \frac{\alpha_s}{r} + \kappa r, \quad (1)$$

62 where  $\kappa$  is constant. The second term of equation 1 dominates at large radii ( $>1 \text{ fm}$ ),  
 63 and is thus responsible for the long distance behavior of the strong force. The energy  
 64 stored in the field between two particles can be found by  $\delta E(r_1 - r_0) = V(r_1) - V(r_0) =$   
 65  $\int_{r_0}^{r_1} \vec{F} \cdot d\vec{r}$ , i.e. the path integral of the force along the separation between the particles.

66 If the force decreases enough<sup>6</sup> as the distance grows, this allows potential energy to  
 67 be stored in the field between two particles, without this energy becoming infinitely  
 68 large at large distances. However, if the force remains constant even with larger  
 69 distances, the energy stored in the field increases proportionally to the distance  
 70 between particles. For the strong force, this gluon field between two particles which  
 71 are being separated is often called a string. Eventually, enough energy is stored in  
 72 the string that a new antiquark-quark pair can be created, isolating the color charges  
 73 at each end of the string, thus splitting the string in two. The amount of energy stored  
 74 in gluon strings is estimated to be roughly 1 GeV/fm [7]. This mechanism, which is  
 75 shown in figure 2, is called string fragmentation, and is an intuitive explanation for  
 76 why the color charges of the strong force cannot be isolated.

77

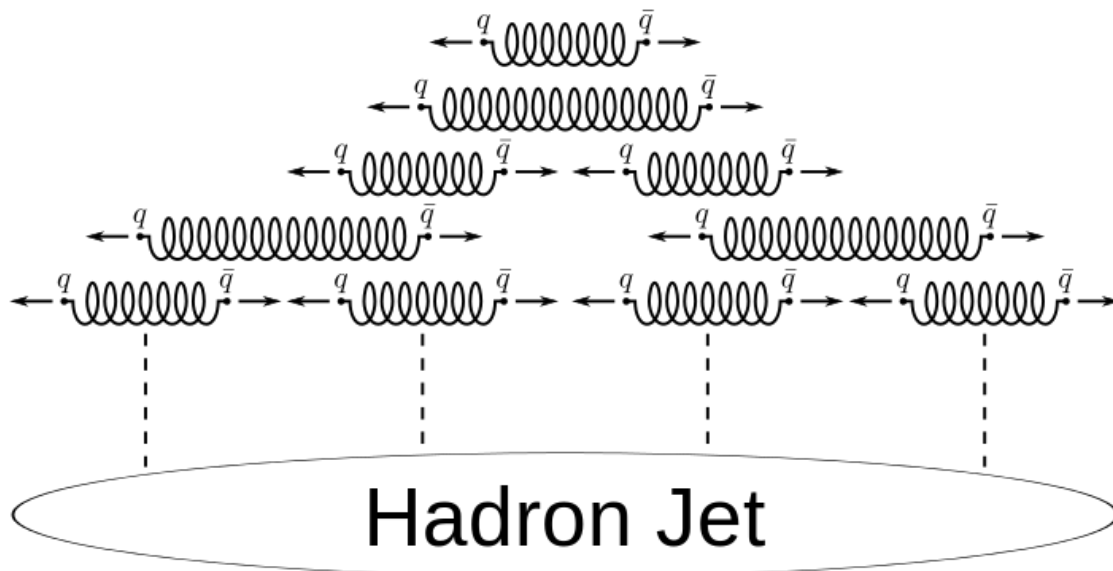


**Figure 2:** Color confinement by string fragmentation. As the antiquark-quark pair moved away from each other, more and more energy is stored in the color flux tube between them. Eventually, there is sufficient energy to create a new quark-antiquark pair, and thus truncate the flux tube. This process continues until the (anti)quarks run out of sufficient energy to create new quark-antiquark pairs. The quarks can then hadronise. The figure is taken from [8].

<sup>6</sup>If the force decreases as  $1/r$ , the integral of  $\int_{x_0}^{\infty} \frac{1}{r} \cdot d\vec{r} \propto \ln(r)$  will go to infinity at infinite distances, therefore the force simply decreasing is not sufficient. However, if the force decreases as  $1/r^2$  – as it does for the electromagnetic and gravitational forces – the integral is finite at infinite distances.

### 78 1.2.1 Symmetries and symmetry breaking within the standard model

79 Symmetries are a fundamental aspect of the standard model. A symmetry can be  
 80 defined as a global operation under which the laws of physics remain the same, and  
 81 they can be deceptively powerful. In fact, something as fundamental as conservation  
 82 of energy can be shown to be equivalent to a symmetry to translations in time. Other  
 83 continuous symmetries such as spatial translation and spatial rotation give rise to  
 84 conservation of momentum and angular momentum, respectively<sup>7</sup>. But there are  
 85 also symmetries which are not continuous, but discrete<sup>8</sup>. The standard model of  
 86 particle physics contains three important and related discrete symmetries [5]. Under  
 87 these symmetries, the laws of physics are expected to behave the same. C-symmetry,  
 88 which stands for charge and represents replacing particles with their antiparticles.  
 89 P-symmetry, which stands for parity symmetry, which represents spatial inversion  
 90 along the 3 physical axes. And finally T-symmetry, which stands for time-inversion  
 91 symmetry, which represents inversion of the direction of time.

92  
 93 They are called near symmetries, because each of them is individually broken  
 94 within the standard model. A symmetry can be broken in two ways: explicitly or  
 95 spontaneously. Explicit symmetry breaking is when the Lagrangian corresponding  
 96 to an interaction does not itself respect the symmetry, while spontaneous symmetry  
 97 breaking is when the Lagrangian respects the symmetry, but its ground state solution  
 98 does not. The most famous individual violation is the breaking of P-symmetry  
 99 of the weak force, which couples only to left-handed fermions and right-handed  
 100 antifermions. In other words, a system of fermions and antifermions inverted under  
 101 P-symmetry would no longer couple to the weak force, as the fermions are now right  
 102 handed and the antifermions left handed. It is then obvious that replacing particles  
 103 by their antiparticles would restore this symmetry. This combined symmetry is called  
 104 CP-symmetry, and is thought to be respected by the strong and electromagnetic  
 105 forces, however, there is a degree of CP violation in the mixing of different quark  
 106 generations by means of the weak force, as described by the Cabbibo-Kobayashi-  
 107 Masakawa (CKM) matrix. Introducing a complex phase in the quark mixing allows  
 108 for the weak force to violate CP symmetry [10].

109 This can be exemplified by the following consideration. Consider a process  
 110  $a \rightarrow b$ , and the corresponding process with the antiparticles  $\bar{a} \rightarrow \bar{b}$  and denote

<sup>7</sup>The relations between physical symmetries and conservation laws was established by Noether's first theorem [9].

<sup>8</sup>In order to distinguish between a continuous and discrete symmetry, consider the difference between spatial translations and spatial inversions. The first is an operation which moves a system to a different point in space. It does not matter if the movement happens by 1m or 1km, the symmetry should hold all the same and is thus considered continuous. Meanwhile, spatial inversion inverts the direction of the axes, similar to how a mirror inverts one axis. This is not a continuous operation, since it is impossible to "half-mirror" an object.

111 the amplitudes with  $M$  and  $\bar{M}$ . By CP symmetry (i.e. before the violation), these  
 112 numbers must be the same. We can separate them into a magnitude and a phase as  
 113  $M = \bar{M} = |M|e^{i\theta}$ . If there is a complex phase term introduced (for example by the  
 114 CKM matrix) the amplitudes become  $M = |M|e^{i\theta}e^{i\phi}$  and  $\bar{M} = |M|e^{i\theta}e^{-i\phi}$ . Since  
 115 measurable rates are proportional to  $|M|^2$ , CP symmetry is still conserved. However,  
 116 now consider the case where the reaction can take two different routes,  $a \rightarrow 1 \rightarrow b$   
 117 and  $a \rightarrow 2 \rightarrow b$  and the amplitudes become:  $M = |M_1|e^{i\theta_1}e^{i\phi_1} + |M_2|e^{i\theta_2}e^{i\phi_2}$  and  
 118  $\bar{M} = |M_1|e^{i\theta_1}e^{-i\phi_1} + |M_2|e^{i\theta_2}e^{-i\phi_2}$ . This allows the calculation of the differences in  
 119 amplitudes as  $|M|^2 - |\bar{M}|^2 = -4|M_1||M_2|\sin(\theta_1 - \theta_2)\cos(\phi_1 - \phi_2)$ . Thus, the introduction  
 120 of a complex phase causes a violation between matter and antimatter.

121 CP violation was first observed in the decays of neutral Kaons [11] in 1964, and was  
 122 confirmed in 1999 [12]. Since then it has also been observed in the decays of  $B$  and  
 123  $D$  mesons [13, 14]. CP violation is also necessary (but not sufficient) in order to  
 124 produce the matter-antimatter asymmetry, as is elaborated in section 1.3.3. Even  
 125 though the CP symmetry is being violated, the combined CPT symmetry is expected  
 126 to be conserved in all standard model processes [15, 16].

127 Lastly, let us consider what is known as the strong CP problem. The QCD La-  
 128 grangian must include a CP violating term in order to account for the difference  
 129 between the pion and  $\eta$  masses [17], which is characterised by a free parameter  
 130  $0 < \bar{\theta} < 2\pi$ . But by measurements of the neutron electric dipole moment it has  
 131 been shown that  $\bar{\theta} \lesssim 10^{-10}$ . This represents a fine tuning problem: there must be  
 132 a CP violating term in QCD, but it must also be set to be almost 0. So far, only one  
 133 convincing solution has been introduced: the Peccei-Quinn (PQ) model. This model  
 134 introduces a new global symmetry to the QCD Lagrangian, and a corresponding  
 135 scalar field. This symmetry is then spontaneously broken at low energies, creat-  
 136 ing the axion<sup>9</sup>, a promising alternative dark matter model. For a more detailed  
 137 mathematical description of the axion see [18].

## 138 1.3 Matter and antimatter in the universe

### 139 1.3.1 Origin of baryonic matter

140 The majority of the baryonic matter we see in the universe was created within the  
 141 first instances after the Big Bang. Initially, the universe was in a hot dense state,  
 142 with temperatures much higher than the masses of the elementary particles. In fact,  
 143 the temperature was so high that the higgs mechanism did not yet provide mass to  
 144 particles [19] ( $T \gtrsim 150$  GeV). During this time, quarks, leptons and bosons were in a  
 145 thermodynamic equilibrium. As the universe underwent inflation, it became colder  
 146 and colder, until eventually the higgs mechanism started to make particles massive

<sup>9</sup>The name axion comes from a brand of laundry detergent, and was chosen because the axion "cleans up" the strong CP problem.

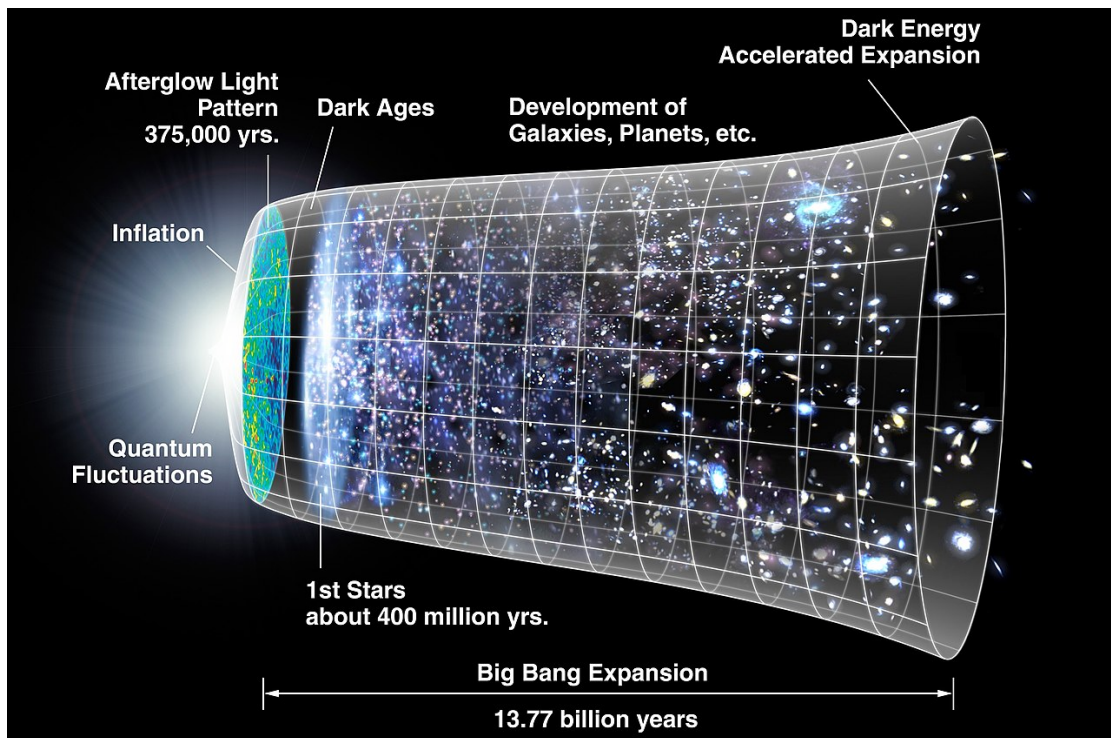


**Figure 3:** Timeline of the universe, starting from the Big Bang [22].

147 [19] (see section 1.3.4 for more details). This phase transition of the universe is one  
 148 option for the source of the matter excess in the universe. As the universe continued  
 149 to evolve and temperatures cooled, quarks and gluons first formed a quark-gluon  
 150 plasma – a state of matter in which color charges can move freely [20, 21] – and  
 151 eventually hadrons, which decay leaving only the most stable hadrons (protons and  
 152 neutrons) behind. At this point about 1s had passed since the Big Bang. From about  
 153 10s to 20 minutes after the Big Bang, the temperatures enabled nuclear fusion. It was  
 154 during this time that most of the deuterium, helium-4 and lithium in the universe  
 155 were formed.

156

157 The immediate period after the big bang shaped our universe in more ways than  
 158 simply creating an excess of matter over antimatter. The gravitational collapse of  
 159 dark matter during this time is thought to be responsible for the formation of galactic  
 160 structures [23]. The creation of nuclear matter determines the majority of the make  
 161 up of the universe to this day. The timeline of the evolution of the universe is shown  
 162 in figure 3.

### 1.3.2 A matter dominated universe: antimatter-matter asymmetry

To the best of our knowledge our universe is entirely dominated by matter over antimatter. This observation is staggering, because in all the reactions we can observe in particle physics experiments near earth, whenever new matter is produced the same amount of antimatter is produced as well. So the a priori assumption is that the universe houses as much antimatter as it does matter. And at first glance, this doesn't seem to impose any impossible constraints, as from a distance matter and antimatter are indistinguishable<sup>10</sup>. So while our solar system might be made of matter, what is to keep other solar systems, or even other galaxies from being made of antimatter? The issue arises when we look at the surroundings of solar systems or galaxies. Interstellar/intergalactic space is not completely empty, but populated at very low densities by protons and helium-4 from surrounding stars/galaxies. We know the density of protons in these regions to be about  $n_H \approx 1 \text{ cm}^{-3}$  for interstellar space [24], and  $n_H \approx 1 \text{ m}^{-3}$  for intergalactic space [25]. And when a matter dominated region and an antimatter dominated region are next to each other, then in this vast space of low density matter, plenty of annihilations would occur. These annihilations would produce distinctive signals in gamma ray searches, due to high energy photons emitted from  $e^+e^-$  annihilations or from the decay of  $\pi^0$ s produced in  $p\bar{p}$  annihilations [26]. The lack of any such signals places stringent limits on any large areas of antimatter within the observable universe, and leads us to believe that our universe is indeed dominated by matter. The source of this matter-antimatter asymmetry is one of the big remaining mysteries of physics.

It isn't known exactly how the different populations of matter and antimatter came to be. Perhaps only a minute difference between the two caused a tiny fraction more matter to be produced than antimatter. And since the majority of both annihilated, what we see today might be this tiny leftover fraction. For this reason, searches for differences between matter particles and their antimatter counterparts are looking to find even the tiniest discrepancy between the two [27, 28].

### 1.3.3 Sakharov condition

Given the a priori assumption that the same amount of matter and antimatter would be produced, it is necessary to clarify the conditions under which this could be altered. In [29], the necessary conditions for the creation of a baryon excess were shown to be:

- Some interactions of elementary particles must violate baryon number conservation, since the net baryon number of the universe must change over

<sup>10</sup>This means to say that matter atoms would produce the same spectral lines as antimatter atoms, and undergo the same fusion reactions we see in stars.



199 time

- 200 • C and CP must be violated so that there is no equality in the forward and  
201 backward rates of the baryon number violating processes.
- 202 • The net flux must be created in out-of-equilibrium conditions, since otherwise  
203 CPT symmetry would assure compensation of the effect.

204 The first condition is trivial. The second condition means that there must be a  
205 reaction which differentiates between the matter and antimatter, in order to give  
206 rise to a process which would preferably create baryons over antibaryons. The  
207 third condition requires some more explanation. It is based on the fact that we  
208 believe the CPT symmetry to be exact. Therefore, there must be a process which only  
209 happens in one direction in time. This cannot occur in an equilibrium condition,  
210 since in equilibrium all reactions occur in both the forward and backward directions.  
211 Therefore, it must be a reaction linked to out-of-equilibrium processes.

#### 212 1.3.4 Baryogenesis within the standard model

213 It is possible to account for the matter-antimatter asymmetry in the universe through  
214 standard model processes. One such process was outlined in [30]. The main argu-  
215 ments of this paper are reproduced here, to exemplify how the Sakharov condition  
216 above can be applied.

217  
218 The main idea of the mechanism is threefold: i) the existence of a first order phase  
219 transition as the universe cools below the electroweak phase transition. The phase  
220 transition satisfies the out-of-equilibrium part of the Sakharov conditions. ii) quarks  
221 and antiquarks scattering of the phase boundary in an asymmetric fashion, due to  
222 CP-violating effects. This results in a net baryon flux through the phase boundary.  
223 And iii), the excess antiquarks in the hot medium are removed by an effect which  
224 does not conserve baryon number, before the phase transition is complete in the  
225 entire universe.

226 In the standard model, particles get their mass by their Yukawa coupling to the  
227 higgs vacuum expectation value [31]. The vacuum expectation value of the higgs  
228 field vanishes at temperatures above the electroweak phase transition, such as were  
229 present during the early universe [19]. If this phase transition is treated as a first  
230 order phase transition, with bubbles of the colder phase forming out of the hot  
231 medium, then the vacuum expectation value of the higgs will change while crossing  
232 the phase boundary. This will change the masses of fermions as they move across  
233 this phase boundary, which thus acts as a potential barrier. This causes both quarks  
234 and antiquarks to scatter from this barrier. However, due to the CP-violating nature  
235 of the weak interaction, the transmission through the barrier can be different for  
236 quarks and antiquarks, resulting in a baryon flux through the phase boundary. Excess  
237 antiquarks in the medium are then removed by sphalerons. A sphaleron is a solution

238 to the electroweak field equations, geometrically represented by a saddle point which  
 239 connects a 3 baryon system to a 3 antilepton system<sup>11</sup> [32]. Sphaleron effects are  
 240 expected to be frozen out below about 10 TeV. Since the temperature is higher on one  
 241 side of the phase transition than the other, the baryon number symmetry violating  
 242 process is hypothesised to occur only on the hot side, and thus leave a net baryon  
 243 number.

244

245 While sphalerons are currently hypothetical, it is expected that the high luminos-  
 246 ity upgrade of the LHC will be able to start the experimental search for sphalerons  
 247 [33].

## 248 1.4 Antimatter-matter annihilations

249 The lightest quarks –  $u$  and  $d$  – make up normal nuclear matter, i.e. protons  $uud$   
 250 and neutrons  $udd$ , which are the two lightest baryons with masses of  $938 \text{ MeV}/c^2$   
 251 and  $939 \text{ MeV}/c^2$ , respectively. Since the proton is the lightest baryon, and the baryon  
 252 number must be conserved, any reaction of the proton with other matter must leave  
 253 an intact proton at the end, thus never making the energy stored in the proton’s mass  
 254 available to create new particles. When baryons interact with their antibaryons, they  
 255 annihilate, releasing their entire mass as available energy to create new particles.  
 256 This is because by definition, the total baryon number of such a reaction is 0. The  
 257 same is true for the annihilations of leptons and lepton number conservation, and  
 258 for the conservation of electric charge in the annihilations of leptons and baryons.  
 259 In principle, if a quantum number is antisymmetric under the C symmetry, it will be  
 260 conserved by construction in antimatter-matter annihilation events and thus will  
 261 never limit the available phase space of reactions.

262

### 263 1.4.1 Annihilation of $q\bar{q}$ and $l\bar{l}$ pairs

264 It is simplest to start with the Feynman diagrams for the annihilations of elementary  
 265 quarks and leptons. The lowest order diagrams are given in figure 4. Their relative  
 266 contribution is proportional to the force’s interaction strength to the exponent of  
 267 the number of vertices, so  $\alpha$  for the electromagnetic force,  $\alpha_w$  for the weak force  
 268 and  $\alpha_s$  for the strong force. At low energies, the three parameters have an ordering  
 269  $\alpha_s \gg \alpha \gg \alpha_w$ <sup>12</sup>. Essentially, quark and leptons can annihilate with their antiparticles  
 270 through electromagnetic and weak channels, which can also convert from quarks to

<sup>11</sup>And equivalently 3 antibaryons to 3 leptons.

<sup>12</sup>The couplings depend on the energy scale, as all of them are running coupling constants. At high energies, the weak force is actually stronger than the electromagnetic force. This difference is due to the mass of the weak bosons.

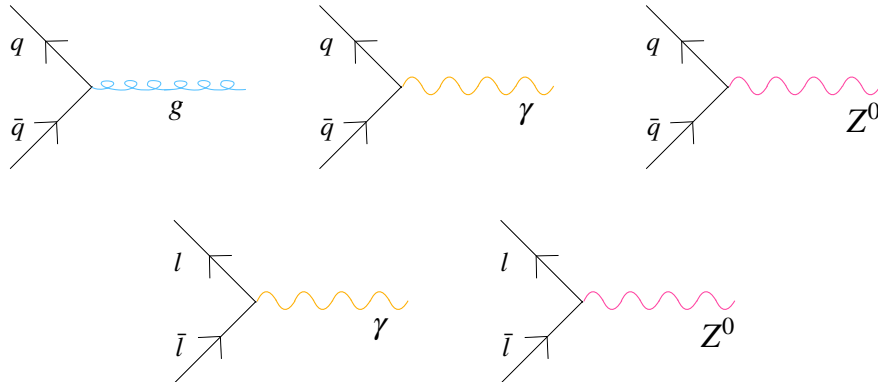


**Figure 4:** First order Feynman diagrams showing the annihilations of elementary particles. Top row: quark-antiquark annihilation through the strong (left), electromagnetic (middle) and weak (right) force. Bottom row: lepton-antilepton annihilation through the electromagnetic (left) and weak (right) force.

271 leptons and vice versa. Quarks can additionally annihilate via a gluon into either  
 272 another quark-antiquark pair or into hadron jets. For quarks, annihilation through  
 273 the strong force should outweigh annihilation through the electromagnetic force by  
 274 a factor  $\alpha_s^2/\alpha^2 \gg 1$ , which means that the strong channel should dominate.

#### 275 1.4.2 Antiproton-proton annihilations

276 It is important to note at the start of this chapter that there is currently no theory or  
 277 even model which can describe the available data for antiproton-proton annihila-  
 278 tions, or offer up an explanation for the underlying mechanism [34]. This is in stark  
 279 contrast to quark-antiquark annihilation, which is just a first order QCD process.  
 280 In this section I shall attempt to give an overview of the difficulties in describing  
 281 this process, and thereby offer up a qualitative picture of the possible annihilation  
 282 mechanisms.

283

284 It is tempting to assume that in order to scale up an annihilation event, one might  
 285 just be able to scale up the single Feynman diagrams for quark-antiquark annihila-  
 286 tion in order to get a description for antiproton-proton annihilation. However,  
 287 the picture is far more complicated. This can be intuitively understood by the fact  
 288 that (anti)protons are made up of 3 valence (anti)quarks, but in the annihilation

289 of (anti)proton pair, some of their valence (anti)quarks may well survive. In fact,  
 290 consider the following reaction  $p\bar{p} \rightarrow 3M$ , where  $M$  denotes a meson. This reaction  
 291 can occur by simply rearranging the quark content of the proton and antiproton,  
 292 which is illustrated in figure 5. Such a rearranging of the quarks can happen if the  
 293 quarks can feel each others strong potential, which can be mediated through pion  
 294 exchange. This can be seen as equivalent to nucleon-nucleon interactions through  
 295 pion exchange, at distances beyond the confines of color confinement. This effec-  
 296 tively allows the potential for quark rearranging to be felt at further distances than  
 297 the potential for quark-antiquark annihilation. The annihilation potential between  
 298 an antiproton-proton pair therefore can have a long range ( $\gtrsim 1 \text{ fm}$ ) and a short  
 299 range ( $\lesssim 1 \text{ fm}$ ) term, where the long range term is dominated by the rearrangement  
 300 of quarks and antiquarks into mesons, and the short range term is dominated by  
 301 quark-antiquark annihilation. The common notation of these processes is  $An$  and  
 302  $Rn$  for annihilation ( $A$ ) and rearrangement ( $R$ ) into  $n$  mesons.

303

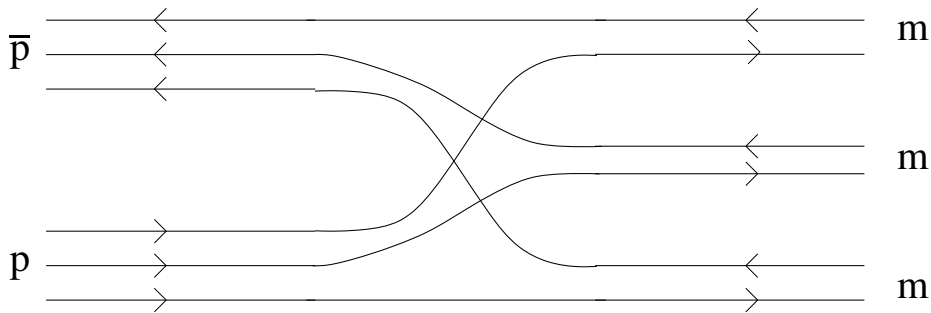


**Figure 5:** Schematic of  $p\bar{p}$  annihilation into 3 mesons, done by rearranging the valence quarks but without annihilating any quark-antiquark pair.

304 One important observable to distinguish between these two different annihila-  
 305 tion mechanisms is the production of strangeness, i.e. by the reaction  $p\bar{p} \rightarrow 2K + XM$ .  
 306 This reaction cannot occur with a simple rearrangement of quarks<sup>13</sup>, as a new  $s\bar{s}$   
 307 pair has to be created. If antiproton-proton annihilation would be dominated by the  
 308 rearrangement of quarks, we would expect to see almost no produced kaons, while if

<sup>13</sup>Neglecting quark-antiquark creation by string fragmentation.

309 the quark annihilation channel would dominate, we would expect to produce Kaons  
 310 almost as much as pions. In fact we observe about 5% of final states which include  
 311 kaons [34, 35], which suggests that the annihilation channel is suppressed compared  
 312 to the quark rearrangement channels.

313

314 Given these considerations, the antiproton-proton annihilation cannot easily be  
 315 described by perturbative QCD, and we are still missing an effective model capable  
 316 of explaining the data. This is why a quantitative description of this interaction  
 317 is so difficult. Instead, an empirical parameterization is commonly used to describe  
 318 the antiproton-proton inelastic cross section. A description accurately fitting the  
 319 available data has been proposed by Tan et al. [36], and is reproduced in equation 2,  
 320 where  $T_{\bar{p}}$  is the antiproton kinetic energy in the proton rest frame.

$$\sigma_{\text{inel}}^{p\bar{p}} = 24.7(1 + 0.584T_{\bar{p}}^{-0.115} + 0.856T_{\bar{p}}^{-0.566})\text{mb.} \quad (2)$$

321 Another description – which is implemented in the propagation code Geant4 – is  
 322 based on attempting to assign cross sections to each individual process which might  
 323 occur and is explained in [37]. In their model, they split the antiproton-proton anni-  
 324 hilation into the sub processes laid out in figure 6. The momentum dependence of  
 325 these processes is given by Regge theory [38, 37, 39]. This method works for deter-  
 326 mining the cross sections of particular channels, which is necessary for an accurate  
 327 description of particle propagation, as is shown in figure 7. However, this model does  
 328 not match experimental data better than within a factor two. This highlights the  
 329 difficulties in accurately predicting the inelastic cross section of antiproton-proton  
 330 annihilations.

331 An overview of available data on the antiproton-proton annihilation data is given  
 332 in [35, 41, 40].

### 333 1.4.3 Antiproton-nucleus annihilation: the Glauber model

334 In the previous section it has been established that while the antiproton-proton  
 335 inelastic cross section has been well measured, a theoretical model is still lacking. In  
 336 this section we therefore focus on the experimental results for antiproton-matter  
 337 annihilations, and how we can use them to infer the annihilation mechanism.

338

339 When moving from antiproton-proton to antiproton-nucleus annihilations, sev-  
 340 eral new effects come into play. The question is if only one nucleon in the nucleus  
 341 interacts in the initial annihilation, and then how the antinucleus acts after the anni-  
 342 hilation occurs. Thankfully, while those points certainly raise additional difficulties  
 343 in finding a theoretical description, we can benefit from measurements of antiproton

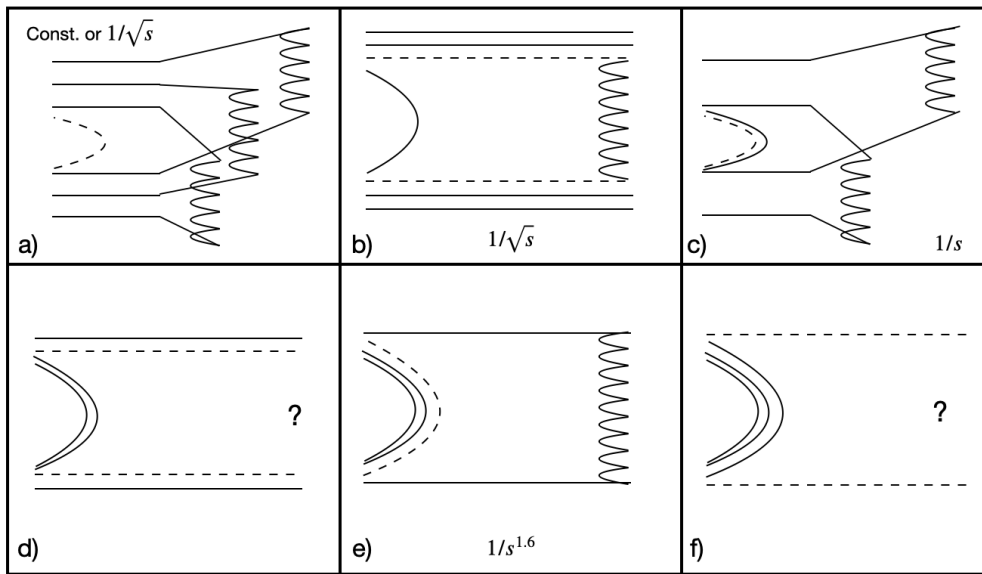


**Figure 6:** Annihilation channels for antiproton-proton. The solid lines represent quarks and the dashed lines represent a gluonic string (which can then decay via string fragmentation, as shown in figure 2). Curled lines represent  $\bar{q}q$  annihilations. The diagrams thus represent: a) 3 antiquark-quark annihilations; b) a single antiquark-quark annihilation into 2 mesons and a gluon string; c) corresponds to a quark-antiquark and string annihilation, with the creation of 2 quark-antiquark strings. Diagrams e) and f) can produce exotic mesons. Figure taken from [38].

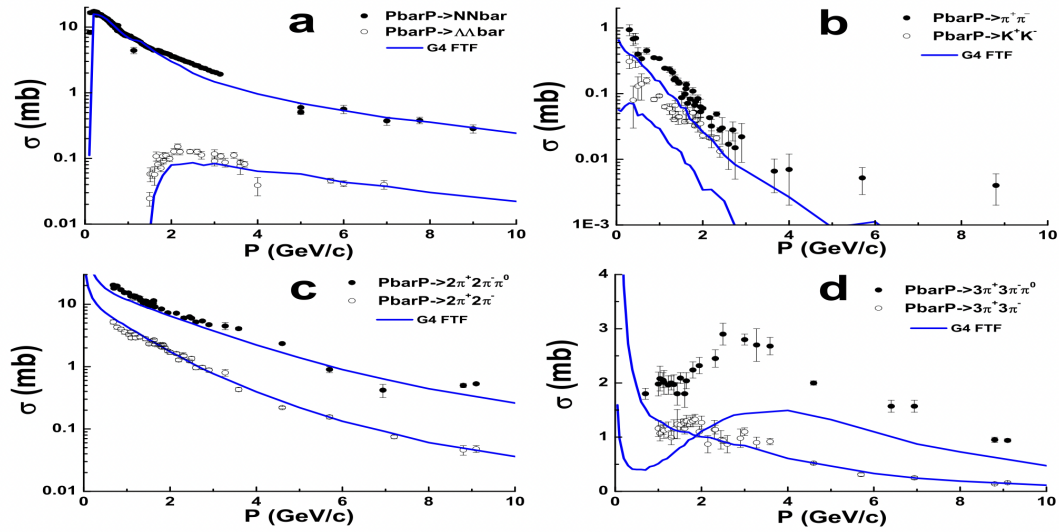


**Figure 7:** A comparison of antiproton-proton inelastic cross section data with the model used in Geant4 [37]. Points are experimental data as described in [40], the blue line represents the model. See text for details.

344 absorption. These are parameterised according to the Glauber model [42, 43, 44].  
 345 The Glauber model parameterises the inelastic cross section of antiprotons on nuclei  
 346 as a geometric scaling of the antiproton-proton cross section, according to equation  
 347 3, where  $R_A$  is a free parameter which can be roughly understood as the target nu-  
 348 cleus' radius, and characterised as  $R_A = r_0 A^{1/3} f(A)$ .  $r_0 = 1.1$  fm, and  $0.8 < f(A) < 1.1$   
 349 is a correction factor as a function of  $A$ .  $h$  denotes the hadron in question,  $A$  is the  
 350 mass number of the target nucleus and  $\sigma_{hN}^{tot}$  is the total antiproton-nucleon cross  
 351 section

$$\sigma_{hA}^{in} = \pi R_A^2 \ln \left[ 1 + \frac{A \sigma_{hN}^{tot}}{\pi R_A^2} \right]. \quad (3)$$

#### 352 1.4.4 Antinuclei-matter annihilations: the Glauber model and geometric scaling

353 Having established the details of the antiproton inelastic cross section, we can now  
 354 start to consider the process of antinuclei annihilation. All the considerations made  
 355 for the antiproton inelastic cross section still hold true, but additionally there is  
 356 also the potential between the antinucleons to consider. This means that one not  
 357 only has to consider the breakup of the matter nucleus, but also the breakup of the

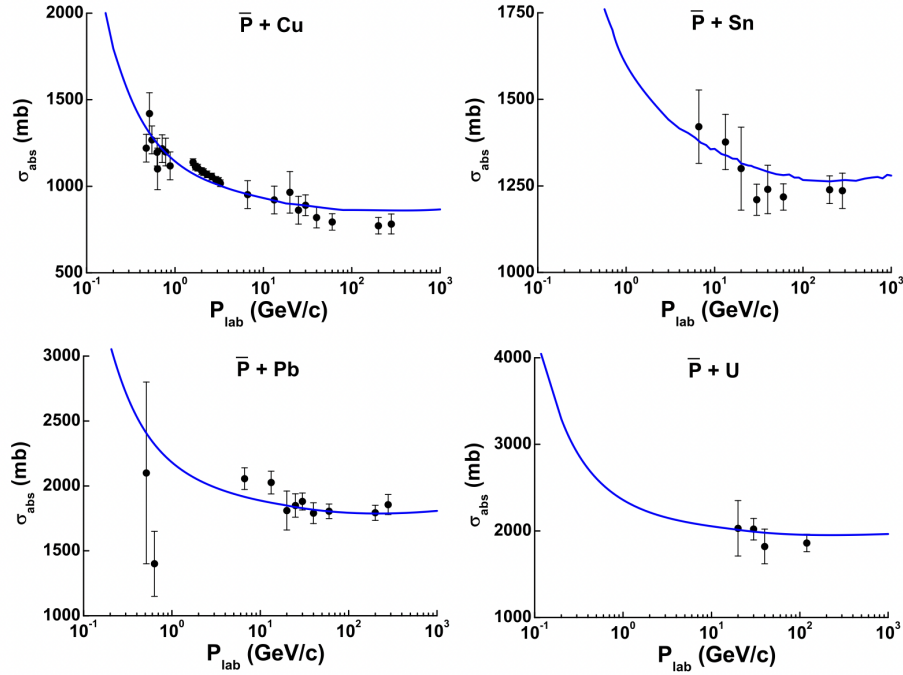


**Figure 8:** Antiproton-nucleus annihilation for different materials, taken from [44].

358 antimatter nucleus, leaving a smaller antinucleus behind. This has been observed  
 359 for antideuterons in the reaction  $\bar{d} + A \rightarrow \bar{p} + X$  [45, 46]. However, it is not clear if  
 360 the antiproton which was measured survived the initial collision or if it was created  
 361 from the annihilation of the antideuteron.

362

363 In order to scale up the cross sections from antiproton-nucleus to antinucleus-  
 364 nucleus annihilations, we can also employ the Glauber model. The full mathematical  
 365 treatment can be found in [47], however, due to the computational effort required to  
 366 do real time Glauber calculations, Geant4 uses a parameterization to approximate  
 367 the result of Glauber calculations. This parameterization is based on extending  
 368 3 to light antinuclei, according to equation 4, where  $B$  is the mass number of the  
 369 antinucleus

$$\sigma_{BA}^{in} = \pi(R_A^2 + R_B^2) \ln \left[ 1 + \frac{BA\sigma_{hN}^{tot}}{\pi(R_A^2 + R_B^2)} \right]. \quad (4)$$

370  $R_A$  is then used as a fit parameter to tune the simplification to the expected value of  
 371 full Glauber calculations. The form of  $R_A$  is given by equation 5



antinucleus	$c_1$	$c_2$
$\bar{p}$	1.31	0.9
$\bar{d}$	1.38	1.55
${}^3\bar{\text{He}}/{}^3\bar{\text{H}}$	1.34	1.51
${}^4\bar{\text{He}}$	1.30	1.05

**Table 1:** Constant values for determining the fit parameter  $R_A$  used in the Geant4 Glauber approximation for antinucleus-nucleus collisions [44].

$$R_A = c_1 A^{0.21} + c_2 A^{1/3}, \quad (5)$$

372 where  $c_1$  and  $c_2$  are constant whose exact value depends on the antinucleus on  
373 question. The values are given in table 1 for the antinuclei up to  $A = 4$ .

## 374 1.5 Antinuclei in the cosmos

### 375 1.5.1 Why producing antinuclei is so difficult: production mechanisms of anti- 376 uclei

377 The difficulty in producing antinuclei is not just to the necessary energy to create  
378 them, but also due to their production mechanism.

379  
380 The exact production mechanism for composite antinuclei in high energy particle  
381 collisions is still unknown. There are currently two models aiming to describe this  
382 phenomenon. The first is the statistical hadronization model, which models the  
383 production of the nuclei as a statistical process with a characteristic temperature (at  
384 heavy ion collisions at the LHC this temperature is 156 MeV [48]). This model has  
385 had great success by describing particle yields over 9 orders of magnitude in yield,  
386 as is shown in figure 9. The SHM is a grand canonical ensemble, since new particles  
387 can be created in hard scatterings.

388 The problem with the statistical hadronization model is that it predicts a the  
389 production of nuclei from a thermalized medium, when the binding energy of the  
390 nuclei is far below the temperature given by the model. For example, the deuteron  
391 binding energy is  $\approx 2.2$  MeV, compared to the temperature of 156 MeV predicted  
392 by the model. This has been dubbed the "snowball forming in hell" problem. Ad-  
393 ditionally, the statistical hadronisation model says nothing about the underlying  
394 mechanism by which the nucleons form antinuclei.

395  
396 The second model is the coalescence model. This model considers the relative  
397 momenta of nucleons produced in the collision, and if they are close enough together,

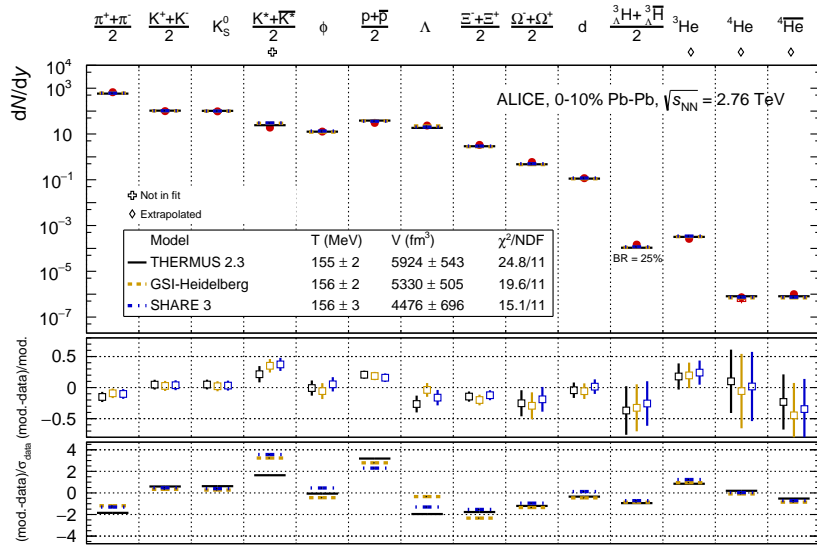


**Figure 9:** Statistical hadronisation model fits, with three different implementations, to the light flavour hadron yields in central (0-10%) Pb–Pb collisions at  $\sqrt{s_{NN}} = 2.76$  TeV. The upper panel shows the fit results together with the data, whereas the middle panel shows the difference between model and data normalised to the model value and the lower panel the difference between model and data normalised to the experimental uncertainties. Figure and caption taken from [48].

398 assigns them a chance to bond together and form a nucleus. The advantage of this  
 399 is then that given a set of space and momentum coordinates<sup>14</sup>, the coalescence  
 400 model can predict the nuclei spectra from the spectra of protons and neutrons. This  
 401 relation is then experimentally characterized by equation 6:

$$B_A = E_A \frac{d^3 N_A}{d p_A^3} \left[ \left( E_{p,n} \frac{d^3 N_{p,n}}{d p_{p,n}^3} \right)^A \Big|_{\vec{p}_p = \vec{p}_n = \vec{p}_{A/A}} \right]^{-1} \quad (6)$$

402 , where  $B_A$  is the coalescence parameter. While this model also requires fits to ex-  
 403 perimental data in order to give predictions of the yields and spectra of antinuclei,  
 404 it gives an explanation for the mechanism of how nucleons bond together. Several  
 405 versions of the coalescence model exist, which differ mostly in the criteria for when  
 406 two nucleons coalesce. The simplest form – often called "hard sphere" coalescence –  
 407 is to consider a threshold relative momentum in the pair rest frame, and any pair  
 408 below this threshold will coalesce. This model is not very predictive, since it requires  
 409 fits to data of each energy of interest in order to determine this threshold value  $p_0$ .  
 410 Expanding on this approach, the wave functions of the nucleons and the resulting  
 411 nucleus can be considered. This is called "Wigner function coalescence"; it is out-  
 412 lined in [49, 50] and was recently tested against data in [51]. This approach considers  
 413 both momentum and space coordinates, and therefore can take the system size  
 414 into account. The size of the system is important, since a priori it is expected that if  
 415 particles are further apart, they are less likely to coalesce. For a more comprehensive  
 416 review of the coalescence model, see [52, 53].

417  
 418 What can we infer from these models on the production of antinuclei? The impor-  
 419 tant takeaway for this thesis is that their production relies on significant amounts of  
 420 available energy, and on producing two nucleon close in both space and momentum.  
 421 These restrictions limit the production of antinuclei to high energy collisions or  
 422 exotic production channels.

### 423 1.5.2 Why to we care: antinuclei as a golden channel for new physics

424 The main reason why cosmic ray antinuclei make such an interesting probe for new  
 425 physics is twofold: i) the rarity of the standard model processes which produce them  
 426 means that any signal does not have to contend with a copious background and ii)  
 427 that there are already viable theories of new physics – namely WIMP dark matter –

<sup>14</sup>Traditionally coalescence models neglect the spatial correlation part, assuming that the nucleons are close enough together in space to coalesce. And any difference between the sizes of collision systems is then accounted for by a different coalescence parameter.

428 which predict a detectable antinuclei signal. This has led to the coining of cosmic  
429 ray antinuclei as a "smoking gun" for new physics.

430  
431 The first discovery of antimatter in cosmic rays was also the first discovery of  
432 antimatter in general: the discovery of the positron in charged particle showers from  
433 cosmic rays, in 1932 [54]. The discovery of antiprotons in cosmic rays would take  
434 almost half a century more, finally being observed in 1979 [55, 56]. During this time,  
435 antiprotons in cosmic rays were a probe into the matter-antimatter asymmetry of  
436 the universe, as their abundance could give a hint to the presence of antimatter  
437 dominated regions in our galaxy. Their discovery and study to the present day are  
438 consistent within uncertainties with production from high energy collisions of cos-  
439 mic rays with the interstellar medium, providing no evidence for any antimatter  
440 dominated regions<sup>15</sup>. The antiproton to proton ratio in cosmic rays is roughly  $10^{-4}$ .

441  
442 Nowadays, the focus is on the search for antinuclei as a probe of new physics. The  
443 expected production from high energy cosmic ray collisions is very low, particularly at  
444 low energies (see section 5 for exact values), while several dark matter models predict  
445 an antinuclei flux within reach of current or next generation detectors [57]. The  
446 antinuclei of interest are antideuterons ( $\bar{d}$ ) and anti Helium-3  ${}^3\bar{\text{He}}$ .  $\bar{d}$ s are expected to  
447 be produced in greater amounts than  ${}^3\bar{\text{He}}$ , since they only consist of 2 antinucleons  
448 rather than 3. However, since  $\bar{d}$  have the same charge as the antiproton, which  
449 exist far more copiously, they are more difficult to detect experimentally. This is  
450 because the signal for  $\bar{d}$ s can overlap with the tail of the antiproton signal.  ${}^3\bar{\text{He}}$  on  
451 the other hand is much easier to detect experimentally, due to its double charge,  
452 and the associated quadrupled specific energy loss (see equation 12). For both,  
453 the background in the low energy region (below a few GeV/nucleon) is expected to  
454 several orders of magnitude below the expected signal strength. This is in strong  
455 contrast to searches involving gamma rays [58], or antiprotons [59, 60], where the  
456 signal to background ratio is expected to be on or below the % level. Thus, an  
457 observation of a low energy antinuclei flux would be a sign for new physics.

### 458 1.5.3 What affects antinuclei in cosmic rays: production, propagation and anni- 459 hilation

460 As explained in the previous section, low-energy antinuclei in cosmic rays provide  
461 a uniquely background free probe into new physics. But in order to interpret any  
462 future observation, it is necessary to understand what affects their abundance and  
463 spectral shape. These factors can be summed up as 3 things: their production, propa-

<sup>15</sup>Nowadays constraints on antimatter dominated regions are more stringently set by gamma ray searches.

464 gation and annihilation. While a more detailed description of each is given in section  
 465 5, this section aims to give a brief introduction on the importance of the three aspects.

466  
 467 The production of antinuclei in cosmic rays can be classed into two categories:  
 468 i) production in high energy collisions of cosmic rays with the interstellar medium  
 469 and ii) new, exotic sources. This is different to light nuclei in cosmic rays, whose  
 470 production is dominated by their production in the stellar cycle. Their production  
 471 in high energy cosmic ray collisions can be somewhat constrained by experiments  
 472 at accelerators, which probe fundamentally the same reaction of  $p + p \rightarrow \bar{d}/^3\bar{\text{He}} + X$ .  
 473 However, the energies and rapidities at which production mostly occurs are usually  
 474 at much lower energies than the ones probed by accelerators, e.g. for antideuterons  
 475 the most important centre-of-mass energy for production in high energy cosmic  
 476 rays is  $\sqrt{s} \approx 25$  GeV (see figure 55). For a more detailed and quantitative discussion  
 477 of the relevant energies please see section 5. Furthermore, the experiments most  
 478 capable of studying antinuclei, the ALICE (A Large Ion Collider Experiment) experi-  
 479 ment at the LHC and the STAR experiment [61] at the Relativistic Heavy Ion Collider,  
 480 probe their production at midrapidity, rather than at the highly forward rapidities  
 481 relevant for production in cosmic ray collisions. This means that for much of the  
 482 relevant parameter space for production, extrapolation from experimental data is  
 483 necessary. On the other hand, production from new physical processes – such as  
 484 the annihilation of WIMP dark matter which is discussed in detail in this thesis – is  
 485 even less constrained, and has to be probed by letting Monte Carlo simulations run  
 486 from an assumed standard model state in the annihilation.

487  
 488 Once the antinuclei are produced, they travel through the galaxy until they even-  
 489 tually reach earth. On this journey they are affected by magnetic fields, bulk motion  
 490 (i.e. diffusion and convection effects), as well as other effects. The good thing is that  
 491 these affects are the same for all cosmic rays, and can therefore be constrained by  
 492 observations of more abundant cosmic ray species. Recent work on the topic was  
 493 done in [62, 63], and is explained in more detail in section 5.

494  
 495 On their journey, antinuclei do not merely travel through empty space; the space  
 496 between stars is filled with the diffuse interstellar medium (ISM), which is made up  
 497 of about 0.9 protons per cubic centimeter [24]. As antinuclei traverse this matter,  
 498 they might interact and annihilate with it. To account for this loss it is necessary  
 499 to quantify the inelastic cross section of antinuclei down to low energies. The mea-  
 500 surement of these cross sections and the quantification of their effect on antinuclei  
 501 losses is the topic of this thesis.

## 502 **1.6 Antinuclei on earth**

503 On earth, we have the ability to artificially produce antinuclei at high energy physics  
 504 facilities, like the LHC. In fact, antideuterons were first observed in 1965 in collisions  
 505 of protons on Beryllium at the Proton Synchrotron [64]. Since then, antinuclei  
 506 have been observed in higher energy collisions in much larger amounts, both at  
 507 CERN facilities [65, 66, 67, 68], and heavy ion facilities [69]. The ALICE experiment  
 508 in particular, has published spectra of antinuclei up to  ${}^4\overline{\text{He}}$  [65, 66, 67, 68] in both  
 509 pp and Pb-Pb collisions. This section aims to give an overview of the studies of  
 510 antinuclei on earth.

### 511 **1.6.1 Production at accelerators**

512 Production at accelerators can be classed by energy, and by collisions system. En-  
 513 ergy affects the barychemical potential <sup>16</sup>, while the collisions system determines  
 514 the penalty factor for producing heavier (anti)nuclei. The penalty factor – which  
 515 describes the amount by which the production of (anti)nuclei is suppressed for each  
 516 additional nucleon – is roughly 1/300 in Pb–Pb collisions at 5.02 TeV, while being  
 517 roughly 1/1000 in pp collisions at 13 TeV [72]. The relative  $p_T$  integrated yields of  
 518 nuclei are shown in figure 10.

### 520 **1.6.2 Annihilation at accelerators**

521 Traditionally, annihilations have been studied in fixed target experiments [46, 45, 40].  
 522 In those experiments, a beam of antiparticles is produced and then fired at a target.  
 523 The number of particles before and after the target are measured, and the resulting  
 524 disappearance probability is used to calculate the inelastic cross section. However,  
 525 this method relies on the ability to produce a clean beam of antiparticles, with suf-  
 526 ficient statistics to conduct such an experiment. This comes with two challenges:  
 527 i) the difficulty of producing antinuclei due to the required energy thresholds and  
 528 ii) producing the antinuclei in a focused direction, so that they can be captured  
 529 directed towards a target. These two constraints are unfortunately counterproduc-  
 530 tive. In order to compensate the difficulty of meeting the energy requirement for the  
 531 collisions, it is far more energetically favourable to collide in the particles rest frame,  
 532 however, this produces particles in all directions, not focused towards the beam  
 533 direction. This makes such measurements increasingly more difficult for higher

---

<sup>16</sup>The baryochemical potential is a measure of how much more energy is required to produce antibaryons to baryons. A value of 0 means that they are produced in equal amounts, and is found at LHC energies at mid-rapidity [70, 71].

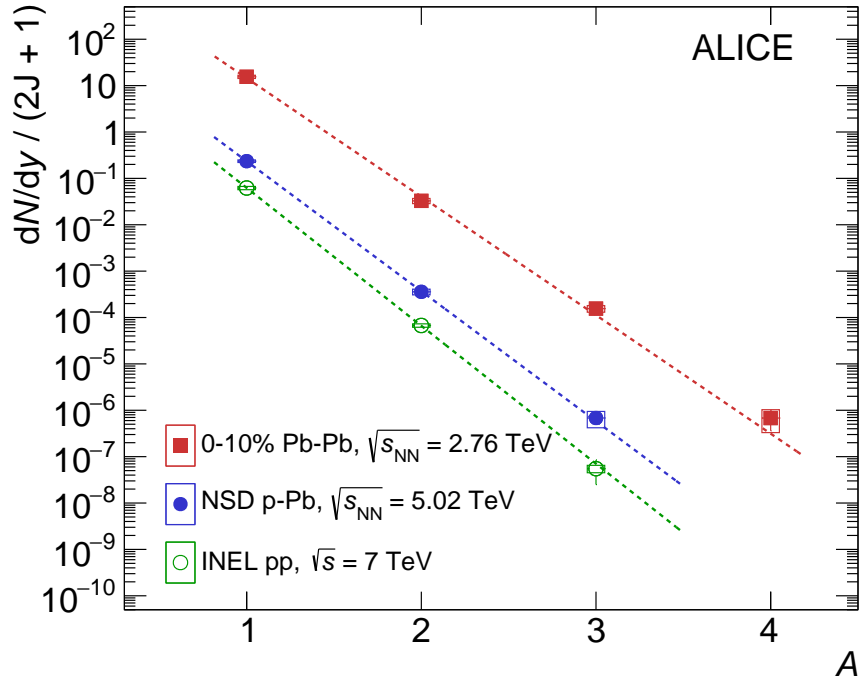


**Figure 10:** Production yield  $dN/dy$  normalised by the spin degeneracy as a function of the mass number for inelastic pp collisions, minimum-bias p-Pb and central Pb-Pb collisions. The empty boxes represent the total systematic uncertainty while the statistical errors are shown by the vertical bars. The lines represent fits with an exponential function. Figure taken from [72].

534 mass antinuclei.

535

536 However, since antinuclei up to  $A = 4$  have been observed in heavy ion collisions  
 537 [48], they also have to annihilate in the detector. But it is far more difficult to find  
 538 an equivalent observable to the fixed target experiment within such an experiment,  
 539 because it is a priori not possible to know how many particles get produced, and  
 540 therefore the "loss" of particles is not trivial to measure. The methods developed  
 541 to measure this loss are the topic of this thesis and will be explained in section 2,  
 542 so just a brief introduction is given here. The first method is based on using the  
 543 knowledge of nuclei production and the baryochemical potential to calculate how  
 544 many antinuclei should have been produced. The second is based on measuring  
 545 the particles individually in two different detector systems, and to calculate the loss  
 546 between the two.

## 1.7 Dark matter and its connection to antinuclei

In this section a brief introduction into the motivation and evidence for dark matter is given, several prominent dark matter models are discussed, with a particular focus on WIMP dark matter. Furthermore, the connection with WIMP dark matter and antinuclei is discussed.

### 1.7.1 The evidence for dark matter

The first evidence for dark matter was observed by Zwicky [73] in 1933, who realised that the rotation curves in galaxy clusters could not be caused solely by the luminous matter observed. His conclusions were not taken seriously until almost 40 years later, when the search for missing mass caused by the advent of cosmology made his theory of dark matter attractive. During this time, the big bang cosmology had prevailed, but left open the question of the ultimate fate of universe. Within big bang cosmology, there are three options. The first is that the universe expands forever, with the gravitational pull merely slowing down the expansion over time, never stopping it. The second is a closed universe, where the density of matter is bigger than some critical density, and therefore will eventually outperform the expansion, causing a collapse of the universe back towards a hot dense medium. And finally, a flat universe, where the density is exactly this critical density, such that eventually the gravitational pull of galaxies will exactly counterbalance the expansion, asymptotically reducing the expansion to 0. From Einstein's theory of general relativity, it can be shown that these fates correspond to the geometry of the universe, and are characterised by a density  $\Omega$ , where the critical density leading to a flat universe is given by  $\Omega_c h^2 = 1$  [74, 75]. It was expected that the geometry of the universe is flat<sup>17</sup>, but observations from galaxy clusters showed that luminous matter only made up a fraction of this density [75]. Cosmologists turned back to Zwicky's discovery [76, 77], claiming that dark matter made up the missing mass.

More evidence of dark matter was soon to follow. Tracking the rotation curve in galaxies provided evidence for dark matter bound in galaxies [78, 79, 76]. Measuring the dispersion velocities of galaxies around other galaxies (such as the

<sup>17</sup>This means that the local geometry of spacetime is euclidean, which means that all the angles in a triangle in this space add up to 180 degrees. As a counterexample to euclidean space, consider the surface of a sphere, like the surface of earth. It seems locally euclidean, when you lay a triangle on flat ground and add up the angles, they come out to 180 degrees within the measurement uncertainties. But now consider an airplane which starts at the equator flying due north to the north pole. Once it reaches there it makes a 90 degree turn, and flies due south until it once again reaches the equator. It then turns 90 degrees again so it flies along the equator back towards its original destination. The triangle made by the airplane consists of 3 90 degree angles, or 270 degrees. As such, the surface of a sphere like earth is not a euclidean space.



577 velocities of dwarf galaxies around a more massive one) or around galaxy clusters  
 578 provided evidence for dark matter trapped in larger gravitationally bound structures,  
 579 as did gravitational lensing [80]. For a comprehensive review of the evidence for dark  
 580 matter see the particle data group [74]. Each piece of evidence points to a type of  
 581 matter which does not interact electromagnetically (hence "dark"), and makes up  
 582 the majority of the mass found in cosmic structures.

583

584 Further evidence for dark matter can be found in structure formation in cos-  
 585 mology. From anisotropies in the cosmic microwave background (CMB), it can  
 586 be inferred that at the time of CMB decoupling the baryonic density fluctuations  
 587 were of order  $\delta\rho_{\text{rec}}/\rho \approx 10^{-5}$ . Since these fluctuations scale linearly with the ex-  
 588 pansion of the universe, today's baryonic density anisotropies can be calculated  
 589 as  $\delta\rho_b/\rho|_{\text{today}} \approx 10^{-2}$  [74]. Since matter is highly concentrated into galaxies in the  
 590 present day universe, fluctuations are  $\delta\rho_b/\rho|_{\text{obs}} \gg 1$ . This discrepancy can be  
 591 solved by adding a dominant non-relativistic, collisionless component the mix,  
 592 which decoupled from thermal equilibrium well before the CMB. In other words, in  
 593 order to explain structure formation from the early universe, one needs a dominant  
 594 component of the mass to be in a form which does not interact electromagnetically,  
 595 and does not heavily self-interact, which is also what is needed in order to explain  
 596 the present-day observations of galactic motion.

597

598 Finally, it is important to discuss the difference between hot and cold dark matter.  
 599 Dark matter which was thermally produced in the early universe – called a thermal  
 600 relic – can be split into two categories: hot relics, which were still ultra-relativistic  
 601 when they decoupled from thermal equilibrium, and cold relics, which were no  
 602 longer relativistic, or cold enough to significantly cool from the expansion of the  
 603 universe. Due to the different velocities of these relics, hot relics are expected to  
 604 cause sharp features in the large scale structure of the universe, while cold dark  
 605 matter is expected to cause a smooth large scale structure. This can be understood  
 606 as how easily a particle is trapped in a gravitationally collapsed structure. After an  
 607 initial overdense region forms and a gravitational well builds, slow (cold) particles  
 608 will be trapped in the well first, while fast (hot) particles will not be trapped in the  
 609 well until the gravitational well becomes much deeper. To get an idea of the order of  
 610 magnitude of velocities, consider the escape velocity of our galaxy, which lies around  
 611 600 km/s [81], which is equivalent to  $\beta \approx 2 \times 10^{-3}$ . Thus, relativistic particles would  
 612 provide a counterbalance to the formation of gravitationally collapsed structures,  
 613 and thus require deeper wells for large scale structures to form. This feature can be  
 614 seen in 11, which shows that the large scale structure of our universe prefers the cold  
 615 dark matter model.

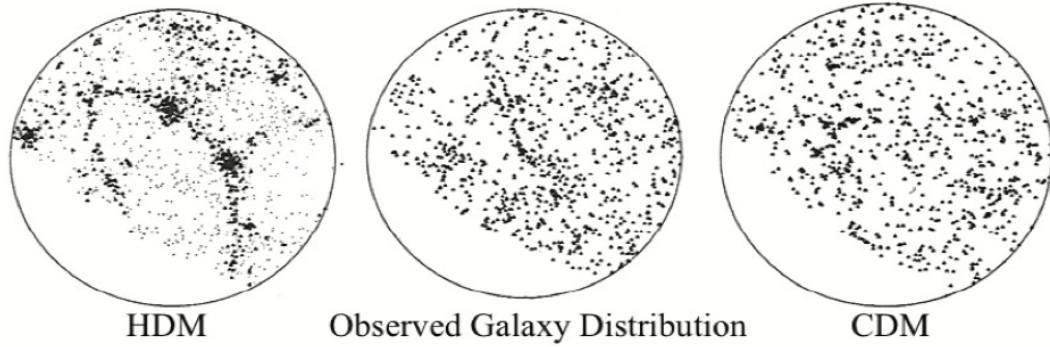


**Figure 11:** Computer simulations of the distribution of galaxies within our universe, with hot dark matter (left) and cold dark matter (right), compared to the observed distribution (middle). Figure is taken from [23].

### 616 1.7.2 WIMP dark matter and the WIMP miracle

617 WIMP dark matter is a candidate model for dark matter, which explains dark matter  
 618 as heavy particles which only interact gravitationally and through the weak force.  
 619 WIMPs are a tempting choice for dark matter, since their properties could explain all  
 620 the observed phenomena (galactic motion and structure formation). A WIMP is a  
 621 stable particle<sup>18</sup>, with a mass from a few GeV to a few TeV. At their inception there  
 622 were several promising WIMP candidates from supersymmetric extensions to the  
 623 standard model, although since then the parameter space available for WIMPs has  
 624 been probed and become far more constrained. But the real allure of the WIMP is  
 625 the WIMP "miracle".

626

The WIMP miracle is well known to be the fact that when one considers a particle of the weak mass scale with a self annihilation cross section close to the weak interaction strength (on the pb level), the present day dark matter relic density can be obtained. Additionally, in many versions of supersymmetry, the lightest supersymmetric particle is indeed a weakly interacting heavy particle, the ideal scenario for the WIMP [82]. In the following section the derivation of the WIMP abundance is shown, which is reproduced here from [83]. The WIMP is denoted as  $\chi$ , and it is assumed to be in thermal equilibrium with other matter while the temperature is  $T > m_\chi$ . During this time, the WIMP density  $n_\chi$  evolves according to the Boltzmann equation, shown in equation 7

$$\frac{dn_\chi}{dt} = -3Hn_\chi - \langle \sigma_{ann} v \rangle (n_\chi^2 - n_{eq}^2), \quad (7)$$

<sup>18</sup>The WIMP lifetime must be greater than the current age of the universe, since otherwise most would have decayed by now.

627 where  $H$  is the Hubble constant at that time, which in a radiation dominated uni-  
628 verse<sup>19</sup> is given by  $H^2 = \rho_{rad}/3M_P^2$ , where  $M_P$  is the Plank mass. While the system is  
629 in equilibrium, the number density tracks the equilibrium density  $n_{eq}$ .  $n_{eq}$  is num-  
630 ber density of dark matter where it is in equilibrium with the thermalised medium.  
631 In a radiation dominated universe, this depends dominantly on the radiation den-  
632 sity, which scales with the expansion of space with a different dependence than the  
633 matter density [84]. Subsequently, at some temperature  $T_f < m_\chi$ , the expansion rate  
634 will exceed the annihilation rate, and dark matter will freeze out, and their comoving  
635 number density (i.e. the number density accounting for the volumetric expansion of  
636 the universe) will remain constant from this point on. An approximate solution to the  
637 Boltzmann equation at this point gives equation 8, where  $\Omega_\chi h^2$  is the dimensionless  
638 dark matter density in the universe<sup>20</sup>,  $s_0$  is the present day entropy density of the  
639 Universe,  $g_*$  is the number of relativistic degrees of freedom of the particle  $\chi$  at freeze  
640 out, and  $x_f = T_f/m_\chi \approx 1/25$  is the freeze out temperature scaled to the dark matter  
641 mass. The value for  $x_f = 1/25$  is obtained from solving the Friedmann equation<sup>21</sup>  
642 numerically for the freezeout temperature (see [83] for more details). This means  
643 that WIMPs would have still moved at relativistic speeds at freezeout, with velocities  
644  $\langle v \rangle \approx c/3$

$$\Omega_\chi h^2 \approx \frac{s_0}{\rho_c/h^2} \left( \frac{45}{\pi^2 g_*} \right)^2 \frac{1}{x_f M_P \langle \sigma_{ann} v \rangle}. \quad (8)$$

645 Plugging in the known values for the parameters [75] and setting  $\Omega_\chi h^2 = 0.12$  from  
646 the latest Planck Collaboration results [75], one obtains equation 9

$$\frac{\Omega_\chi h^2}{0.12} = \frac{1}{\frac{\langle \sigma_{ann} \rangle v/c}{10^{-36} \text{ cm}^2} \cdot 0.1}. \quad (9)$$

647 Thus, setting the thermally averaged annihilation cross section to a value of  $1 \text{ pb} \cdot c$ ,  
648 and using average velocities of the order one would expect from a WIMP at freeze-  
649 out, the current dark matter abundance is recovered. A schematic representation  
650 of this process is shown in figure 12, where the decoupling temperature  $T_{dec}$  and  
651 the freezeout temperature  $T_f$  are shown separately. The decoupling temperature is  
652 the temperature at which the dark matter and luminous matter stop being in ther-  
653 mal equilibrium, while the freeze out temperature the point where the expansion  
654 rate becomes the dominant term for the density change for dark matter, over the  
655 annihilation term.

<sup>19</sup>The universe was dominated by radiation until roughly 47ky after the Big Bang, which is many orders of magnitude longer than the dark matter decoupling time, which is at  $\lesssim 1$  s.

<sup>20</sup> $\Omega_\chi$  can be interpreted as the curvature of space which dark matter is responsible for.

<sup>21</sup>This is the solution to Einstein's field equations for an open, closed or flat universe.

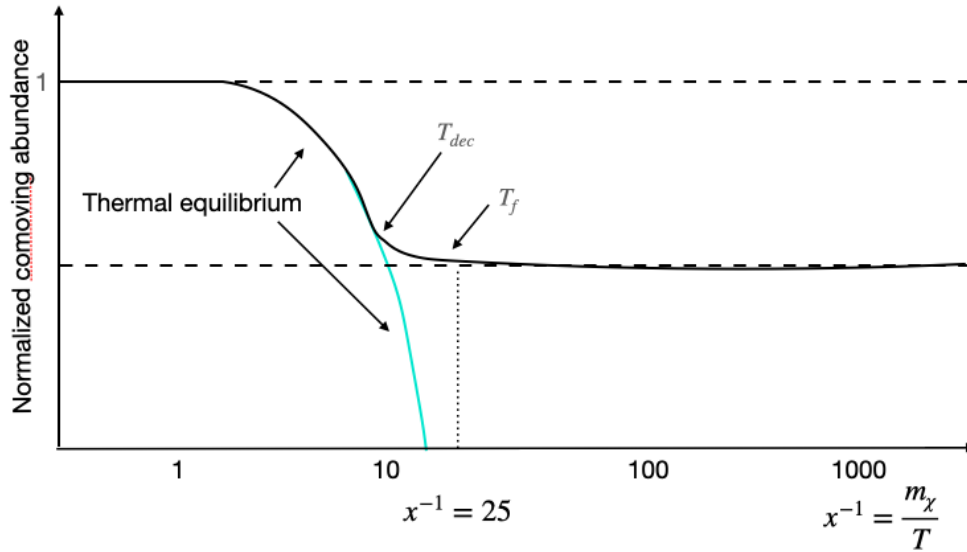


**Figure 12:** Transition of dark matter from thermal equilibrium to freeze out. Both the decoupling temperature (where dark matter stops being in thermal equilibrium with luminous matter) and the freeze out temperature (when the rate of expansion has dropped the annihilation rate to negligible amounts, so that the comoving density can be considered constant) are indicated on the schematic. Figure is based on the figure in [83].

### 656 1.7.3 Other dark matter models

657 WIMP dark matter is not the only dark matter model on the market, indeed, dark  
 658 matter models span over  $\approx 30$  orders of magnitude in mass. A collection of models  
 659 and their mass ranges is shown in figure 13. Notable other dark matter candidates  
 660 are neutrinos, sterile neutrinos, axions and primordial black holes (not shown in  
 661 figure 13). In this section we shall briefly discuss their main concepts, advantages  
 662 and disadvantages. Promising candidates usually share the quality that they solve  
 663 not just the nature of dark matter, but also another problem in physics. As discussed  
 664 earlier, the WIMP neutralino was considered the supersymmetric extension to the  
 665 standard model at its inception.

666  
 667 Let us first consider axion dark matter. Axions arise naturally in the Peccei-Quinn  
 668 (PQ) solution to the strong CP problem [85, 86] (see section 1.2.1 for more details),  
 669 by arguing that the CP violating term  $\bar{\theta}$  of the QCD Lagrangian is relaxed to 0 due to  
 670 an additional PQ symmetry. This symmetry is accompanied by a scalar field which

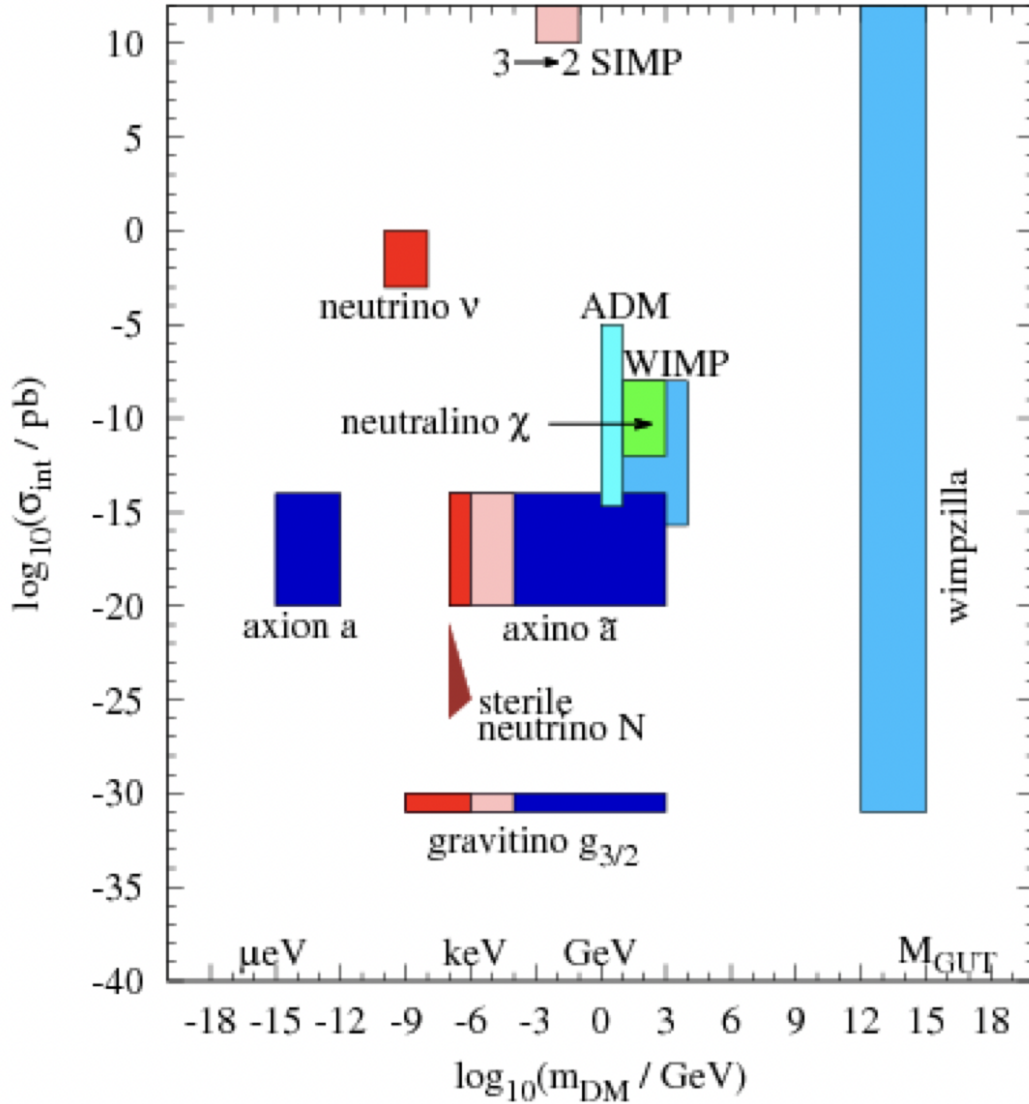


**Figure 13:** Collection of candidate dark matter models over a wide mass range. The most prominent candidates are WIMP dark matter, axion dark matter and sterile neutrinos. Primordial black hole dark matter is not shown on this plot. Figure taken from [83].

671 spontaneously breaks the symmetry at low energy, giving rise to the axion. While the  
 672 initial model, which predicted axion masses of order  $O(100\text{keV})$  has long since been  
 673 experimentally ruled out, it has been replaced by models using the same mechanism  
 674 to dynamically solve the strong CP problem. Axions of such fields are expected to

675 have masses in the  $\mu\text{eV}$  range. As a side effect, the scalar field would populate the  
 676 universe with axions, which – since they are produced non-thermally at rest [1] –  
 677 would be considered cold dark matter even though they have such low masses. As  
 678 such, a dark matter theory which is not at least partially made up of axions has to  
 679 provide an alternate solution to the strong CP problem.

680

681 Out of all the standard model particles, the neutrino is the only particle which  
 682 does not interact through either the strong or electromagnetic forces. This makes it  
 683 a promising initial candidate for dark matter. However, the present-day abundance  
 684 of neutrinos would be given by equation 10 (further details can be found in [83]).  
 685 Current constraints on the sum of the neutrino masses  $\sum m_\nu$  limit the amount of  
 686 dark matter in the form of neutrinos to about 0.5%-1.6% [74]. These constraints  
 687 come from neutrino mixing experiments, as well as from cosmological bounds.  
 688 This is because neutrinos – being hot dark matter – have a direct impact on large  
 689 scale structure formation. A related dark matter model is that of sterile neutrinos.  
 690 This group of models postulates that the right handed neutrinos (and left-handed  
 691 antineutrinos), are far more massive than their chiral partners. Since they interact  
 692 only gravitationally (neutrinos carry no electromagnetic or color charge, and the  
 693 weak force couples only to left-handed neutrinos and right-handed antineutrinos),  
 694 they would constitute a viable candidate for dark matter [87]. Recent observations of  
 695 neutrino mixing [74], show that neutrinos are not massless but have a finite mass. The  
 696 higgs mechanism responsible for giving SM particles their mass requires both left-  
 697 handed and right-handed fermions, and thus suggests the existence of the neutrinos'  
 698 chiral partners. Their mass also means that their chirality is not relativistically  
 699 invariant, since their velocities are slower than the speed of light; i.e. it is possible  
 700 for an observer to travel faster than the neutrinos and thus observe them with a  
 701 different chirality. However, it is not known why the couplings to for the left- and  
 702 right-handed neutrinos would be so different

$$\Omega_\nu h^2 = \frac{\sum m_\nu}{91.5\text{eV}}. \quad (10)$$

703 The final dark matter candidates to consider are primordial black holes. They are  
 704 discussed more closely in section 5.1.4, but a brief overview is given here for complete-  
 705 ness. Very shortly after the big bang ( $O(10^{-23})\text{s}$ ), overdense regions in the universe  
 706 might have collapsed into black holes. Depending on the time of their formation,  
 707 they would have consumed most of the available mass within their observable uni-  
 708 verse at the time, i.e. within their horizon. Such black holes would have expected  
 709 masses today ranging over many orders of magnitude, well below the critical mass  
 710 for a stable black hole [88]. Black holes below this mass tend to radiate energy off  
 711 at a rate faster than their mass accretion, via Hawking radiation [89, 88]. The rate

712 at which such small black holes radiate off energy is higher the smaller they are,  
 713 meaning towards the end of their lifetime they disappear via runaway evaporation.  
 714 During such a process, new antiparticles and particles can be produced. Such pri-  
 715 mordial black holes fit the required properties of dark matter, being collisionless  
 716 uncharged matter which interacts gravitationally. However, due to null observation  
 717 of the particles expected to be released from the evaporation of black holes, their  
 718 abundance can be tightly constrained. As such, they can at most make up a tiny  
 719 fraction ( $\approx 10^{-11}$ ) of the observed dark matter in our galaxy.

#### 720 1.7.4 Dark matter annihilations into antinuclei

721 The null results from searches for direct detection of WIMPs, either from evidence  
 722 for supersymmetry at the LHC or from direct detection experiments [90, 91], have  
 723 motivated other probes for WIMPs. Antinuclei observations from WIMP annihila-  
 724 tions have become one of the most promising of such probes, since many WIMP  
 725 candidates are expected to produce a detectable flux of low energy antinuclei [4, 2].  
 726 By definition WIMPs can couple weakly to standard model particles, and their wide  
 727 plausible mass range leaves open a large parameter space with sufficient energy to  
 728 create antinuclei. Additionally, since dark matter is expected to be cold, the produc-  
 729 tion of antinuclei occurs in the galactic rest frame, providing no boost to artificially  
 730 increase their momentum. Thus, considering WIMP annihilations into an initial  
 731 standard model state, the production of antinuclei is plausible. In a given point  
 732 in space, the amount of antinuclei produced is then dependent on the number  
 733 of dark matter annihilations times the spectrum of produced antinuclei in such  
 734 annihilations, as given in equation 11

$$q(\vec{r}, E) = \frac{1}{2} \left( \frac{\rho_\chi(\vec{r})}{m_\chi} \right)^2 \langle \sigma v \rangle (1 + \epsilon) \frac{dN}{dE}, \quad (11)$$

735 where  $\rho_\chi$  is the measured dark matter density at a given point, and  $(1+\epsilon)$  accounts  
 736 for the contribution from other annihilation products which later decay into the  
 737 antinucleus in question. This process is discussed in more detail in section 5.

#### 738 1.7.5 Majorana vs. Dirac dark matter

739 To current knowledge, every fermion in the standard model has an antiparticle, with  
 740 the same mass and quantum numbers, but opposite charge. This was first predicted  
 741 by Paul Dirac, who realised that the wave equation he developed to account for spe-  
 742 cial relativity in the motion of electrons implied a second solution, corresponding to  
 743 a particle with opposite charge [92]. This particle, the positron, was subsequently

744 discovered, and was the first discovery of antimatter [54].

745  
746 However, it is mathematically possible for a particle to be its own antiparticle;  
747 such particles are called Majorana particles. Out of the fermions in the standard  
748 model, only the neutrino could be a majorana particle, since all other fermions have  
749 known antiparticles. The majorana nature of the neutrino is being investigated by  
750 searching for neutrinoless double beta decay, a process by which two beta decays  
751 happen almost simultaneously, the produced neutrinos annihilate and thus provide  
752 additional energy to the electrons. The GERDA experiment is currently looking for  
753 such an effect [93], but has so far found no signal.

754  
755 WIMP dark matter is often assumed to be a majorana fermion. Given the lack  
756 of any known majorana particles, this seems somewhat unintuitive. The reason is  
757 mainly historical, since the original motivation for the WIMP was the supersym-  
758 metric neutralino, which is a hypothetical Majorana particle [82]. The reason this  
759 convention is still used, is that the effects of the assumption on the Dirac or Majorana  
760 nature of a WIMP are degenerate with the assumed WIMP self-annihilation cross  
761 section and therefore they produce the same signal. To show this, let us consider  
762 equation 11, which describes the source term for antinuclei from Majorana dark  
763 matter annihilations. The Dirac nature of the WIMP enters the equation in two ways.  
764 First, the density considered. Since the total gravitational effect of dark matter is  
765 known, the total measured dark matter density is the sum of the densities of dark  
766 matter and anti dark matter  $\rho_{\text{DM}}^{\text{meas}} = \rho_{\chi} + \rho_{\bar{\chi}}$ . Thus – assuming symmetric popula-  
767 tions of dark matter and anti-dark matter – the density term in equation would be  
768  $\rho_{\chi}\rho_{\bar{\chi}} = \frac{\rho_{\text{DM}}^2}{4}$ . This is a factor of 2 lower than original density term (the symmetry  
769 factor of 1/2 in equation 11 is due to the Majorana nature and thus falls away). How-  
770 ever, the second effect is on the thermally averaged annihilation cross section  $\langle \sigma v \rangle$ .  
771 When predicting the value of  $\langle \sigma v \rangle$  required for the currently observed abundance  
772 (as was done in section 1.7.2) the same density alteration is required, which means  
773 that the prediction for the thermally averaged cross section remain the same. This  
774 is shown in figure 14. Thus, these two effects cancel, yielding the same results for  
775 Dirac or Majorana dark matter.

776  
777 The only possible difference between the two models would come from an asym-  
778 metry in the population of dark matter and anti dark matter, and only if this was  
779 created after decoupling. If the asymmetry was caused prior to decoupling, the  
780 derivation for the expected WIMP cross section would account for this. Thus, such  
781 an asymmetry would have had to be caused by a process after dark matter decou-  
782 pled from thermal equilibrium, which suggests it would have had to form through  
783 purely dark matter interactions. It is therefore difficult to suggest any process which



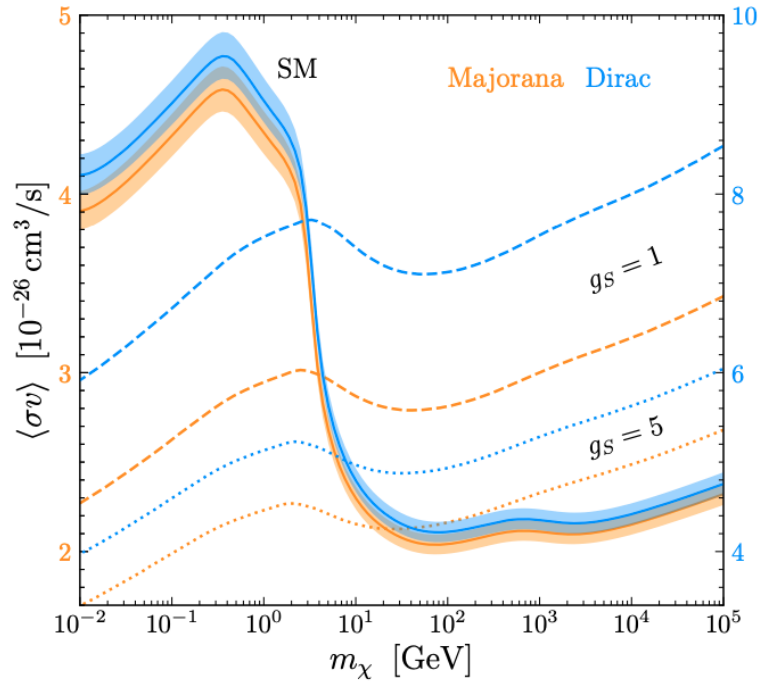


**Figure 14:** Thermally averaged annihilation cross section for WIMP dark matter as a function of the dark matter mass as it is required to reproduce the measured present-day abundance of dark matter. The left y-axis shows the values for Dirac dark matter, while the right y-axis shows the values for Majorana dark matter, showing the difference of a factor 2. Taken from [94].

784 would cause such an asymmetry. However, assuming an asymmetry was formed, the  
 785 number of annihilation would be reduced by the factor  $4x(1-x)$  in respect to the  
 786 case of symmetric Dirac dark matter, where  $x = \rho_\chi / \rho_{\chi+\bar{\chi}}$  is the asymmetry factor.  
 787 For further discussion of asymmetric dark matter, see section 4D in [83].

### 788 1.7.6 The search for dark matter: the link between WIMP dark matter and anti- 789 nuclei

790 Searches for dark matter can be classed into 3 categories: production searches, direct  
 791 detection experiments and astrophysical searches. Production searches look to de-  
 792 tect the production of dark matter particles in high energy collisions at accelerators.  
 793 Technically, if WIMP dark matter is weakly interacting and within a mass range which  
 794 can be produced at accelerators, it might be detectable. However, there is currently  
 795 no evidence for the production of dark matter at accelerators. Such production  
 796 searches usually constitute only a small part of the physics programs of accelerator

797 experiments. The second category of experiments are direct detection experiments.  
798 These experiments look for WIMP-nucleon interactions and the corresponding re-  
799 coil, and include the XENON [95, 90] and LUX collaborations [91]. These will be  
800 discussed in more detail in section 5.

801

802 The final probes are astrophysical searches. These focus on signals produced  
803 by potential WIMP dark matter which can be differentiated from standard model  
804 sources. These signals can come either from annihilations or decay of WIMP dark  
805 matter<sup>22</sup>, and we have to chose detection channels in which we could both get a  
806 reliable signal and differentiate it from other cosmic sources. The most promising  
807 searches are gamma rays and antinuclei [96], both of which could be produced in  
808 the annihilation of many WIMP candidates, and would produce signals which are  
809 expected to be distinguishable from common astrophysical backgrounds. This thesis  
810 focuses on measuring antinuclei inelastic cross section and their effect on such an  
811 antinuclei signal, in order to help interpret any future antinuclei measurements in  
812 cosmic rays.

---

<sup>22</sup>Technically WIMP dark matter could also scatter of baryonic matter, but this would be much easier to observe in direct detection experiments than in space.

## 2 Experimental data and experimental method

### 2.1 ALICE

This section aims to highlight the capabilities of the ALICE detector, in particular in the context of identifying antinuclei and measuring their inelastic cross sections. Measuring antinuclei inelastic cross section was not considered in the design of the ALICE detector. Rather, the excellent tracking and particle identification capabilities of the detector enable these measurements, which go beyond the scope originally envisioned for the detector. We shall therefore discuss the full chain of experimental methods, starting from the particle identification in each of the detectors, to the ALICE data structure and how they are used to obtain the antiparticle-to-particle ratios.

#### 2.1.1 Overview

ALICE is one of the four major experiments at the large hadron collider (LHC) near Geneva, Switzerland. It is the only dedicated heavy-ion experiment at the LHC, with its main physics motivation being the study of the quark-gluon-plasma (QGP). The experiment has 19 subdetector systems [97], of which the most important for this analysis are the Time-Projection-Chamber (TPC), the Inner Tracking System (ITS) and the Time-of-Flight detector (TOF). In particular the TPC sets ALICE apart from the other major LHC experiments, by enabling very precise tracking of particles, good particle identification via momentum and specific energy loss measurements, and its sensitivity low momentum particles (down to  $p_T \approx 0.2 \text{ GeV}/c$ ). In particular the TPC is special because it maintains the capability to do all this in an environment with more than 10k charged tracks at mid-rapidity in central Pb–Pb collision. The momentum measurement is enabled by a solenoid magnetic field, which is usually operated at  $0.5 \text{ T}$ <sup>23</sup>. The central detector systems are constructed in a cylindrical shape, providing full azimuthal coverage. The coverage in the forward and backward direction can conveniently be described using the measure of pseudorapidity ( $\eta$ ), which is defined as  $\eta(\theta) = -\ln[\tan(\theta/2)]$ , where  $\theta$  is the angle which the emitted particle has to the beam axis. This measure is anti-symmetric around  $\theta = \pi/2$ , i.e. the angle normal to the beam axis, and is 0 at this angle. The central detectors of ALICE cover the midrapidity range of  $|\eta| \lesssim 1$ . A schematic representation of ALICE with all its subdetector systems can be found in figure 15. It is important to note that the detector discussed in this section is the ALICE detector as it existed during the Run 2 data taking period (2015-2018). The main limitation of this version of the ALICE detector was its moderate interaction and data readout rates, the latter of which was limited to about 1kHz in Pb–Pb collisions and 200kHz in pp collisions.

<sup>23</sup>There are also dedicated low B field runs, where the field is set to only 0.2 T.

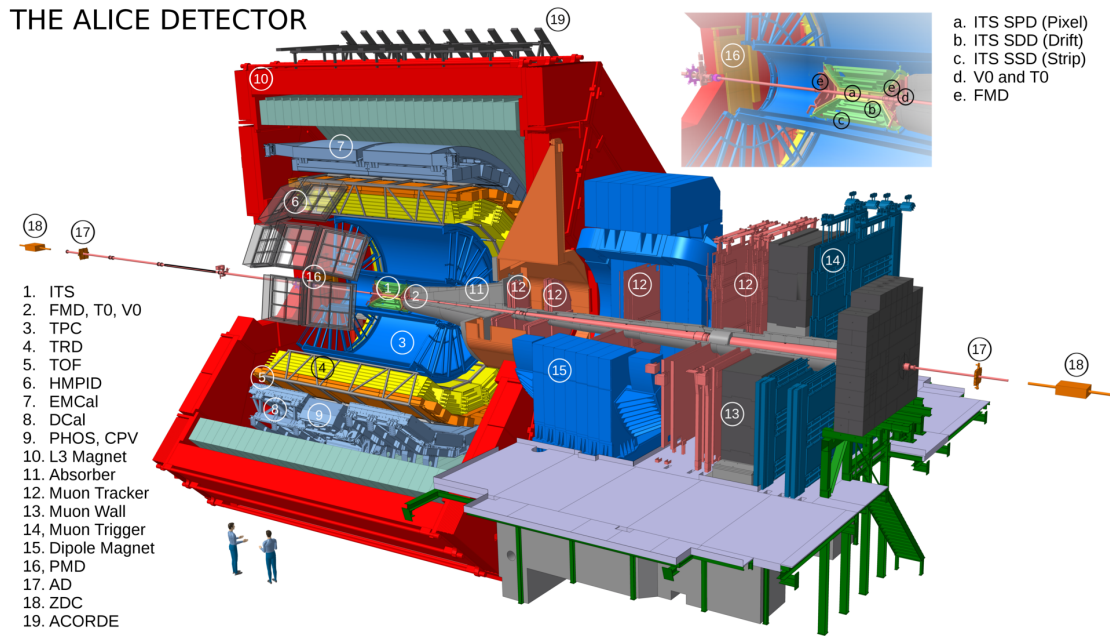


**Figure 15:** Schematic representation of the ALICE detector and its subdetector systems, during the Run 2 data taking period (2015-2018).

849 This is due to the  $1\mu s$  timespan required for reading out a single event, dead-time  
 850 for the detector. The ALICE upgrade for LHC Run3 which has started in 2022 will  
 851 instead be able to read out data at rates up to 50 kHz, and provide a significant boost  
 852 to the statistics which the ALICE detector can provide.

### 853 2.1.2 The ALICE Trigger System

854 The ALICE detector cannot read out all events which occur, both due to the detector  
 855 dead-time when reading out an event and due to the data rates which would be  
 856 involved. Instead, interesting events are selected by predefined criteria, and then  
 857 triggered upon. This trigger system then initiates the entire read-out sequence of  
 858 the detector. The most basic trigger is the so called minimum bias (MB) trigger,  
 859 which should trigger in the presence of any beam-beam collisions and not intro-  
 860 duce any bias based on the occurring physics. This is an important data sample to  
 861 check against, however, it is interesting to bias the selected events in favor of "more  
 862 interesting" physics. Such triggers look for less common conditions more favorable  
 863 to rare physics events, such as e.g. the presence of more charged particles. These  
 864 triggers exploit the fact that data acquisition is limited by the ALICE read-out rate  
 865 – not by the occurrence rate of rare events – in order to collect data for rare events  
 866 at the same 200kHz (1kHz) rate in pp (Pb-Pb) collisions at which MB data can be

867 collected.

868

869 For pp collisions, the trigger-criterion used in the analyses presented in this thesis  
 870 is the multiplicity in the V0 detectors (V0A and V0C), which is correlated with the  
 871 charged particle multiplicity at midrapidity. The V0 detectors are plastic scintillator  
 872 arrays in the forward and backwards regions, covering a pseudorapidity range of  
 873  $2.8 < \eta < 5.1$  and  $-3.7 < \eta < -1.7$ , respectively. They are located 3.4 m and 0.9  
 874 m from the interaction point. The high multiplicity trigger is configured so that  
 875 the highest 0.17% of multiplicity events are selected by the V0 detectors, while also  
 876 requiring a minimum of 1 charged particle at midrapidity. This proxy works well for  
 877 high multiplicities also at midrapidity, as this selection results in an average of 30-40  
 878 charged particles at mid-rapidity, as opposed to  $\approx 7$  particles for MB collisions.

### 879 2.1.3 Inner Tracking System (ITS)

880 The Inner Tracking System (ITS) is the innermost detector in ALICE, starting at a  
 881 radius of just 3.9 cm from the interaction point and reaching a radius of 43 cm. It  
 882 consists of 3 lightweight silicon bases sub-systems, called the Silicon Pixel Detector  
 883 (SPD), the Silicon Strip Detector (SSD) and the Silicon Drift Detector (SDD). The  
 884 ITS covers a pseudorapidity range of  $|\eta| < 0.9$ <sup>24</sup>. A schematic of the ITS is shown  
 885 in figure 16. Since the ITS is the closest detector to the interaction point, it plays  
 886 a vital role in determining the position of the initial vertex of the collision, called  
 887 the primary vertex. Indeed, its ability to accurately reconstruct particle trajectories  
 888 enables the reconstruction of the primary vertex to a precision of 100  $\mu\text{m}$ , and  
 889 constrains the particles' distributions of their distance-to-closest-approach (DCA).  
 890 This is particularly important when analysing nuclei at low momenta, since for  
 891 deuterons,  $^3\text{He}$  and  $^3\text{H}$  the contribution from secondaries from material spallation  
 892 is the dominant contamination in the nuclei signal. The requirement of a cluster  
 893 in the first ITS layer (SPD), removes any tracks from particles which get created  
 894 from material interactions at larger radii, unless there is a matchable cluster on  
 895 their trajectory by chance. The ITS also allows the rejection of pile-up events<sup>25</sup>.  
 896 The particle identification capabilities of the ITS become less reliable for very large  
 897 specific energy loss ( $dE/dx$ ) due to saturation effects, which makes the ITS less  
 898 useful for PID of doubly charged particles such as  $^3\text{He}$ .

<sup>24</sup>The SPD can detect particles with a wider range, up to  $|\eta| < 1.95$ .

<sup>25</sup>Pile-up is what happens when tracks from a different physical collision are incorrectly matched to the same event.

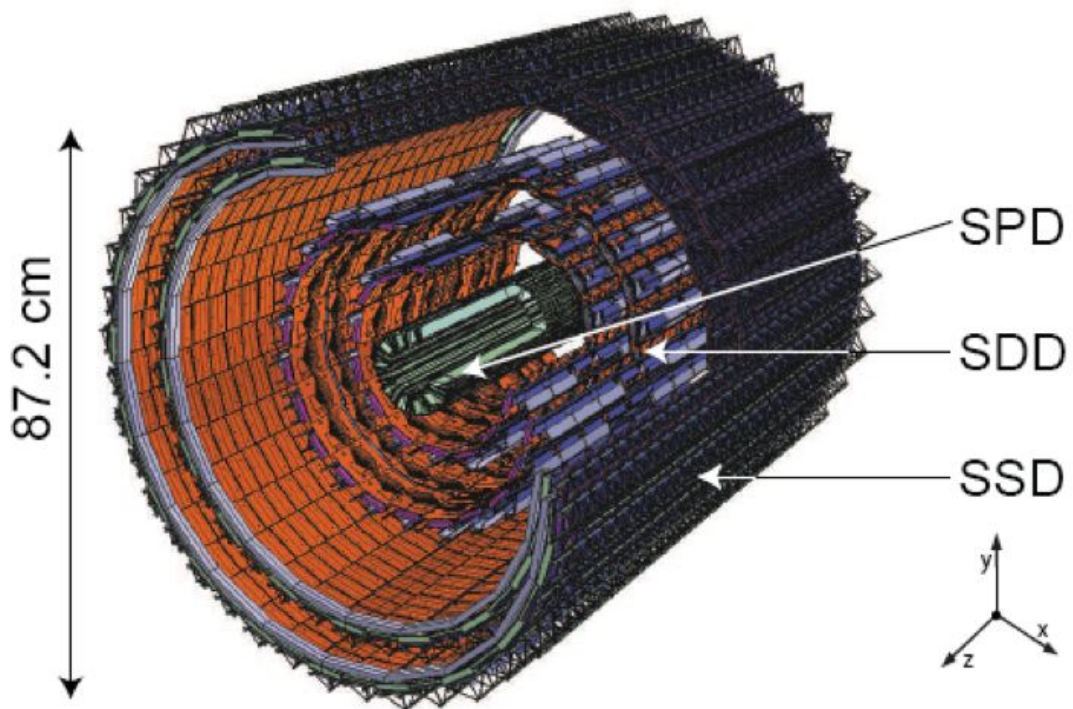


**Figure 16:** A schematic of the ALICE Inner Tracking System. The three layer groups (SPD, SSD, SDD) are marked.

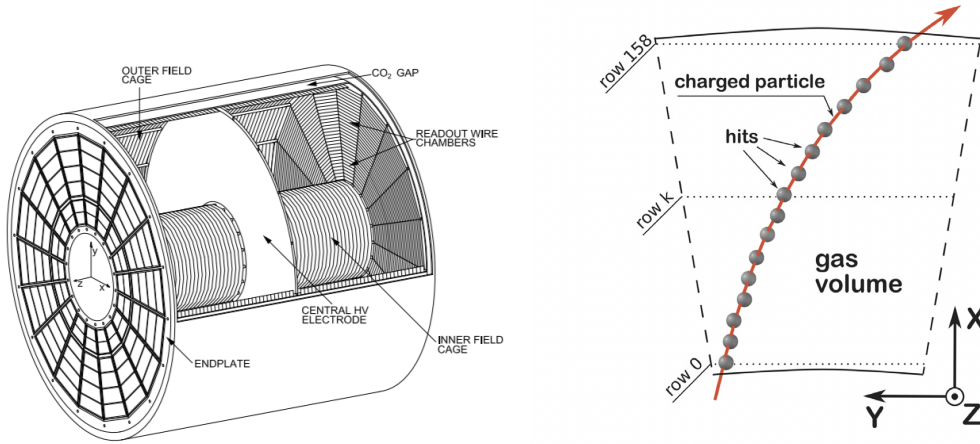


**Figure 17:** Left: Schematic of the field cage of the TPC detector [98]. Right: Schematic of the reconstruction mechanism for tracks in the TPC [99].

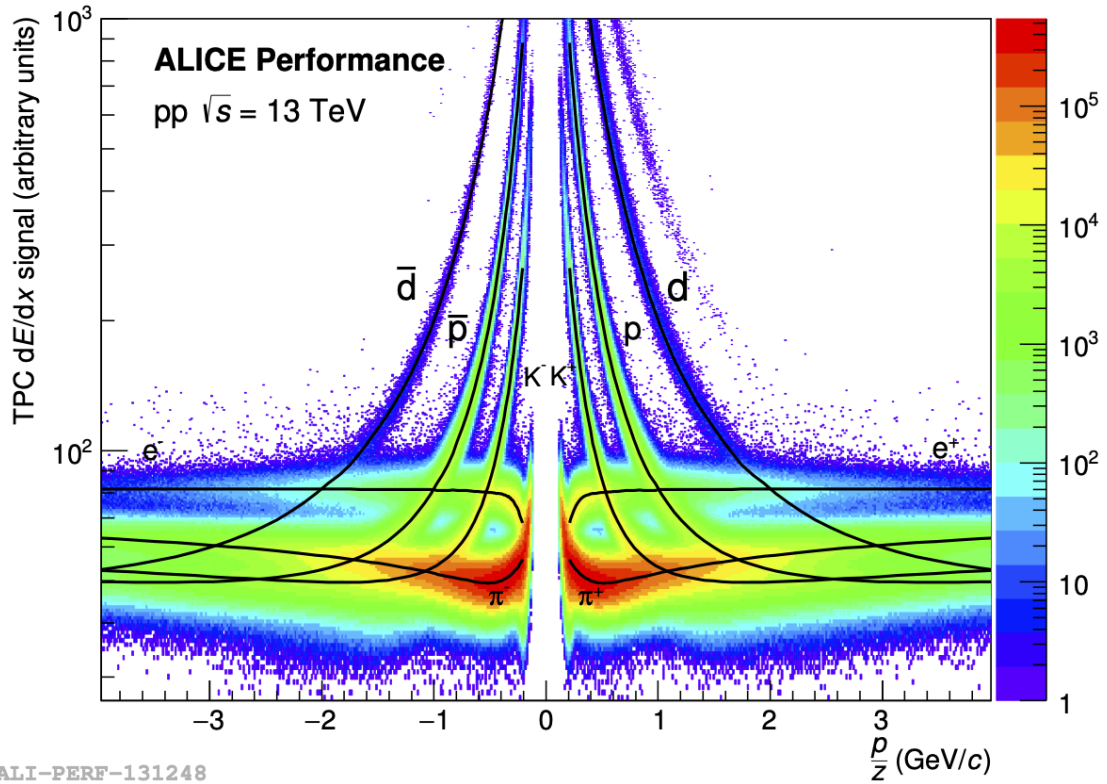
#### 899 2.1.4 Time Projection Chamber

900 The Time Projection Chamber (TPC) is the main tracking detector of the ALICE  
 901 experiment. It follows the ITS in the central barrel, at radii from 85 cm to 247 cm from  
 902 the interaction point, covering a pseudorapidity range of  $|\eta| < 0.9$ . The schematic  
 903 layout of the TPC is shown in figure 17. It consists of a gas filled field cage, which  
 904 can measure the ionisation caused by charged particles travelling through the gas.  
 905 Due to the applied electric field, the electrons created from ionisation drift towards  
 906 the read out cathodes of the field cage. The amplitude of the measured signal then  
 907 gives a measure of the specific energy loss of the particles ( $dE/dx$ ), while the position  
 908 of the clusters at the readout cathode gives the 2-dimensional (x and y) position of  
 909 the tracks of the particles. Finally, by measuring the time of arrival of the electrons  
 910 relative to the timing of the initial collision, the z position of the clusters can be  
 911 calculated. This method is shown on the right of figure 17. Measuring the position  
 912 and therefore the curvature of the track allows the determination of the momentum  
 913 of the particles.

914 Due to the combination of a momentum and a specific energy loss measurement,  
 915 the TPC has excellent particle identification abilities. The energy loss of relativistic  
 916 particles<sup>26</sup> is given by the Bethe-Bloch formula, which is reproduced in equation 12

$$-\frac{dE}{dx} = \frac{4\pi n z^2}{m_e c^2 \beta^2} \left( \frac{e^2}{4\pi\epsilon_0} \right)^2 \left[ \ln \left( \frac{2m_e c^2 \beta^2}{I(1-\beta^2)} \right) - \beta^2 \right], \quad (12)$$

<sup>26</sup>At very low energies below  $\lesssim 0.5\text{MeV}$  and at very high energies  $> 100\text{GeV}$ , the Bethe-Bloch formula does not apply.



ALI-PERF-131248

**Figure 18:** Specific energy loss in the TPC as a function of the rigidity  $p/z$ . Due to their masses, particles can be differentiated according to equation 12. This shows the identifying power of the TPC for low momentum particles.

917 where  $n$  is the electron density of the material,  $I$  is the mean excitation energy of the  
 918 material, and the other symbols have their usual meaning. Since equation 12 is a  
 919 function of only  $\beta$  and  $z$  for a given material, a measurement of both the momentum  
 920  $p = \frac{\beta}{\sqrt{1-\beta^2}} m$  and the energy loss will differentiate particles of different masses. This  
 921 separating power of the TPC is shown in figure 18, which shows that at low momenta,  
 922 particles are very well identified by the TPC alone.

923

924 The TPC Particle identification (PID) response can be expressed as the variable  
 925  $n\sigma_{\text{TPC}}$ , which is a measure of how close a track follows the Bethe-Bloch curve of a  
 926 given particle hypothesis, according to equation 13

$$n\sigma_{\text{TPC}} = \frac{\left(\frac{dE}{dx}\right)_{\text{meas}} - \left\langle \frac{dE}{dx} \right\rangle_{\text{exp}}}{\sigma_{\text{resolution}}}, \quad (13)$$



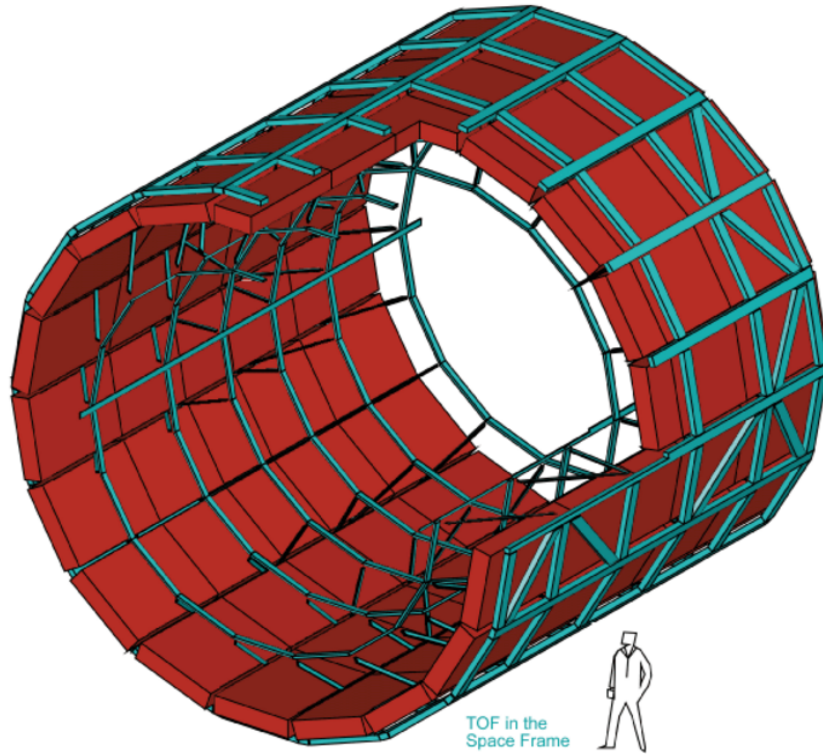


**Figure 19:** The TOF detector of the ALICE experiment.

927 where  $\frac{dE}{dx}$  is the specific energy loss at a given momentum and  $\sigma_{resolution}$  is the  
 928 resolution of the TPC.

### 929 2.1.5 Time-of-flight detector (TOF)

930 As can be seen from figure 18, the differentiating power of the TPC decreases dras-  
 931 tically at higher momenta, as the energy loss of particles tends towards the value  
 932 for a minimum ionising particle (MIP), and their bands thus start overlapping with  
 933 each other. In order to distinguish between particles of different masses at higher  
 934 momenta, an additional information is required. The detector used for this purpose  
 935 in ALICE is the Time-of-flight (TOF) detector. The TOF is a detector based on multi-  
 936 gap resistive plate chambers [100], which measures the time difference between  
 937 the initial collision and the formation of a cluster in one of its readout pads. It is  
 938 arranged in a cylindrically symmetric structure between 370 cm and 399 cm from the  
 939 interaction point and has the same coverage in pseudorapidity as the TPC ( $|\eta| < 0.9$ ).  
 940 The TOF is mounted in a steel structure called the space frame [100, 97]. A schematic  
 941 representation of the TOF detector is shown in figure 19.

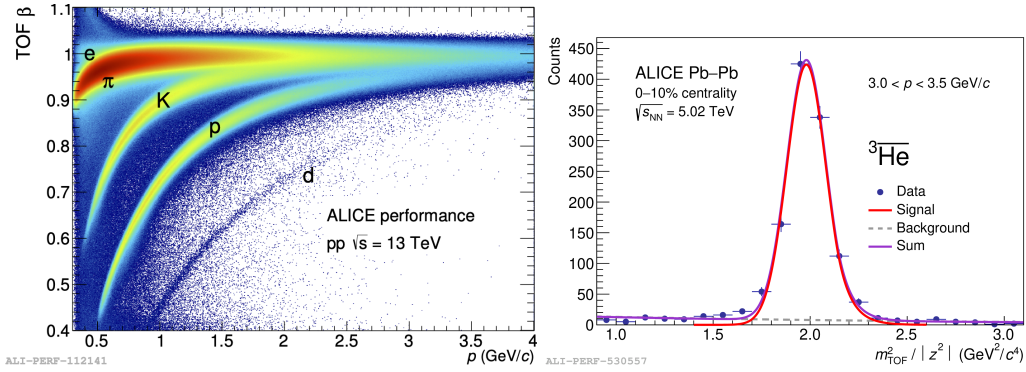


**Figure 20:** Left: Measurement of the track velocity  $\beta_{\text{TOF}}$  as a function of the reconstructed momentum of the particle associated to the track, from the TOF detector in pp collisions at  $\sqrt{s} = 13$  TeV.  $\beta_{\text{TOF}}$  is classically measured as length of the track divided by the time-of-flight. Right: Performance figure showing the TOF used for the identification of  ${}^3\text{He}$  nuclei.

942 The time resolution of the TOF readout pads is  $\approx 50$  ps<sup>27</sup>. In order to measure the  
 943 time-of-flight, the initial time of the collision must be known. This can be done by  
 944 the TOF itself with large enough multiplicities, and for lower multiplicities it is done  
 945 with the T0 detector, which consists of Cherenkov arrays [101]. Thus, a measure of  
 946 the particle velocity, called the TOF beta, can be measured as  $\beta = L/t$ , where  $L$  is the  
 947 length of the track on its curved trajectory through the TPC, and  $t$  is the measured  
 948 time-of-flight. From the relation  $p = \gamma\beta mc$ , equation 14 can be derived, which  
 949 relates the measured  $\beta_{\text{TOF}}$  to the tracks mass. The factor  $1/Z^2$  cannot be neglected  
 950 here since the detector cannot know the particles mass a priori. Thus, when analysing  
 951 multicharged particles such as  ${}^3\text{He}$ , the observable from the TOF is  $m_{\text{TOF}}/Z^2$

$$m^2/Z^2 = \frac{p^2}{c^2 Z^2} (\beta_{\text{TOF}}^2 \gamma^2) = \frac{p^2}{c^2 Z^2} \left( \frac{c^2 t^2}{L^2} - 1 \right). \quad (14)$$

952 The performance of the TOF detector is shown in figure 20. A clear separation  
 953 between particles can be seen up to much higher momenta than in the TPC. This is  
 954 particularly true for higher mass particles. The deuteron line can be seen below the  
 955 marked proton line, and is well differentiable well beyond the merging of the proton  
 956 and pion lines.

<sup>27</sup>In order to get an idea of this resolution, a particle travelling at the speed of light will travel roughly  $c * 50\text{ps} = 1.5$  cm.

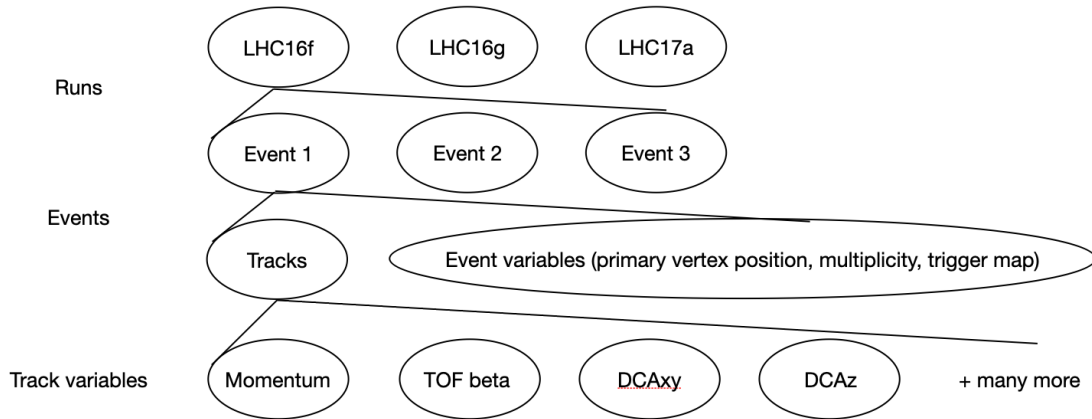


**Figure 21:** Schematic of the data structures within ALICE. The data is split by run periods, then by event, and within the event by tracks.

957 **2.1.6 Basics of ALICE data structure**

958 ALICE data is split by periods, which in turn consist of runs, then by events, and  
 959 within the event by tracks, as is shown in figure 21. Runs are the periods of time  
 960 during which collisions occurred under the same conditions, which means that the  
 961 data taking is started and kept up until either the LHC beam cycle comes to an end or  
 962 there is some problem which requires the run to be ended. This means that runs are  
 963 of arbitrary length. Once the raw data is taken, the Data Preparation Group (DPG) is  
 964 responsible for doing a reconstruction pass over the data, which means to build the  
 965 tracks from the individual detector hits, correcting for any calibration or distortion  
 966 effects. The data structure one is left with is a list of events, each of which contain  
 967 a list of tracks. This is what is subsequently used by analysers<sup>28</sup>. This hierarchy is  
 968 shown in figure 21.

969 **2.2 Identifying antinuclei and building the antiparticle-to-particle**  
 970 **ratio**

971 This section described the process to identify (anti)nuclei using the ALICE detector,  
 972 and the method by which the antiparticle-to-particle ratio is then reconstructed. For  
 973 this purpose,  $10^9$  high multiplicity pp events at  $\sqrt{s} = 13$  TeV were analysed.

<sup>28</sup>There are two files available for runs: ESD and AOD files. The difference is the level of lossy compression in each track. ESD files keep more information – such as a track’s momentum at different points in the TPC – while AOD files are faster to analyse due to the smaller memory required.

974 **2.2.1 Collision system and event selection**

975 The data provided in ALICE by necessity includes a large range of particles. For  
976 analyses which do not want all charged particles, these act as impurities. Therefore,  
977 cuts are applied at the analysis level, to provide a much cleaner environment for  
978 the actual analysis. Within the analysis, these cuts happen on both an event and a  
979 track level, leaving a subset of tracks which can be analyzed. The goals of these cuts  
980 are: i) to cut bad quality tracks, such as ones where the PID is not certain, ii) to cut  
981 tracks of uninteresting particles for the specific analysis, e.g. particles produced by  
982 material spallation in the analyses in this thesis and iii) to reduce the background,  
983 such as from secondary particles from weak decays. These cuts also vary between  
984 collision systems, which is necessitated by their different properties. To exemplify  
985 this, lets compare a relevant difference between high multiplicity pp and Pb–Pb  
986 collisions. In HM pp collisions the mean multiplicity is 34, while in central Pb–Pb  
987 collisions it is about 1000. This means that the mean occupancy of the detectors is  
988 much greater in Pb–Pb collisions, which in turn means that the tracking algorithm  
989 has a higher chance to assign a wrong cluster to a track. In order to reduce this effect,  
990 the matching window for the TOF detector is reduced in Pb–Pb collisions, from 10  
991 cm to 3 cm. For the analysis method explained in section 3.1.2, this introduces an  
992 uncertainty, as some tracks could be elastically scattered in the TRD or space frame,  
993 causing them to miss the matching window without having interacted inelastically.  
994 To evaluate and counteract this, a special reconstruction of the Pb–Pb data was used,  
995 where the matching window was set to 10 cm instead of 3 cm. The effect of this  
996 change is explained in section 3.1.2.

997

998 **2.2.2 Reconstruction of raw (anti)nuclei spectra**

999 In order to obtain the raw antinuclei spectra, the tracks first have to be identified  
1000 as antinuclei. This particle identification (PID) occurs on the basis of two main  
1001 detectors: the TPC and the TOF. Due to the distinct masses of antinuclei (they are  
1002 heavier than most other long lived particles), they leave a distinct signal in each  
1003 detector. In the TPC, antideuterons are clearly separated by their energy loss up to  
1004 a momentum of about 1.4 GeV.  ${}^3\overline{\text{He}}$  is well separated from lighter particles in the  
1005 TPC for all momenta, due to its double charge<sup>29</sup>. Since the energy loss rises with  $Z^2$ ,  
1006 the energy loss of  ${}^3\overline{\text{He}}$  is characteristically much higher than those of singly charged  
1007 particles. The particle identification of  ${}^3\overline{\text{H}}$  uses the TOF for all considered momenta.

---

<sup>29</sup>This means that  ${}^3\overline{\text{He}}$  has to contend with impurities from  ${}^4\overline{\text{He}}$ , which is also doubly charged. However, given that for each additional nucleon a penalty factor is introduced for the production (as shown in figure 10), this contribution is below the % level and therefore negligible with the uncertainties of this analysis.

1008 In the TOF, the time of flight measurement combined with the track length and  
 1009 curvature gives a measurement of the particles mass, according to equation 14. This  
 1010 allows a clean signal for  ${}^3\overline{\text{H}}$  and  ${}^3\overline{\text{He}}$ . For antideuterons, there is still a significant  
 1011 contamination from the tail of the proton distribution at those masses, which re-  
 1012 quires a fit to the signal and the background to extract the antideuteron yield. Figures  
 1013 22 and 23 show the extraction procedure in the TPC and TOF for  ${}^3\overline{\text{He}}$ . Figure 24  
 1014 shows the extraction for  ${}^3\overline{\text{H}}$ . The particle and antiparticle  $n\sigma_{\text{TPC}}$  distributions are  
 1015 fit with a gaussian function. For  ${}^3\overline{\text{He}}$ , a second gaussian is used to account for the  
 1016 background from (anti)triton<sup>30</sup>. Both the  ${}^3\overline{\text{He}}$  and  ${}^3\overline{\text{H}}$  signals in the TOF detector  
 1017 are very clean, as is shown in figures 23 and 24, therefore, the TOF signal is used  
 1018 by applying a cut on the  $m_{\text{TOF}}^2$ . The combination of these measurement allows the  
 1019 extraction of the (anti)nuclei spectra, which are shown in 25.

1020 It is important to note that the histograms in this analysis are low statistics his-  
 1021 tograms, i.e. they have many bins with 0 counts towards their sidebands. This  
 1022 presents challenges when using the default implementations of  $\chi^2$  fitting algorithms,  
 1023 since those tend not to treat empty bins rigorously, if they are included in the fit at  
 1024 all. Therefore, a minimised log-likelihood fit was done, using proper Poisson errors  
 1025 on empty bins (i.e. empty bins are assigned an uncertainty of  $\pm 1.14$ , for further  
 1026 information see the statistics chapter in [74]).

### 1027 2.2.3 Correction for secondaries from material spallation

1028 In order to obtain pure samples of nuclei, any secondary nuclei not created in the  
 1029 initial collision need to be subtracted from the obtained raw spectrum. Two sources  
 1030 of secondary particles exists: weak decays and material spallation. For  ${}^3\overline{\text{He}}$  and  ${}^3\overline{\text{H}}$   
 1031 weak decays are negligible, since the amount of  ${}^3\text{H}_\Lambda$  measured in pp collisions is  
 1032 much less than the amount of  ${}^3\overline{\text{He}}$ . The branching ratio of  ${}^3\text{H}_\Lambda \rightarrow {}^3\overline{\text{He}}$  is expected  
 1033 to be 25% [74]. Thus, secondary nuclei (both  ${}^3\text{He}$  and  ${}^3\text{H}$ ) from material spallation  
 1034 remain, which shall simply be referred to as secondaries hereinafter. Since these  
 1035 secondaries are created by essentially "knocking out" these nuclei from larger nuclei  
 1036 in the ALICE detector material and in the beampipe, no secondary antinuclei exist.  
 1037 In order to differentiate between secondaries and primaries, we make use of the fact  
 1038 that all primaries have a common origin (the primary vertex), while the distribution  
 1039 of secondaries should not point to the primary vertex. The measure of how close

<sup>30</sup>The reason why the contamination shows up in the low momentum bins for helium but not for tritons is due to the double charge of  ${}^3\overline{\text{He}}$ . This means that by grouping particles in bins of measured momentum, we are actually grouping them in bins of  $p/Z$ . Thus, when looking at a given bin in  $p/Z$ , tritons have half the momentum of  ${}^3\overline{\text{He}}$ . Since this contamination is at values of  $p/Z$  before the start of the triton analysis, the inverse contamination does not need to be corrected for in the  ${}^3\overline{\text{H}}$  measurement.

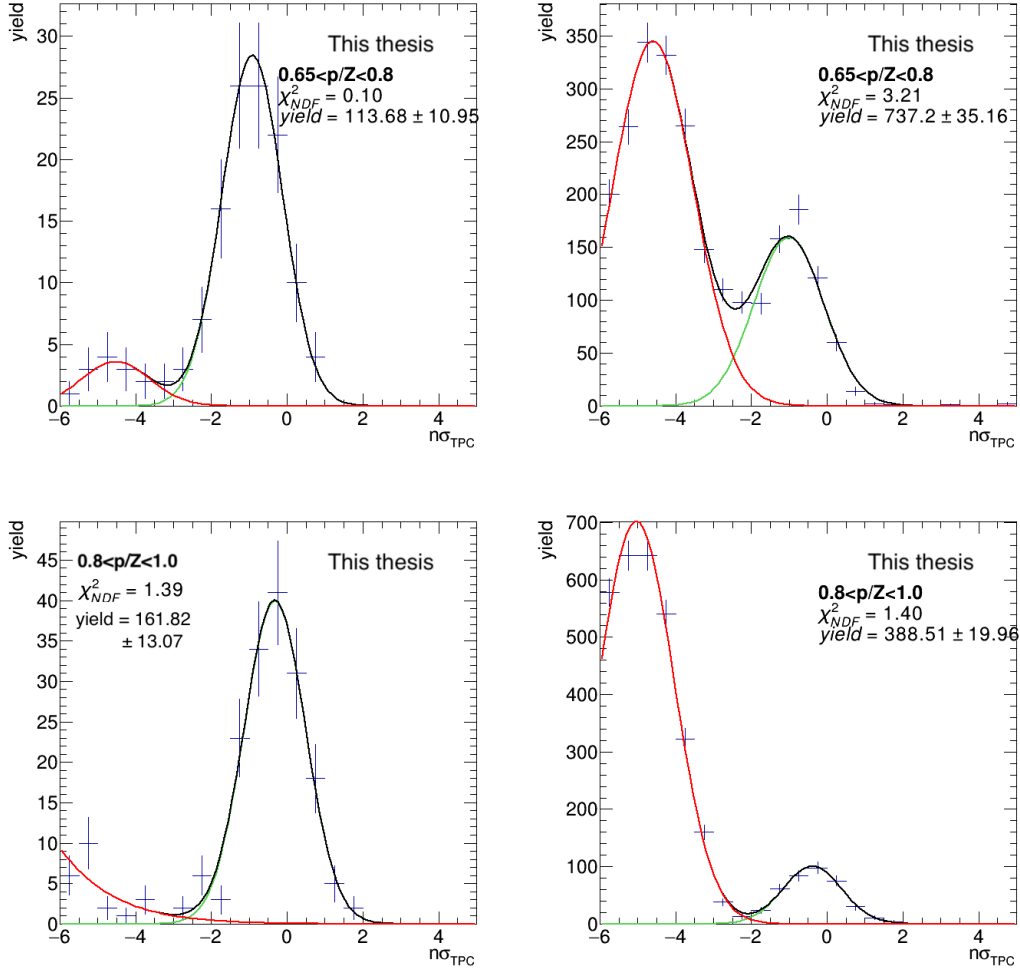


**Figure 22:** Particle identification procedure for  ${}^3\overline{\text{He}}$  (left) and  ${}^3\text{He}$  (right), showing the distribution of  $n\sigma_{\text{TPC}}$  for the momentum bins in the TPC only part of the analysis. The green line is the fitted signal, the red line is to fit the contamination towards negative  $n\sigma_{\text{TPC}}$ . The black line shows the combined fit.

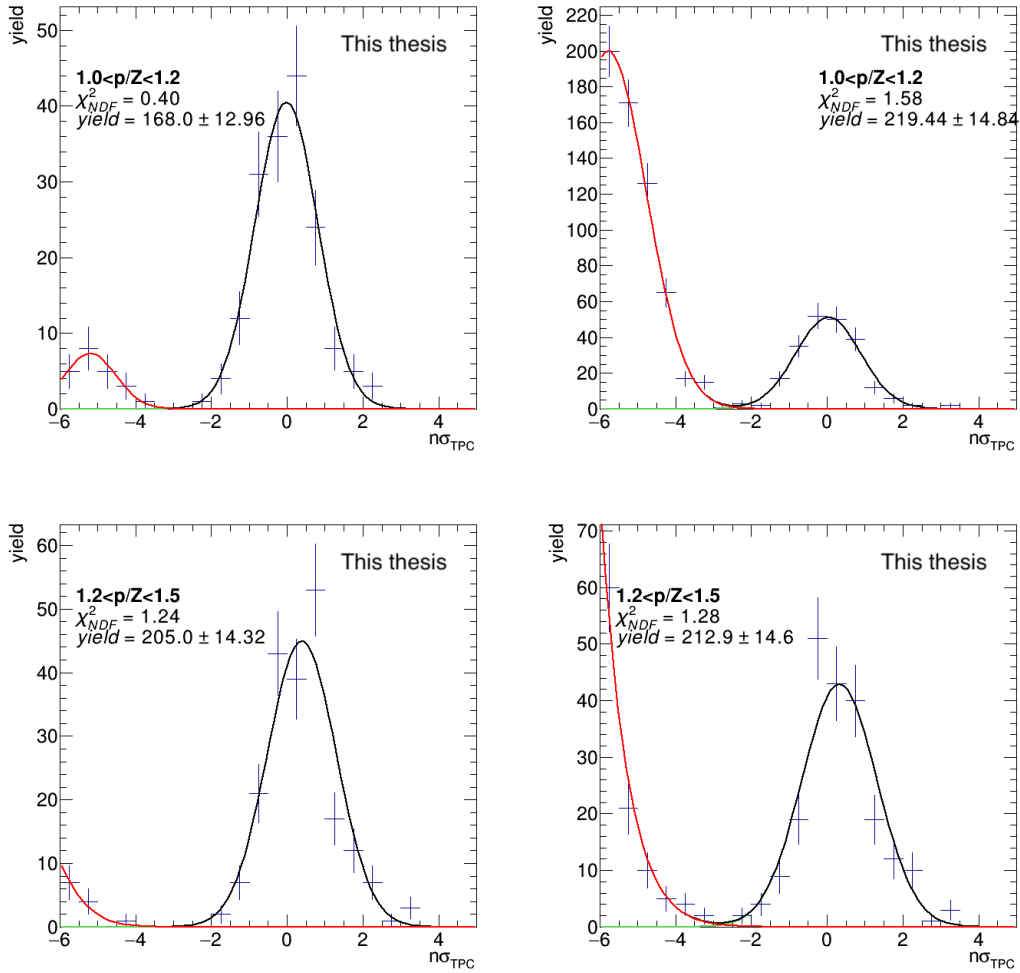


**Figure 23:** Plots of the  $n\sigma_{\text{TPC}}$  distribution for  ${}^3\overline{\text{He}}$  (left) and  ${}^3\text{He}$  (right), for the momentum bins in the TPC+TOF only part of the analysis, i.e. after a cut on  $m_{\text{TOF}}^2$  is applied. The green line is the fitted signal.

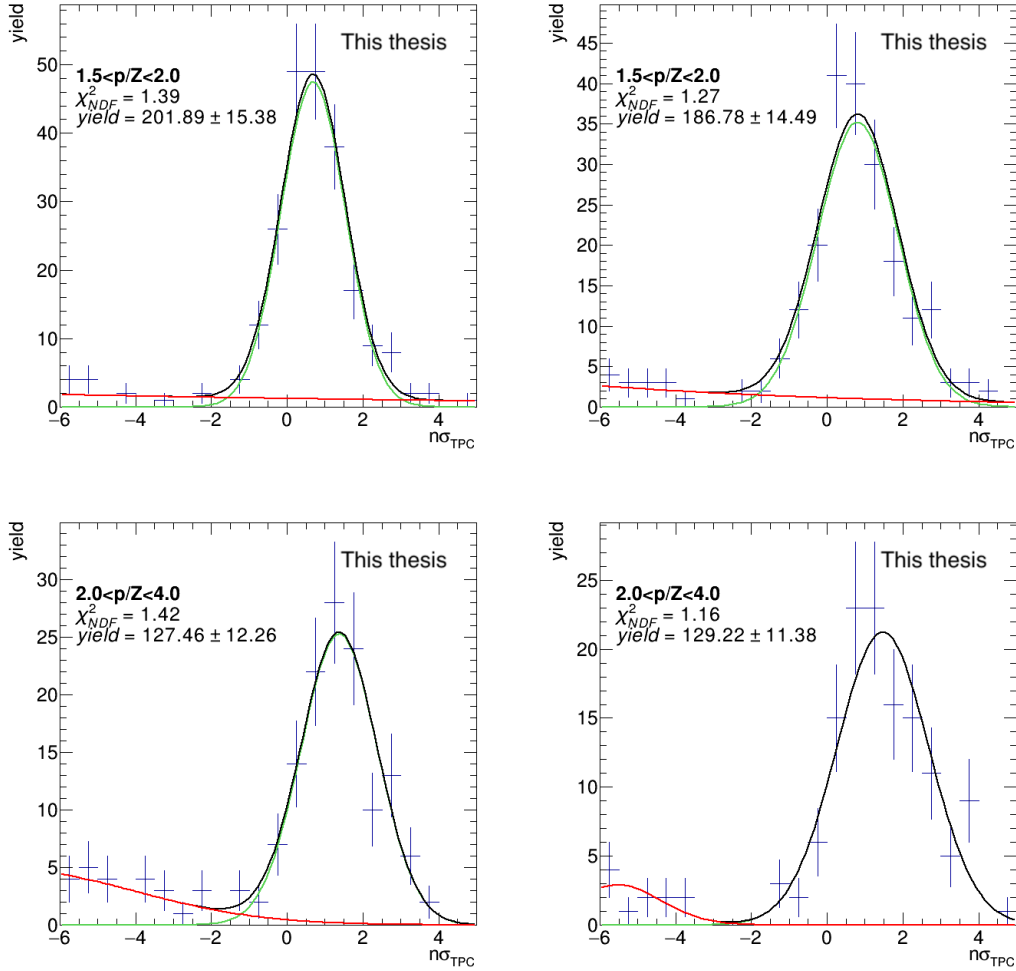


**Figure 23:** (Continued) Plots of the  $n\sigma_{\text{TPC}}$  distribution for  ${}^3\overline{\text{He}}$  (left) and  ${}^3\text{He}$  (right), for the momentum bins in the TPC+TOF only part of the analysis, i.e. after a cut on  $m_{\text{TOF}}^2$  is applied. The green line is the fitted signal.



## 2. Experimental data and experimental method

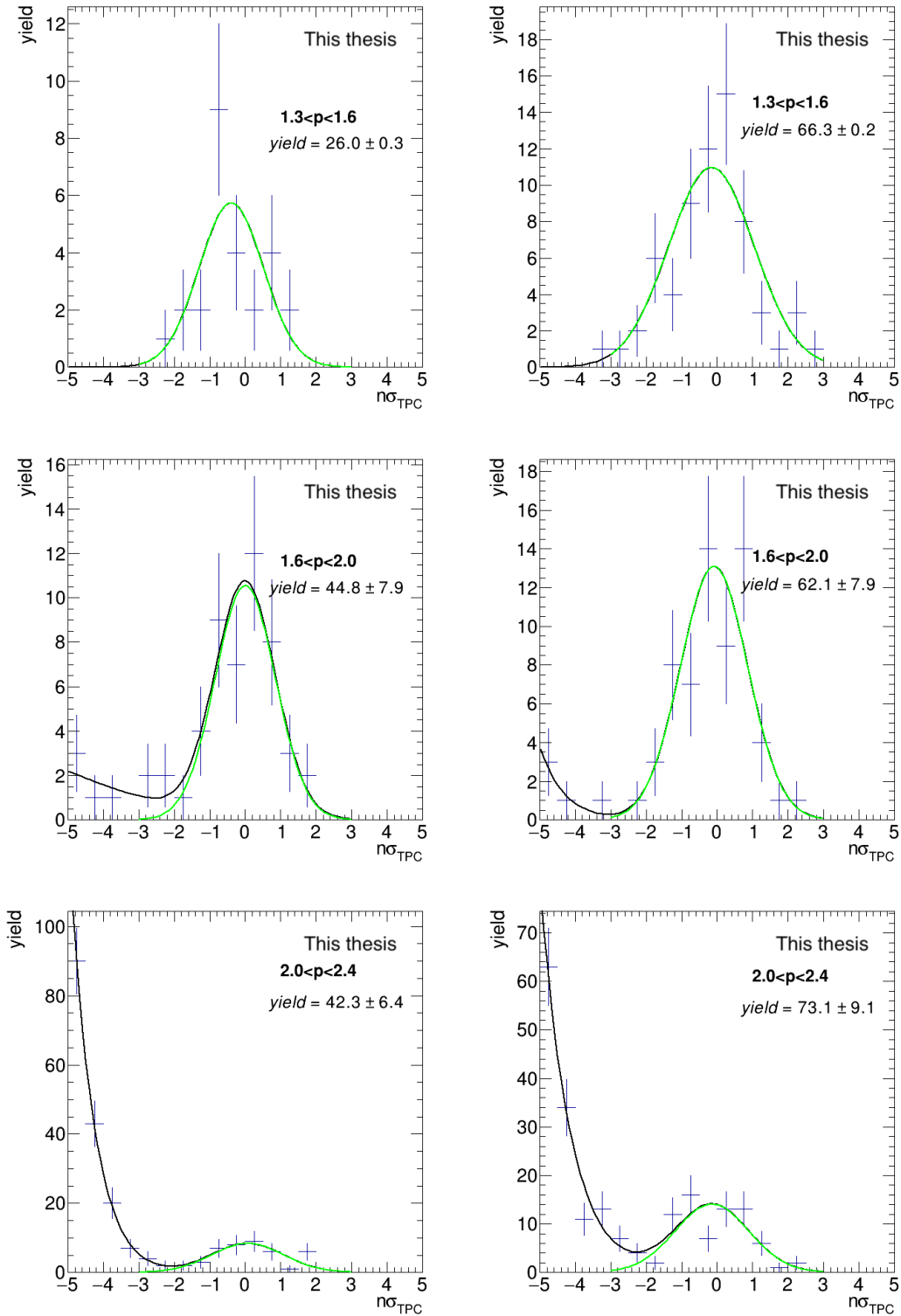


**Figure 24:** Particle identification procedure for  ${}^3\bar{\text{H}}$  (left) and  ${}^3\text{H}$  (right), showing the  $n\sigma_{\text{TPC}}$  distribution for each momentum bin, after a cut on  $m_{\text{TOF}}^2$  is applied. The green lines represent the fitted signal, and the black lines the fitted signal+background.

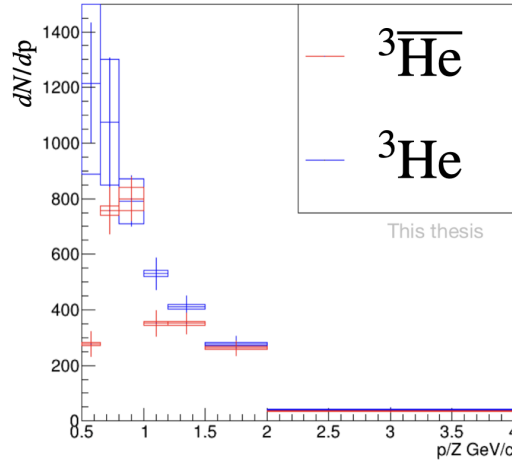


**Figure 25:** (Anti)nuclei spectra for  ${}^3\text{He}$   ${}^3\overline{\text{He}}$ . Blue points show  ${}^3\text{He}$  while the red points show  ${}^3\overline{\text{He}}$ . Statistical uncertainties are shown as errorbars while systematic uncertainties are shown as boxes. These spectra are not yet corrected for secondary particles from material spallation.

1040 a particle's track reaches to the primary vertex is known as the distance of closest  
 1041 approach (DCA), and within ALICE is resolved in both the  $x$   $y$  and the  $z$  planes.  
 1042 In order to fit these distributions, they have to be projected onto one of the two  
 1043 directions, which involves cutting on the other. The  $\text{DCA}_{xy}$  distributions were used  
 1044 for the fits described later in this chapter. The resulting changes in the primary  ${}^3\text{He}$   
 1045 yields depending on the values of  $\text{DCA}_z$  which are selected is shown in figure 26. An  
 1046 uncertainty of 8% is applied to the first bin as a result of this cut.

1047 We expect the primary DCA distribution to be peaked sharply at 0, while the  
 1048 distributions for secondaries should be mainly flat. Example distributions from  
 1049 Monte Carlo Simulations are shown in figure 27.

1050 Figure 27 shows that while the distribution for primaries is indeed sharply peaked  
 1051 at 0, the distribution of secondaries is not flat, but also peaks around 0. This is an ex-  
 1052 perimental effect due to the tracking algorithm, which prefers reconstructing tracks  
 1053 pointing towards the primary vertex. This is exacerbated by the possibility to assign  
 1054 a wrong ITS cluster to the track. Several cuts can be made on the tracks to minimize  
 1055 this effect, which are outlined in section 2.2.2. The most important cut is on the  
 1056 number of clusters in the first ITS layer, which reduces the number of secondary  
 1057 tracks by  $\approx 85\%$ , as is shown in figure 28.

1058

1059 The biggest challenge with secondary corrections is to get reliable templates  
 1060 for secondary nuclei from material. For a combinatorial background, a side band  
 1061 analysis can be done, since no deviating behaviour in the signal region is expected,

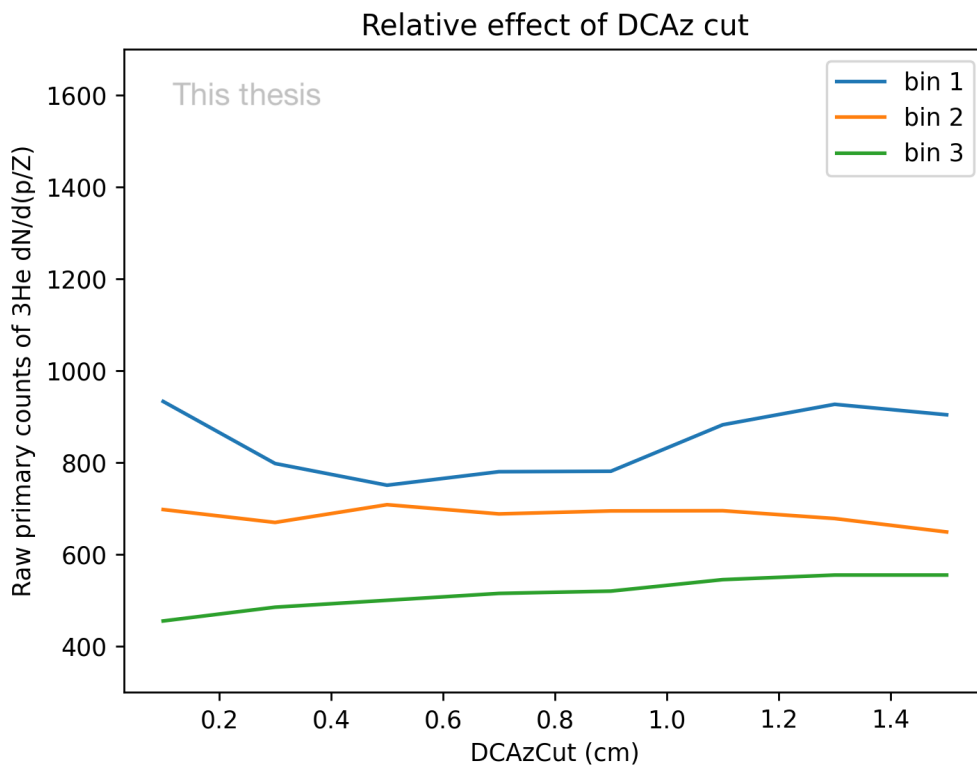


**Figure 26:** Extracted primary  $^3\text{He}$  yields in each analysis bin as a function of the value of the cut on  $|\text{DCAz}|$ . Due to the variations in the first bin, an 8% uncertainty was assigned.

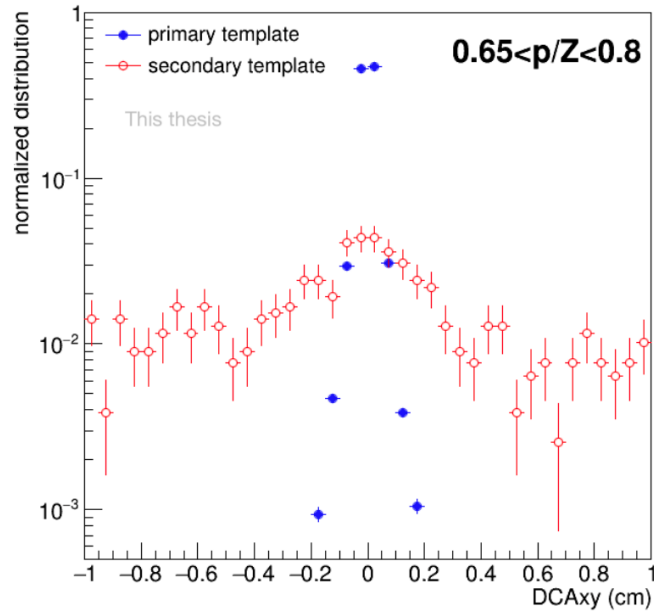


**Figure 27:** Example  $DCA_{xy}$  distributions of particles from primary and secondary particles in Monte Carlo simulations. The particle shown here is  ${}^3\overline{\text{He}}$  with a  $|DCA_z| < 1$  cm requirement.

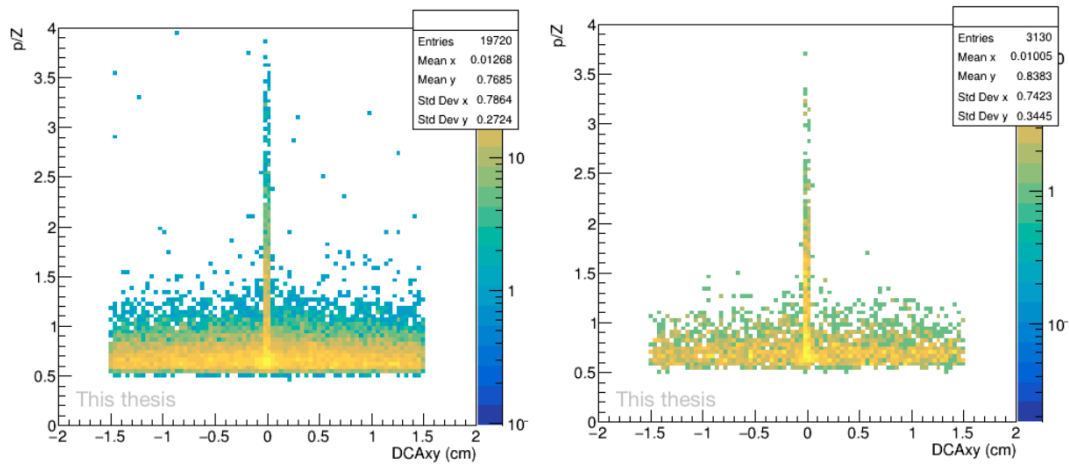


**Figure 28:**  $DCA_{xy}$  distributions of  ${}^3\text{He}$  candidates without any cut on ITS hits (left) and after a hit in one of the two first layers of the ITS is required (right). The reduction in the number of candidates is mainly in the sidebands, and therefore from secondaries.

1062 but since we have already seen in figure 27 that secondary tracks are also peaked  
1063 towards the primary vertex, the sideband analysis cannot help us account for this.  
1064 It is however also impossible to extract a pure secondary distribution from data,  
1065 since the peak region always necessarily includes the particles produced in the initial  
1066 collision. Thus, we need to simulate the distribution with Monte Carlo simulations.  
1067 This means that we rely on the assumption that the angular distribution of the spal-  
1068 lation processes are accurately reproduced in Monte Carlo<sup>31</sup>. The advantage of this  
1069 method, is that in full ALICE Monte Carlo simulations, the same tracking algorithm  
1070 is used as in data reconstruction, which means that if the spallation processes are  
1071 accurately simulated, the distribution will match the true distribution. Also, these  
1072 simulations rely on the correct underlying event, i.e. for high multiplicity pp colli-  
1073 sions, such collisions need to be accurately simulated. This is due to the fact that  
1074 the spallation is triggered by particles produced in the primary collision. A final  
1075 challenge to obtaining the template fits is the rarity of these spallation processes in  
1076 MC simulations.

1077

1078 In order to extract the secondary fraction from the DCA distributions, template  
1079 fits are used. These fits take the shape of input templates (in this case from pri-  
1080 maries and from secondaries) and try to match their relative contribution in order  
1081 to reproduce the shape in data. Two different fitting algorithms were investigated:  
1082 the TFractionFitter and RooFit. The main difference between the two is that the  
1083 TFractionFitter can change the shape of the templates within uncertainties in or-  
1084 der to better reproduce the data. In the limit of infinite statistics, both of these  
1085 methods should produce the same result. In the analyses shown in this thesis, the  
1086 TFractionFitter was used as the default method, and RooFit was used to crosscheck  
1087 these results. Additionally, a sideband analysis of the templates was performed as an  
1088 additional crosscheck. A comparison of the template fits obtained using these three  
1089 methods is shown in figure 29. As can be seen, the uncertainty introduced by the  
1090 scaling of the histogram (the comparison of the left and central panels in figure 29) is  
1091 smaller than the uncertainty returned by the fit. The detailed fits and corresponding  
1092 primary fraction are shown in sections 3 and 4.

1093

1094 One could also ask the question of which primary particles are responsible for  
1095 the largest amounts of nuclei secondaries from spallation. In order to investigate this  
1096 question, a toy Monte Carlo simulation was used, where beams of primary particles  
1097 were fired on layers of beryllium and beryllium + carbon, corresponding to the  
1098 materials of the beampipe and the support structure of the first ITS layers. This

---

<sup>31</sup>The absolute value of the cross section is not important for the accuracy of the templates, since the relative weight is later determined by the template fits. However, too low a cross section means that far more events have to be simulated in order to gain sufficient statistics to obtain the template.

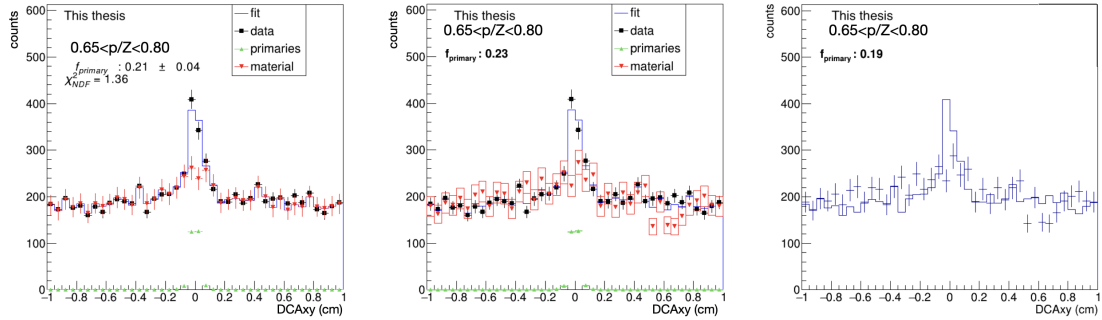


**Figure 29:** Comparison of different methods for determining the primary fraction from the template fits, shown in the second bin of the  ${}^3\text{He}$  analysis, with a  $|\text{DCA}_z| < 1\text{cm}$  cut. (Left) Fit using the TFractionFitter. (Middle) Default templates scaled according to the weights assigned by the TFractionFitter, but without changing their shapes. (Right) Fits performed by scaling the material templates to the region outside  $|\text{DCA}_{xy}| < 0.1\text{ cm}$ . The solid line represents the data and the histogram points are the fitted material template. See text for more details.

1099 configuration was chosen since if the spallation occurs later, the missing hit in the  
 1100 first ITS layer allows a large degree of rejection<sup>32</sup>. An exponential energy spectrum  
 1101 was used for the primary particles, tuned to the proton spectrum measured by ALICE  
 1102 [102]. Geant4 was employed for this simulation [103, 104]. The resulting yields of  
 1103 secondary deuterons and  ${}^3\text{He}$  are shown in figure 30. Interestingly, the primary  
 1104 antiparticles produce a larger portion of the secondary nuclei than their primary  
 1105 particles. Also, while antideuterons produce a larger amount of secondary nuclei  
 1106 than antiprotons (by roughly 2x), given that their relative abundance in pp collisions  
 1107 is 1000x less, their contribution is expected to be on the sub % level. This leads to the  
 1108 conclusion that it is mainly (anti)protons and pions which are responsible for creating  
 1109 secondary antinuclei. Therefore, when using ALICE Monte Carlo simulations, it is  
 1110 not necessary to employ a coalescence afterburner with the underlying event in  
 1111 order to accurately simulate the secondary distributions. A caveat to this is that  
 1112 the simple toy Monte Carlo simulation only probed absolute yields, rather than the  
 1113 angular distribution, and as already noted above, the latter is the important factor.  
 1114 However, given that the contribution to the yields is on the sub % level, any difference  
 1115 in the distribution is expected to be negligible.

<sup>32</sup>This is somewhat less true in Pb-Pb collisions, since the multiplicities are so much higher and therefore a wrongly associated ITS cluster is far more likely.

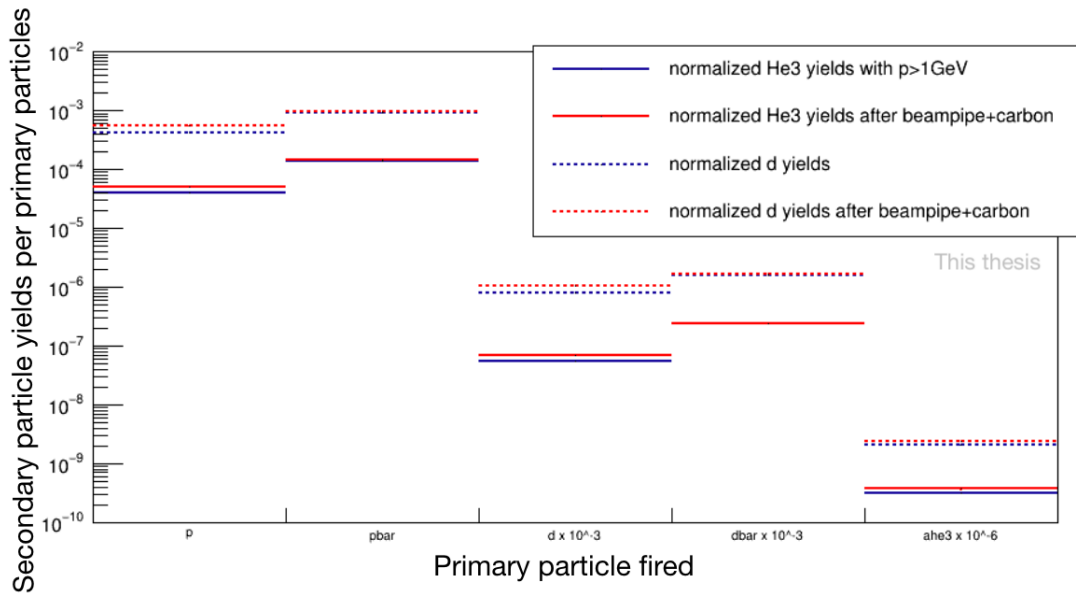


**Figure 30:** Normalized secondary particle yields as a function of primary particles fired obtained from a toy Monte Carlo simulation of a particle beam on materials mimicking the LHC beampipe in ALICE and the beampipe + ITS support structure. The resulting secondary deuterons and  $^3\text{He}$  are shown as a function of the primary particle fired, where the results are roughly scaled by the primary particles relative abundance.

### 1116 2.2.4 Annihilations within the detector

1117 Annihilations within the detector material can occur at any point within the detector,  
 1118 but are of course more likely in denser materials. For the purpose of this discus-  
 1119 sion we shall differentiate between 3 different scenarios: i) annihilations before the  
 1120 middle of the TPC, since such tracks cannot be identified and will therefore not be  
 1121 reconstructed in our spectra. ii) annihilations between the middle of the TPC and  
 1122 the TOF, since these annihilations can be directly probed by the comparison of the  
 1123 yields in the TPC and TOF. And finally annihilations outside of the TOF detector,  
 1124 which for the purposes of this analysis is not seen at all, i.e. such annihilations are  
 1125 not measured.

1126  
 1127 Let us first consider the case where the annihilation occurs before the middle of  
 1128 the TPC. A track with less than half of the TPC clusters will be removed by the track  
 1129 cuts, therefore this track will not show up in our analysis, and will never even be  
 1130 identified as an antinuclei candidate track. The situation is slightly different when  
 1131 considering tracks which annihilate between the TPC and the TOF. Those tracks can  
 1132 be identified in the TPC. For  ${}^3\overline{\text{He}}$  this identification can occur over the whole momen-  
 1133 tum range ( $0.5 < p/Z < 4 \text{ GeV}/c$  in HM pp collisions), while for antideuterons this  
 1134 identification only works up to  $p < 1.4 \text{ GeV}/c$  and for  ${}^3\overline{\text{H}}$  it only works up to  $p < 1.5$   
 1135  $\text{GeV}/c$ . However, since the antinucleus does not reach the TOF, the TOF hit will either  
 1136 be missing, or at a wrong time (i.e. giving an incorrect TOF mass). This allows for two  
 1137 options in these analyses: in the case where the TPC is sufficient to clearly identify  
 1138 the antinucleus, and it is within the acceptance of the TOF, the difference between  
 1139 the TPC and TOF yields can be used in order to probe the antinuclei inelastic cross  
 1140 section without being reliant on the corresponding nuclei yields. The second option  
 1141 is to use the TOF information in order to increase the amount of material which  
 1142 the particles need to traverse before being considered in the analysis, which makes  
 1143 the ratio more sensitive to the inelastic cross section. This increase is rather drastic,  
 1144 since the material budget increases by a factor of  $\approx 5$  when switching between a TPC  
 1145 only analysis and one which includes the TOF. This can be seen in figure 31, which  
 1146 shows the cumulative material budget in ALICE as a function of radius.

1147  
 1148 We are thus left with the two possible methods for measuring annihilations  
 1149 within our detector. The first is based on quantifying the loss of antiparticles as they  
 1150 move through the detector, by comparing them to their particle counterparts. This  
 1151 method works for any particles and momentum range which the detectors can probe  
 1152 a priori<sup>33</sup>. As part of this thesis, this method was performed for  ${}^3\overline{\text{He}}$  and  ${}^3\overline{\text{H}}$ . The  
 1153 second is based on comparing the yields in the TPC and the TOF, in regions where

<sup>33</sup>As we have seen in section 2.2.3, the unreliability of the secondary correction at low momentum limits the low momentum reach of this method.



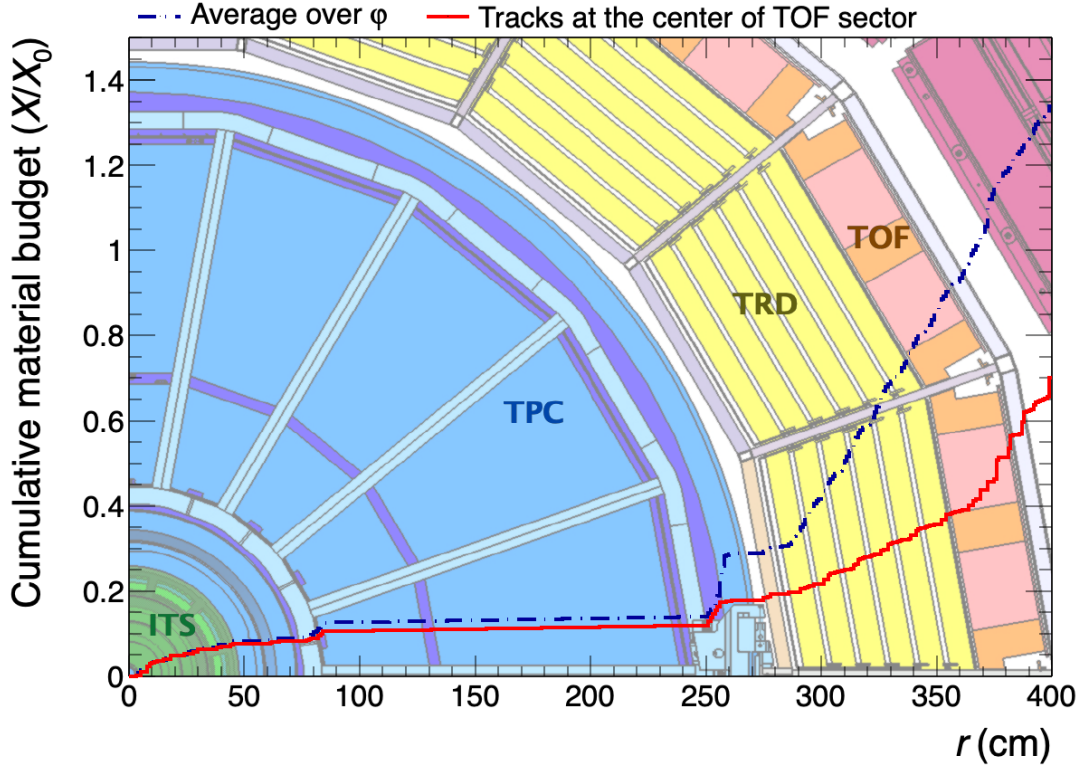


**Figure 31:** Cumulative material budget of the ALICE detector, as a function of radius from the beampipe, taken from [105]. The solid red line is the value for straight tracks which hit the centre of the TOF sector, while the dashed blue line is the average value over azimuthal angle.

1154 the antinucleus can be clearly identified in the TPC alone, and which include the  
 1155 acceptance of the TOF.

1156

1157 The analyses utilising the TOF-to-TPC method for the measurement of the in-  
 1158 elastic cross sections of  ${}^3\overline{\text{He}}$  and  ${}^3\overline{\text{H}}$  were performed by others, and are reproduced  
 1159 in this thesis since they are closely related to the results shown in this thesis. The  
 1160 measurement of the antideuteron inelastic cross sections in pp and p-Pb collisions  
 1161 were also not done as part of this thesis, however the comparison of the two results to  
 1162 show the independence of the antiparticle-to-particle ratio on the chosen collision  
 1163 system was performed as part of this thesis.

### 1164 **2.3 Extracting the inelastic cross section from the antimatter-to-** 1165 **matter ratio**

1166 The idea behind using the antimatter-to-matter ratio as the observable to measure  
 1167 the antinuclei inelastic cross section, is that antinuclei will annihilate in the detector  
 1168 material, and therefore disappear from our measurement<sup>34</sup>. In order to quantify  
 1169 the inelastic cross section we thus need to know how many particles were origi-  
 1170 nally produced, i.e. we need to normalise the antinuclei spectrum to the number  
 1171 of originally produced antinuclei. However, we cannot use theoretical predictions  
 1172 tuned to this data, since that would be a circular argument, i.e. we would get out the  
 1173 same inelastic cross section as we put in. Therefore, the matter nuclei are used as a  
 1174 proxy instead. This works very well for a few reasons. First, the matter inelastic cross  
 1175 section can be easily measured, and have been measured for deuterons [106], <sup>3</sup>He  
 1176 [107]. For <sup>3</sup>H, the inelastic cross section could be measured with the same method,  
 1177 but has not been measured yet. Second, other effects on the acceptance or efficiency  
 1178 will largely cancel between the nuclei and antinuclei counterparts, since the two  
 1179 only differ in their charge sign. Third and perhaps most important, is the fact that  
 1180 at LHC energies, the primordial ratio is very close to unity, and has been accurately  
 1181 measured for antiprotons [108]. This means that we know to a very high degree of  
 1182 accuracy how many antinuclei are produced relative to the produced nuclei, and  
 1183 the other processes by which both might be lost within the detector are also well un-  
 1184 derstood. Thus, the antimatter-to-matter ratio is sensitive to the antinuclei inelastic  
 1185 cross section, and other variables it is sensitive to are well understood and under  
 1186 control. This makes this ratio such a promising probe to measure the inelastic cross  
 1187 section.

1188  
 1189 Having established that the antimatter-to-matter ratio is sensitive to the inelastic  
 1190 cross section, it is still not trivial to extract the inelastic cross section from this  
 1191 observable. This difficulty is due to having to account for many processes. One  
 1192 example is the path which the particles take through the detector. In the magnetic  
 1193 field, (anti)nuclei travel on curved tracks, so the amount of matter they interact with  
 1194 will depend on their initial trajectory. This thus needs to be averaged over the  $\eta$   
 1195 distribution of the antinuclei. This is just one of many similar effects which make an  
 1196 analytical relationship between the antimatter-to-matter ratio and the antinuclei  
 1197 inelastic cross section difficult to achieve. Fortunately, detailed simulations of the  
 1198 ALICE detector using Geant4 account for all pertinent interactions of (anti)nuclei. We  
 1199 therefore compare our measured ratios to ones obtained using Geant4 simulations,

---

<sup>34</sup>Annihilation of antinuclei is the dominant inelastic process at low energies, however, it is not the only process we observe. Antinuclei – being composite objects – may also break apart in inelastic reactions which leave the antinucleons intact. The measurement techniques described in this section measure the total inelastic cross section, which includes all inelastic processes.

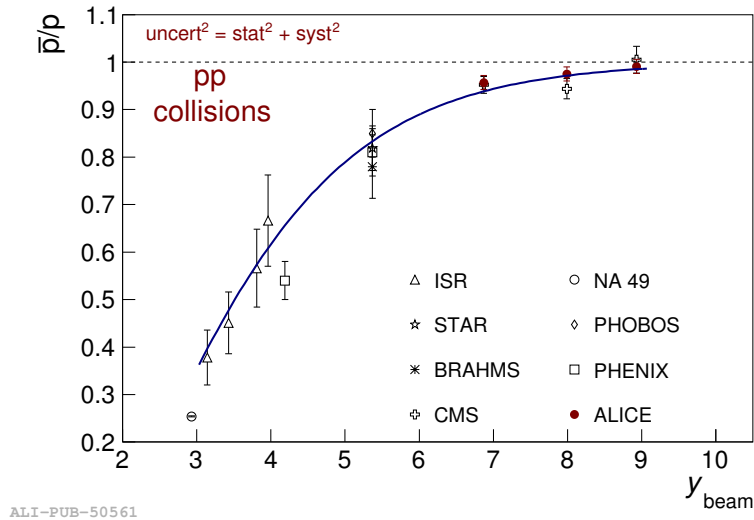


**Figure 32:** Ratio of antiprotons to protons produced at mid-rapidity as a function of beam rapidity. At LHC energies the value approaches unity, demonstrating that at such high energies antimatter and matter are produced in almost equal amounts. Figure taken from [108].

1200 in order to obtain our results on the inelastic cross section. In order to probe the  
 1201 relationship of the antinuclei-to-nuclei ratio to the inelastic cross section, the Geant4  
 1202 code was modified to vary the inelastic cross section, keeping all other interactions  
 1203 the same.

### 1204 2.3.1 Using the antiparticle-to-particle ratio from Monte Carlo simulations

1205 In order to fairly compare the Monte Carlo simulations to the produced data, it is  
 1206 vital to account for the primordial ratio<sup>35</sup> at such high energies. The relevant ratio  
 1207 of antiprotons-to-protons is shown in figure 32. Based on the same arguments as  
 1208 the formula for the coalescence parameter  $\kappa$ , the effect on the ratio of antinuclei will  
 1209 be the same as to the antiproton-to-proton ratio taken to the exponent of the mass  
 1210 number of the antinucleus.

### 1211 2.3.2 Ratios as a function of the inelastic cross section scaling factor

1212 In order to extract the inelastic cross section measurement from the antiparticle-  
 1213 to-particle ratio, we have to compare the measured ratio in each bin to values from

<sup>35</sup>In other words: how much more antimatter particles we have for each matter particle. Given that we collide purely matter particles, there is a penalty for producing antimatter, even though at such high energies it is vanishingly small.

1214 MC simulation with varied values of the inelastic cross section. The use of MC is  
 1215 necessary in order to obtain the dependence of the inelastic cross section on the  
 1216 antiparticle-to-particle ratio. This then allows the bin-by-bin extraction of the inelas-  
 1217 tic cross section by comparing the dependence in MC to the measured value of the  
 1218 ratio in the data<sup>36</sup>. These plots are shown for the  ${}^3\overline{\text{He}}/{}^3\text{He}$  and  ${}^3\overline{\text{H}}/{}^3\text{H}$  ratios in figures  
 1219 33 and 34, respectively. These plots also show fit lines to the Monte Carlo points,  
 1220 which were with with an exponential according to the Lambert-Beer absorption law  
 1221 [109], which is reproduced in equation 15

$$N_{\text{surv}} = N \cdot \exp(-\sigma \cdot \rho \cdot L), \quad (15)$$

1222 where  $L$  is the distance travelled through a medium,  $\sigma$  is the absorption cross section  
 1223 and  $\rho$  is the density of the medium. The only difference between the different Monte  
 1224 Carlo simulations is the implemented inelastic cross section,  $\sigma = \sigma_{\text{inel}}$ . Thus, by  
 1225 mapping the measured antiparticle-to-particle ratio onto the fitted dependence to  
 1226 find the intercepts, the corresponding value of the scaling factor on the inelastic  
 1227 cross section is found from the x values of the intercepts. In order to reconstruct  
 1228 the values of the inelastic cross section corresponding to the values of the scaling  
 1229 factor, 2 things are necessary: the average material of the ALICE detector (to pick the  
 1230 corresponding cross section implemented in Geant4) and the average energy loss of  
 1231 antinuclei before annihilation occurs (in order to multiply the correct momentum  
 1232 values). These two factors are discussed below in sections 2.3.4 and 2.3.3, respec-  
 1233 tively.

1234  
 1235

1236 For the TPC/TOF method, a similar method is used in order to extract the mea-  
 1237 surement of the inelastic cross section from the TPC/TOF ratio. However, due to the  
 1238 increased amount of material budget which particles have to traverse and the much  
 1239 reduced statistical uncertainties provided by the Pb–Pb data set, the exponential  
 1240 functions are much less steep in the area of interest. An example of such a fit is  
 1241 shown in figure 35.

### 1242 **2.3.3 Accounting for energy losses between the primary vertex and the point of** 1243 **annihilation**

1244 We collect the histograms leading to the antiparticle-to-particle ratio as functions  
 1245 of the momentum these particles have at the primary vertex  $p_{Vtx}$ . However, the

---

<sup>36</sup>This is a proxy for the actual inelastic cross section measurement. However, the mapping from the scaling factor to the inelastic is not exact, but is subject to the uncertainty from any energy loss before annihilation occurs, as will be discussed in section 2.3.3.

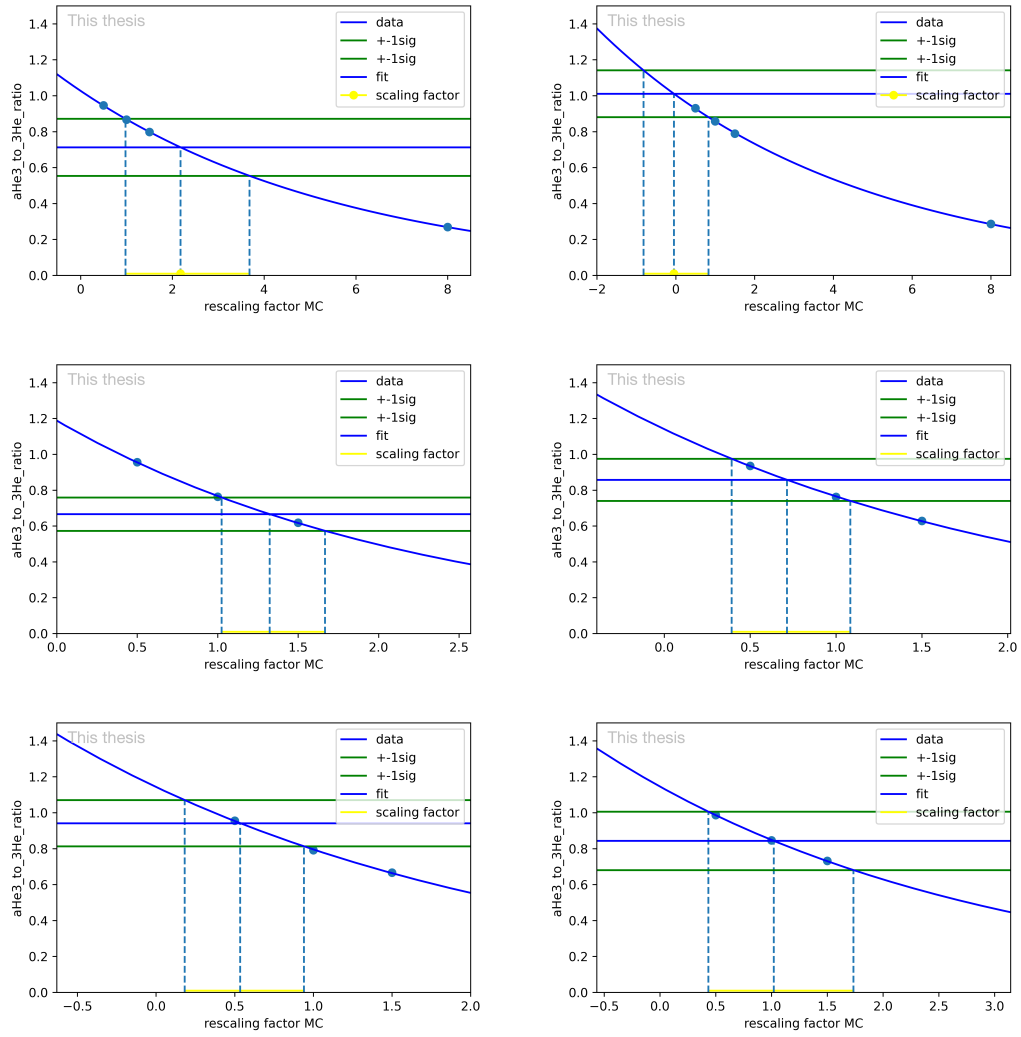


**Figure 33:** Bin by bin plots of the  ${}^3\overline{\text{He}}/{}^3\text{He}$  ratio as a function of the varied inelastic cross section in Monte Carlo simulations, together with the one measured in data. The fitted line is an exponential fit according to the Lambert-Beer law 15, and is used to extract the cross section scaling factor.

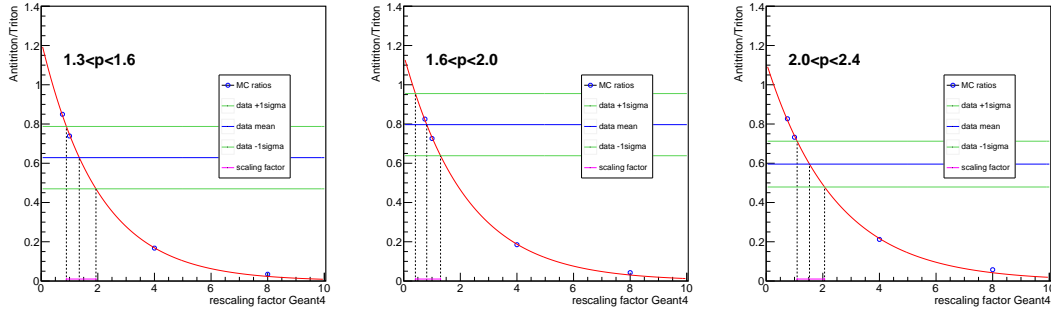


**Figure 34:** Bin by bin plots of the  $\overline{^3\text{H}}/{}^3\text{H}$  ratio as a function of the varied inelastic cross section in Monte Carlo simulations, together with the one measured in data. The fitted line is an exponential fit according to the Lambert-Beer law 15, and is used to extract the cross section scaling factor.

1246 cross section should be given as a function of the momentum which the particles  
 1247 have during annihilation,  $p^*$ . This means energy losses which occur before anni-  
 1248 hilation need to be accounted for. Since we do not see tracks for particles which  
 1249 annihilate, this cannot be done on a case-by-case basis, but must be done statistically.  
 1250

1251 In order to correct for this, let us consider 2 extreme scenarios for where the  
 1252 annihilation might occur. If the annihilation occurs immediately when the particle  
 1253 is produced and meets the beampipe, then it will still have its initial momentum  
 1254  $p_{Vtx}$ . The latest point at which a particle can annihilate and still be included, is just  
 1255 before it would get recognized by the detector. This can be denoted as  $p_{\text{TPC}}$  and  $p_{\text{TOF}}$ ,  
 1256 for the TPC and TOF regions of the analysis, respectively.  $p_{\text{TPC}}$  can be determined  
 1257 very accurately in data, since the tracking of the TPC allows the determination  
 1258 of the momentum. Since the annihilation must occur somewhere between these  
 1259 two momenta, we can assume a mean value of  $p^* = \frac{p_{\text{TPC}} + p_{Vtx}}{2}$ , and evaluate the  
 1260 uncertainties by evaluating the cross section using the 3 different scenarios MIN  
 1261  $p^* = p_{Vtx}$ , MEAN  $p^* = \frac{p_{\text{TPC}} + p_{Vtx}}{2}$  and MAX  $p^* = p_{\text{TPC}}$ . A schematic representation of  
 1262 how this uncertainty is then applied to the inelastic cross section is shown in figure  
 1263 36. The uncertainty from this correction is less than 3% for  $\overline{^3\text{He}}$  and 2.5% for  $\overline{^3\text{H}}$ .  
 1264  $p_{\text{TOF}}$  can similarly be found from the measurement of  $\beta_{\text{TOF}}$ .

### 1265 2.3.4 Evaluating the average ALICE material budget

1266 The annihilations in the ALICE detector can occur on any of the materials in the  
 1267 detector. Therefore, the inelastic cross section can only be shown on an average  
 1268 material. In order to obtain the average detector material, a weighted average is  
 1269 evaluated, based on the density of a given material  $\rho$ . This was calculated over 1 cm

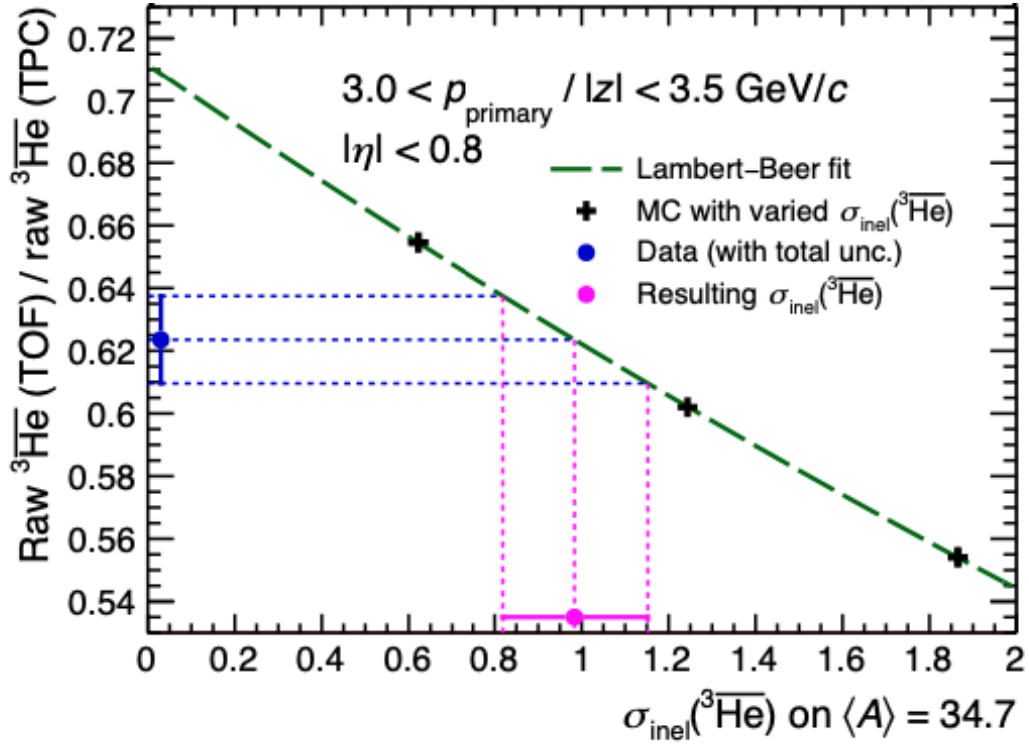


**Figure 35:** TPC/TOF ratio for  $^3\overline{\text{He}}$  as a function of the varied inelastic cross section, for one momentum bin. Figure taken from [110]. The dashed green curve is the a fit of the Lambert-Beer law (equation 15) to the values of the TPC/TOF ratio obtained from MC simulations with varied inelastic cross section (black crosses). The blue datapoint is the ratio in data, and the pink point is the corresponding measurement of the inelastic cross section.

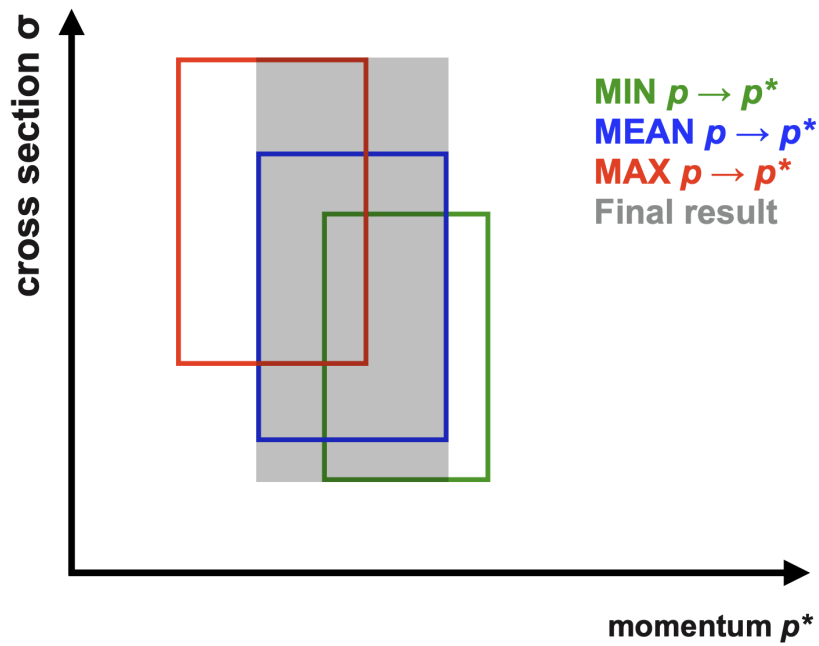


**Figure 36:** Schematic representation for how the correction for the energy loss of antinuclei – and the corresponding systematic uncertainty – is applied to the measurements of the inelastic cross sections. In order to map from the scaling factor to the inelastic cross section, the default parameterization used in Geant4 is employed.



Average mass number	TPC only	TPC + TOF	TPC/TOF matching
$\langle A \rangle$	17.4	31.8	34.7

**Table 2:** Values for the average atomic mass number of the ALICE detector material  $\langle A \rangle$ , for different analysis methods. They are evaluated according to equation 16.

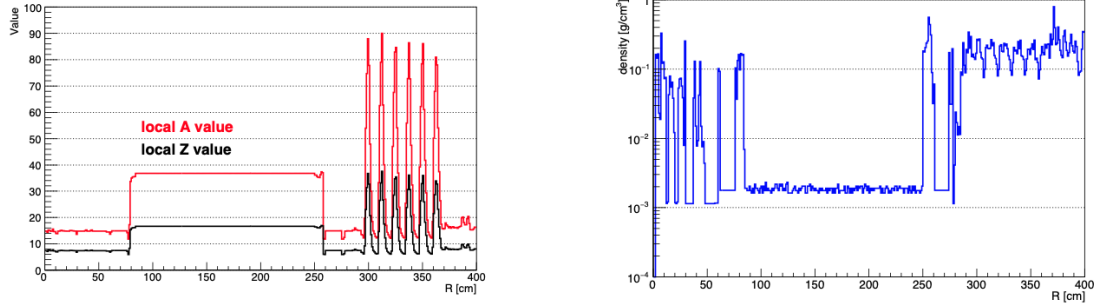


**Figure 37:** Local  $A$  and  $Z$  values (left) and density (right) of the ALICE detector material at mid-rapidity as a function of the radial distance from the interaction point.

1270 steps (which are denoted as  $i$ ) from 0 cm up to a radius  $R$ , which is the last position in  
 1271 the detector at which the particles could be identified. This means that annihilations  
 1272 before this point are accounted for in the inelastic cross section measurements.  
 1273 Since the distribution of the ALICE detector is non-uniform in azimuthal angle  $\phi$ ,  
 1274 the material values were averaged over many random azimuthal angles (denoted as  
 1275  $j$ ). This is shown in equation 16

$$\langle A \rangle = \frac{\sum_{i=1}^R \rho_i A_i}{\sum_{i=1}^R \rho_i} = \frac{\sum_{i=1}^R \sum_{j=1}^N \rho_{ij} A_{ij}}{\sum_{i=1}^R \sum_{j=1}^N \rho_{ij}}. \quad (16)$$

1276 The local  $A$  and  $Z$  values of the ALICE detector, as well as its density, as a function  
 1277 of radius is shown in figure 37. This yields different values for different measuring  
 1278 methods, depending on the range of radii in which the annihilation can occur. If  
 1279 only the TPC is used for determining the antiparticle-to-particle ratio, then only  
 1280 the distance between the beampipe and the middle of the TPC (ca. 168 cm from  
 1281 the beampipe) is considered. When the TOF detector is also used, distances up to  
 1282 the TOF detector (370 cm) are considered. Finally, for the TOF/TPC method, the  
 1283 radii from the middle of the TPC (168 cm) to the TOF detector (370 cm) are evaluated.  
 1284

1285 Once the scaling factors are extracted by comparing the ratios in data to the  
 1286 ones obtained in MC, they need to be multiplied by the inelastic cross sections used

1287 in MC in order to obtain the measured value for  $\sigma_{\text{inel}}$ . Since Geant4 only has cross  
 1288 sections implemented on existing materials, the one with the closest mass number  
 1289  $A$  was chosen, and then scaled according to the parameterizations used in Geant4,  
 1290 as described in equations 3 and 4 in section 1.4.3.

### 1291 2.3.5 Uncertainty coming from the material budget

1292 The measurement outlined in this thesis relies on the accurate knowledge of the  
 1293 ALICE material budget. This is because the loss of antinuclei is proportional to  
 1294  $e^{-\sigma_{\text{inel}}\rho l}$ , where  $\rho$  is the density of the material traversed and  $l$  is the path length of  
 1295 the antinucleus through the material. Thus, the material budget can be quantified  
 1296 as the sum of  $\rho_i l_i$ , over all the materials  $i$  in the detector. This means that the con-  
 1297 straints on the cross section are actually on the product of the cross section and the  
 1298 material budget, and thus any uncertainty on the material budget is 1:1 applied to  
 1299 the inelastic cross section measurement.

1300

1301 Originally, the uncertainty on the material budget was quantified to be about 5%  
 1302 using photon conversions [111], up to the middle of the TPC (since later conversions  
 1303 would result in tracks which have less than half of the TPC clusters and thus cannot  
 1304 we well identified). However, this method left out the bulk of the material budget  
 1305 considered in any analysis using the TOF, as can be seen from figure 31. Therefore,  
 1306 the material between the TPC and TOF detectors needed to be validated using a  
 1307 different method. In order to to this, the same underlying idea as the TPC/TOF  
 1308 analysis was used, but rather than assuming a well known material budget and mea-  
 1309 suring the cross section, a particle with an accurately measured cross section was  
 1310 used in order to probe the material budget. The trick was to find a particle which  
 1311 could be identified cleanly enough in the TPC alone. For this purpose,  $\pi^+$  and  $\pi^-$   
 1312 from  $K_s^0 \rightarrow \pi^+ + \pi^-$  decays and protons from  $\Lambda$  or  $\bar{\Lambda}$  decays were used [112]. Due to  
 1313 their decay topology, they could be cleanly identified in the TPC alone, and their  
 1314 cross section was very accurately known. The measured ratio was then compared  
 1315 to ratios from simulation with varied ALICE material budget, in order to ascertain  
 1316 the uncertainty on the material budget between the TPC and TOF. The resulting  
 1317 uncertainties are shown in figure 38. It can be seen that an uncertainty of  $\approx 5\%$  is  
 1318 achieved using this method.

1319

1320 Therefore, a global uncertainty of about 5% is assumed on the material budget.  
 1321 This uncertainty is included in the total uncertainty calculated on the the primordial  
 1322 ratio, which is the ratio of how many antiparticles are produced in respect to their  
 1323 particle equivalents, at the energies probed. This measurement is based on the  $\bar{p}/p$   
 1324 ratio as measured by ALICE [70, 71, 108]. The uncertainty on this ratio is 1.5%, which  
 1325 is applied for each nucleon in question for both analyses, i.e. 3% for antideuterons

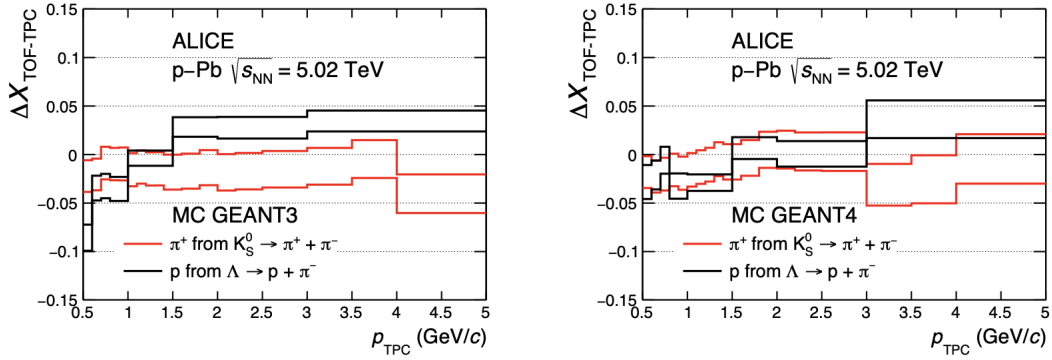


**Figure 38:** Uncertainty on the ALICE material budget between the TPC and TOF detectors, as found by comparing the yields in the TPC to the ones in the TOF for pions from  $K_s^0$  decays (red) and protons from  $\Lambda$  decays (black). The uncertainty is determined by comparing the measured ratio to ones obtained from detailed Monte Carlo simulations of the ALICE detector with varied material budgets, using Geant3 (left) and Geant4 (right). Figures taken from [113].

1326 and 4.5% for  ${}^3\overline{\text{He}}$  and  ${}^3\overline{\text{H}}$ , which therefore includes the uncertainty on the material  
 1327 budget.

### 1328 2.3.6 Non-linear error propagation

1329 The experimental observable is the antiparticle-to-particle ratio, which is then used  
 1330 to calculate the inelastic cross section. Thus, it is necessary to propagate the errors  
 1331 from the former to the latter. This is however non-trivial, since the two are related  
 1332 via an exponential as described in the previous section. Thus, the initially symmetric  
 1333 uncertainties on the ratio become asymmetric when propagated to the inelastic  
 1334 cross section. Additionally, the systematic and statistical uncertainties – which are  
 1335 independent on the ratio and thus sum up in quadrature – can no longer be summed  
 1336 in quadrature on the inelastic cross section, since the scaling between them is no  
 1337 longer linear but exponential. Indeed, as the slope of the exponential is not known  
 1338 a priori, the uncertainties cannot be added at all without knowledge of the depen-  
 1339 dence of the antiparticle-to-particle ratio in a given bin on the inelastic cross section.  
 1340 This leaves two options for the representation of uncertainties on the inelastic cross  
 1341 section: i) show the statistical and systematic uncertainties separately, and give the  
 1342 parameterization of the exponential curve used to add them together for each bin or  
 1343 ii) sum the two uncertainties on the ratio and then propagate the total uncertainty.  
 1344 The second option is significantly more practical since it gives the reader immediate  
 1345 access to the total uncertainty, and does not require extra explanation. The separate

1346 uncertainties can be recovered using the fits shown in figures 33 and 34.

1347

1348 An important note is that this asymmetry arises far more prominently in the  
1349 antiparticle-to-particle analysis than in the TOF/TPC analysis. This is due to 2  
1350 factors: the much reduced statistical uncertainties for the TPC/TOF analysis and  
1351 the increased material budget required (as opposed to the TPC only part of the  
1352 antiparticle-to-particle analysis). This results in the fact that within the uncertainties,  
1353 the effect of the inelastic cross section on the TPC/TOF ratio is well approximated  
1354 with a linear function. Thus, the error propagation from the TPC/TOF ratio to the  
1355 inelastic cross section has only barely noticeable asymmetries.

### 1356 2.3.7 Systematic uncertainties

1357 In this section we will discuss the sources of systematic uncertainties on the in-  
1358 elastic cross section measurements using the antiparticle-to-particle method for  
1359  $A=3$  antinuclei. The uncertainties are dominated by statistical uncertainties at high  
1360 momenta, while at low momenta the uncertainties are dominated by the correction  
1361 for secondary nuclei.

1362

1363 The systematic uncertainties can be categorised into two camps: 1) accounting  
1364 for explicit biases in the analysis techniques or 2) uncertainties coming from a lack  
1365 of knowledge on one or more involved quantities.

1366 An example of an explicit bias is the selection of bin sizes in the histograms used for  
1367 particle identification. The size chosen was  $0.5 n\sigma_{\text{TPC}}$ , but in essence this could have  
1368 been any continuous value able to resolve the peak structure. In the limit of infinite  
1369 statistics, the choice would not matter, but for the limited statistics present in this  
1370 work, such choices can introduce a bias to the extracted (anti)nuclei yields, since the  
1371 distributions are fitted in order to extract the yields. To account for this, variables  
1372 which might introduce a difference to the results were investigated by varying  
1373 them around the chosen value until the extracted yields changed by  $\pm 10\%$ , and  
1374 the variance of the results were used to assign them an uncertainty. Finally, before  
1375 applying this uncertainty to the final results, a Barlow check was performed [114]. A  
1376 Barlow check is a statistical test which evaluates if the variance seen by changing a  
1377 parameter is what is expected within statistical uncertainties, and ensures that an  
1378 uncertainty is not doubly counted (once in the statistical uncertainty of the data,  
1379 and once in the systematic uncertainty). There were two relevant uncertainties of  
1380 this kind in the  $^3\overline{\text{He}}$  and  $^3\overline{\text{H}}$  analyses: track cuts and the PID procedure. The eval-  
1381 uation of the PID procedure is explained above, with the additional evaluation of  
1382 the effect of the fit ranges, with the same method. The uncertainty due to the track  
1383 cuts was slightly more complicated, due to the possible interdependence of different  
1384 parameters. The track parameters on which cut were performed were each assigned

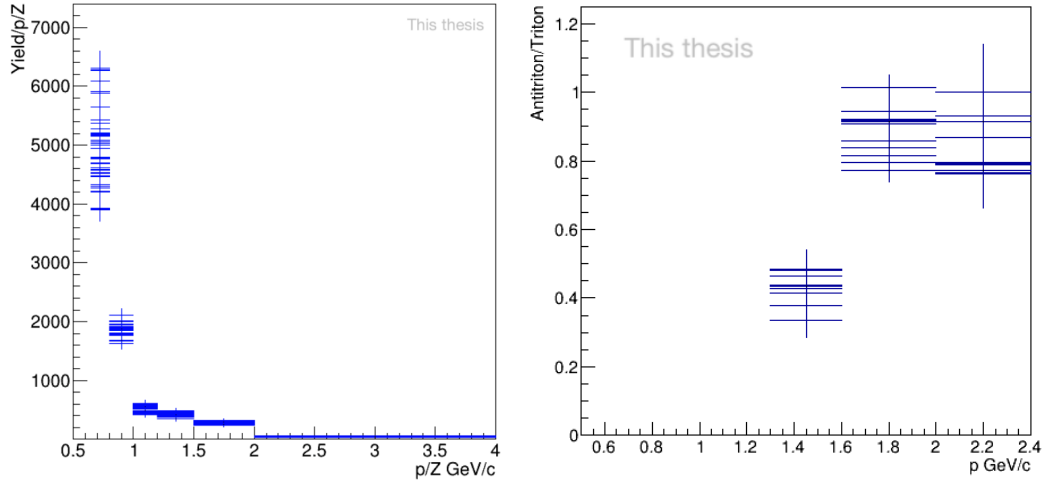


**Figure 39:** Evaluation of the systematic uncertainty due to track cuts, for  ${}^3\overline{\text{He}}$  (left) and  ${}^3\overline{\text{H}}$  (right). The same analysis was re-performed over 100 times with random permutations of "tight", "default", and "loose" cuts on each considered parameter.

1385 a "tight", "default", and "loose" value, and the analysis was checked with random  
 1386 permutations of these cuts over 100 times, as shown in figure 39. The standard  
 1387 deviation of these results was thus taken as the uncertainty.

1388

1389 The second type of systematic uncertainty is due to lack of knowledge on a given  
 1390 parameter. An example of this is uncertainty on the material budget, which is only  
 1391 known to a precision of 4.5%. This effect is evaluated on the primordial antiproton-  
 1392 to-proton ratio, causing an uncertainty of 1.5%. Since the relationship between the  
 1393 antiproton-to-proton ratio and the antiparticle-to-particle ratio for nuclei goes to  
 1394 the exponent of  $A$  (see equation 6), the resulting uncertainty on  $A = 3$  ratios is 4.5%.  
 1395 The next uncertainty is due to the correction for secondary nuclei. This uncertainty  
 1396 is due to the limited statistics of both the templates and the data, making a fit be-  
 1397 tween them difficult. This uncertainty is also applied on the antiparticle-to-particle  
 1398 ratios. Another uncertainty is the uncertainty on the measured matter inelastic cross  
 1399 section<sup>37</sup> on the antiparticle-to-particle ratio. This uncertainty was evaluated by  
 1400 varying the cross section in Monte Carlo simulations using Geant4, and was found  
 1401 to be 0.75% for  $p < 1 \text{ GeV}/c$ , and 2.3% for  $p > 1 \text{ GeV}/c$ . This is the same for  ${}^3\overline{\text{He}}$   
 1402 and  ${}^3\overline{\text{H}}$ . The effect of the elastic cross section of both matter and antimatter were  
 1403 also studied, with an effect  $< 1\%$  for both  ${}^3\overline{\text{He}}$  and  ${}^3\overline{\text{H}}$  in all momentum bins. This is  
 1404 shown in figure 40.

<sup>37</sup>Inelastic processes for matter can be hard scattering events which lead to breakup. The result is the same: a loss of the track in the analysed data.

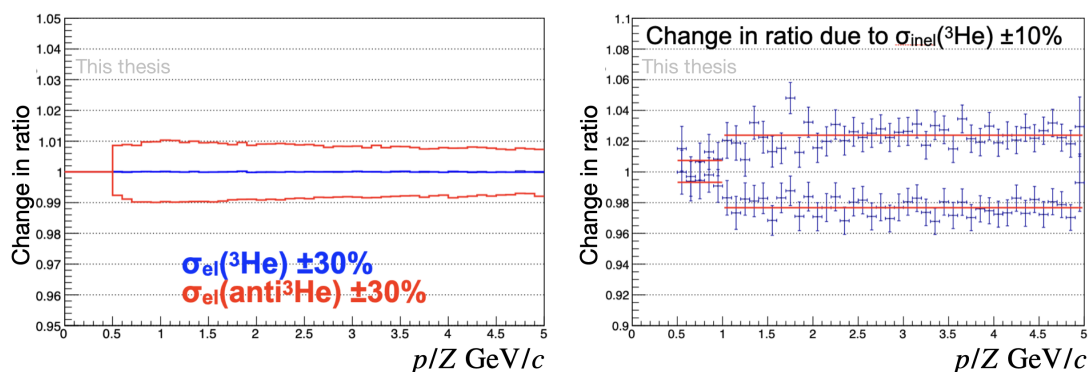


**Figure 40:** Uncertainty on the antiparticle-to-particle ratio introduced by varying the elastic cross sections by 30% (left) and the inelastic matter cross section by 10% (right). Since the cross section for  ${}^3\text{H}$  and  ${}^3\text{He}$  are the same in Geant4, these values are valid for both species.

1405

1406 Finally, the uncertainty coming from the energy loss correction, which is due  
 1407 to our lack of knowledge at what momentum the annihilation occurs. It is applied  
 1408 during the extraction of the inelastic cross sections from the ratios, as described in  
 1409 section 2.3.3.

### 1410 2.3.8 Bench-marking the method on the antiproton inelastic cross section

1411 In order to be sure that the antiparticle-to-particle method gives an accurate mea-  
 1412 surement of the inelastic cross section, the method first had to be benchmarked by  
 1413 evaluating it using a particle for which the inelastic cross section was well known.  
 1414 This was done using antiprotons in [105]. The resulting inelastic cross sections are  
 1415 shown in figure 41. They match the parameterization implemented in Geant4 very  
 1416 well.

1417

1418 Since the antiproton inelastic cross section has been well measured, reproducing  
 1419 it with the antiparticle-to-particle method benchmarks the validity of the method.  
 1420 This allows its application to previously unmeasured quantities: the inelastic cross  
 1421 sections of  $\bar{d}$ ,  ${}^3\bar{\text{He}}$  and  ${}^3\bar{\text{H}}$ . For  ${}^3\bar{\text{He}}$  and  ${}^3\bar{\text{H}}$  the TOF-to-TPC method was in ad-  
 1422 dition to the antiparticle-to-particle method, to take advantage of the increased  
 1423 statistics available in Pb–Pb collisions. The validity of this new method had to be  
 1424 established by comparing it to the measurements using the already benchmarked  
 1425 antiparticle-to-particle method, showing not just the complementary nature of these  
 1426 two measurements, but also the necessity for both to be used in parallel.

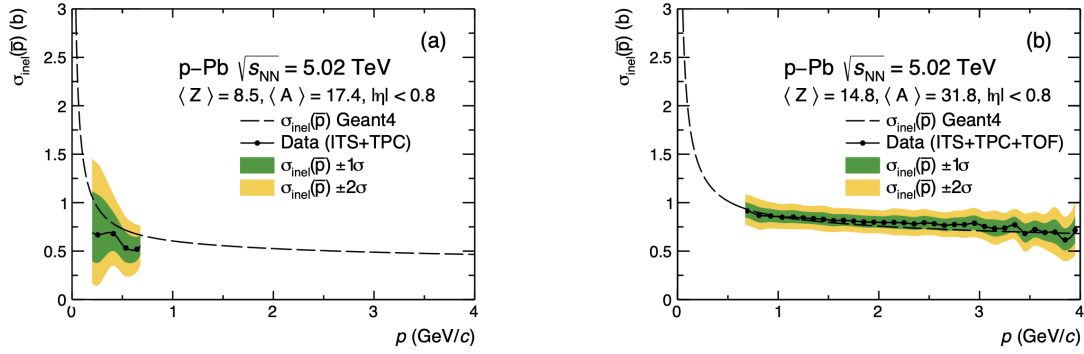


**Figure 41:** The antiproton inelastic cross section on the average ALICE detector material, taken from [105]. The black line and dots show the datapoints, while the green and yellow bands show the 1 and 2 sigma total uncertainties ( $\text{stat}^2 + \text{syst}^2$ ). The dashed line is the parameterization for this cross section in Geant4, which is fitted to data.

### 1427 2.3.9 Independence of collision system

1428 The antimatter-to-matter ratio method's dependence on collision system has been  
 1429 investigated by applying the same analysis method employed in pPb collisions in  
 1430 [105] to high multiplicity pp collisions. The dependence on the collision system  
 1431 is due to the differences in the collision energy, and the resulting difference in the  
 1432 primordial ratio is discussed in section 2.3.1. By taking the antiproton-to-proton  
 1433 ratio for the different collision systems and comparing them, the predicted difference  
 1434 between the antideuteron-to-deuteron ratio was obtained. The results are shown in  
 1435 figure 42, which show that the differences between collisions systems are consistent  
 1436 with the expected deviation. Thus, the inelastic cross section measurements for the  
 1437 two are consistent. This independence of the inelastic cross section on the collision  
 1438 system is expected, since the inelastic cross section is completely independent on  
 1439 the collision system. This becomes especially self-evident when considering that  
 1440 the annihilations do not occur in the initial collisions, but rather as the antiparticles  
 1441 travel through the detector material.

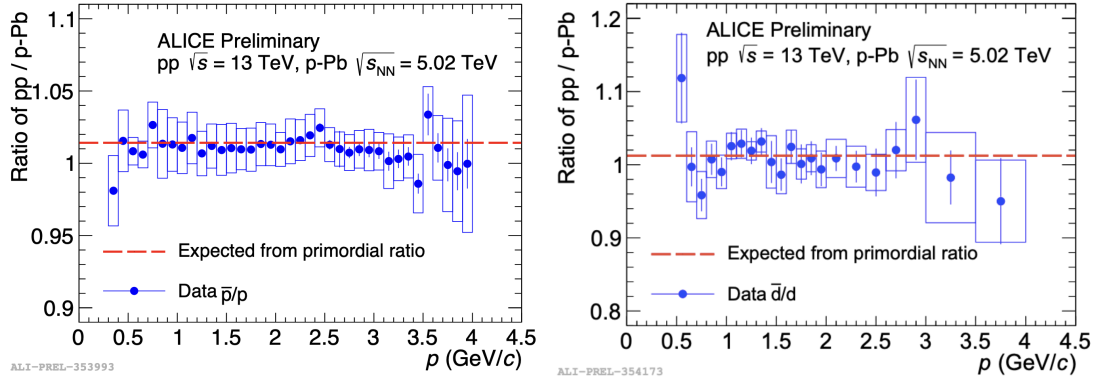


**Figure 42:** Ratio of the antiproton-to-proton ratios (left) and antideuteron-to-deuteron ratios (right) as a function of momentum, obtained in high multiplicity pp collisions and in pPb collisions, compared to the expected difference from the different collision energies (dashed red line). The agreement with the red line shows that this analysis technique is consistent across different collision systems, as expected.

### 1442 3 Measurement of the ${}^3\overline{\text{He}}$ inelastic cross section

1443 The measurement of the  ${}^3\overline{\text{He}}$  inelastic cross section is one of the main results of  
 1444 this thesis. This is the first measurement of this inelastic cross section, which is  
 1445 important not just for nuclear physics, but also for astrophysical searches for physics  
 1446 beyond the standard model, as discussed in section 1.5.2. Historically, inelastic cross  
 1447 section measurements were performed using fixed target experiments: a beam of the  
 1448 particle of interest with well-determined momentum was isolated, and then fired on  
 1449 a material target with known properties. By measuring the abundance of the particle  
 1450 before and after the target, the cross section could be measured. The difficulty in  
 1451 doing this for antinuclei lies in the production and isolation of an antinuclei beam,  
 1452 since antinuclei production is so rare and has a high  $\sqrt{s}$  threshold. Even at the places  
 1453 where antinuclei are produced (at the LHC and at the relativistic heavy ion collider  
 1454 (RHIC) [115]), further isolating a beam of such particles is not feasible within current  
 1455 experimental constraints. In fact, out of all antinuclei ( $A > 2$ ), this method has only  
 1456 been applied to high energy antideuterons [46, 45], at the U-70 proton synchrotron  
 1457 in the 70s, for particles at very high momenta of 13 GeV/c and 25 GeV/c. Recently,  
 1458 roughly half a century later, the new measurement technique using the antiparticle-  
 1459 to-particle ratio has been shown to be able to measure the antideuteron inelastic  
 1460 cross section down to 500 MeV/c [105]. This measurement has now been expanded  
 1461 to  ${}^3\overline{\text{He}}$  [110] and  ${}^3\overline{\text{H}}$ , and a separate complementary method (TPC/TOF method)  
 1462 has enabled the use of the high statistics Pb–Pb data to boost the measurements’  
 1463 precision. Both these new methods rely on quantifying the absorption of antinuclei



1464 as they travel through the detector material, rather than a dedicated target. The  
1465 disadvantage of this approach is that the detector material is optimised to have  
1466 little material budget as possible, as to not interfere with the particles of interest.  
1467 Nevertheless, these methods allow us to further our knowledge of antinuclei inelastic  
1468 cross sections for the first time in half a century.

### 1469 **3.1 Physics motivation and overview of the analysis method**

1470  ${}^3\overline{\text{He}}$  nuclei are a promising probe for indirect dark matter searches, but in order to  
1471 understand any potential signal, it is necessary to know their disappearance proba-  
1472 bility as they travel to earth from their cosmic sources, as is extensively discussed  
1473 in sections 1.5.2 and 5.1.2. While this is the astrophysical motivation for this mea-  
1474 surement, it also has applications in nuclear physics, in particular for improved  
1475 modelling of antinuclei propagation through the detector material using Geant4.  
1476 This is particularly important in the low energy region (*lessim* 2 GeV/c), where  
1477 Glauber model calculations are less reliable. Measurements of (anti)nuclei produc-  
1478 tion rely on efficiencies to be well reproduced by Monte Carlo simulation, which  
1479 requires the inelastic cross sections as input.  
1480 The analysis methods used to measure the inelastic interaction cross section are laid  
1481 out below.

#### 1482 **3.1.1 Antiparticle-to-particle ratio method**

1483 The detailed steps of this method are described in section 2.  
1484 The antiparticle-to-particle method is based on using the ratio of antiparticles to  
1485 particles as an observable for the cross section. This works since at LHC energies,  
1486 the relative amounts of matter and antimatter which are produced are well known.  
1487 They are produced in almost equal amounts, and therefore dividing the number of  
1488 antiparticles by the number of particles acts as a normalization of the number of  
1489 antiparticles produced<sup>38</sup>. The detector material itself acts as a target. Since antipar-  
1490 ticles and particles have the same interactions with the detector material apart from  
1491 annihilation, uncertainties due to particle identification and tracking cancel to a  
1492 large extent.

#### 1493 **3.1.2 TOF-TPC matching method**

1494 The second method for measuring  $\sigma_{\text{inel}}({}^3\overline{\text{He}})$  uses the fact that over a wide momen-  
1495 tum range,  ${}^3\overline{\text{He}}$  can be clearly identified in both the TPC and the TOF detectors. We  
1496 can therefore check the amount of  ${}^3\overline{\text{He}}$  nuclei present in the TPC, and how many

---

<sup>38</sup>This method does not in principle require equal amounts of matter and antimatter, merely a very precise knowledge of the ratio of antimatter to matter which is produced.

1497 of those make it all the way to the TOF detector. This method works akin to a fixed  
1498 target experiment, in that a "beam" is identified by measuring  ${}^3\overline{\text{He}}$  in the TPC, this  
1499 beam is then fired upon the "target", which in this case is the space frame and the  
1500 TRD. Some of the nuclei will annihilate, while the others which make it through will  
1501 generate a matching TOF hit, thus allowing us to quantify the "beam" loss between  
1502 two detectors.

1503 The advantage of this method is that only the antiparticles are required; no specific  
1504 assumptions about the antimatter-to-matter ratio need to be assumed and tested.  
1505 This also means that no correction for secondary nuclei from material spallation  
1506 needs to be applied, since the origin of the  ${}^3\overline{\text{He}}$  has no impact on the result<sup>39</sup>. The  
1507 disadvantage is that the acceptance of the TOF detector limits the applicability of  
1508 this method to higher momenta, so it is more difficult to measure the low energy rise  
1509 of the inelastic cross section.

1510  
1511 The measurement of  $\sigma_{\text{inel}}({}^3\overline{\text{He}})$  using the TPC-TOF matching method is thus com-  
1512 plementary to the antiparticle-to-particle method described above. This analysis  
1513 was not carried out as part of this work, but ties in closely with the results shown both  
1514 in this chapter and in chapter 5, and is thus described here. The measurement is  
1515 also shown together with the measurement using the antimatter-to-matter inelastic  
1516 cross section. More details about the analysis can be found in [116, 110].

## 1517 3.2 Secondary correction

1518 In order to extract the cross section from the antiparticle-to-particle ratio, only parti-  
1519 cles produced at the primary vertex must be considered. Thus, secondary particles  
1520 need to be accounted for by using template fits, as described in section 2.2.3.

1521  
1522 The template fits done for the secondary correction of  ${}^3\text{He}$  are shown in figure  
1523 43. The cut on  $|\text{DCA}_z| < 1$  cm was chosen in order to include more secondaries, and  
1524 improve the statistical constraints on the fit. As can be seen, in the second bin there  
1525 is a slight shoulder towards the negative side of 0, where the fitted material template  
1526 exceeds the data, which is the biggest systematic discrepancy of the fits. This effect  
1527 has been investigated, and since i) it is outside of the signal region and ii) it is within  
1528 the uncertainties, it was concluded to be a negligible effect.

---

<sup>39</sup>Also, there are no secondary  ${}^3\overline{\text{He}}$  nuclei from material spallation, so the secondary correction is even less important.

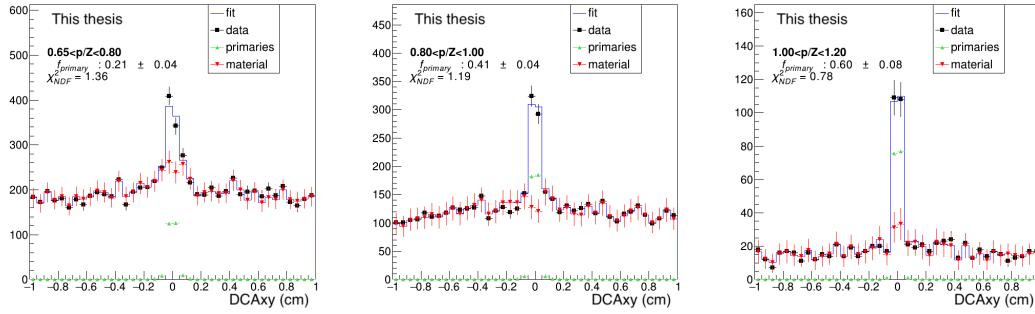


**Figure 43:** Template fits for determining the primary fraction of  ${}^3\text{He}$  in the first 3 momentum bins (above this momentum the primary fraction goes to 1), for a  $|DCA_z| < 1$  cm cut. The fits were performed using the TFractionFitter method available in ROOT.

### 1529 3.3 Results

1530 After all the corrections are applied, we can now obtain the final  ${}^3\overline{\text{He}}/{}^3\text{He}$  and the  
 1531 corresponding  $\sigma_{\text{inel}}({}^3\overline{\text{He}})$ , which are shown in figure 44. The measurement is in  
 1532 agreement with the parameterization used in Geant4 at a significance of slightly  
 1533 above  $1\sigma$ . The lowest momentum bin shows a hint at a steeper rise than the pa-  
 1534 rameterization. The second bin is shown as an upper limit since the uncertainties  
 1535 reached below 0, which would be an unphysical value for the cross section.

1536

1537 This represents the first measurement of  $\sigma_{\text{inel}}({}^3\overline{\text{He}})$ .

1538 The measurement of  $\sigma_{\text{inel}}({}^3\overline{\text{He}})$  done in Pb–Pb collisions using the TOF-to-TPC  
 1539 method is shown for comparison in figure 45. The much increased statistics available  
 1540 for the Pb–Pb data sample results in much reduced statistical uncertainty. The two  
 1541 measurements deliver consistent results in the overlapping momentum region.

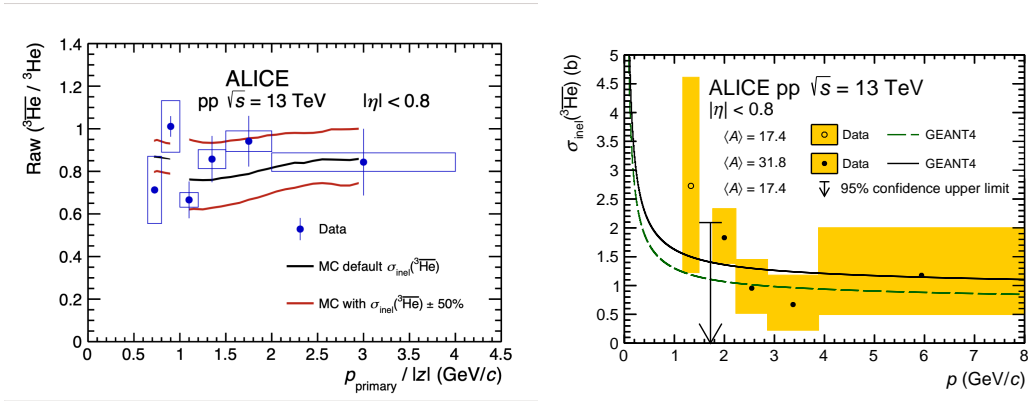


**Figure 44:** (Left)  ${}^3\overline{\text{He}}/{}^3\text{He}$  measured in pp collisions at  $\sqrt{s} = 13$  TeV, as a function of the particle momentum at the primary vertex. Statistical uncertainties are shown as lines, and systematic uncertainties are shown as boxes. The discontinuity at  $p/Z = 1$  GeV/c is due to the additional requirement of a TOF hit, thus requiring tracks to traverse more material. (Right)  $\sigma_{\text{inel}}({}^3\overline{\text{He}})$  as measured using the antiparticle-to-particle method in pp collisions at  $\sqrt{s} = 13$  TeV, as a function of the antinuclei momentum at annihilation. The uncertainties include both statistical and systematic uncertainties. Open points are from the analysis using the TPC only for particle identification, while closed points require a matching hit in the TOF in addition to the TPC, which therefore has a different averaged material value. The lines show the parameterization used in Geant4.

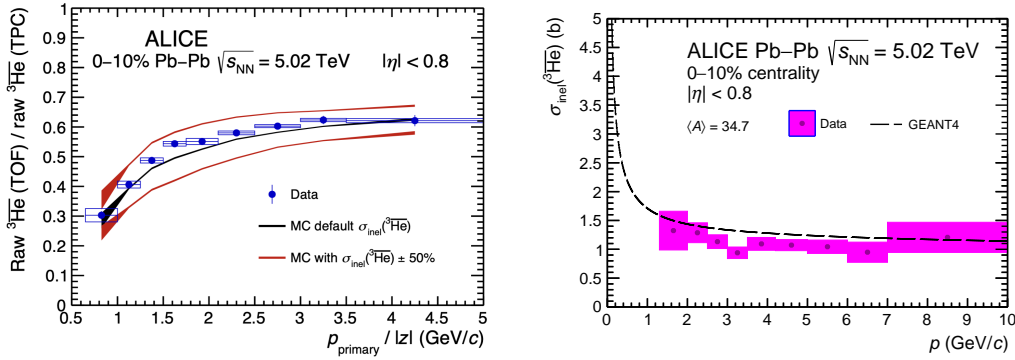


**Figure 45:** (Left) TOF-to-TPC ratio for  ${}^3\overline{\text{He}}$  in Pb–Pb collisions at  $\sqrt{s_{\text{NN}}} = 5.02$  TeV, as a function of the particle momentum at the primary vertex. Statistical uncertainties are shown as bars, and systematic uncertainties are shown as boxes. The colored lines are the same ratio in Monte Carlo simulations with varied  $\sigma_{\text{inel}}({}^3\overline{\text{He}})$ . (Right)  $\sigma_{\text{inel}}({}^3\overline{\text{He}})$  as measured using the TOF-to-TPC method in Pb–Pb collisions at  $\sqrt{s_{\text{NN}}} = 5.02$  TeV, as a function of the antinuclei momentum at annihilation. The uncertainties include both statistical and systematic uncertainties. The line shows the parameterization used in Geant4. Figures taken from [110].

## 1542 4 Measurement of the antitriton inelastic cross section

### 1543 4.1 Physics motivation and overview of the analysis method

1544 The measurement of  $\sigma_{\text{inel}}({}^3\overline{\text{H}})$  does not have the same astrophysical motivation as  
 1545 the measurement of  $\sigma_{\text{inel}}({}^3\overline{\text{He}})$ , since  ${}^3\overline{\text{H}}$  is an unstable nucleus with a half-life of  
 1546  $\approx 12.3$  years. Instead, the main motivation for this measurement is the comparison  
 1547 to the  ${}^3\overline{\text{He}}$  inelastic cross section. This could shine light on any isospin dependence  
 1548 of the annihilation probability of antinuclei. Such an effect might also elucidate  
 1549 how the strong force interacts with isospin, in a potentially more sensitive way than  
 1550 observing neutrons, since they are much harder to detect due to not being charged.  
 1551 And while the current statistical uncertainties are unable to resolve any difference,  
 1552 the two measurements provide a proof of concept that this dependence can be  
 1553 measured by means of comparing the inelastic cross sections of  $A = 3$  antinuclei.

### 1554 4.2 Accessible momentum range of the measurement

1555 Due to the single charge of  ${}^3\overline{\text{H}}$ , there are a few noteworthy differences in the particle  
 1556 identification in comparison to  ${}^3\overline{\text{He}}$ . The first and most important difference is  
 1557 that it is not clearly identifiable in the TPC alone at high momenta. This can be

#### 4. Measurement of the antitriton inelastic cross section

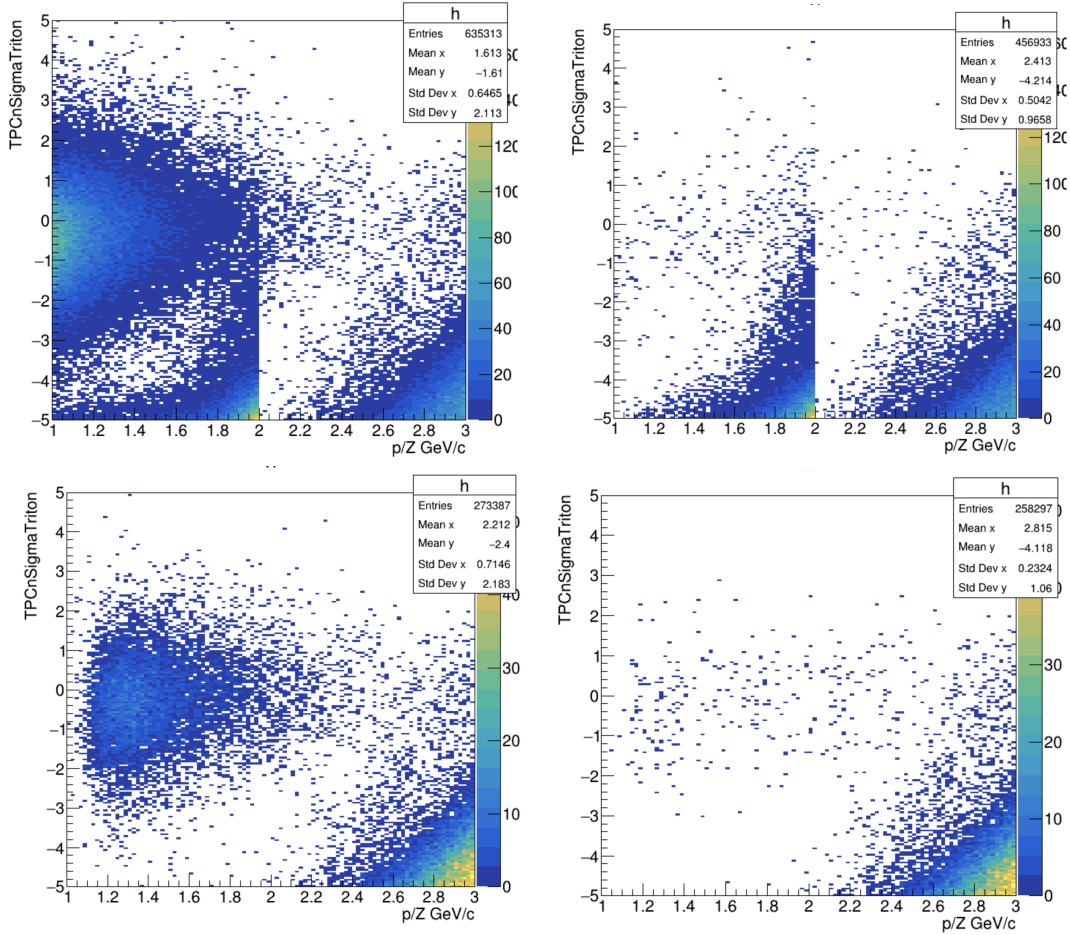


**Figure 46:**  $n\sigma_{\text{TPC}}$  vs momentum plots for tritons. A cut on the  $m_{\text{TOF}}$  is applied above 2 GeV/c in all figures. (Top left) the original distribution without an additional cut on either DCA or  $m_{\text{TOF}}$ . (Top right) the distribution after a cut of  $|DCA_{x,y}| < 1$  mm and  $|DCA_z| < 1$  mm is applied. (Bottom left) the distribution after the cut on  $m_{\text{TOF}}$  is extended to momenta as low as 1 GeV/c. (Bottom right) the distribution after both the DCA and  $m_{\text{TOF}}$  cuts were applied.

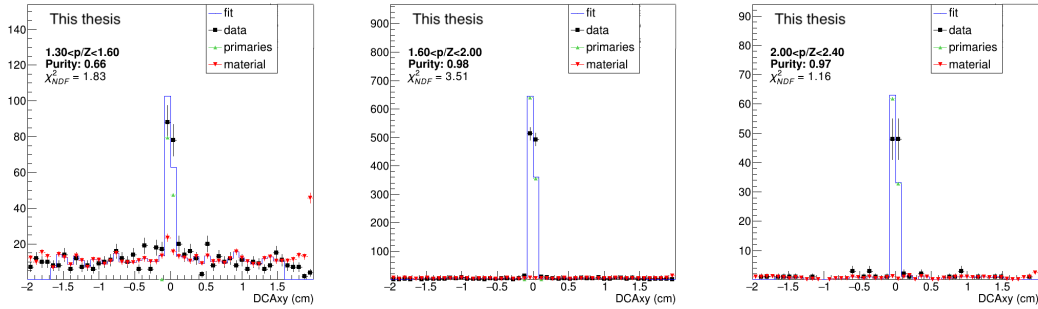


**Figure 47:** Template fits to the DCA distribution of  ${}^3\text{H}$ , to account for the contributions from secondary nuclei from spallation processes. The primary fraction is evaluated as  $f_p = \int_{-0.1\text{cm}}^{0.1\text{cm}} \text{fit}_{\text{signal}} d\text{DCA} / \int_{-0.1\text{cm}}^{0.1\text{cm}} \text{data} d\text{DCA}$ . The results are shown for each momentum bin.

1558 seen in figure 18, which shows that the expected energy loss for (anti) ${}^3\text{H}$  merges  
 1559 with the bands from other particles at about 1.5 GeV. The considerations for the  
 1560 identification are shown in figure 46, which shows how the TOF cut is able to remove  
 1561 the contamination up to a momentum of  $\approx 2.4$  GeV/ $c$ , while the DCA cut removes  
 1562 much of the secondary contribution at low momentum. Additionally, by comparing  
 1563 the top and bottom panels on the right side of figure 46, which show the effect of  
 1564 the TOF cut after the DCA cut is applied, we can see that the additional requirement  
 1565 of the TOF removes all the contamination at low momentum, while preserving a  
 1566 large fraction of the signal. Furthermore, the fact that the TOF is required means  
 1567 that the particles have to traverse more material, and thus the ratio becomes more  
 1568 sensitive to the inelastic cross section. Thus, the TOF is used in the whole momentum  
 1569 range for the measurement of the  ${}^3\bar{\text{H}}/{}^3\text{H}$  ratio.

### 1570 4.3 Secondary correction

1571 Similarly as for  ${}^3\bar{\text{He}}$ , the  ${}^3\bar{\text{H}}/{}^3\text{H}$  ratio still needs to be corrected for the remaining  
 1572 secondary nuclei from material spallation. This is done using template fits, according  
 1573 to the method described in 2.2.3. The fits are shown in figure 47. It can be seen  
 1574 that the contribution is negligible in the second and third bin. In the first bin, the  
 1575 contribution from secondaries is well constrained. The resulting primary fraction is  
 1576 shown in the bottom of the figure. The uncertainty of the primary fraction is added  
 1577 to the systematic uncertainties on the  ${}^3\bar{\text{H}}/{}^3\text{H}$  ratio in quadrature.

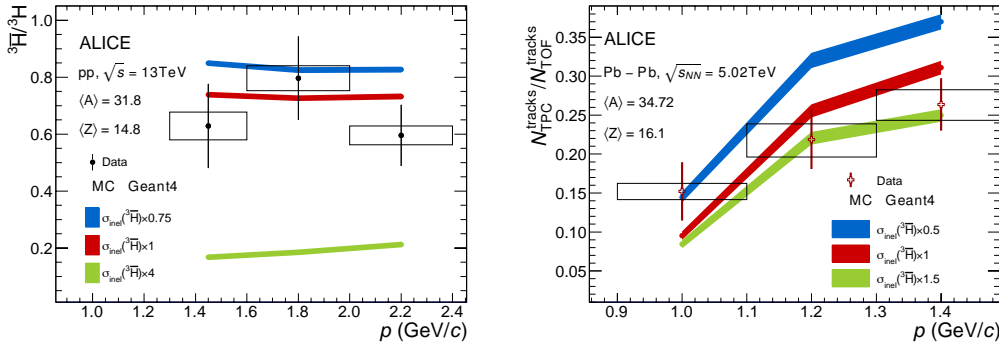


**Figure 48:** (Left)  ${}^3\bar{\text{H}}/{}^3\text{H}$  ratio as a function of momentum, with statistical uncertainties as bars and systematic uncertainties as boxes. The colored lines represent Monte Carlo simulations with varied inelastic cross sections. (Right)  ${}^3\bar{\text{H}}$  TOF-to-TPC ratio as a function of momentum, with statistical uncertainties as bars and systematic uncertainties as boxes. The colored lines represent Monte Carlo simulations with varied inelastic cross sections.

#### 1578 4.4 Results

1579 In this section, the measurements of  $\sigma_{\text{inel}}({}^3\bar{\text{H}})$  are presented. The left side of figure  
 1580 48 shows the  ${}^3\bar{\text{H}}/{}^3\text{H}$  ratio as measured in pp collisions, and the left side of figure  
 1581 49 shows the resulting inelastic cross section measurement with the open circles.  
 1582 The measurement is consistent with the parameterization used in Geant4 within  
 1583 a significance of  $2\sigma$ , but shows a hint at a systematically larger value for  $\sigma_{\text{inel}}({}^3\bar{\text{H}})$   
 1584 . The right side of figure 48 shows the TOF/TPC ratio of  ${}^3\bar{\text{H}}$  in Pb – Pb collisions  
 1585 at  $\sqrt{s_{\text{NN}}} = 5.02$  TeV<sup>40</sup> and the corresponding measurement of  $\sigma_{\text{inel}}({}^3\bar{\text{H}})$  is shown  
 1586 on the left of figure 49 as full circles. The measurements are compared with the  
 1587 results for  ${}^3\bar{\text{He}}$  in the right panel of figure 49, all scaled to the same average material,  
 1588 which shows that the results for  ${}^3\bar{\text{H}}$  and  ${}^3\bar{\text{He}}$  are consistent within uncertainties.  
 1589 This means that within the current uncertainties, the annihilation cross sections  
 1590 are consistent with isospin symmetry. Improvements on the statistical precision of  
 1591 these measurements will help constrain this assumption further using the data from  
 1592 the upcoming Run 3 and Run 4 campaigns at the LHC.

<sup>40</sup>These were not obtained as part of this thesis, but were obtained for the same publication as the cross section in Pb–Pb collisions (publication is in preparation).



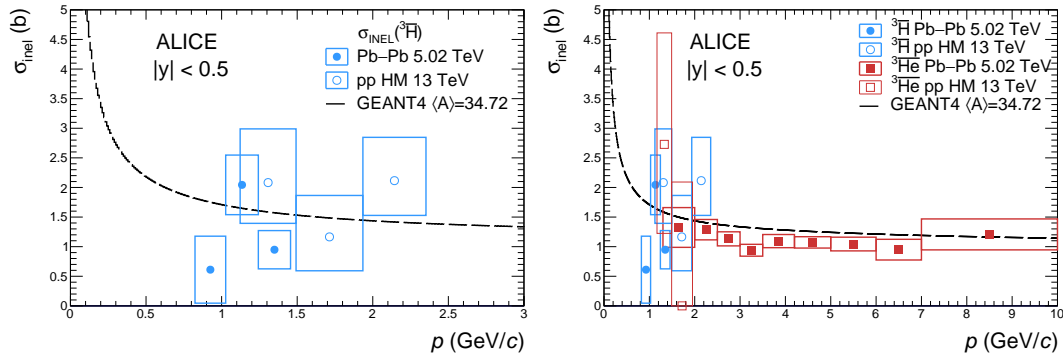


**Figure 49:** (Left) the resulting measurement of  $\sigma_{\text{inel}}(^3\bar{\text{H}})$  using the antibaryon-to-baryon method ( $\bar{\text{B}}/\text{B}$ ) and the TOF-to-TPC method, on the average ALICE material. The colored boxes show the total uncertainty ( $\text{stat}^2 + \text{syst.}^2$ ). The line shows the parameterization as used in Geant4. (Right) comparison of the  $\sigma_{\text{inel}}(^3\bar{\text{He}})$  and  $\sigma_{\text{inel}}(^3\bar{\text{H}})$  measurements.

## 1593 5 Antinuclei in the cosmos

1594 Antinuclei are some of the rarest stable objects in cosmic rays, in fact, no compound  
 1595 antinuclei have ever been conclusively observed in cosmic rays. But it is this exact fact  
 1596 that makes them such promising candidates for the search of new physics beyond  
 1597 the Standard Model. Whereas for other particle species the signal-to-background  
 1598 ratio might be minuscule for any new effect, antinuclei production is so rare in  
 1599 standard model processes that any new physics might produce signals orders of  
 1600 magnitude greater than what can be explained with our current knowledge. While no  
 1601 conclusive observation of antinuclei in cosmic rays has been published, the AMS-02  
 1602 Collaboration has repeatedly reported potential signals of antihelium [117, 118, 119],  
 1603 motivating a renewed push of research interest into cosmic-ray antinuclei.

1604

1605 The goal of this section is to discuss possible exotic sources of antinuclei in our  
 1606 galaxy focusing on WIMP dark matter and extragalactic WIMP dark matter. For  
 1607 antideuterons primordial black holes are also discussed as a possible source. These  
 1608 are compared to antinuclei produced in high-energy cosmic-ray collisions with the  
 1609 interstellar medium, which in the respective rest frame is an analogous process to  
 1610 the one used to produce antinuclei at accelerators. In the lab frame the collision is  
 1611 heavily boosted, which affects the produced spectra. Crucially, the new measure-  
 1612 ments of the inelastic cross sections of antihelium laid out in Section 3, and the  
 1613 first low-energy measurements of the antideuteron–matter inelastic cross section  
 1614 laid out in [105], are for the first time incorporated in such studies. The discussion

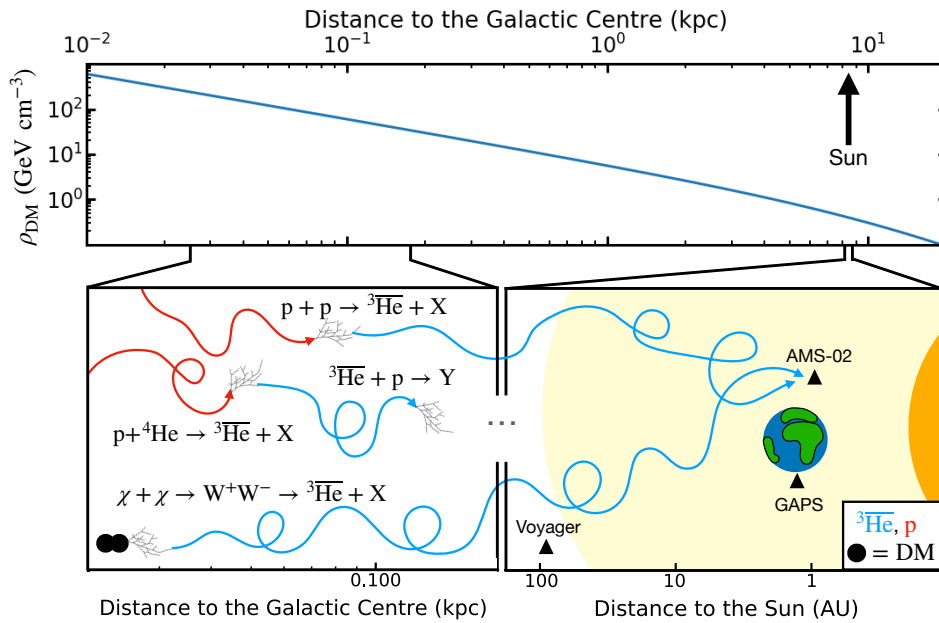


**Figure 50:** Illustrated story of the journey which antinuclei undertake before being observed near earth. Red lines shown high energy cosmic ray protons, Blue lines shown  ${}^3\overline{\text{He}}$ . The antinuclei get created all throughout the galaxy, and in the galactic centre antinuclei from dark matter is the most concentrated, due to the higher dark matter density. Similarly, antinuclei from high energy cosmic rays are created all over the galaxy. The created antinuclei then travel through the interstellar medium, some of them annihilating along the way. The ones which do make it to earth then are affected by the solar magnetic field, before reaching detectors near earth. All these processes need to be understood in order to be able to interpret an antinuclei signal in cosmic rays.

1615 therefore focuses in particular on propagating these measurements to obtain the  
 1616 experimental uncertainties from inelastic interactions on the antinuclei flux near  
 1617 earth. This journey from creation to observation for antinuclei is illustrated in figure  
 1618 50.

1619

1620 In order to study the two sources we employ the GALPROP framework [120]. This  
 1621 framework propagates particles through our galaxy, simulating various effects such  
 1622 as diffusion, convection and also inelastic processes. The resulting fluxes near earth  
 1623 are then presented for both antideuterons and  ${}^3\overline{\text{He}}$ , for different dark matter masses  
 1624 and profiles. Finally, current and planned experiments for detecting antinuclei in  
 1625 cosmic rays are discussed. The antinuclei fluxes from high-energy cosmic-ray colli-  
 1626 sions shown in this thesis as comparisons to the fluxes from possible dark-matter  
 1627 sources are taken from [121] and [113], for antideuteron and  ${}^3\overline{\text{He}}$  respectively.

1628

## 1629 5.1 Sources of antinuclei in the cosmos

1630 Antinuclei are some of the rarest stable particles in our galaxy, since very few abun-  
 1631 dantly occurring processes will produce them in any detectable amount [122, 123].  
 1632 This is in contrast to nuclei, which are the most abundant stable particles within our  
 1633 galaxy. Indeed, nuclei up to Iron have been observed by a variety of methods: in the  
 1634 spectral lines of stars, in cosmic rays by the AMS collaboration [124] and of course  
 1635 on earth. A large amount of the light matter nuclei (up to Lithium) was produced  
 1636 during Big Bang Nucleosynthesis (BBN) [74], while all heavier nuclei were produced  
 1637 during stellar nucleosynthesis [125]. This process involves fusing hydrogen nuclei to  
 1638 create the necessary energy inside a star to counteract its own gravitational pull, cre-  
 1639 ating helium in the process. This continues for most of the lifetime of the star, until  
 1640 its reserves of hydrogen run low. Without the sustained temperature and pressure  
 1641 provided by hydrogen fusion, the star's core will become inert and contract under  
 1642 gravity. Meanwhile, fusion will start in the outer layers of the star, where residual  
 1643 hydrogen is still found. This causes those layers to expand and cool, and the star  
 1644 forms what is called a red giant [125] or red supergiant [125]. Over time, the core will  
 1645 contract and heat up<sup>41</sup>, until the conditions allow for even heavier elements (helium  
 1646 and sometimes carbon) to start fusing to create energy [125]. During this process,  
 1647 elements up to iron are created through nuclear fusion, and heavier elements can be  
 1648 created through slow neutron capture processes [125]. This process accounts for the  
 1649 production of roughly half of the elements heavier than iron [125]. When this source  
 1650 of energy becomes insufficient, the red giant's will implode and expel its outer shell,

<sup>41</sup>Red supergiants may have sufficient pressure immediately to commence helium fusion in their core. For more information on stellar information please refer to [125].

1651 creating a planetary nebula. Red supergiants will explode in a supernovae, expelling  
 1652 huge amounts of energy and matter. In this process, rapid neutron capture occurs,  
 1653 producing the other half of elements heavier than iron [126].

1654 However, due to the asymmetry of matter and antimatter in our galaxy, neither BBN  
 1655 nor stellar nucleosynthesis is thought to be a dominant source for antinuclei. Anti-  
 1656 matter produced during BBN is likely to have annihilated propagating through the  
 1657 galaxy from the Big Bang until today. This can be shown by a back of the envelop  
 1658 calculation. Assuming an antinucleus with an annihilation cross section of  $\approx 1\text{b}$   
 1659 and a momentum of  $\gtrsim 0.1\text{ GeV}/n$ , the fraction surviving until this day is given by  
 1660  $N/N_0 = \exp(-\sigma n \beta c t)$ , where  $n$  is the average matter density in the regions traversed.  
 1661 Taking  $n = 1\text{cm}^{-3}$  and using  $\beta = p/\gamma m$  one finds that only about  $e^{-100} \approx 10^{-44}$  of the  
 1662 initial population would still be left today. And in order for stellar antinucleosyn-  
 1663 thesis to occur, anti-starts – or at least large clouds of antimatter – would have to  
 1664 exist. Any such regions would by default have to come in contact with  
 1665 the matter dominated regions which predominantly make up our galaxy. In those  
 1666 overlap regions, significant amounts of annihilations would cause a visible gamma  
 1667 ray signal [122]. No signal of this kind has been reported, although if such regions  
 1668 were small enough, they would appear as point sources to current instruments and  
 1669 thus make up a part of the currently unidentified point sources within our galaxy  
 1670 [127]. Recent work has claimed that such antimatter regions may have formed during  
 1671 the big bang and survived to this day [128, 58], making up  $\approx 20$  of the roughly 1000  
 1672 unidentified point sources. However, these studies also note the necessity for the  
 1673 antimatter regions to have formed in places where the proton density is  $O(10^{-8})$   
 1674 of the cosmic average. The authors do not provide a viable mechanism by which this  
 1675 could have occurred.

1676 We therefore have to look to other processes which could produce antinuclei. Due  
 1677 to baryon number conservation, all such processes are likely to produce at least an  
 1678 equal amount of light nuclei as well. However, since nuclei are far more abundant  
 1679 than antinuclei, these processes will only contribute a negligible amount to the  
 1680 total nuclei flux in our galaxy, while they might dominate the antinuclei flux. This  
 1681 extremely high expected signal-to-background ratio is the reason why antinuclei are  
 1682 considered such a promising probe into new physics.

### 1683 5.1.1 High-energy cosmic-ray collisions

1684 The most well-known source for antinuclei in cosmic rays — and the only one which  
 1685 does not require new physics or as of yet undiscovered objects — are collisions  
 1686 of high-energy cosmic rays with the interstellar medium. Such collisions, akin to  
 1687 collisions at particle accelerators, will produce antinuclei by converting the available  
 1688 mass–energy from the collision into (anti)nucleons which then coalesce (see section  
 1689 1.5.1 for a more detailed discussion on antinuclei production). In order to predict

1690 the production of antinuclei in such high energy collisions we need to know the  
 1691 differential production cross section of the antinuclei in question, for each collision  
 1692 which can occur, and we need to know which collisions those are, i.e. we need to  
 1693 know the composition of cosmic rays and of the interstellar medium, as a function  
 1694 of energy. For both the interstellar gas and cosmic rays, the composition is  $\approx 90\%$   
 1695 protons,  $\approx 9\%$  Helium-4 and  $< 1\%$  heavier nuclei. Thus, the source term for nuclei  
 1696 from such secondary collisions can be written as

$$q(\vec{r}, p) = \sum_{CR=H,He} \sum_{ISM=H,He} n_{ISM}(\vec{r}) \int dp'_{CR} \beta_{CR} c \frac{d\sigma(p, p'_{CR})}{dp} n_{CR}(\vec{r}, p'_{CR}) \quad (17)$$

1697 , where  $\sum_{CR=H,He} \sum_{ISM=H,He}$  denote the sums over the particle species in cosmic  
 1698 rays and the interstellar medium,  $n_{ISM}(\vec{r})$  is the density of the interstellar gas at a  
 1699 given point,  $n_{CR}(\vec{r}, p'_{CR})$  is the density of cosmic rays at a given position and energy,  
 1700 and  $\frac{d\sigma(p, p'_{CR})}{dp}$  is the differential production cross section for an antinucleus, as a func-  
 1701 tion of the momentum of the produced antinucleus  $p$  and the momentum of the  
 1702 incoming cosmic ray  $p'_{CR}$ . The particles in the interstellar medium are considered to  
 1703 be at rest in this calculation, which is a valid approximation since they move at very  
 1704 low speeds in comparison to the incoming cosmic rays<sup>42</sup>.

1705

1706 The production cross section of antinuclei in such small collisions systems is  
 1707 suppressed at low energies due to the baryon number conservation, since it is nec-  
 1708 essary to produce at least 4 (6) new nucleons in order to produce antideuterons  
 1709 ( $\overline{{}^3\text{He}}$ ). The requirement for these additional nucleons means that the threshold of  
 1710 the required COM energy is about  $\sqrt{s}_{\text{th}} \approx 6(8)m_p$  for antideuterons ( $\overline{{}^3\text{He}}$ ). Given that  
 1711 the ISM target is at rest, all the energy must come from the incoming cosmic ray  
 1712 particle. This means that the frame of reference of the collision will be highly boosted  
 1713 in comparison to the galactic frame, and that the centre of mass energy will only rise  
 1714  $\propto \sqrt{E_{CR}}$ . In the case of  $\overline{{}^3\text{He}}$  this corresponds to a threshold energy of the incoming  
 1715 proton of  $E_p \approx 31$  GeV. In order to estimate these cross sections, Monte Carlo event  
 1716 generators are used to create the proton and neutron spectra and distributions, and  
 1717 coalescence afterburners are then applied in order to estimate the production of  
 1718 antinuclei. In this work, the production cross sections by [129] and [130] are used,  
 1719 referred to hereinafter as Shukla et. al. For  $\overline{{}^3\text{He}}$   $O(10^{11} - 10^{12})$  events are needed to  
 1720 get a statistical precision on the % level on the total yield for a given incoming beam  
 1721 energy [129]. The resulting production cross sections for  $\overline{{}^3\text{He}}$  and antideuterons are  
 1722 shown in figure 51, where they are shown for a wide array of incoming beam energies.

<sup>42</sup>Interstellar gas particles can be expected to move at speeds of the order of the rotational velocity  
 of the milky way, which is  $O(100 \text{ km/s})$  or  $O(\beta = 10^{-4})$ . This is much lower than the velocity of  
 incoming protons at the threshold for antinuclei production, where  $O(\beta > 0.999)$ .

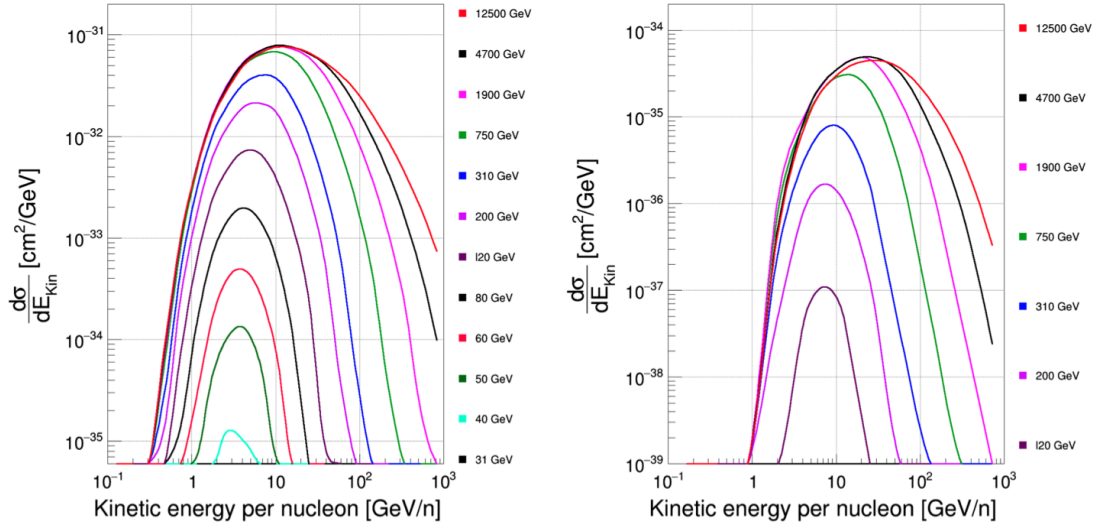


**Figure 51:** Production cross section for antideuterons (left) and  ${}^3\overline{\text{He}}$  (right), as a function of the energy of the antinucleus produced, for a range of different projectile energies, taken from Shukla et. al. The  ${}^3\overline{\text{He}}$  cross section includes the effect of antitritons which are produced and subsequently decay to  ${}^3\overline{\text{He}}$ .

1723 As can be seen, it requires significantly above the threshold energy of  $\sqrt{s} = 31$  GeV in  
 1724 order to produce any significant  ${}^3\overline{\text{He}}$  flux<sup>43</sup>.

1725 The cross sections shown are constrained by data from a variety of accelerator  
 1726 experiments. The list of experiments used to constrain the production cross for  
 1727 antideuterons is shown in figure 52, while for  ${}^3\overline{\text{He}}$  the data is very scarce for p-p  
 1728 collisions at low energies. In order to validate the production, the authors instead  
 1729 used their model to simulate pp collisions at  $\sqrt{s} = 7$  TeV, in order to compare with  
 1730 ALICE data. The resulting fit is shown in figure 53, where the uncertainties are  
 1731 obtained by varying the coalescence momentum by 30%. It can be seen from figure  
 1732 52, for  $\sqrt{s} \gtrsim 25$  GeV, there are only measurements at mid-rapidity. However, due to  
 1733 the highly boosted nature of the frame in CR collisions, antinuclei are likely to be  
 1734 produced at very forward rapidities. Thus, further experimental searches at forward  
 1735 rapidity are needed in order to better constrain antinuclei production in high energy  
 1736 CR collisions.

1737 Once these cross sections are obtained, they need to be folded with the galactic  
 1738 cosmic ray spectrum at each point in space. This spectrum spans over more than 11  
 1739 orders of magnitude if all particles are considered, and at least 6 orders of magnitude  
 1740 for protons. A compilation of available data on the cosmic ray spectrum can be

<sup>43</sup>It is the lowest energy considered for antideuterons since the same simulations were used to determine both sets of spectra in Shukla et. al.

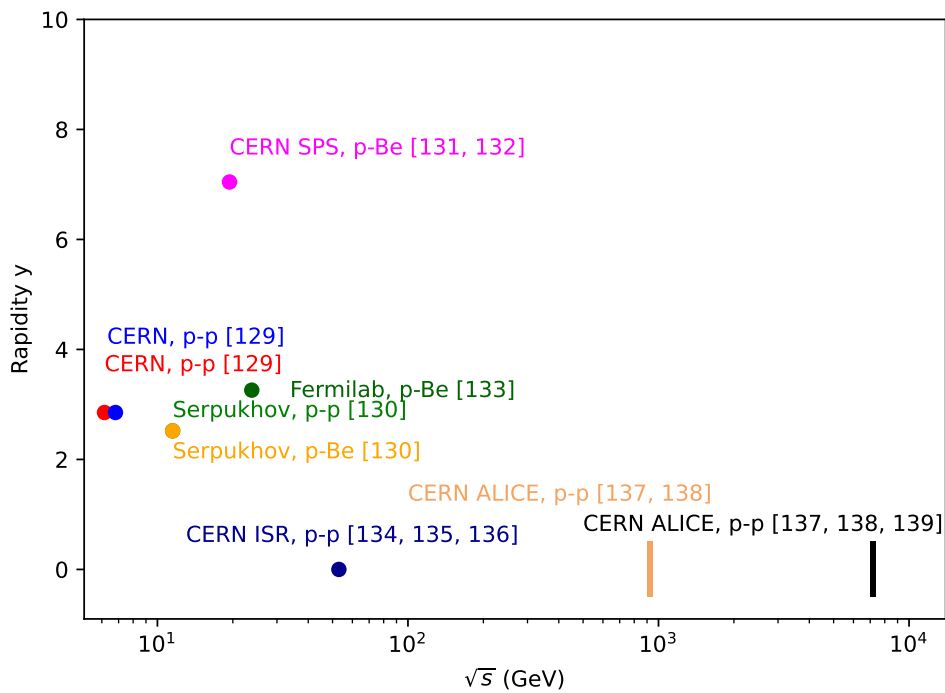


**Figure 52:** A list of experiments with measurements of (anti)deuteron production, as a function of rapidity and  $\sqrt{s}$ . The compilation is taken from table 2 in [130], based on data in [131, 132, 133, 134, 135, 136, 137, 138, 139, 140, 141].

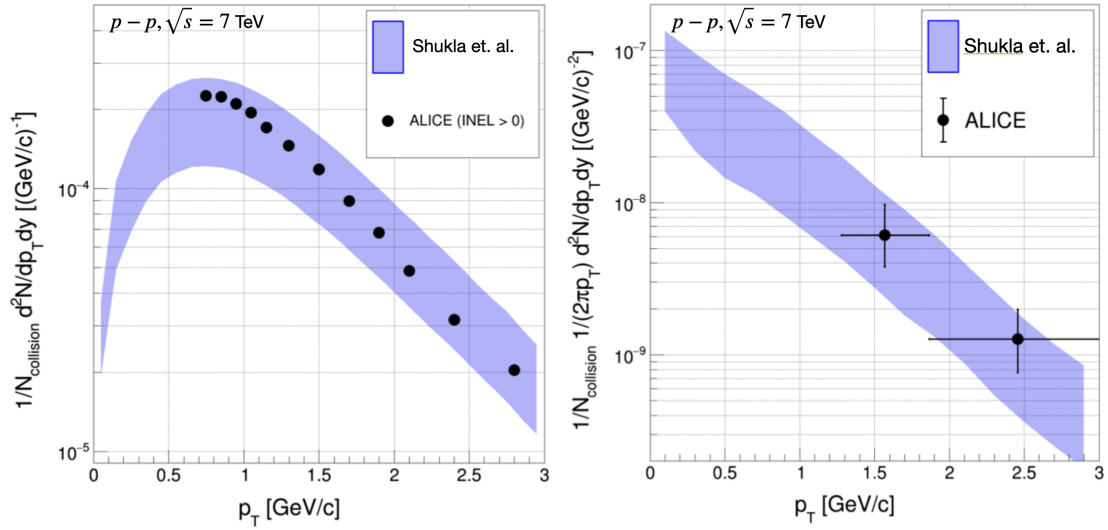


**Figure 53:** Comparison of the antideuteron (left) and  ${}^3\overline{\text{He}}$  (right) spectra obtained by Shukla et. al. with ALICE data for  $\sqrt{s} = 7$  TeV pp collisions.

1741 found in figure 54. The implementation of this process in Galprop is done by imple-  
 1742 menting the cross section above, and thus calculating equation 17 at each point in  
 1743 the space/momentum grid employed in GALPROP. For a more detailed discussion  
 1744 of Galprop see section 5.3. Also shown in the left of this figure is the source term  
 1745 of antideuterons, as a function of both the incoming particle momentum and the  
 1746 momentum of the produced antideuteron. From this it can be seen that the most  
 1747 important momentum range to probe is 100-500 GeV/ $c$ .

### 1748 5.1.2 Weakly interacting massive particles (WIMPs) dark matter

1749 Some WIMP dark matter theories predict that WIMP annihilations can produce a  
 1750 significant amount of antinuclei [4, 2, 1]. Such theories are based on the assumption  
 1751 that dark matter is made of particles (hereinafter denoted  $\chi$ ), which during the big  
 1752 bang were in thermal equilibrium with SM particles. This requires that some SM  
 1753 processes were able to create  $\chi$ . This can be understood kinematically from the  
 1754 available energy in such a process. If the SM particles colliding would have an energy  
 1755 which exceeds  $\sqrt{s} = 2m_\chi$ , they could create a dark matter particle pair. Similarly, the  
 1756 dark matter particles would have to be able to either decay or annihilate into SM  
 1757 particles, in order to maintain the equilibrium, as shown in figure 56. We shall first  
 1758 consider the scenario that the dominant mechanism of interaction for dark matter  
 1759 into SM particles was decou. If they would only decay, there would have to be some  
 1760 mechanism which reduces this decay rate by many orders of magnitude once the



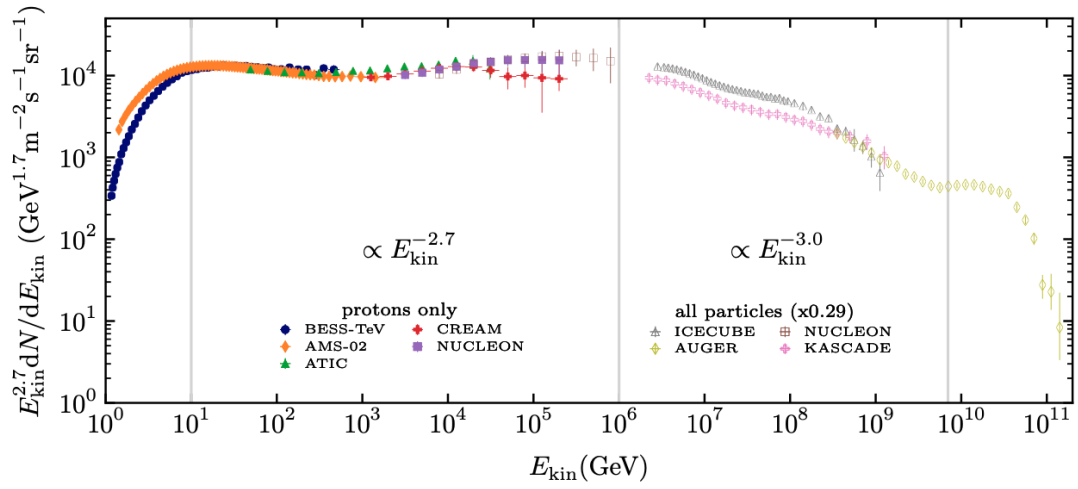


**Figure 54:** Cosmic ray particle spectra, for protons and all particles, from relevant experiments. Figure taken from [142].

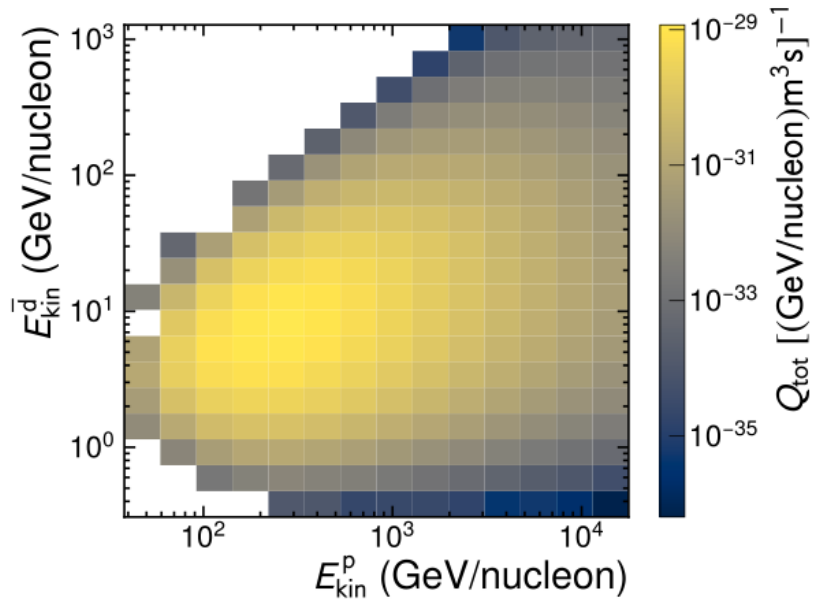


**Figure 55:** The source term of antideuteron from high energy cosmic ray collisions, as a function of the incoming proton energy and the outgoing antideuteron energy. The figure is taken from [121].

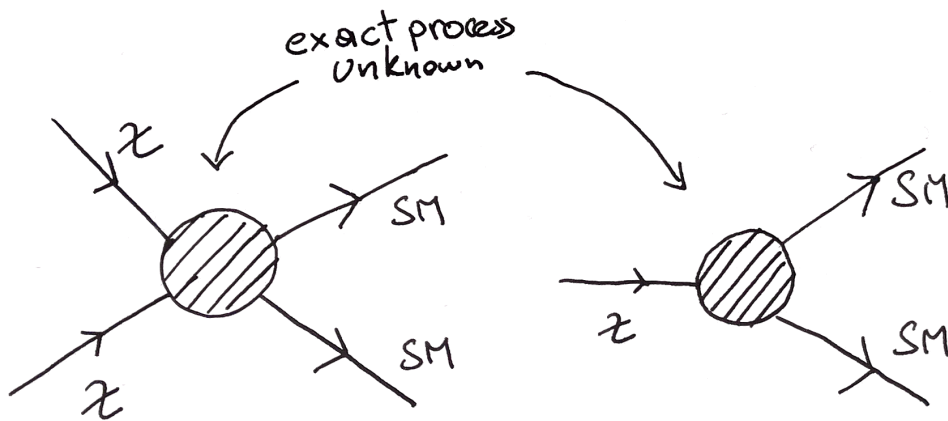


**Figure 56:** A schematic of dark matter pair annihilation into standard model particles (left) and of dark matter decay into standard model particles (right) for a WIMP particle. The exact process by which this would occur is not known, and therefore currently model dependent. Note that a scattering process between a dark matter and a standard model particle would look very similar to the diagram on the left, with the space and time axes inverted (i.e. change the arrow direction of the top dark matter and bottom standard model particle). However, this scattering might happen via a very different internal process, so the two cannot be directly related in a model independent way.

1761 thermal equilibrium is broken and dark matter decoupled from baryonic matter,  
 1762 since otherwise dark matter would have continued to decay rapidly and almost none  
 1763 would be left today<sup>44</sup>. For dark matter annihilations no such effect is necessary, since  
 1764 the annihilation rate naturally decreases with the dark matter density squared (this  
 1765 will be explained in equation 18). Thus, as the universe expands, dark matter with a  
 1766 coupling into baryons through annihilation will naturally freeze out and its abun-  
 1767 dance from this point would remain almost constant. However, given that residual  
 1768 annihilations are still possible when two dark matter particles meet, any SM particles  
 1769 produced could be observed and shine a hint on its nature. It is this exact process  
 1770 which is looked for in cosmic ray antinuclei signals. A cold dark matter particle pair  
 1771 annihilating at rest has  $\sqrt{s}= 2m_\chi$ . The net baryon number would be 0 in such a  
 1772 process, resulting in no further penalty for the production of multiple antinucleons.  
 1773 Per definition, WIMPs interact only weakly, and thus their initial annihilation would  
 1774 occur through a weak channel. Since the weak bosons couple to all other standard  
 1775 model particles, this enables the production of particles such as antinuclei.

1776  
 1777 The spectrum and yield of antinuclei produced in these annihilations has to be  
 1778 estimated based on known standard model processes. To this end, Monte Carlo  
 1779 event generators are employed [4, 123, 1], in which the initial state is the first state  
 1780 of standard model particles which is assumed to occur in the annihilation process,  
 1781 with a COM energy equal to twice the dark matter mass  $m_\chi$  cookbook. The exact  
 1782 initial state of SM particles is not known, but commonly the channels  $W^+W^-$  and  
 1783  $b\bar{b}$  are considered [123, 4]. These two form a convenient subset, as over the range  
 1784 of expected masses ( 10 GeV to about 1 TeV), they are consistently two of the more  
 1785 optimistic scenarios, and cover the different parameter space within these optimistic  
 1786 scenarios [1]. This can be seen from figure 57. Since event generators do not produce  
 1787 (anti)nuclei – but only the individual nucleons – the (anti)nuclei yields and spectra  
 1788 have to be calculated using the coalescence model. One particular annihilation  
 1789 channel has recently been proposed [144], which suggests a boost of the  ${}^3\overline{\text{He}}$  yield  
 1790 through an intermediate decay to  $\overline{\Lambda}_b$ . While the branching ratio for the process  $\overline{\Lambda}_b \rightarrow$   
 1791  ${}^3\overline{\text{He}} + X$  is not well constrained by data, the default tunes<sup>45</sup> of the event generators  
 1792 tends to underestimate this, and thus the amount of  ${}^3\overline{\text{He}}$  production (it also has an

<sup>44</sup>This would require a mechanism to destabilize dark matter particles in the very hot and dense medium which existed just after the big bang. During the period before dark matter decoupled – which is assumed to have occurred around the quark-gluon-plasma phase of the early universe, i.e.  $10^{-12}\text{s} - 10^{-5}\text{s}$  after the big bang – the decay rate would have had to be much less than  $10^{-5}\text{s}$  in order to achieve thermal equilibrium. In order to remain stable after decoupling, its lifetime would have to exceed the current lifetime of the universe, around  $10^{17}\text{s}$ . In medium modifications of decay widths is a known effect [143], however, it is difficult to imagine a process which modifies the lifetime of such particles by at least 20 orders of magnitude.

<sup>45</sup>Tunes when used to talk to event generators are the specific settings which are used for the event generator to more accurately reproduce a given result, e.g. the proton spectra at a given energy.

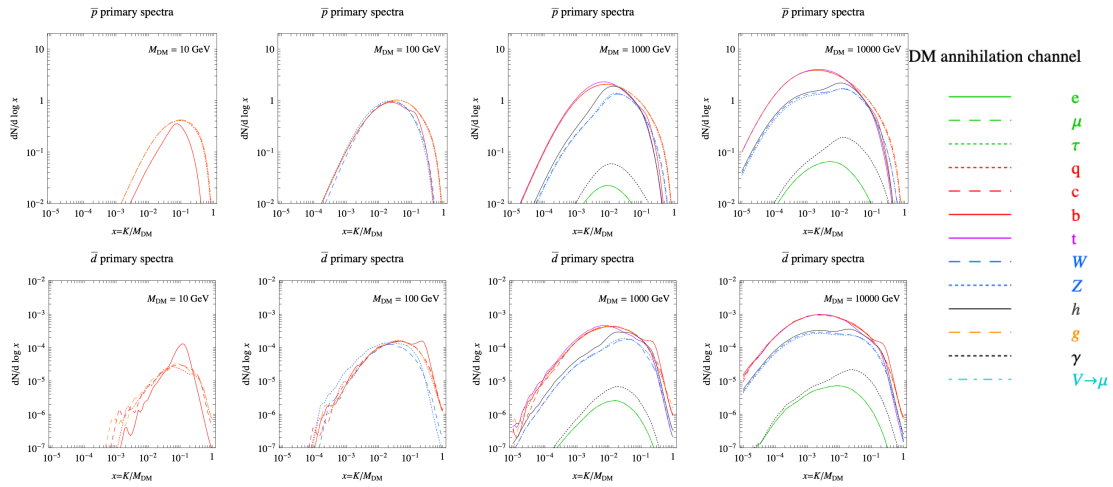


**Figure 57:** Antiproton (top) and antideuteron (bottom) spectra from dark matter annihilations as a function of the antinuclei kinetic energy per nucleon, normalized to a single annihilation event, for a wide variety of initial SM states. This figure is taken from [1].

1793 impact on the antideuteron production, but far less, as can be seen in section 68  
 1794 below). In particular, a discrepancy is observed between two commonly used event  
 1795 generators (Pythia [145] and EPOS [146]) of about a factor 3. In order to rectify this,  
 1796 a special setting of the Pythia event generator is used to reproduce the branching  
 1797 fraction close to the one of EPOS. This setting is referred to as the  $\bar{\Lambda}_b$  tune in the  
 1798 following discussion. According to these results, there is an almost 10 fold increase in  
 1799 the resulting detectable  ${}^3\bar{\text{He}}$  flux, in particular at high energies around 10 GeV/A. This  
 1800 is of particular interest since according to the authors, such an increase would cause  
 1801 a signal detectable by the AMS-02 experiment, with an event rate of about 1/year.  
 1802 The authors also consider the decay of  $\bar{\Lambda}_b$  through light mediator particles,  
 1803 which provides a slightly different spectrum.  
 1804 So in addition to the spectra obtained using default event generators from [123, 4],  
 1805 the spectra incorporating the  $\bar{\Lambda}_b$  decay are also considered as part of this thesis. All  
 1806 the relevant spectra from these processes for antideuterons and  ${}^3\bar{\text{He}}$  are shown in  
 1807 figure 58.

1808

1809 Since decoupling from baryonic matter, the dark matter would have cooled with  
 1810 the expanding universe, and thus is assumed to be at a similar temperature as the

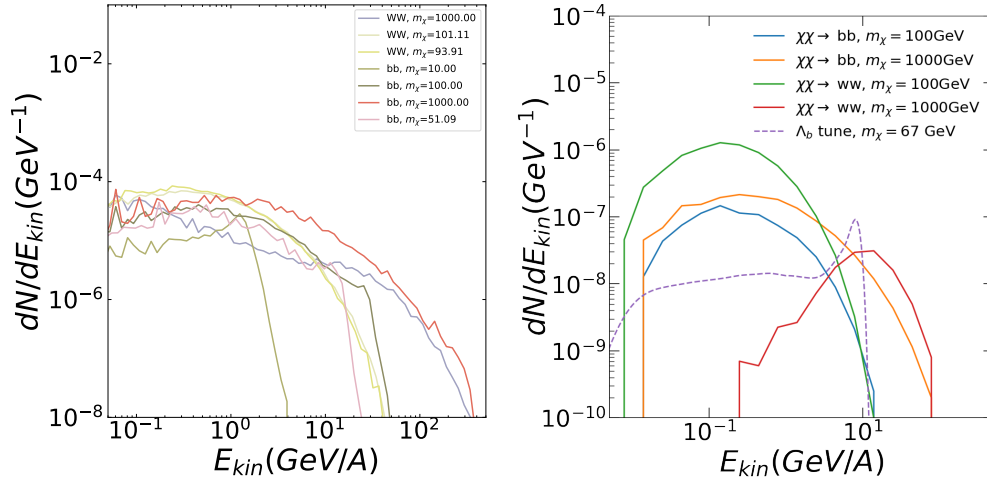


**Figure 58:** Antideuteron (left) and  ${}^3\overline{\text{He}}$  (right) spectra from dark matter annihilations as a function of the antinuclei kinetic energy per nucleon, normalized to a single annihilation event. Spectra for  $W^+W^-$  and  $b\overline{b}$  channels are taken from [4],  $\overline{\Lambda}_b$  tune is taken from [144].

1811 cosmic microwave background (CMB) today, of about 2.7K [147]. This is referred to  
 1812 as cold dark matter. Another consideration which supports cold dark matter is that  
 1813 the majority seems to be gravitationally bound within galaxies and galaxy clusters  
 1814 [57, 148, 149, 150]. As such, the COM frame is assumed to be the same as the galactic  
 1815 frame, and no boost from the initial velocities are necessary. This is convenient, since  
 1816 one can therefore simply take the spectrum of produced antinuclei per dark matter  
 1817 annihilation – which is obtained from applying a coalescence afterburner to the  
 1818 output of a Monte Carlo event generator – and multiply it by the local annihilation  
 1819 rate of dark matter. Thus, one can write the source term  $q(\vec{r}, E)$  for WIMP dark matter  
 1820 as

$$q(\vec{r}, E) = \frac{1}{2} \left( \frac{\rho_\chi(\vec{r})}{m_\chi} \right)^2 \langle \sigma v \rangle (1 + \epsilon) \frac{dN}{dE}, \quad (18)$$

1821 where the factor 1/2 comes from symmetry considerations for majorana dark mat-  
 1822 ter<sup>46</sup>, the term  $\left( \frac{\rho_\chi(\vec{r})}{m_\chi} \right)^2$  is the square of the number density of the WIMP dark matter,  
 1823 which is then multiplied by the velocity averaged dark matter annihilation cross  
 1824 section  $\langle \sigma v \rangle$ , giving the rate of dark matter annihilations for a given point in space.  
 1825 The term  $1 + \epsilon$  accounts for contributions from other particles which are produced

<sup>46</sup>See section 1.7.5 for a discussion on the difference between Majorana and Dirac dark matter.

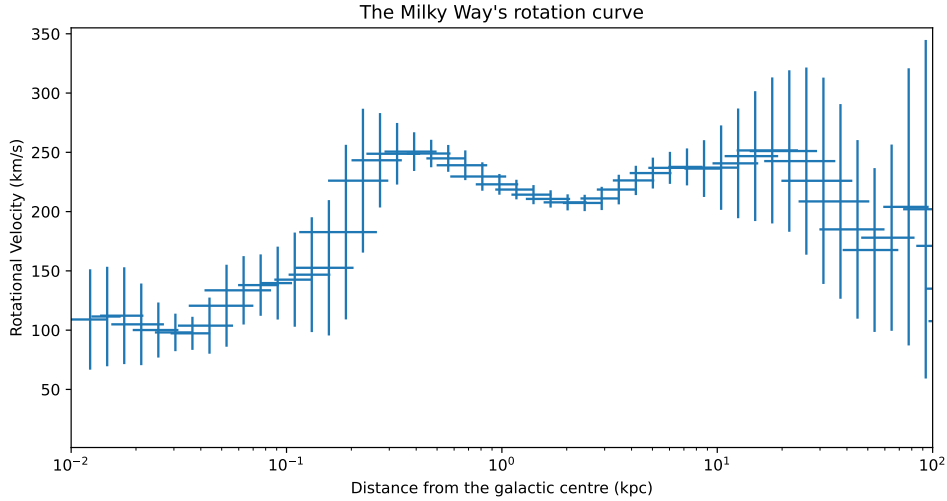


**Figure 59:** Rotation curve of stars in the Milky Way, as a function of distance from the galactic center. Reproduction of data reported in [78].

1826 and subsequently decay into the antinucleus in question, at timescales longer than  
 1827 the consideration of the MC event generator. The value of  $\epsilon$  is 0 for antideuterons  
 1828 and 1 for  ${}^3\overline{\text{He}}$ , to account for  ${}^3\overline{\text{H}}$ . The final term of equation 18 is the spectrum  
 1829 of produced antinuclei normalised to a single dark matter annihilation. The terms  
 1830 of equation 18, their constraints and degeneracies are discussed below.

1831

1832 The dark matter density profile  $\rho_\chi(\vec{r})$  affects both the total amount of antinuclei  
 1833 produced as well as their initial distribution. This parameter can be constrained  
 1834 from measurements of the Milky Way's rotation curve, similarly to how it is done  
 1835 for other galaxies. However, measuring the rotation curve of the Milky Way involves  
 1836 extra challenges, given that we are measuring from within. This is due to the fact  
 1837 that for other galaxies, measuring the difference in velocity through red/blue shift at  
 1838 different positions is sufficient to measure the rotation curve, whereas for our own  
 1839 galaxies we need the measure both the 3d position and velocity of many stars. The  
 1840 most promising technique to do this is Very-Long-Baseline-Interferometry, which  
 1841 essentially uses telescope arrays spanning multiple continents as interferometers  
 1842 [151]. A more detailed discussion of measuring rotation curves can be found in  
 1843 [79, 78]. Our galaxy's rotation curve has been reported in [78], found by combining  
 1844 multiple existing measurements. It is reproduced in figure 59.

1845

1846 In order to fit such rotation curves, our galaxy is conventionally split into in-  
 1847 dividual parts, each of which can be assumed to have a simpler shape. The usual

1848 breakdown of these parts is shown in table 3, and further details can be found in [79].  
 1849 The gravitational potentials of these parts can then be summed up linearly, and the  
 1850 rotational velocities caused by each such potential can be added in quadrature. In  
 1851 order to fit the contribution from dark matter, the shape of the dark matter distri-  
 1852 bution has to be chosen a priori, such that the exact parameters and normalization  
 1853 can then be obtained from the fit. This is an important point, since the total normal-  
 1854 ization of the dark matter profile is not well constrained. Rather, the relatively well  
 1855 constrained rotation curve in the proximity of the solar system results in the fact  
 1856 that the local dark matter density  $\rho_\chi(\vec{r} = r_\odot) := \rho_\chi^\odot$  is much better constrained than  
 1857 the total normalization of the dark matter profile. Thus, the different dark matter  
 1858 profiles are constrained to their value at  $r_\odot = 8.5\text{kpc}$ <sup>47</sup>, the estimated position of our  
 1859 sun.

Part	Shape	Extent	Total Mass
Central black hole	Point mass	< 0.1pc	$3.6 \times 10^6 M_\odot$
Buldge(s)	Spherical exponential	< 1kpc	$10^{11} M_\odot$
Flat disk	Constant flat disk	< 15kpc	$\approx 10^{10} M_\odot$
Dark matter halo	vaires	100s of kpc	$10^{12} M_\odot$

**Table 3:** Individual axissymmetric parts of the Mikly Way used for fitting rotation curves. The distinction is made in order to simplify the fit, rather than a hard distinction within the actual galaxy. Non-axissymmetric components are neglected for rotation curves, based on the assumption that any effects would cancel out when averaged over the full rotation. The values for the total mass were taken from [79]. The extent column is approximate and given in order to help the reader visualise the distributions. Due to the distributions being exponential, they only asymptotically approach 0.

1860

1861 There are several profiles on the market, which achieve similar goodness-of-fit  
 1862 when fit to account for the dark matter component in the rotation curve [4], while  
 1863 also achieving the required normalisation at  $r_\odot$ . The ones used in this work are the  
 1864 Navarro-Frenk-White(NFW) profile [152], shown in equation 19

$$\rho_\chi^{NFW}(\vec{r}) = \frac{\rho_0}{(r/r_s)[1+(r/r_s)]^2}, \quad (19)$$

1865 with scale radius  $r_s = 24.42\text{kpc}$ , the Einasto profile [153], shown in equation 20

$$\rho_\chi^{Einasto}(\vec{r}) = \rho_0 \exp\left\{-\frac{2}{\alpha} \left[\left(\frac{r}{r_s}\right)^\alpha - 1\right]\right\}, \quad (20)$$

<sup>47</sup>The value is currently estimated to be  $0.4\text{GeVcm}^{-3}$  [150, 4, 79, 78, 74].

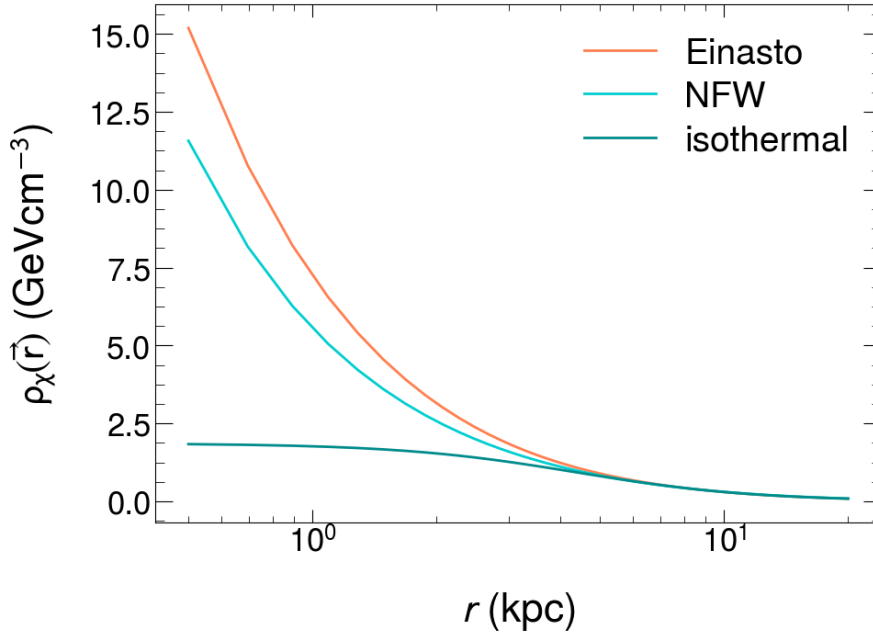


**Figure 60:** Dark matter density profiles used in this work, as a function of the distance to the galactic centre. The best fit values for each profile are taken from [4].

with  $\alpha=0.17$  and  $r_s=28.44\text{kpc}$ , and the much shallower isothermal profile [154] and the isothermal profile, shown in equation 21

$$\rho_{\chi}^{\text{isothermal}}(\vec{r}) = \frac{\rho_0}{r^2 + r_s^2}, \quad (21)$$

1866 with  $r_s=4.38\text{kpc}$ . The profiles are plotted in figure 60, using best fit values taken from  
 1867 [4]. It can be seen that the isothermal profile has a very shallow rise towards the galac-  
 1868 tic center, while the Einasto profile rises very steeply. The NFW profile lies between  
 1869 the two<sup>48</sup>, and is often used preferentially [2, 4, 123]. The stark difference between  
 1870 them is due to their origin. The isothermal profile is motivated purely by the fit to  
 1871 galactic rotation curves, while the NFW and Einasto profiles are motivated by the  
 1872 addition of numerical N-body simulations, which the isothermal profile struggles to  
 1873 replicate [155]. All these profiles assume spherical symmetry. Numerical simulations  
 1874 seem to prefer a triaxial ellipsoid, however, given the lack of data for the tidal motion  
 1875 of stars in the Milky Way, it is currently not possible to narrow down the shape more  
 1876 exactly than a simple spherically symmetric model. These three profiles cover most  
 1877 of the available parameter space for the dark matter profile.

1878

<sup>48</sup>At very small radii, the NFW profile becomes larger than the Einasto profile.



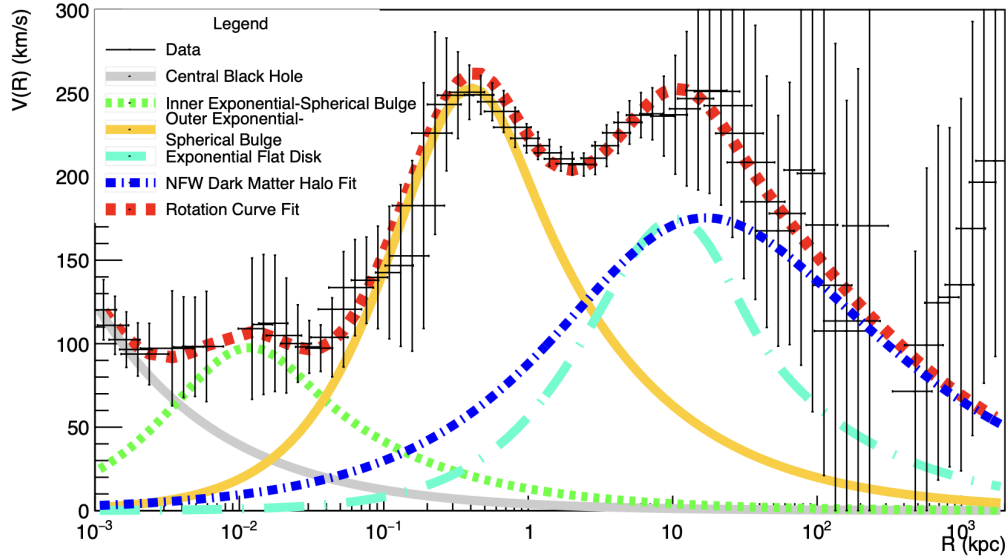


**Figure 61:** Fit of the rotation curve of the Milky Way, with a NFW profile. Figure is taken from [156], based on work in [149].

1879 It is important to ask why the stark differences towards the center of the galaxy  
 1880 play such a reduced role that all three of these profiles are able to fit the data, and  
 1881 if such differences would therefore make any interpretation of an antinuclei flux  
 1882 from dark matter impossible. The answer to the first part of the question is twofold.  
 1883 Firstly, it is very challenging to measure the rotation curve of our own galaxy with high  
 1884 precision at positions far from the solar system, as can be seen from the uncertainties  
 1885 in figure 59. Secondly, the gravitational effect of the dark matter halo contributes  
 1886 mainly at distances larger than  $\approx 2$  kpc from the galactic center, where the presence  
 1887 of extra mass at the centre of our galaxy (from a steeper profile) is not as strongly felt.  
 1888 This can be seen from figure 61. The second question also has a fortunate answer:  
 1889 the effect of different profiles on a potential local flux of antinuclei from a dark matter  
 1890 source is rather small, as is discussed in section 5.6.

1891 To summarize: the dark matter density profile in our galaxy is constrained by  
 1892 measurements of the Milky Way's rotation curve. Measuring the rotation curve  
 1893 is a non-trivial process, which involves measuring the 3d position of stars within  
 1894 our own galaxy. The most modern method to achieve this is Very-Long-Baseline-  
 1895 Interferometry (VLBI), which uses telescope arrays spanning continents as a giant  
 1896 interferometer. Once the rotation curve is measured, the effect from luminous mat-  
 1897 ter is accounted for, and the remainder is assigned to the dark matter component.  
 1898 Due to the experimental uncertainties involved in measuring the velocity of far away

1899 objects, this leaves a significant plausible parameter space for the shape of the dark  
 1900 matter profile towards the center of our galaxy.

1901

1902 The second term of equation 18 is the dark matter mass,  $m_\chi$ . The dark matter  
 1903 mass is a free parameter, with possible values ranging from very light dark matter<sup>49</sup>  
 1904 below the eV range all the way to the WIMP dark matter discussed in this work, with  
 1905 plausible mass ranges from 10s of GeV to the TeV range. As discussed in section  
 1906 1.7.2, the appeal of WIMP dark matter is that the expected weak cross section of  
 1907 such a particle in the very early universe would yield a population today of the same  
 1908 magnitude as we observe (a mathematical derivation can be found in [150] and  
 1909 is reproduced in section 1.7.2). It would also explain the lack of evidence for the  
 1910 production of dark matter at accelerators, since we might at this point not yet have  
 1911 reached the energies required to produce such particles. Finally, many extensions of  
 1912 the standard model naturally include such a particle, most notably super symmetry,  
 1913 which requires the neutralino, a particle which would fit the WIMP description [82].  
 1914 This was a rather enticing argument at the inception of WIMPs in the 80s, however,  
 1915 by now the parameter space for supersymmetric theories has become very small  
 1916 [82], due to null observations at accelerators including the LHC. This has made  
 1917 the question of how to incorporate such a particle into the Standard Model more  
 1918 difficult, and thus increased the interest in alternative dark matter candidates, which  
 1919 are discussed in section 1.7.3.

1920 Since the exact nature of dark matter remains a mystery, a priori a wide range of  
 1921 masses is possible. However, direct detection experiments have placed limits on the  
 1922 dark matter-matter interaction cross sections, as a function of the dark matter mass  
 1923 [90, 91] and a recent compilation of these limits is shown in figure 62. It is not possible  
 1924 to relate this interaction cross section with the dark matter self annihilation cross  
 1925 section  $\langle \sigma_{ann} v \rangle$  on general grounds, since they might depend on very different  
 1926 couplings. But it can help us make an informed decision on WIMP masses. As can be  
 1927 seen from figure 62, for masses over a few 10s of GeV, constraints become very strong,  
 1928 limiting the cross section to below a billionth of a pb. Upcoming next generation  
 1929 experiments, such as XENONnT [95] and Darkside20k [157], are expected to push  
 1930 these limits within reach of the neutrino coherent scattering background. If these  
 1931 experiments also do not see a signal, it would eliminate the possibility of background  
 1932 free detection using direct detection methods.

1933 The chosen mass has a direct effect on all three remaining terms of equation  
 1934 18: i)  $\frac{1}{m_\chi^2}$ , ii)  $\frac{dN_{\bar{p},\bar{d},\bar{3}\bar{He}}}{dE}$  and iii)  $\langle \sigma v \rangle$ . The effect on i) is trivial, and reduces the overall  
 1935 normalization of the antinuclei source term for higher  $m_\chi$ . The mass' effect on ii) is  
 1936 based on the amount of energy available for the production of (anti)nuclei, as well as  
 1937 for their kinetic energy. For higher masses, the antinuclei yields increase non-trivially,

<sup>49</sup>A popular light dark matter model is the axion model [18].

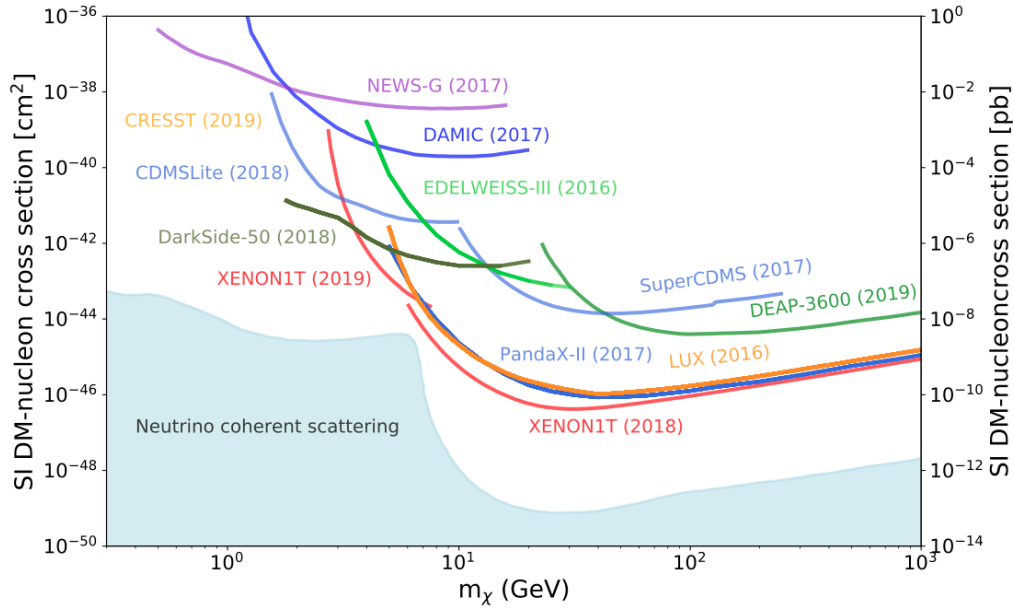


**Figure 62:** Limits from direct detection experiments on the dark matter - nucleon interaction cross section, as a function of the dark matter mass. The figure is taken from [158].

1938 but slower than the inverse square reduction from the first term. Additionally, the  
 1939 extra energy available for higher masses translates into a spectrum peaked at higher  
 1940 momenta. This depends not only on the available energy, but also on the decay  
 1941 channel. The  $\frac{dN_{\bar{p}, \bar{d}, \bar{^3\text{He}}}}{dE}$  spectra used for the antideuteron and  $\bar{^3\text{He}}$  results shown in this  
 1942 chapter are shown in figure 58. The effect of  $m_\chi$  on  $\langle \sigma v \rangle$  is mostly experimental,  
 1943 since  $\langle \sigma v \rangle$  is constrained from antiproton measurements.

1944 Any dark matter annihilation process which can result in antideuterons must of  
 1945 course also produce antiprotons. However, contrary to heavier antinuclei, antipro-  
 1946 tons are also copiously produced in other processes, due to the much lower energy  
 1947 threshold required for producing a single antinucleon, and the loss of the need to  
 1948 coalesce multiple antinucleons into a single compound antinucleus. This results  
 1949 in a significant and well constrained antiproton flux, which has been measured by  
 1950 the AMS collaboration [60, 59]. Thus, any model chosen must not produce a dark  
 1951 matter component for antiprotons which is incompatible with those measurements.  
 1952 These limits are expressed in terms of  $\langle \sigma v \rangle$  as a function of  $m_\chi$ . This representa-  
 1953 tion is chosen since  $\rho_\chi$  can be measured independently, and  $\langle \sigma v \rangle$  varies much  
 1954 more slowly with  $m_\chi$  than the other terms. The limits – which have been extracted  
 1955 by several groups [159, 160, 161, 162] and compiled by [57]– are shown in figure 63.  
 1956 Indicated in the figure is the maximum limit on  $\langle \sigma v \rangle$ , as well as the thermal relic

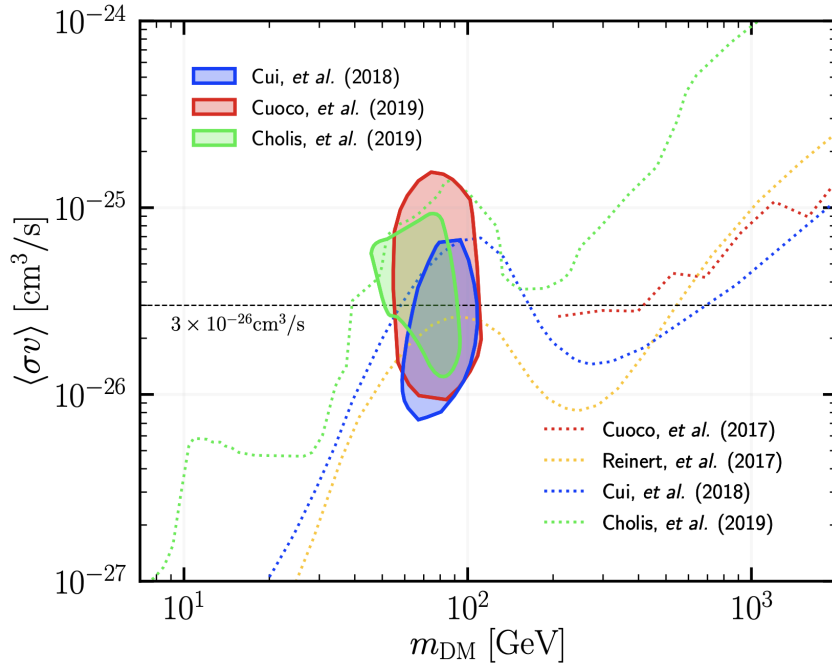


**Figure 63:** Limits on  $\langle \sigma v \rangle$  based on AMS antiproton data. Figure is taken from [57].

1957 cross section ( $\approx 1 pb \times c$ )<sup>50</sup>.

1958 Also indicated in this figure is the area in which a possible excess of antiprotons  
 1959 was observed in the  $\bar{p}$  spectrum measured by the AMS collaboration, which  
 1960 could hint at a dark matter particle within this mass range of 50-100 GeV/ $c^2$ . The  
 1961 different areas correspond to analysis of the same AMS-02 data by different groups,  
 1962 using either a frequentist or a Bayesian approach [57]. It can be seen from the left  
 1963 hand side of the figure that for low dark matter masses, the limits lie significantly  
 1964 below the thermal value for this cross section. Thus,  $m_\chi$  affects the constraints on  
 1965  $\langle \sigma v \rangle$ , particularly for low masses. It is also worth noting that these limits have to  
 1966 be extracted for a given dark matter density profile, and thus when exploring the  
 1967 maximum allowed antinuclei flux given the antiproton constraints, the choice of  
 1968  $\rho_\chi(\vec{r})$  is degenerate with the limits on  $\langle \sigma v \rangle$  set by the AMS antiproton limits.

1969  
 1970 To summarise: WIMP dark matter models predict that dark matter can annihilate  
 1971 and produce antinuclei. The resulting antinuclei source term depends on 4 things:  
 1972 i) the dark matter density profile, ii) the dark matter mass, iii) the dark matter self-  
 1973 annihilation cross section and iv) the produced spectrum of antinuclei, normalised

<sup>50</sup>See the derivation in section 1.7.2 for more details.

1974 to a single dark matter decay. i) is constrained by looking at the rotation curve  
 1975 of our galaxy, ii) is a free parameter, iii) is constrained from above by antiproton  
 1976 measurements as a function of  $m_\chi$  and iv) is calculated based on coalescence models,  
 1977 which depend on the total available energy and thus  $m_\chi$ . Thus, there are a few  
 1978 notable degeneracies between the different terms of this source function. However,  
 1979 current constraints on these parameters are not stringent and leave open a large,  
 1980 reasonable parameter space which could result in a measureable antinuclei flux  
 1981 from a dark matter source, affirming antinuclei studies as a great tool for the indirect  
 1982 search for dark matter.

### 1983 5.1.3 Extragalactic dark matter

1984 Dark matter is not exclusively bound within galaxies, but is also present in larger  
 1985 cosmological structures, such as galaxy groups [149]. However, the profiles com-  
 1986 monly used in order to fit the distribution of dark matter within our galaxy only  
 1987 take into account galactic dark matter, which can be inferred from the fact that  
 1988 such profiles go to 0 at large distances from the galactic centre. This is because to  
 1989 first order, the extragalactic component will vary over length scales bigger than our  
 1990 galaxy, so the gravitational potential caused by the extragalactic dark matter will  
 1991 be roughly constant within our galaxy, thus causing no active force which could  
 1992 be measured. However, such an additional flux of dark matter could indeed an-  
 1993 nihilate within our galaxy, thus providing an additional source for antinuclei. In  
 1994 this section the difference of this source to the galactic WIMP dark matter source  
 1995 will be qualitatively discussed. Previous work on the topic expects the extragalactic  
 1996 dark matter component to make up about 12% of the local dark matter abundance  
 1997 close to our solar system [149]. From this, it can be estimated that the extragalac-  
 1998 tic dark matter is responsible for no more than  $\approx 20\%$  of the antinuclei flux near earth.  
 1999

2000 In order to determine whether the antinuclei flux caused by extragalactic dark  
 2001 matter follows the same assumptions as the galactic component, it is necessary to  
 2002 examine the differences between galactic and extragalactic dark matter. The first  
 2003 difference would be their velocity. Since the galactic component is bound and the  
 2004 extragalactic is not, the extragalactic component's velocity must exceed the escape  
 2005 velocity of the Milky Way, which lies at about 600km/s. This change in velocity may  
 2006 affect 2 terms in equation 18: the self annihilation cross section and the spectrum of  
 2007 produced antinuclei due to the boosted frame in which the collision takes place.  
 2008 Starting with the effect on the self annihilation cross section, the difference might  
 2009 be due to the momentum dependence of the s-wave and p-wave contributions.  
 2010 The s-wave is velocity independent, while the p-wave contribution has a square  
 2011 dependence on the velocity. However, the speeds of 600km/s still only equate to a  
 2012 beta of 0.002, thus the contribution of the s-wave still dominates at these speeds,

2013 resulting in no change in regards to galactic dark matter. In a similar fashion it can  
 2014 be shown that the effect of the increased speed on the produced antinuclei spectrum  
 2015 is negligible.

2016  
 2017 The effect which remains is that of the overall normalisation, which is influenced  
 2018 by the extragalactic component to  $\rho_\chi$ . This extra component would have little to  
 2019 no effect on the rotation curve of our galaxy, and therefore causes a positive offset  
 2020 in comparison to the purely galactic case. The exact nature of this offset should  
 2021 to first order be roughly constant over our galaxy, however, the interaction of the  
 2022 extragalactic dark matter with our galaxy's gravitational pull would cause an increase  
 2023 in the local extragalactic dark matter density in comparison to another point within  
 2024 the local group. Thus, the main difference between the extragalactic dark matter and  
 2025 the galactic dark matter is the consideration of where the majority of annihilations  
 2026 would occur. Finally, we can conclude that since the overall normalisation for antinuclei  
 2027 fluxes from dark matter annihilations is constrained by the maximal allowed  
 2028 flux from antiprotons – as discussed in section 5.1.2 – the increase in flux due to  
 2029 an additional extragalactic dark matter component does not significantly impact  
 2030 expectations.

2031

#### 2032 5.1.4 Primordial black holes

2033 Another possible source of antinuclei in the cosmos are primordial black holes  
 2034 (PBHs). These objects would have formed very early in the universe, created from  
 2035 overdense regions shortly after the big bang. Their mass is therefore given by the  
 2036 particle horizon at the time of formation,  $M_{\text{PBH}} \approx c^3 t / G \approx 10^{15} (t / 10^{-23} \text{ s}) g$  [88, 163],  
 2037 where  $t$  is the time at their formation. These objects can have a large range in differ-  
 2038 ent masses, depending on their formation time. Since such low mass black holes  
 2039 would interact only gravitationally, they would meet the criteria for dark matter  
 2040 [121, 163]. However, as we shall see in this section, they cannot make up the domi-  
 2041 nant portion of dark matter in the galaxy.

2042 Classically, it is impossible for anything - even light - to escape a black hole. How-  
 2043 ever, as shown by [88], quantum mechanics predicts that black holes will indeed  
 2044 thermally emit (anti)particles, with a characteristic temperature  $T = \frac{\hbar c^3}{8\pi G M k_B} \approx$   
 2045  $1.06 \left( \frac{M}{10^{13} g} \right)^{-1} \text{ GeV} k_b^{-1}$ . This process can be understood as particles tunneling out of  
 2046 the black hole, or as virtual antiparticle-particle pairs being created and one partner  
 2047 tunneling through the event horizon into the black hole, preventing recombination.  
 2048 Both methods yield the same results. The lifetime of such black holes scales with  
 2049 their mass as  $\tau_{\text{PBH}} \propto M_{\text{PBH}}^{-3}$ , i.e. they evaporate faster the smaller they are. This  
 2050 results in PBHs emitting many (anti)particles almost simultaneously when they fully

2051 evaporate at the end of their lifespan, a process akin to an explosion. The mass of  
 2052 currently evaporating PBHs is in the range of about  $\approx 10^{15}g$ , since lighter black holes  
 2053 would have already evaporated in the past, while heavier ones will only evaporate  
 2054 in the future. Such PBHs could produce antinuclei during the final stage of their  
 2055 evaporation.

2056 The current abundance of PBHs in this mass range is most tightly constrained from  
 2057  $\gamma$ -ray searches [127], to  $\frac{\rho_{\text{PBH}}}{\rho_{\text{tot}}} < 10^{-26}(M_{\text{PBH}}/10^{15}g)^{-5/2}$ , which means that PBHs cannot  
 2058 make up all the dark matter in our galaxy. These limits include the extragalactic  
 2059 gamma ray background (for masses down to  $10^{13}g$ ) and the galactic gamma ray  
 2060 spectrum (for masses of  $\approx 10^{15}g$ ). Modification of the PBH lifetime due to an extra  
 2061 dimension in string theory could rectify this, allowing PBHs to make up 100% of dark  
 2062 matter [164].

2063

2064 In this thesis PBHs were considered as a possible source for antideuterons, using  
 2065 a PBH mass of  $9.35 \times 10^{14}g$ . For this mass, PBHs were found from antiproton con-  
 2066 straints to make up no more than  $f_{\text{PBH}} = 4 \times 10^{-11}$  of all the dark matter in the galaxy.  
 2067 This corresponds to a local rate of PBH explosions of  $2 \times 10^{-4}pc^{-3}yr^{-1}$ . The source  
 2068 term of antideuterons from such events is given by equation 22

$$q(\vec{r}, p) = \frac{f_{\text{PBH}}\rho_{\text{CDM}}(\vec{r})}{M_{\text{spectrum}}} \frac{dN}{dT}, \quad (22)$$

2069 where  $M_{\text{spectrum}}$  is the typical mass of the PBHs considered, and  $\rho_{\text{CDM}}$  is the cold dark  
 2070 matter density profile, equivalent to the one used for WIMPs. The corresponding  
 2071 antideuteron spectrum per second  $\frac{dN}{dT}$  is taken from [4], and is shown in figure 64.

## 2072 5.2 Constraining the propagation of antinuclei through the galaxy

In the process of propagating thorough our galaxy, particles undergo several different effects. They get produced at various points in both space and time, for example most heavy nuclei are produced in supernovae [126]. As they then propagate from their source towards their eventual detection point near earth, they undergo diffusion effects, undergo elastically scattered and are diverted by the magnetic fields of the galaxy and individual celestial objects. They are also under the effect of bulk motion via convection effects. Finally, there are various effects which might cause a particle to disappear, mainly inelastic interactions with the interstellar medium, or breakup for unstable particles. All of these processes are characterised by the transport

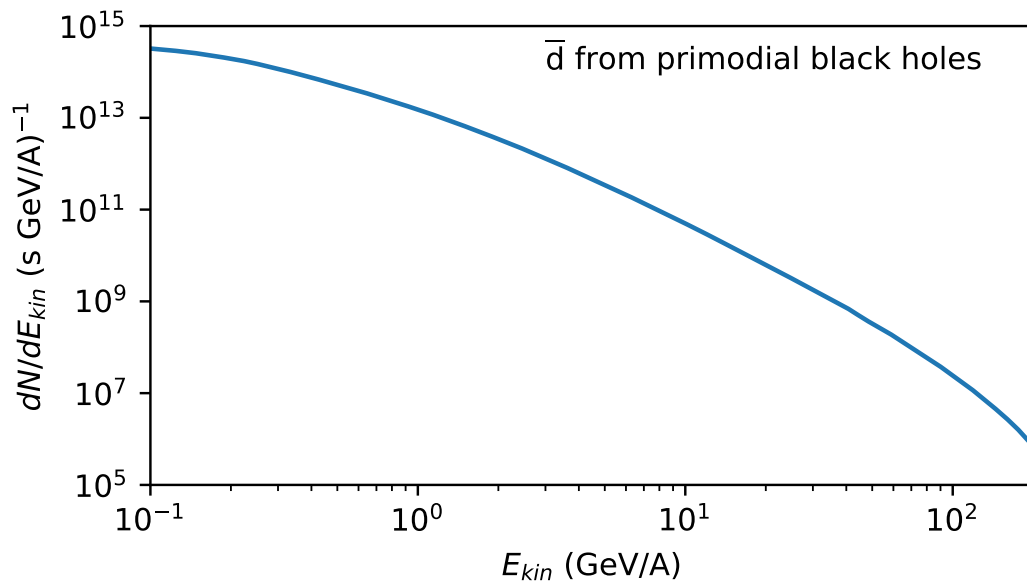


**Figure 64:** Spectrum of produced antideuterons per second, as a function of kinetic energy per nucleon, from a primordial black hole evaporation. Data from [4], provided in private communication.



equation [120], which is reproduced in equation 23

$$\frac{\partial \psi}{\partial t} = q(\mathbf{r}, p) + \mathbf{div}(D_{xx} \mathbf{grad} \psi - \mathbf{V} \psi) + \frac{\partial}{\partial p} p^2 D_{pp} \frac{\partial \psi}{\partial p} - \frac{\partial}{\partial p} \left[ \psi \frac{dp}{dt} - \frac{p}{3} (\mathbf{div} \cdot \mathbf{V}) \psi \right] - \frac{\psi}{\tau_f} - \frac{\psi}{\tau_r}, \quad (23)$$

2073 where  $\psi$  is the time and space dependent flux of a given cosmic ray species,  $q(\mathbf{r}, p)$  is  
 2074 the source term as a function of position and momentum,  $D_{xx}$  and  $D_{pp}$  are the spatial  
 2075 diffusion and diffusive re-acceleration coefficients,  $V$  is the convection velocity, and  
 2076  $\tau_f$  and  $\tau_r$  are parameters characterising the annihilation and fragmentation rates,  
 2077 respectively. The relationship between the last term and the inelastic cross section  
 2078 of a cosmic ray species is given by equation 24

$$\frac{1}{\tau_r} = \beta c \left( n_{\text{H}}(\vec{r}) \sigma_{\text{inel}}^{3\overline{\text{He}}p}(p) + n_{\text{He}}(\vec{r}) \sigma_{\text{inel}}^{3\overline{\text{He}}^4\text{He}(p)} \right), \quad (24)$$

2079 where,  $n_{\text{H}}$  is the number density of hydrogen gas (approximately  $1 \text{ cm}^{-3}$ ),  $n_{\text{He}}$  is the  
 2080 number density of helium gas (approximately  $0.1 \text{ cm}^{-3}$ ).

2081

2082 Equation 23 can be solved for a given set of parameters both analytically or nu-  
 2083 merically. Several tools exist in order to solve this equation, with the most well known  
 2084 being GALPROP (available under <https://galprop.stanford.edu/>) [120], Dragon [165]  
 2085 and PICARD [166]. In this work, GALPROP was used, which solves the transport  
 2086 equation numerically and will be explained in section 5.3. Galprop uses astrophysi-  
 2087 cal measurements for the interstellar gas and cosmic ray source distributions, and  
 2088 employs nuclear physics measurements for interaction cross sections of particles  
 2089 and nuclei. Many different particle species can be en- or disabled in GALPROP, which  
 2090 affects the runtime of the simulations. For antinuclei from dark matter, other species  
 2091 need not be included, since the result is independent of other particle species. How-  
 2092 ever, for antinuclei from secondary cosmic rays, other cosmic ray species can affect  
 2093 the total flux and therefore need to be considered.

2094

2095 It is important to note that only the first and final term of equation 23 – i.e. the  
 2096 source and loss terms – depend on the species of particle which is being considered.  
 2097 The other terms, which cover the actual propagation through the galaxy, depend  
 2098 solely on parameters which are common to all particle species. This can be under-  
 2099 stood as the same magnetic fields and bulk motion affecting all particles. Thus,  
 2100 these parameters can be constrained by fitting abundant cosmic ray species which  
 2101 are sensitive to a particular parameter, in order to constrain the propagation for all

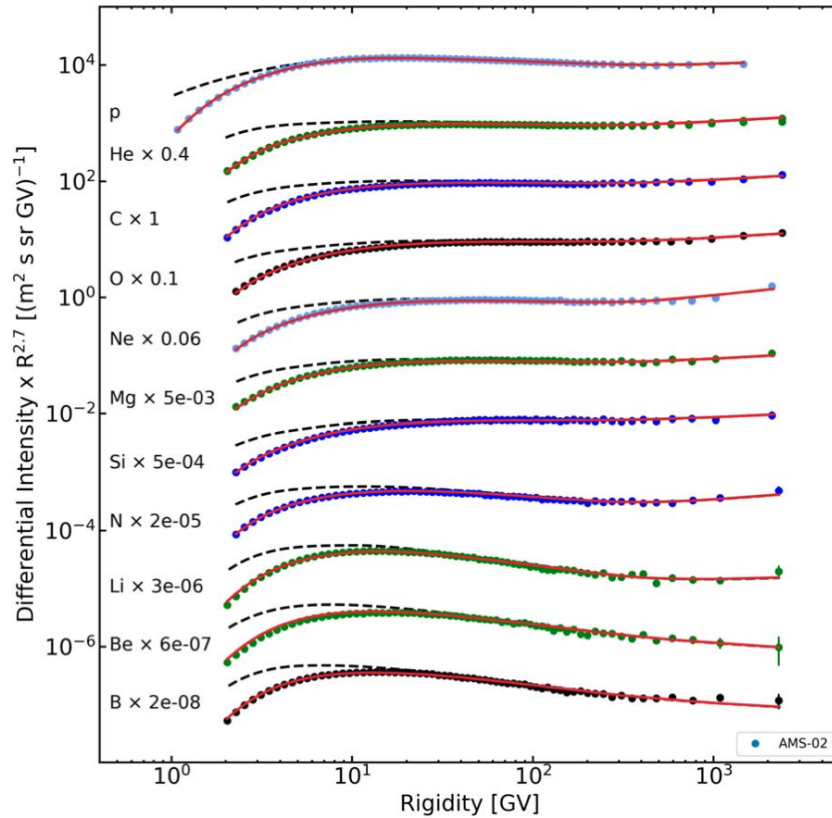


**Figure 65:** Fluxes of several cosmic ray nuclei, as measured by AMS-02, compared to the predictions of the best-fit values obtained by fitting several key species. Figure taken from [63]

2102 species. This is particularly important for the propagation of antinuclei, which are  
 2103 extremely rare. These propagation parameters have been investigated and reported  
 2104 by e.g. Boscini [62, 63] and Cuoco [161]. The effectiveness of these fits can be seen by  
 2105 comparing predicted spectra of protons, antiprotons and heavier cosmic ray nuclei  
 2106 with the measurements done by AMS-02, which are shown in figure 65. The solid  
 2107 lines are the predictions from the Boscini model after solar modulation is applied,  
 2108 while the dashed lines are the predictions before solar modulation. It can be seen  
 2109 that the predictions work very well for large energies, and there is a smooth response  
 2110 at low energies, which is well understood based on the effects of the heliosphere.  
 2111 This shows that the propagation is well under control.

2112

2113 The effect at low energies is due to the effect of the heliosphere, which is not  
 2114 included in codes such as GALPROP. These codes can only simulate large scale effects,

2115 and as such they output the particle fluxes outside of our solar system. Within our  
 2116 solar system, the solar magnetic field will affect incoming charged particles, and this  
 2117 needs to be accounted for. The solar magnetic field is not constant, but rather it  
 2118 varies over an 11 year period [167]. Thus, the effect of the solar modulation is also  
 2119 time dependent and needs to be calculated for a specific scenario. In this thesis,  
 2120 a solar minimum is considered, in order to discern the most optimistic flux of low  
 2121 energy antinuclei. There are tools which treat this in great detail for cosmic rays,  
 2122 such as HELMOD [168], but there are currently no such tools on the market which  
 2123 are able to treat antinuclei. Thus, a simple force field model has been commonly  
 2124 used for this purpose in the literature [4, 123, 2]. The advantage of this model is its  
 2125 broad applicability, while its disadvantage is mainly a large uncertainty induced for  
 2126 low momentum particles [169]. The force field model is a simplified solution to the  
 2127 Parker equation [170], which treats the full extent of the problem including solar  
 2128 winds and turbulences. This complete treatment relies on knowledge of turbulences  
 2129 and boundary spectra of the particle species involved, and thus lies beyond the scope  
 2130 of this thesis and similar analyses [2, 4, 63]. The force field approximation reproduces  
 2131 the overall effect of solar modulation, although the exact values it produces are not  
 2132 exact at low energies [169]. It also relies only on a single parameter, the so called Fisk  
 2133 potential  $\phi_F$ , and related the unmodulated flux  $F$  to the modulated flux  $F'$  according  
 2134 to equation 25, while modifying the corresponding kinetic energies according to  
 2135 equation 26

$$F'(E', \phi) = F(E) \frac{(E - Z\phi)^2 - m^2}{E^2 - m^2}, \quad (25)$$

$$E' = E - Z\phi, \quad (26)$$

2136 where  $m$  denotes the mass of the cosmic ray species in question. For the analyses in  
 2137 this thesis, the Fisk potential is assigned a value of 0.4 GV.

2138

2139 It is important to note that some of the propagation parameters which are degen-  
 2140 erate for one source are not necessarily so for another. In particular, the source from  
 2141 dark matter is strongly dependent on the height of the galaxy considered (since this  
 2142 increases the total amount of dark matter considered), rather than the ratio of the  
 2143 diffusion and the height,  $D_{xx}/z_h$ , which is the common factor for antinuclei from  
 2144 high-energy cosmic rays. This degeneracy for secondaries can be seen in table 4,  
 2145 where the aforementioned ratio is shown to be consistent between the two paramter-  
 2146 izations. Since propagation parameters are constrained by nuclei following roughly  
 2147 the same source distribution as secondaries, this difference in sensitivity causes a  
 2148 much larger uncertainty in the possible fluxes for antinuclei from dark matter than

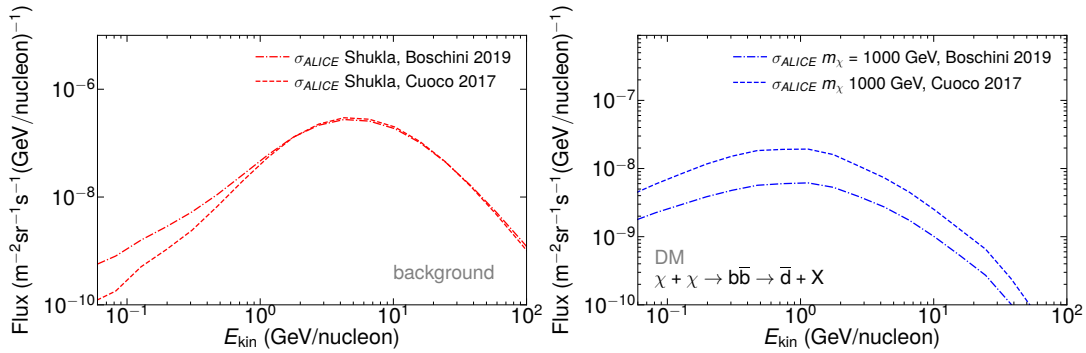


**Figure 66:** Comparison between the different GALPROP propagation parameters used in this work, for antideuterons from high energy cosmic ray collisions (left) and from dark matter annihilations (right).

2149 for antinuclei fluxes from high-energy cosmic rays [121]. This is also shown in figure  
 2150 66, where it can be seen that for a wide energy range, both different propagation  
 2151 parameterization used in this work give near identical antideuteron fluxes from high  
 2152 energy cosmic ray collisions, while for dark matter the difference is more than a  
 2153 factor 2. For antideuterons from high-energy cosmic rays the discrepancies between  
 2154 the two different parameterizations only become non-negligible at very low ener-  
 2155 gies, where the propagation is less well constrained and complicated by the need to  
 2156 disentangle solar modulation effects.

2157 At this point it is also important to note the composition of both cosmic rays and  
 2158 the interstellar medium. For the interstellar medium, its composition determines  
 2159 the targets for incoming cosmic rays. This is important both for the production of  
 2160 secondary antinuclei in high energy cosmic ray collisions, and also for the annihila-  
 2161 tion of antinuclei as they travel through our galaxy. Both the interstellar medium and  
 2162 baryonic cosmic rays share similar compositions: 90% protons and 9%  $^4\text{He}$  [171].  
 2163 The remaining elements is made up of heavier elements.

### 2164 5.3 The Galprop framework

2165 The technical details of the implementation of antinuclei propagation in GALPROP  
 2166 can be found in [112]. The following section aims to give the reader an understanding  
 2167 of the concepts considered.

2168  
 2169 As already discussed in section 5.2, the Galprop framework functions by solving  
 2170 the transport equation numerically (equation 23). It does so by finding a steady state  
 2171 solution, iterating in smaller and smaller timesteps until a stable solution is found.  
 2172 During each timestep, it iterates over a position and momentum grid, the former  
 2173 of which can either be expressed in 2 dimensions ( $r$  and  $z$ ) or 3 ( $x$ ,  $y$ ,  $z$ ). Since we

2174 assume axial symmetry, the two are mathematically equivalent, so for the purpose  
2175 of this work, the 2 dimensional method was chosen.

2176

2177 Galprop is configured by passing a set of parameters from an external text file.  
2178 The important parameters are shown in table 4. Of particular note are the Galaxy  
2179 half height  $z_h$ , and the diffusion parameter  $D_{xx}$ , since these two are degenerate for  
2180 cosmic rays from non-exotic sources. The actual parameter which is being fixed is  
2181 the ratio of the two. This is because for non-exotic sources, the number of sources  
2182 doesn't change so any change in position is compensated by increased diffusion. For  
2183 a dark matter source however, the height of the galaxy has direct implications for the  
2184 number of dark matter sources, so this degeneracy is broken.

2185

Parameter	Units	Best fit value from Boscini	Best Fit value from Cuoco
$z_h$	kpc	4	6.78
$D_{xx}$	$\text{cm}^2\text{s}^{-1}$	$4.5 \times 10^{28}$	$7.48 \times 10^{28}$

**Table 4:** Two of the parameters for the tuning of Galprop, which show the degeneracy between them.

It is important to note that the main parameter which affects a lot of propagation is the so called grammage, which is the amount of matter of the interstellar medium which particles have to traverse. This is the product of the density of the interstellar medium and the path length of the particles, and can be constrained by the ratio of primary to secondary cosmic rays, according to equation 27<sup>51</sup>

$$\psi_s/\psi_p = \frac{n\Delta z\sigma\beta cz_h}{2D_{xx}}, \quad (27)$$

2186 where  $n$  is the density of matter in the interstellar medium,  $\psi_p$  and  $\psi_s$  are the pri-  
2187 mary and secondary fluxes, and  $\sigma$  is the production cross section of the secondary  
2188 particles when the primary cosmic rays interact with the interstellar medium. This  
2189 means that this ratio is simply the amount of matter traversed  $\times$  the production  
2190 cross section  $\times \frac{z_h}{2D_{xx}}$ , which shows the degeneracy for these parameters. The primary  
2191 to secondary ratio is best constrained from the Boron-to-Carbon (B/C) ratio, since  
2192 Carbon is expected to be produced mostly during stellar processes, while all Boron  
2193 is produced in collisions of heavier nuclei with the ISM [124]. This ratio has been  
2194 measured by the AMS collaboration to very high accuracy [124], with errors less than  
2195 3% up to rigidities of 100 GV.

2196

<sup>51</sup>This is the simplified equation without losses, for more details see [172], section 7.1.

2197 Antinuclei are not by default included in Galprop. Fortunately, the framework is  
 2198 capable of handling negative nuclei with antiprotons, therefore the extension was  
 2199 done by providing the mass of the antideuteron/antihelium, their inelastic cross  
 2200 sections on the interstellar medium, and their source functions. Separate entries  
 2201 were used for the secondary production from high-energy cosmic rays and from  
 2202 dark matter annihilations. The inelastic cross section had to be provided on a proton  
 2203 and helium target, which are significantly lighter than the average detector materials  
 2204 probed in the measurements shown in section 3, therefore the results had to be  
 2205 extrapolated to these lighter targets. The exact methods of the extrapolations are  
 2206 explained in section 5.4.

2207  
 2208 The source functions for antinuclei from either high-energy cosmic-ray collisions  
 2209 or from dark matter annihilations were included in GALPROP as a function of the  
 2210 distance from the galactic centre. For the dark matter part, this can be done simply  
 2211 by evaluating equation 18 described above for a specific radius and kinetic energy.  
 2212 However, for antinuclei from high-energy cosmic rays this is not possible, since the  
 2213 spectrum of cosmic rays at a given point enters into the equation. Therefore, the  
 2214 production cross sections for the relevant collision systems (pp, p-He, He-p, He-He)  
 2215 were implemented in GALPROP, and the interactions between those cosmic-ray  
 2216 species were calculated as described in [113], based on the production cross sections  
 2217 in [129].

## 2218 **5.4 Annihilations within our galaxy**

2219 As antinuclei travel through our galaxy, they might inelastically interact with matter  
 2220 in the interstellar medium. This can either be in the form of inelastic scattering<sup>52</sup> or  
 2221 annihilation, although of the two the latter is expected to be dominant. The result of  
 2222 these interaction is thus mostly the disappearance of the antinuclei. The produced  
 2223 particles are mostly pions, and thus not stable enough to detect them and maybe  
 2224 extract a signal from them. Some high-energy photons could also be produced, and  
 2225 such gamma rays are the target of specific sky surveys looking for large areas of anti-  
 2226 matter, which when coming into contact with matter should produce a detectable  
 2227 signal. However, a single annihilation would be undetectable at any significant

---

<sup>52</sup>Non-annihilating inelastic scattering of antinuclei on matter is expected to be very rare. An example of this would be the collision of  ${}^3\overline{\text{He}}$  with a  ${}^4\text{He}$  nucleus which causes the  ${}^4\text{He}$  nucleus to break up, and thus a drastically different momentum for the  ${}^3\overline{\text{He}}$ . Since such particles would be lost to the tracking algorithm in the ALICE detector, these processes are included in the measurements of the inelastic cross section. However, in the galaxy such particles would not disappear and thus could in theory be detected (this is usually called tertiary production). Since the expected flux caused by this effect is several orders of magnitude lower than a signal, it is neglected for the purposes of this thesis.

2228 distance. We can therefore conclude that the relevant result of annihilation is the  
2229 disappearance of the antinucleus in question.

2230

2231 The loss of antinuclei in Galprop was taken into account by implementing the  
2232 inelastic cross section. As antinuclei are propagated throughout our galaxy, the total  
2233 amount of matter they interact with is calculated for each timestep, position and  
2234 momentum grid point (see section 5.3 for details). In order to do so, both the distri-  
2235 bution and the composition of the interstellar medium is required. The composition  
2236 is known to a relatively high accuracy [171], and is dominated by hydrogen, which  
2237 makes up  $\approx 90\%$  of the total mass in the interstellar medium. The remainder is mainly  
2238 helium, making up  $\approx 9\%$  of the total mass. During each calculation step, the inelastic  
2239 cross sections on the dominant species of the interstellar medium (hydrogen and  
2240 helium) are used to calculate how many antinuclei are lost in each momentum bin.  
2241 Therefore, it is necessary to evaluate the cross sections on these very light targets,  
2242 rather than the heavy targets on which they were measured.

2243

2244 In order to extrapolate the results of the inelastic cross sections to light targets, the  
2245  $A$  scaling from Geant was applied. To achieve this, the deviation of the inelastic cross  
2246 section from the default implemented in Geant was obtained for the mean material  
2247 in ALICE, as described in section 3, and proportionally applied to the antinucleus-  
2248 proton cross section in Geant. This assumes that the relative scaling is the same  
2249 regardless of the target nucleus, and an additional 8% uncertainty is assigned to  
2250 allow for any deviation from this assumption. This value was achieved by comparing  
2251 the  $A$  scaling used in Geant4 and in full Glauber calculations [110, 43]. For values  
2252 outside the range of the measurements detailed in sections 3, the scaling factor at  
2253 the last available momentum was used. The resulting cross sections are shown for  
2254 both antideuterons and  ${}^3\text{He}$  in figure 67. The Geant lines shown in these figures are  
2255 based on Glauber model calculations, as discussed in section 1.4.4.

## 2256 5.5 Antinuclei fluxes for different dark matter masses and annihilation channels

2257

2258 In this section the effects of different dark matter masses on antinuclei fluxes will be  
2259 discussed. The fluxes are compared to a prediction for secondary antinuclei from  
2260 high-energy cosmic ray collisions with the interstellar medium. In the lower panel  
2261 on figure 69 and on the right side of figure 70, the transparency of the galaxy to  
2262 antinuclei is shown. This is defined in equation 28 as the ratio of the obtained flux  
2263 with a given non-zero inelastic cross section, to the flux obtained when all inelastic  
2264 interactions are turned off. The dark matter self annihilation cross section used for  
2265 the dark matter models shown in this chapter is  $\langle \sigma v \rangle = 2.7 \times 10^{-26} \text{cm}^3 \text{s}^{-1}$ , unless

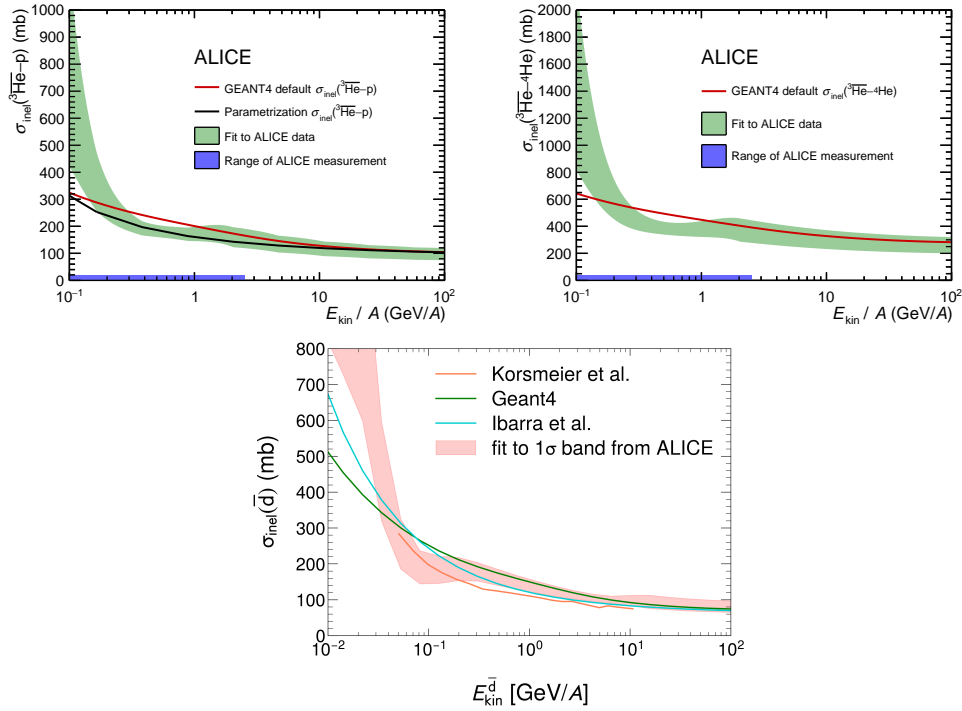


**Figure 67:** Scaled inelastic cross sections of  $^3\overline{\text{He}}$  (top) on proton (left) and Helium-4 (right) targets and antideuterons on proton targets (bottom). The band shows the experimental uncertainty from the ALICE measurements [105, 110], plus an additional 8% uncertainty associated with the scaling from heavier targets (C, O, Al) to protons (H). The parameterization shown in the top left panel (labeled Korsmeier et al in the bottom panel) is taken from [2], and is based on scaling the total deuteron-antiproton cross section by the inelastic portion of the antiproton-proton cross section, and then scaling the obtained value by 3/2 to account for the extra nucleon in  $^3\overline{\text{He}}$ . The cross section in the bottom panel labeled Ibarra et. al. is taken from [4], and is based on taken 2 times the antiproton-proton inelastic cross section, as parameterized by [36]. See section 1.4.4 for a more detailed discussion on calculating inelastic cross sections.



2266 otherwise noted. This is compatible with the currently allowed limit, and also at  
2267 the thermal value of the cross section, which is discussed in section 5.1.2.

$$\text{Transparency}(\sigma_{\text{inel}}) = \frac{\text{Flux}(\sigma_{\text{inel}})}{\text{Flux}(\sigma_{\text{inel}} = 0)}. \quad (28)$$

2268 Several parameterizations of the inelastic cross sections were considered and are  
2269 shown for the fluxes in this section. The colored bands represent the results obtained  
2270 using the inelastic cross sections measured by ALICE, and the associated experimen-  
2271 tal uncertainties from this measurement. The solid lines denote the results obtained  
2272 using the default inelastic cross sections implemented in Geant4.

### 2273 5.5.1 Results for antideuterons

2274 The antideuteron fluxes inside and outside of the solar system can be seen in fig-  
2275 ure 68. Of particular note is the signal to background ratio, i.e. the ratio between  
2276 secondaries coming from cosmic-ray collisions and fluxes from dark matter. At low  
2277 energies, for values of  $m_\chi \lesssim 100$  GeV, the signal exceeds the secondaries by several  
2278 orders of magnitude at energies below ca. 3 GeV/A. This reinforces low-  
2279 energy antideuterons as a unique probe for indirect dark matter searches. At larger  
2280 energies the spectral shape of the antideuteron fluxes from dark matter becomes very  
2281 similar to the one expected for secondaries, and also the normalisation becomes  
2282 very similar. This makes WIMP models with masses above ca. 1 TeV difficult to  
2283 differentiate from secondary production, and thus loses the strength for probing  
2284 such dark matter models.

2285 The largest flux is achieved by the 10 GeV dark matter mass model, which is due  
2286 to the increased normalisation due to the  $1/m_\chi$  term. However, for such low dark  
2287 matter masses, the used dark matter self annihilation cross section has been ruled  
2288 out by antiproton limits, as can be seen in figure 63. Thus, the flux at 51 GeV would  
2289 produce the largest allowed antideuteron flux.

2290

2291 For antideuterons, an additional channel was considered in addition to the  
2292 usual  $W^+W^-$  and  $b\bar{b}$  channels: a boosted production via the intermediate produc-  
2293 tion of  $\overline{\Lambda}_b$  and its subsequent decay, as described in [144]. This particular channel  
2294 was only recently considered, and is expected to boost antinuclei yields. The validity  
2295 of the approach rests on the fact that normal tunes of event generators under repre-  
2296 sent both the production of  $\overline{\Lambda}_b$  and its branching fraction into antinuclei, however,  
2297 this needs to be followed up with measurement to clearly determine the actual size  
2298 of this effect.

2299 There are also two different background models considered for antideuterons, la-

2300 beled Shukla et. al. based on [129], and Kachelriess et al. based on [52]. For more  
2301 details see [121].

### 2302 5.5.2 Results for ${}^3\overline{\text{He}}$

2303 In this section the results for antihelium-3 fluxes using different dark matter masses  
2304  $m_\chi$  are shown and discussed. These masses range over 2 orders of magnitude from  
2305 10 GeV all the way to 2 TeV, all of which are valid hypotheses for WIMP masses. As  
2306 can be seen in figure 69, the result is not just a difference in the overall normalization,  
2307 but also in the shape of the produced spectrum. This is because the larger energy  
2308 available with the higher mass translates into more kinetic energy in the final state  
2309 particles, i.e. the produced antinuclei. It can also be seen that the increased pro-  
2310 duction with increased mass does not compensate for the reduction in annihilation  
2311 rate due to the lower number density<sup>53</sup>, thus the magnitude of the flux decreases  
2312 with increasing dark matter mass. Also shown in the bottom panel for each figure, is  
2313 the transparency of the galaxy to  ${}^3\overline{\text{He}}$  defined in equation 28. It is promising that  
2314 the predicted fluxes from  $\overline{\Lambda}_b$  decays in figure 69 reach the AMS-02 sensitivities even  
2315 without accounting for other uncertainties. For other channels, a boost of about 1-2  
2316 orders of magnitude is possible in the most optimistic scenario, as can be seen from  
2317 table 5, which could potentially allow a signal in both the  $b\overline{b}$  and  $W^+W^-$  channels  
2318 for masses of around  $m_\chi = 100$  GeV. And even a null observation would place more  
2319 and more stringent limits on dark matter models, further tightening the available  
2320 parameter space.

## 2321 5.6 Results for different dark matter profiles

2322 The effect of the different dark matter profiles is shown only on one channel and  
2323 one dark matter mass, since it has similar effects on all channels/masses. The  
2324 absolute normalization is degenerate with bounds from antiproton measurements,  
2325 as was discussed in section 5.1.2. However, more insight can be gained from the  
2326 bottom panels of figure 70, where the transparency is shown. The transparency of the  
2327 Milky Way shows a significant shift between the three different profiles. This can be  
2328 understood as the mean distance that antinuclei from dark matter have to traverse  
2329 in order to get to earth. The more peaked the profile is towards the center, the longer  
2330 the mean path. This in turn reduces the transparency. Thus, the transparency of the  
2331 galaxy to antinuclei is lowest for the Einasto profile, which is the most peaked, as  
2332 can be seen in figure 60. It is highest for the isothermal profile, which is relatively  
2333 flat towards the centre of the Milky Way.

<sup>53</sup>This is the  $1/m_\chi^2$  scaling seen in equation 18.

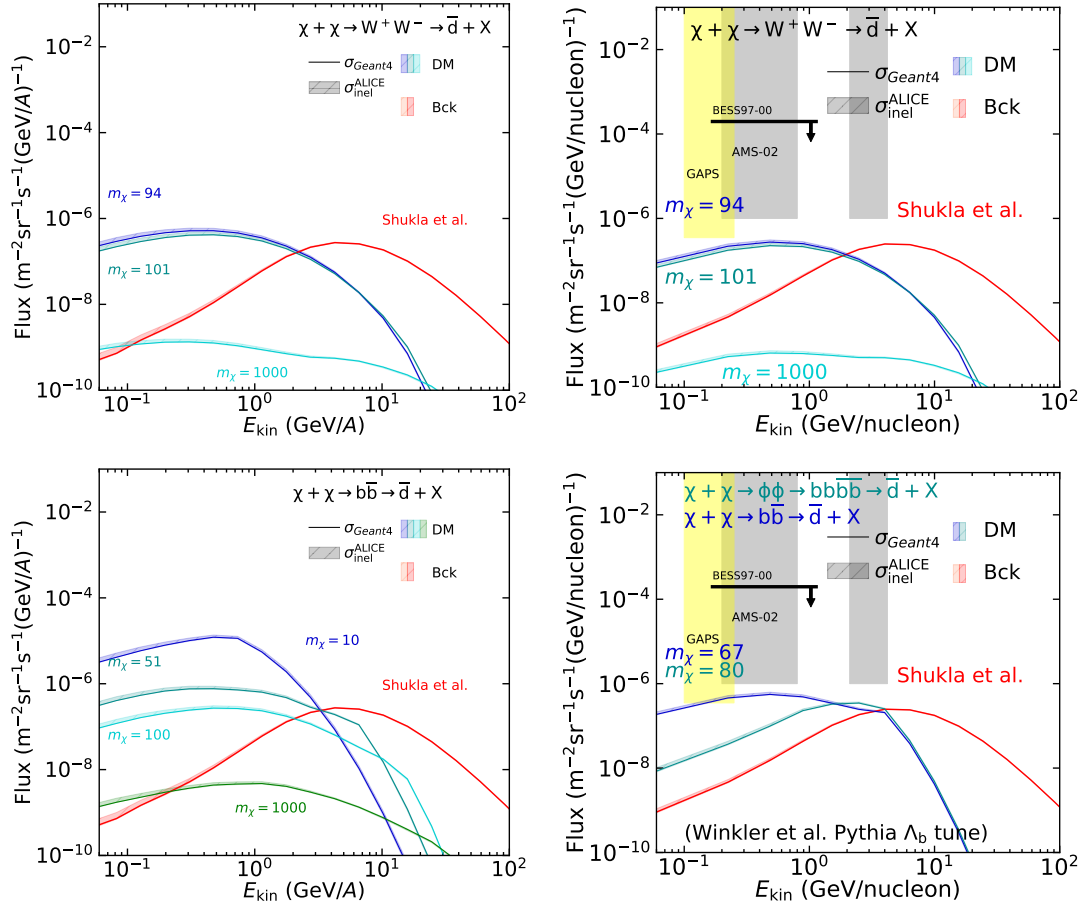


**Figure 68:** Expected antideuteron fluxes for different  $m_\chi$  ranging from 10 GeV to 1 TeV, and from primordial black holes (PBHs). They are compared to an expected spectrum of secondary antideuterons from high-energy cosmic-ray collisions. The results are shown for the position of the solar system. The figures on the left show the results without solar modulation, and on the right with solar modulation included by means of a force field model, as is discussed in section 5.2. The results are also shown for different possible annihilation channels of dark matter, either through  $W^+W^-$  (top) or through  $b\bar{b}$  (bottom).

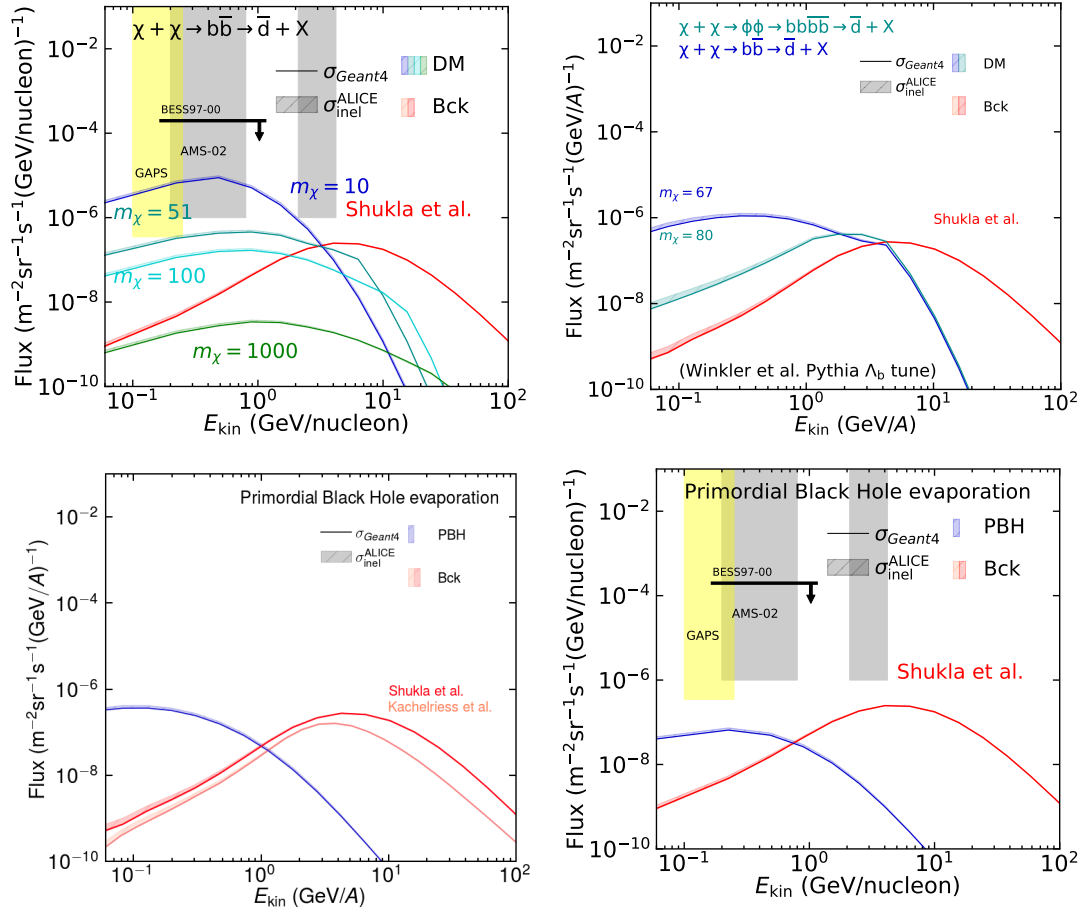


**Figure 68:** Expected antideuteron fluxes (cont.) dark matter annihilations through  $\bar{\Lambda}_{\bar{b}} \rightarrow b\bar{b}$  and light mediators (top) and from primordial black holes (PBHs) (bottom). The figures on the left show the results without solar modulation, and on the right with solar modulation included by means of a force field model, as is discussed in section 5.2.

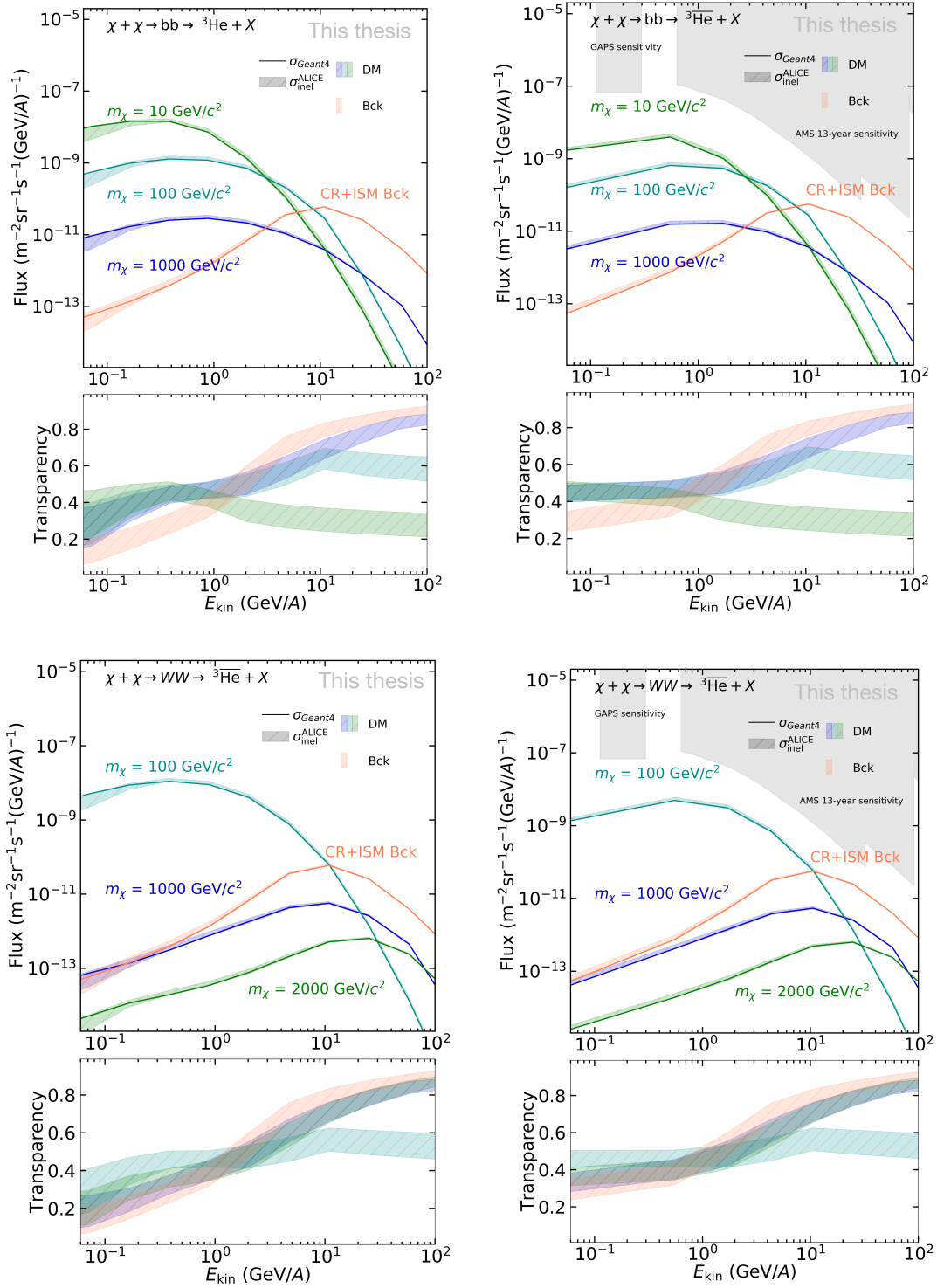


**Figure 69:** Expected  ${}^3\text{He}$  fluxes for different  $m_\chi$  ranging from 1 GeV to 2 TeV. They are compared to an expected spectrum of secondary  ${}^3\text{He}$  from high energy cosmic ray collisions. The results are shown for the position of the solar system. The figures on the left show the results without solar modulation, and on the right with solar modulation included by means of a force field model, as is discussed in section 5.2. The results are also shown for different possible annihilation channels of dark matter, either through  $W^+W^-$  (top), through  $bb$  (bottom).

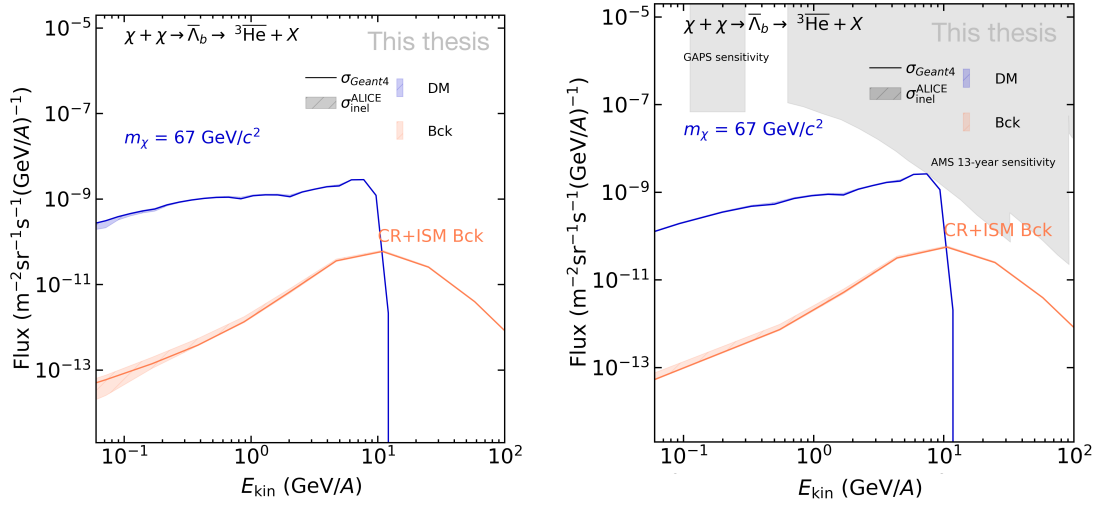


**Figure 69:** Expected  ${}^3\overline{\text{He}}$  fluxes (cont.) from dark matter annihilations through  $\overline{\Lambda}_b$  decays. They are compared to an expected spectrum of secondary  ${}^3\overline{\text{He}}$  from high energy cosmic ray collisions. The results are shown for the position of the solar system. The figures on the left show the results without solar modulation, and on the right with solar modulation included by means of a force field model, as is discussed in section 5.2.

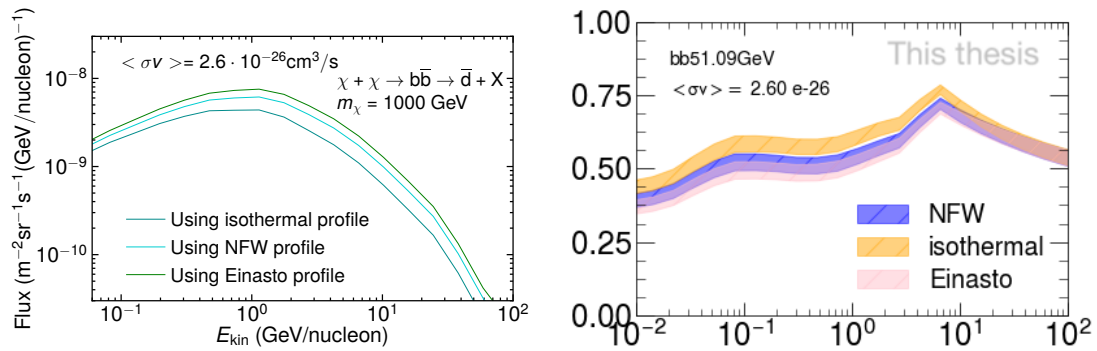


**Figure 70:** Antideuteron fluxes for different dark matter profiles (left) and the corresponding transparencies (right), for antideuterons from dark matter annihilation through the  $b\overline{b}$  channel.

## 5.7 Discussion of the uncertainties on antinuclei fluxes and transparencies

Presented in this chapter are the experimental uncertainties on the effect of inelastic interactions on antinuclei fluxes in cosmic rays, as well as on the transparency of the galaxy to antinuclei from different sources. It is important to note that these uncertainties are now quantified based on experimental data for the first time, and that they uncertainties are much smaller than other uncertainties in the field, as can be seen by comparing the values given in table 5.

Source of effect	Effect for CR	Effect for DM	Source
Inelastic interactions $\bar{d}$ ( ${}^3\bar{\text{He}}$ )	$\pm 20\%$ (15%)	$\pm 10\%$ (15%)	This thesis, [121, 110]
Propagation parameters	$\approx 20\%$	$\approx 200\%$	This thesis, [121]
Production $\bar{d}$ ( ${}^3\bar{\text{He}}$ )	${}^{+27}_{-42}\%$ ( $\pm 10\text{-}20\text{x}$ )	${}^{+63}_{-70}\%$ ( $\pm 10\text{-}30\text{x}$ )	[121, 4, 2]
DM model uncertainties	N/A	$\approx 1000\%$	[121]

**Table 5:** A list of the sizes of uncertainties involved in making predictions for antinuclei fluxes. The second and third column are describing the size of the effect on antinuclei from high energy cosmic ray collisions and from potential dark matter annihilations, respectively.

Another important uncertainty is the model dependence of the transparency, specifically the dark matter mass and annihilation channel dependence. This effect can be seen in the bottom panels of figure 69. When comparing the transparencies associated with different dark matter mass assumptions for the  $W^+W^-$  channel, the momentum dependence of the transparency at high energies varies greatly. For higher dark matter masses, the shape of the  ${}^3\bar{\text{He}}$  flux is more similar to the secondary flux than to the flux with the standard  $m_\chi$  assumption of  $\approx 100\text{GeV}/c^2$ . This results in a transparency which is very similar in both shape and magnitude to the one for secondaries. For the  $b\bar{b}$  channel, the difference in  $m_\chi$  causes a much reduced difference in spectral shape, and the transparencies change shape more slowly with increasing  $m_\chi$ . In particular for the  $b\bar{b}$  channel, a significant difference still remains at low energies, which are the most interesting for indirect dark matter searches. This effect can change the transparencies at high energies from  $\approx 50\%$  for  $m_\chi = 100\text{GeV}/c^2$  to almost 90% at 2 TeV/ $c^2$ .

Another parameter which affects the transparency is the dark matter profile considered. This effect can be seen in figure 70, which shows transparencies for antideuterons from dark matter with different dark matter profiles. It shows that there is an effect depending on the dark matter profile chosen, which can be understood as the mean path length the antinuclei travel before getting to earth. The more

2362 peaked Einasto and NFW profiles have lower transparencies, since a larger amount  
 2363 of antinuclei is produced close to the centre of the galaxy (i.e. further away), and  
 2364 this the chance of antinuclei interacting inelastically increases. This effect causes a  
 2365 difference in the transparency between the profiles of about 10%.

## 2366 **5.8 Summary of propagation of antinuclei through the galaxy**

2367 From the results in this section several conclusions can be drawn. The most impact-  
 2368 ful are the novel experimental uncertainties on the effect of the inelastic cross section  
 2369 on antinuclei propagation, i.e. on the transparency. These uncertainties are of the  
 2370 order of 15% for antihelium, and 10% for antideuterons, and thus significantly below  
 2371 the uncertainties from other effects, dominantly the uncertainty on the production  
 2372 of these antinuclei. The second conclusion is that the exact shape of the dark matter  
 2373 profile is a minor component in determining the normalization of antinuclei, even  
 2374 before possible degeneracies with antiproton limits are taken into account. This  
 2375 means that even though the dark matter profile is a free choice in current models,  
 2376 the final antinuclei fluxes are not sensitive to this. The choice of the dark matter  
 2377 mass however has an important effect, both on the shape and the normalization of  
 2378 the resulting antinuclei spectrum. In particular for large WIMP masses, approaching  
 2379 or exceeding masses of 1 TeV, the shape of the spectrum becomes very similar to  
 2380 the shape of the secondary spectrum, which would make differentiation between  
 2381 them difficult. From the considered channels, only the  $\Lambda_b$  boosted channel sig-  
 2382 nificantly deviated from the others, and only for  ${}^3\overline{\text{He}}$ , which however leaves open  
 2383 the possibility that other not thoroughly considered channels might influence the  
 2384 production of one antinucleus over another. If one were to speculate about the ten-  
 2385 tative antihelium events seen by the AMS collaboration, which are predominantly  
 2386 at high energies, they might originate from a heavy WIMP, with the  ${}^3\overline{\text{He}}$  production  
 2387 significantly boosted relative to antiproton and antideuteron productions, through  
 2388 some unknown mechanism. What is clear however, is that unraveling the mysteries  
 2389 of such a signal could do wonders for our understanding of antinuclei sources in our  
 2390 galaxy, and might even expose new physics.

## 2391 **5.9 Experiments to detect antinuclei in the cosmos**

2392 Given their rarity, antinuclei in cosmic rays are difficult to detect.

2393 Detecting antinuclei in cosmic rays has to be done near the top of our atmo-  
 2394 sphere, since antinuclei would annihilate well before reaching any ground-based  
 2395 detector. This leaves either space borne experiments or high-altitude balloon  
 2396 flights. Currently there are two promising experiments either currently or soon to be  
 2397 deployed: the Alpha Magnetic Spectrometer (AMS) [173] on the international space



2398 station (ISS), and the General AntiParticle Spectrometer (GAPS) [148, 174], which is  
2399 a planned balloon flight experiment. The two are shortly discussed below.

2400

2401 The experiment which currently has the best sensitivity for detecting antinuclei  
2402 is AMS-02, which is a magnetic spectrometer on the international space station.  
2403 As a magnetic spectrometer, AMS-02 is more sensitive to charge differences, and  
2404 therefore more sensitive to  ${}^3\overline{\text{He}}$  nuclei than to antideuterons, since the latter need  
2405 to be distinguished from the significantly more abundant antiprotons. However, it is  
2406 still a big surprise that AMS has reported potential signals consistent with multiple  
2407  ${}^3\overline{\text{He}}$  nuclei, given that none of the currently available models predict a flux within  
2408 the sensitivity of AMS, much less an order of magnitude above. These reports have  
2409 cause a large amount of effort from both experimental and theoretical communities  
2410 to come up with theories which might explain this signal, while also taking into  
2411 account the lack of evidence for an antideuteron signal. It is currently unclear which  
2412 process would produce such a large  ${}^3\overline{\text{He}}$  flux without boosting the antideuteron flux  
2413 in a similar amount, with some suggested options being a boost to  ${}^3\overline{\text{He}}$  production  
2414 via  $\Lambda_b$  decays [144].

2415 The current generation of the AMS experiment – AMS-02 – has been studying cosmic  
2416 rays since 2011, having analyzed over 200 billion cosmic-ray events. It consists of  
2417 several detector systems, including a Time-of-Flight detector, a silicon tracker, a star  
2418 tracker (to determine its orientation), a transition radiation detector, a permanent  
2419 magnet to curve charged particle tracks, a Cherenkov detector and an electromag-  
2420 netic calorimeter. AMS has delivered incredibly precise data on cosmic ray spectra  
2421 of nuclei up to heavy elements, as well for electrons, positrons and antiprotons. In  
2422 particular the antiproton spectra have been studied extensively for hints of WIMP  
2423 dark matter decays, as was already discussed in section 5.1.2.

2424 The "smoking gun" signal which AMS could detect from exotic physics such as dark  
2425 matter would of course be an antinuclei signal. However, as can be seen from the  
2426 fluxes in figure 69, it is not yet clear what source could feasibly reach AMS-02 sensitiv-  
2427 ities, although several models could do so within all their uncertainties. Therefore it  
2428 is extremely interesting that AMS has repeatedly reported the observation of multiple  
2429 possible high-energy  ${}^3\overline{\text{He}}$  and  ${}^4\overline{\text{He}}$  events [117, 118], but as of now these findings  
2430 have not been published, only presented in talks. The results from one such talk are  
2431 shown in figure 71. These events have kinetic energies per nucleon above 10 GeV/c.  
2432 Should the observed signals indeed be from antihelium nuclei, it comes with a few  
2433 puzzling questions. Why is the flux so much greater than expected? This increase is  
2434 possible within uncertainties to be the result of high-energy cosmic-ray collisions,  
2435 but only under the most favorable conditions. They are also significantly above the  
2436 expected flux of most dark matter models, however as shown by the study of the  $\overline{\Lambda}_b$   
2437 boosted  ${}^3\overline{\text{He}}$  flux from dark matter annihilations, some dark matter models could fea-

2438 sibly reproduce these results. One study has concluded that the only standard model  
2439 process that could plausibly produce such a flux would be an antistar within 1 kpc of  
2440 earth [122, 123]. This would however be very visible from gamma-ray observations,  
2441 as the large amounts of antimatter–matter annihilations would produce a distinct  
2442 signal in the gamma-ray spectrum. As such, a confirmation of the reported signals  
2443 would suggest a source beyond the standard model. One possible explanation would  
2444 be dark matter, where the production of antinuclei is boosted by channels not yet  
2445 considered. One such example is the recent study on antinuclei production through  
2446 the  $\bar{\Lambda}_b$  channel [144]. The second question these findings raise is the scaling of the  
2447 antinuclei production with each additional nucleon. The number of  ${}^3\bar{\text{He}}$  to  ${}^4\bar{\text{He}}$   
2448 events observed suggest a ratio close to 1:3, whereas for production in small systems  
2449 at the LHC the penalty factor is 1:1000 [72]. The final question – and perhaps the  
2450 easiest to answer – is why 10 possible  ${}^3\bar{\text{He}}$  events have been observed while AMS has  
2451 so far only seen 7 possible antideuteron events [119]. The most likely explanation  
2452 for this question is simply that differentiating antideuterons from antiprotons is very  
2453 difficult, as they have the same charge. The background from the antiproton signal  
2454 might therefore simply cover the sensitivity to an antideuteron flux.

2455

2456 The current generation of the AMS experiment will hopefully continue to deliver  
2457 data for years to come - and is even currently being upgraded in order to improve  
2458 the accuracy of their antiproton measurements - however, planning for the next gen-  
2459 eration is already ongoing. This next generation experiment is called AMS-100, due  
2460 to its planned acceptance of  $100\text{m}^2\text{sr}$  [175]. It will be a satellite experiment located at  
2461 Lagrange point 2 of the Sun–Earth system, using many of the same technologies and  
2462 systems as the James Webb Space Telescope (JWST). AMS-100 would have a 1000  
2463 fold increase in acceptance compared to AMS-02, and be able to deal with rigidities  
2464 up to 100 TV (AMS-02 up to 2 TV). It will also employ a greater magnetic field, using  
2465 high-temperature superconductors [175]. As such, it is expected to deliver more  
2466 precise measurements of antinuclei in cosmic rays, and thus to shine light on the  
2467 questions posed by current measurements.

2468

2469 GAPS is a more specialised detector, focused less on measuring all kinds of cos-  
2470 mic rays but rather specializing on detecting annihilation events of antimatter. It  
2471 works based on an outer "umbrella" of TOF detectors around a Si tracker, in order to  
2472 identify such annihilation events. The setup is shown in figure 72. A novel technique  
2473 is used to detect annihilations, called the "exotic atom" technique, which is outlined  
2474 in figure 72. The antiparticle travelling through the detector will lose energy due to  
2475 Bethe–Bloch ionization until it stops, at which point it will displace an electron in  
2476 an atom to form an exotic atom with near unit probability. The radiative decay of  
2477 such an excited atom can be uniquely matched to the components of the exotic atom

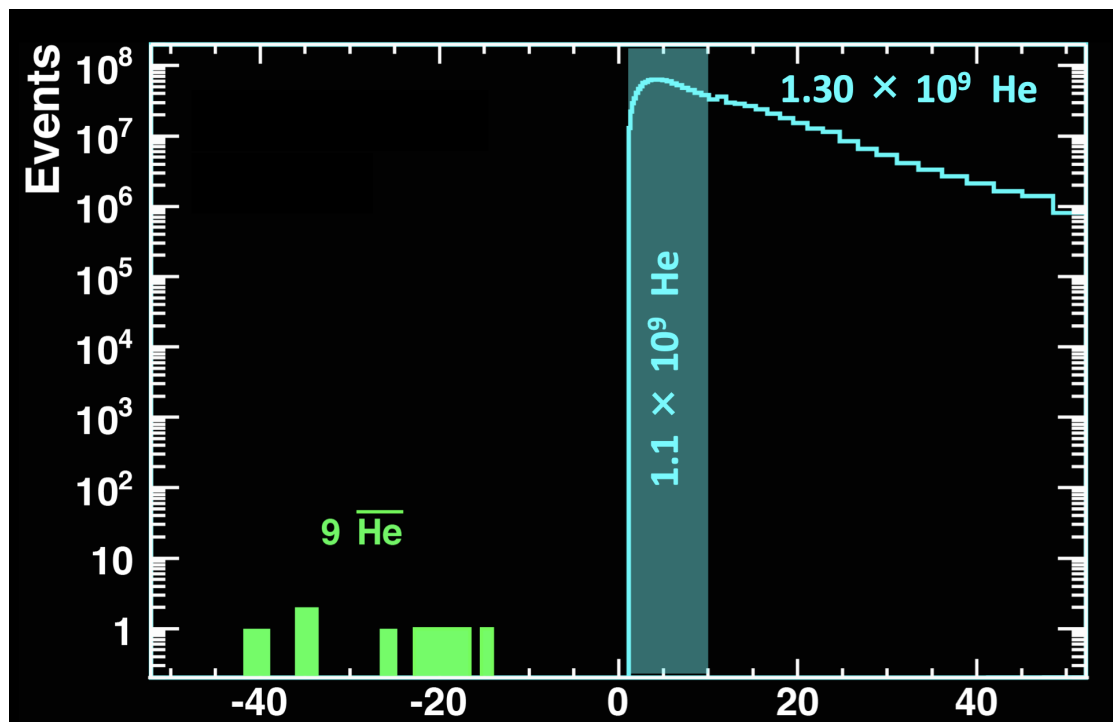


**Figure 71:** Plot of the rigidity resolution of AMS for comparing  ${}^3\bar{\text{He}}$  and  ${}^3\text{He}$  signals. 9 possible  ${}^3\bar{\text{He}}$  events are shown. These findings have not yet been published and this figure is taken from a talk [119].

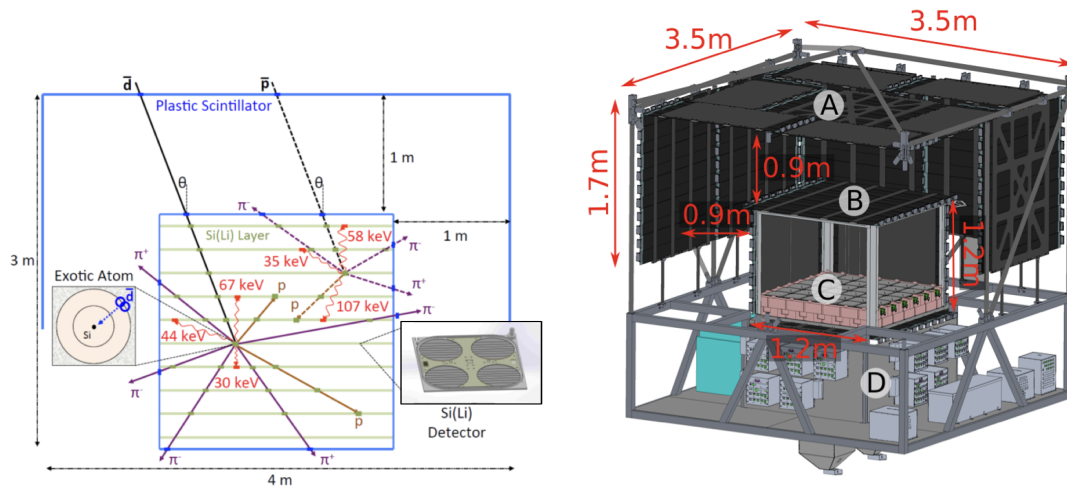


**Figure 72:** (Left) GAPS antiparticle detection method: antiparticles slow down and stop in the Si(Li) target, forming an exotic atom. Atomic X-rays will be emitted as it de-excites, followed by the pion (and proton) emission from nuclear annihilation.  $\bar{d}/\bar{p}$  identification is based on (1) the stopping range, (2) the pion and proton multiplicity, (3) the atomic X-rays energies. Figure and caption taken from [174]. (Right) The GAPS detector, the central tracker (C) is surrounded by the inner (“cube”, B) and outer (“umbrella”, A) TOF layers. The readout electronics, flight computer, ballast and other support infrastructure are located underneath the tracker (D). Solar panels, cooling systems, antennae and thermal insulation are not shown for clarity. Figure and description taken from [148].

2478 [148]. GAPS will fly over the south pole, where the effects from earth’s magnetic field  
 2479 are minimal. The benefit of antinuclei detection via balloon borne experiments  
 2480 over satellite borne ones is the much reduced costs.

2481

2482 The main goal of GAPS is to measure low-energy antideuteron flux, or to improve  
 2483 on the current upper limit, and to follow up on the potential antihelium events  
 2484 seen by the AMS Collaboration. GAPS reach extends to lower energies than those  
 2485 probed by AMS, making such searches complementary. The expected sensitivity to  
 2486 antideuterons of GAPS is shown in figure 68, compared with AMS upper limits. As can  
 2487 be seen, the sensitivities are comparable, but GAPS reaches much lower momenta,  
 2488 while AMS covers a much larger momentum span. The shown antideuteron fluxes  
 2489 in figure 68 do not reach the GAPS sensitivities, however, within the uncertainties  
 2490 outlined in table 5, they can indeed reach the GAPS sensitivities. Therefore, a null  
 2491 observation by GAPS would help to constrain current models. GAPS is also acting as  
 2492 a pathfinder future balloon experiments by demonstrating such new technologies,

2493 and their usefulness for specific searches.

## 6 Final remarks and outlook

The use of the ALICE detector material as a target for measuring antinuclei annihilations by means of their inelastic cross sections has proven a fruitful way to conduct these otherwise challenging measurements. Yet the potential of these measurement techniques is far from exhausted. In this section I want to highlight what has already been achieved (not just by me in this thesis, but also by other works), and talk about the progress still to come.

### 6.1 Measurements of the inelastic cross sections of antinuclei

The full list of the inelastic cross section measurements using both the antiparticle-to-particle method and the TOF-to-TPC method are shown in figure 73. For antideuterons, this represents the first low energy measurement of the inelastic cross section, while for  ${}^3\overline{\text{He}}$  and  ${}^3\overline{\text{H}}$  it is the very first measurement of the inelastic cross sections ever. In the upcoming Run 3 and Run 4 data taking campaigns at the LHC, we will be able to drastically reduce the statistical uncertainties dominating for the  $A = 3$  antinuclei, and hopefully extend this set of measurements to  $A = 4$  antinuclei. Indeed, in Run 3 the expected increase in statistics for Pb–Pb collisions is a factor 100. Considering the penalty factor per additional nucleon in Pb–Pb collisions, this would result in statistical uncertainties for the measurement of the inelastic cross sections of  $A = 4$  antinuclei only  $\sqrt{3.5}$  times larger than the uncertainties on the  $A = 3$  results already measured, making such measurements highly feasible. Additionally, by updating studies on the material budget and improving our secondary distributions in Monte Carlo, the statistical uncertainties are expected to be significantly reduced, so that hopefully we will be able to make precision measurements of these cross sections. Furthermore, there are plans to include a target material in the ALICE detector, in order to probe the annihilation of particles on different materials directly. With this exciting experimental development – and the ever improving understanding of the nature of the strong force due to femtoscopy measurements [176] we hope to inspire new theoretical work on the topic of antinuclei annihilations, and maybe finally even a theoretical framework to describe its low energy behavior.

### 6.2 Use of these measurements

In nuclear physics, the principal use of these cross sections is twofold. The first use is a more accurate description of antinuclei propagation using Geant4, once the Geant4 parameterizations are adjusted with these new results. Additionally, these measurements allow the assignment of an experimental uncertainty due to these

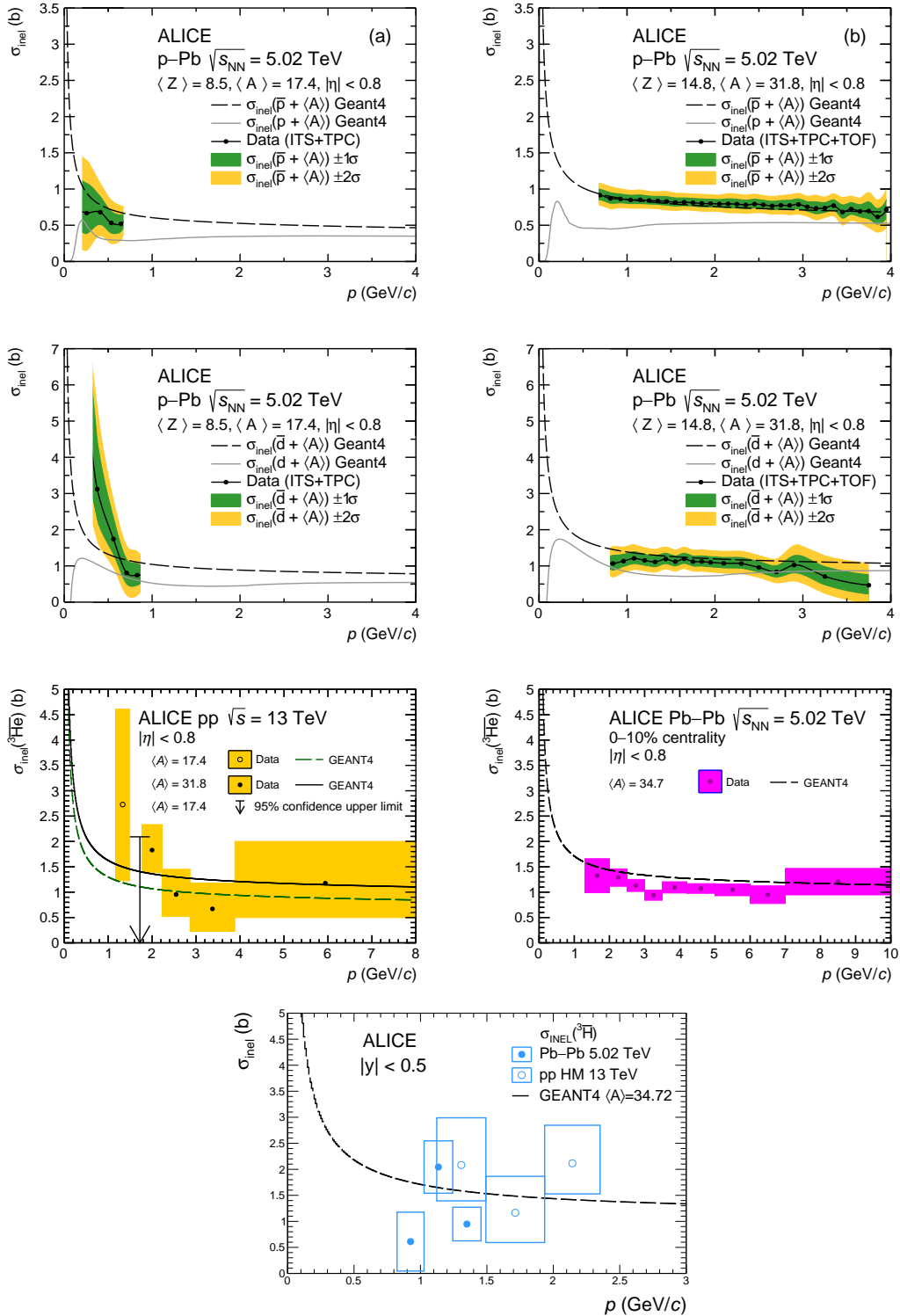


**Figure 73:** The inelastic cross section measurements for the antinuclei from  $A = 1$  to  $A = 3$ , as measured by ALICE in [105, 110] and in an upcoming publication on  ${}^3\bar{\text{H}}$ .

2530 measurements. Ideally, this would allow the study of antinuclei production to lower  
 2531 momenta than is currently common practice [177, 178, 179, 180, 181, 182]. The sec-  
 2532 ond use is a new probe into the isospin dependence of the strong force, using two  
 2533 charged particles in  ${}^3\overline{\text{He}}$  and  ${}^3\overline{\text{H}}$ . With future precision measurements, any possible  
 2534 discrepancy between these isospin partners will complement existing studies using  
 2535 the antiproton and antineutron inelastic cross sections [183].

2536

2537 But the main use of these measurements is in another field: astrophysical dark  
 2538 matter searches using antinuclei. The work done as part of this thesis has shown  
 2539 the effect of the annihilation on the expected antinuclei fluxes and determined an  
 2540 experimental uncertainty on the transparency of our galaxy to  ${}^3\overline{\text{He}}$  from a variety of  
 2541 sources. The inelastic cross section can also be used by the experiments looking for  
 2542  ${}^3\overline{\text{He}}$ , to calculate their own efficiency for detection.

2543 We eagerly await the publication of the tentative  ${}^3\overline{\text{He}}$ -like events seen by the AMS-02  
 2544 experiment, and if confirmed hope that this work will help interpret such a remark-  
 2545 able flux of antinuclei.

2546

### 2547 **6.3 Reevaluating physical and experimental effects on the cosmic** 2548 **antideuteron flux and its uncertainties**

2549 Finally, the cosmic antideuteron flux was reevaluated, in collaboration with theo-  
 2550 reticians and astrophysicists from the GAPS experiment. This included a detailed  
 2551 discussion of sources (the dark matter sources were discussed in detail in section 5,  
 2552 for a more detailed discussion of the cosmic ray background, please see [121]), and  
 2553 propagation; as well as a discussion of the degeneracies between constraints of the  
 2554 two. This has highlighted the importance of a rigorous treatment of propagation,  
 2555 and of performing a full chain analysis when fitting data (such as the cosmic ray  
 2556 antiproton "excess"; the constraints coming from such fits are highly model depen-  
 2557 dent).

2558

2559 Current generation experiments seem to already be able to measure some antin-  
 2560 uclei events, which presents an interesting challenge for theoretical models. Either  
 2561 way either current or next generation experiments should shine a light on cosmic  
 2562 ray antinuclei, and morph any discussion on the uncertainties affecting their fluxed  
 2563 from a theoretical exercise to an experimental necessity.



2564 **6.4 Outlook**

2565 In short, the future of antinuclei inelastic cross section measurement is one of im-  
2566 proving upon these first measurements by measuring with higher precision, and  
2567 many different target materials. Additionally, the  ${}^4\overline{\text{He}}$  is a final important piece for  
2568 astrophysical studies. This will also allow testing the differences between the  ${}^3\overline{\text{He}}$   
2569 and  ${}^3\overline{\text{H}}$  inelastic cross sections, which can take into account isospin dependence  
2570 and size effects.

2571

2572 And as antinuclei searches in space are getting ever closer to the detection of an  
2573 antinuclei signal, the importance of nuclear physics studies as input for theoretical  
2574 predictions becomes ever more important. The crown jewel would be the detection  
2575 of an antinuclei signal far from expectations of high energy cosmic ray collisions,  
2576 which would signal new and exciting physics in any case. And maybe even a first  
2577 look into the nature of dark matter.

## 2578 **7 Appendix**

### 2579 **7.1 Current status of the evidence for and against (but mostly against)** 2580 **the existence of anti-stars**

2581 As has been covered plenty already in this thesis, one of the biggest remaining  
2582 mysteries in physics is the asymmetry between the amount of matter and antimatter  
2583 present in our universe. It is thought that up to 95% of luminous matter consists  
2584 of matter rather than antimatter. But how can it be known that another star is not  
2585 entirely comprised of antimatter, given that the only difference in particles is their  
2586 electric charge? The answer lies in the fact that even though structures within our  
2587 galaxy and even universe are filled with only extremely low densities, they are not  
2588 actually empty. It therefore stands to reason that if there were a region dominated  
2589 by antimatter (even just a single anti-star, although a larger region seems more  
2590 likely), such a region would eventually have to end and come in contact with a  
2591 matter dominated region. In this volume of overlap, antimatter-matter annihilations  
2592 would occur abundantly, resulting in a significant amount of high energy gamma  
2593 rays. Such a specific and localized signal should be relatively easy to detect with  
2594 dedicated gamma ray surveys, such as FermiLAT [127]. The lack of any evidence  
2595 thereof suggests that there are no large antimatter dominated regions, and thus no  
2596 anti-stars.

### 2597 **7.2 Why the statistical hadronization model is not used for calcu-** 2598 **lating (anti)nuclei yields from WIMP dark matter annihilations**

2599 The statistical hadronization model (SHM) [184] is the idea that particles are pro-  
2600 duced in thermal equilibrium, and is able to predict the yields of particles over  
2601 many order of magnitudes based on a single parameter: the temperature. However,  
2602 the model does not predict the correlations in momentum space or the spectra of  
2603 antinuclei. This causes several problems when attempting to use the SHM for the  
2604 prediction of antinuclei from WIMP dark matter. The first is the fact that the spectra  
2605 of produced antinuclei is very relevant for their propagation and for the signal to  
2606 background ratio in this detection channel. Furthermore, the lack of any indication  
2607 of the temperature of this process makes it highly challenging to predict the yields  
2608 produced.

---

**References**

2609

- [1] M. Cirelli, G. Corcella, A. Hektor, G. Hütsi, M. Kadastik, P. Panci, M. Raidal, F. Sala, and A. Strumia, “PPPC 4 DM ID: a poor particle physicist cookbook for dark matter indirect detection,” *Journal of Cosmology and Astroparticle Physics*, vol. 2011, pp. 051–051, mar 2011.
- [2] M. Korsmeier, F. Donato, and N. Fornengo, “Prospects to verify a possible dark matter hint in cosmic antiprotons with antideuterons and antihelium,” *Phys. Rev.*, vol. D97, no. 10, p. 103011, 2018.
- [3] P. von Doetinchem *et al.*, “Cosmic-ray Antinuclei as Messengers of New Physics: Status and Outlook for the New Decade,” 2 2020.
- [4] A. Ibarra and S. Wild, “Prospects of antideuteron detection from dark matter annihilations or decays at AMS-02 and GAPS,” *JCAP*, vol. 1302, p. 021, 2013.
- [5] J. Schwichtenberg, *Physics from Symmetry*. Springer, 2018.
- [6] E. Eichten, K. Gottfried, T. Kinoshita, J. Kogut, K. D. Lane, and T. M. Yan, “Spectrum of charmed quark-antiquark bound states,” *Phys. Rev. Lett.*, vol. 34, pp. 369–372, Feb 1975.
- [7] G. Parisi, R. Petronzio, and F. Rapuano, “A measurement of the string tension near the continuum limit,” *Physics Letters B*, vol. 128, no. 6, pp. 418–420, 1983.
- [8] “Quark confinement graphic.” [https://en.wikipedia.org/wiki/File:Quark\\_confinement.svg](https://en.wikipedia.org/wiki/File:Quark_confinement.svg). Accessed: 2022-11-07.
- [9] E. Noether, “Invariante variationsprobleme,” *Nachrichten von der Gesellschaft der Wissenschaften zu Göttingen, Mathematisch-Physikalische Klasse*, vol. 1918, pp. 235–257, 1918.
- [10] A. Pich, “CP violation; 1993 ed.,” *ICTP Ser. Theor. Phys.*, vol. 10, pp. 14–42, 1993.
- [11] J. H. Christenson, J. W. Cronin, V. L. Fitch, and R. Turlay, “Evidence for the  $2\pi$  decay of the  $k_2^0$  meson,” *Phys. Rev. Lett.*, vol. 13, pp. 138–140, Jul 1964.
- [12] A. Alavi-Harati, I. F. Albuquerque, T. Alexopoulos, M. Arenton, K. Arisaka, S. Averitte, A. R. Barker, L. Bellantoni, A. Bellavance, J. Belz, R. Ben-David, D. R. Bergman, E. Blucher, G. J. Bock, C. Bown, S. Bright, E. Cheu, S. Childress, R. Coleman, M. D. Corcoran, G. Corti, B. Cox, M. B. Crisler, A. R. Erwin, R. Ford, A. Glazov, A. Golossanov, G. Graham, J. Graham, K. Hagan, E. Halkiadakis, K. Hanagaki, S. Hidaka, Y. B. Hsiung, V. Jejer, J. Jennings, D. A. Jensen,

2640

- 2641 R. Kessler, H. G. E. Kobrak, J. LaDue, A. Lath, A. Ledovskoy, P. L. McBride, A. P.  
2642 McManus, P. Mikelsons, E. Monnier, T. Nakaya, U. Nauenberg, K. S. Nelson,  
2643 H. Nguyen, V. O'Dell, M. Pang, R. Pordes, V. Prasad, C. Qiao, B. Quinn, E. J. Ram-  
2644 berg, R. E. Ray, A. Roodman, M. Sadamoto, S. Schnetzer, K. Senyo, P. Shanahan,  
2645 P. S. Shawhan, W. Slater, N. Solomey, S. V. Somalwar, R. L. Stone, I. Suzuki, E. C.  
2646 Swallow, R. A. Swanson, S. A. Taegar, R. J. Tesarek, G. B. Thomson, P. A. Toale,  
2647 A. Tripathi, R. Tschirhart, Y. W. Wah, J. Wang, H. B. White, J. Whitmore, B. Win-  
2648 stein, R. Winston, J.-Y. Wu, T. Yamanaka, and E. D. Zimmerman, "Observation  
2649 of direct cp violation in  $k_s^0$  decays," *Physical Review Letters*, vol. 83, pp. 22–27,  
2650 jul 1999.
- 2651 [13] R. Aaij and et.al., "First observation of cp violation in the decays of  $b_s^0$  mesons,"  
2652 *Physical Review Letters*, vol. 110, may 2013.
- 2653 [14] R. Aaij and et.al., "Observation of cp violation in charm decays," *Physical*  
2654 *Review Letters*, vol. 122, may 2019.
- 2655 [15] V. A. Kostelecký and N. Russell, "Data tables for lorentz and cp violation,"  
2656 *Reviews of Modern Physics*, vol. 83, pp. 11–31, mar 2011.
- 2657 [16] A. Kostelecky, "The status of cpt," 1998.
- 2658 [17] G. 't Hooft, "Computation of the quantum effects due to a four-dimensional  
2659 pseudoparticle," *Phys. Rev. D*, vol. 14, pp. 3432–3450, Dec 1976.
- 2660 [18] K. Choi, S. H. Im, and C. S. Shin, "Recent progress in the physics of axions and  
2661 axion-like particles," *Annual Review of Nuclear and Particle Science*, vol. 71,  
2662 pp. 225–252, sep 2021.
- 2663 [19] D. A. Kirzhnits and A. D. Linde, "Macroscopic Consequences of the Weinberg  
2664 Model," *Phys. Lett. B*, vol. 42, pp. 471–474, 1972.
- 2665 [20] L. C. P. Van Hove, "Theoretical prediction of a new state of matter, the "quark-  
2666 gluon plasma" (also called "quark matter")," 1987.
- 2667 [21] P. Braun-Munzinger, V. Koch, T. Schäfer, and J. Stachel, "Properties of hot and  
2668 dense matter from relativistic heavy ion collisions," *Physics Reports*, vol. 621,  
2669 pp. 76–126, mar 2016.
- 2670 [22] "Timeline of the universe." <https://map.gsfc.nasa.gov/media/060915/index.html>. NASA, Accessed: 2022-11-07.  
2671
- 2672 [23] A. Ibarra, "Neutrinos and dark matter," *AIP Conference Proceedings*, vol. 1666,  
2673 no. 1, p. 140004, 2015.

- 2674 [24] K. M. Ferrière, “The interstellar environment of our galaxy,” *Reviews of Modern*  
2675 *Physics*, vol. 73, pp. 1031–1066, dec 2001.
- 2676 [25] F. Nicastro, S. Mathur, and M. Elvis, “Missing baryons and the warm-hot inter-  
2677 galactic medium,” *Science*, vol. 319, pp. 55–57, jan 2008.
- 2678 [26] V. Schönfelder, “Gamma ray astronomy and search for antimatter in the uni-  
2679 verse,” *Hyperfine Interactions*, vol. 44, pp. 85–96, Mar 1989.
- 2680 [27] R. Aaij and et. al., “Measurement of CP asymmetry in  $D^0 \rightarrow K^+ K^-$  decays,” *Physics*  
2681 *Letters B*, vol. 767, pp. 177–187, apr 2017.
- 2682 [28] M. Ahmadi, et. al., and T. A. Collaboration, “Investigation of the fine structure  
2683 of antihydrogen,” *Nature*, vol. 578, pp. 375–380, Feb 2020.
- 2684 [29] A. D. Sakharov, “Violation of CP Invariance, C asymmetry, and baryon asym-  
2685 metry of the universe,” *Pisma Zh. Eksp. Teor. Fiz.*, vol. 5, pp. 32–35, 1967.
- 2686 [30] G. R. Farrar and M. E. Shaposhnikov, “Baryon asymmetry of the universe in  
2687 the minimal standard model,” *Physical Review Letters*, vol. 70, pp. 2833–2836,  
2688 may 1993.
- 2689 [31] A. Santamaria, “Masses, mixings, yukawa couplings and their symmetries,”  
2690 *Physics Letters B*, vol. 305, no. 1, pp. 90–97, 1993.
- 2691 [32] V. Q. Phong, P. H. Kiem, N. P. D. Loc, and H. N. Long, “Sphaleron in the first-  
2692 order electroweak phase transition with the dimension-six higgs field operator,”  
2693 *Physical Review D*, vol. 101, jun 2020.
- 2694 [33] A. Papaefstathiou, S. Plätzer, and K. Sakurai, “On the phenomenology of  
2695 sphaleron-induced processes at the LHC and beyond,” *Journal of High Energy*  
2696 *Physics*, vol. 2019, dec 2019.
- 2697 [34] J.-M. Richard, “Antiproton physics,” *Frontiers in Physics*, vol. 8, jan 2020.
- 2698 [35] B. El-Bennich, M. Lacombe, B. Loiseau, and S. Wycech, “Paris  $n\bar{N}$  potential  
2699 constrained by recent antiprotonic-atom data and  $\bar{n}p$  total cross sections,”  
2700 *Phys. Rev. C*, vol. 79, p. 054001, May 2009.
- 2701 [36] L. C. Tan and L. K. Ng, “Calculation of the equilibrium antiproton spectrum,”  
2702 *Journal of Physics G: Nuclear Physics*, vol. 9, p. 227, feb 1983.
- 2703 [37] A. Galoyan, A. Ribon, and V. Uzhinsky, “Dynamics of Anti-Proton–Protons and  
2704 Anti-Proton–Nucleus Reactions,” *Nucl. Theor.*, vol. 35, pp. 194–202, 2016.

- 2705 [38] A. Galoyan, “Dynamics of interactions of anti-protons and anti-nuclei with  
2706 nuclei in Geant4,” *PoS*, vol. BaldinISHEPPXXII, p. 049, 2015.
- 2707 [39] T. Regge, “Introduction to complex orbital momenta,” *Il Nuovo Cimento (1955-*  
2708 *1965)*, vol. 14, pp. 951–976, Dec 1959.
- 2709 [40] V. Flaminio, W. G. Moorhead, D. R. O. Morrison, and N. Rivoire, *Compilation of*  
2710 *cross-sections*. Geneva: CERN, 1984. Updated version of CERN HERA 79-03;  
2711 contains all data published up to the beginning of 1982.
- 2712 [41] C. Amsler and F. Myhrer, “Low energy antiproton physics,” *Annual Review of*  
2713 *Nuclear and Particle Science*, vol. 41, no. 1, pp. 219–267, 1991.
- 2714 [42] V. Franco and R. J. Glauber, “High-energy deuteron cross sections,” *Phys. Rev.*,  
2715 vol. 142, pp. 1195–1214, Feb 1966.
- 2716 [43] V. Grichine, “Integral cross-sections of light nuclei in the glauber-gribov repre-  
2717 sentation,” *Nuclear Instruments and Methods in Physics Research Section B:*  
2718 *Beam Interactions with Materials and Atoms*, vol. 427, pp. 60–62, 2018.
- 2719 [44] V. Uzhinsky, J. Apostolakis, A. Galoyan, G. Folger, V. Grichine, V. Ivanchenko,  
2720 and D. Wright, “Antinucleus–nucleus cross sections implemented in geant4,”  
2721 *Physics Letters B*, vol. 705, no. 3, pp. 235–239, 2011.
- 2722 [45] S. P. Denisov *et al.*, “Measurements of anti-deuteron absorption and stripping  
2723 cross sections at the momentum 13.3 GeV/c,” *Nucl. Phys.*, vol. B31, pp. 253–  
2724 260, 1971.
- 2725 [46] F. G. Binon *et al.*, “Absorption cross-sections of 25 GeV/c antideuterons in Li,  
2726 C, Al, Cu and Pb,” *Phys. Lett.*, vol. 31B, pp. 230–232, 1970.
- 2727 [47] V. Uzhinsky *et al.*, “Antinucleus-nucleus cross sections implemented in  
2728 GEANT4,” *Phys. Lett.*, vol. B705, pp. 235–239, 2011.
- 2729 [48] S. Acharya *et al.*, “Production of  ${}^4\text{He}$  and  ${}^4\overline{\text{He}}$  in Pb-Pb collisions at  $\sqrt{s_{\text{NN}}} =$   
2730 2.76 TeV at the LHC,” *Nucl. Phys.*, vol. A971, pp. 1–20, 2018.
- 2731 [49] M. Kachelrieß, S. Ostapchenko, and J. Tjemsland, “Alternative coalescence  
2732 model for deuteron, tritium, helium-3 and their antinuclei,” *Eur. Phys. J. A*,  
2733 vol. 56, no. 1, p. 4, 2020.
- 2734 [50] K. Blum and M. Takimoto, “Nuclear coalescence from correlation functions,”  
2735 *Physical Review C*, vol. 99, apr 2019.

- 2736 [51] S. Acharya and et. al., “Production of light (anti)nuclei in pp collisions at  $\sqrt{s} = 13$  TeV,” *Journal of High Energy Physics*, vol. 2022, jan 2022.  
2737
- 2738 [52] M. Kachelriess, S. Ostapchenko, and J. Tjemsland, “Revisiting cosmic ray antinuclei fluxes with a new coalescence mode,” 2020.  
2739
- 2740 [53] L. Zhu, C. M. Ko, and X. Yin, “Light (anti-)nuclei production and flow in relativistic heavy-ion collisions,” *Phys. Rev. C*, vol. 92, p. 064911, Dec 2015.  
2741
- 2742 [54] C. D. Anderson, “The apparent existence of easily deflectable positives,” *Science*, vol. 76, no. 1967, pp. 238–239, 1932.  
2743
- 2744 [55] R. L. Golden, S. Horan, B. G. Mauger, G. D. Badhwar, J. L. Lacy, S. A. Stephens, R. R. Daniel, and J. E. Zipse, “Evidence for the existence of cosmic-ray antiprotons,” *Phys. Rev. Lett.*, vol. 43, pp. 1196–1199, Oct 1979.  
2745  
2746
- 2747 [56] E. A. Bogomolov, N. D. Lubyanyaya, V. A. Romanov, S. V. Stepanov, and M. S. Shulakova, “A STRATOSPHERIC MAGNETIC SPECTROMETER INVESTIGATION OF THE SINGLY CHARGED COMPONENT SPECTRA AND COMPOSITION OF THE PRIMARY AND SECONDARY COSMIC RADIATION.,” in *16th International Cosmic Ray Conference*, pp. 330–335, 1979.  
2748  
2749  
2750  
2751
- 2752 [57] P. von Doetinchem, K. Perez, T. Aramaki, S. Baker, S. Barwick, R. Bird, M. Boezio, S. Boggs, M. Cui, A. Datta, F. Donato, C. Evoli, L. Fabris, L. Fabbietti, E. F. Bueno, N. Fornengo, H. Fuke, C. Gerrity, D. G. Coral, C. Hailey, D. Hooper, M. Kachelriess, M. Korsmeier, M. Kozai, R. Lea, N. Li, A. Lowell, M. Manghisoni, I. Moskalenko, R. Munini, M. Naskret, T. Nelson, K. Ng, F. Nozzoli, A. Oliva, R. Ong, G. Osteria, T. Pierog, V. Poulin, S. Profumo, T. Pöschl, S. Quinn, V. Re, F. Rogers, J. Ryan, N. Saffold, K. Sakai, P. Salati, S. Schael, L. Serksnyte, A. Shukla, A. Stoessl, J. Tjemsland, E. Vannuccini, M. Vecchi, M. Winkler, D. Wright, M. Xiao, W. Xu, T. Yoshida, G. Zampa, and P. Zuccon, “Cosmic-ray antinuclei as messengers of new physics: status and outlook for the new decade,” *Journal of Cosmology and Astroparticle Physics*, vol. 2020, pp. 035–035, aug 2020.  
2753  
2754  
2755  
2756  
2757  
2758  
2759  
2760  
2761  
2762  
2763
- 2764 [58] M. Hütten and D. Kerszberg, “TeV dark matter searches in the extragalactic gamma-ray sky,” *Galaxies*, vol. 10, p. 92, aug 2022.  
2765
- 2766 [59] F. Calore, M. Cirelli, L. DEROME, Y. Genolini, D. Maurin, P. Salati, and P. D. Serpico, “AMS-02 antiprotons and dark matter: Trimmed hints and robust bounds,” *SciPost Physics*, vol. 12, may 2022.  
2767  
2768

- 2769 [60] J. Heisig, M. Korsmeier, and M. W. Winkler, “Dark matter or correlated errors:  
2770 Systematics of the AMS-02 antiproton excess,” *Physical Review Research*, vol. 2,  
2771 oct 2020.
- 2772 [61] N. Xu, “An overview of STAR experimental results,” *Nuclear Physics A*, vol. 931,  
2773 pp. 1–12, nov 2014.
- 2774 [62] M. J. Boschini *et al.*, “Solution of heliospheric propagation: unveiling the local  
2775 interstellar spectra of cosmic ray species,” *Astrophys. J.*, vol. 840, no. 2, p. 115,  
2776 2017.
- 2777 [63] M. J. Boschini *et al.*, “Deciphering the Local Interstellar Spectra of Primary  
2778 Cosmic-Ray Species with HelMod,” *Astrophys. J.*, vol. 858, no. 1, p. 61, 2018.
- 2779 [64] T. Massam, T. Müller, B. Righini, M. Schneegans, and A. Zichichi, “Experimental  
2780 observation of antideuteron production,” *Nuovo Cimento*, vol. 39, pp. 10–14,  
2781 1965.
- 2782 [65] S. Acharya *et al.*, “Production of light (anti)nuclei in pp collisions at  $\sqrt{s} = 13$   
2783 TeV,” *JHEP*, vol. 01, p. 106, 2022.
- 2784 [66] S. Acharya *et al.*, “Production of light (anti)nuclei in pp collisions at  $\sqrt{s} = 5.02$   
2785 TeV,” 12 2021.
- 2786 [67] J. Adam *et al.*, “Production of light nuclei and anti-nuclei in pp and Pb-Pb  
2787 collisions at energies available at the CERN Large Hadron Collider,” *Phys. Rev.*,  
2788 vol. C93, no. 2, p. 024917, 2016.
- 2789 [68] S. Acharya *et al.*, “Production of deuterons, tritons,  $^3\text{He}$  nuclei and their anti-  
2790 nuclei in pp collisions at  $\sqrt{s} = 0.9, 2.76$  and 7 TeV,” *Phys. Rev.*, vol. C97, no. 2,  
2791 p. 024615, 2018.
- 2792 [69] Y.-G. Ma, “Observation of antimatter nuclei at rhic-star,” *Journal of Physics:*  
2793 *Conference Series*, vol. 420, p. 012036, mar 2013.
- 2794 [70] K. Aamodt and et.al., “Midrapidity antiproton-to-proton ratio in  $pp$  collisions  
2795 at  $\sqrt{s} = 0.9$  and 7 tev measured by the alice experiment,” *Phys. Rev. Lett.*,  
2796 vol. 105, p. 072002, Aug 2010.
- 2797 [71] E. Abbas and T. A. Collaboration, “Mid-rapidity anti-baryon to baryon ratios  
2798 in pp collisions at  $\sqrt{s} = 0.9/2.76$  and 7 tev measured by alice,” *The European*  
2799 *Physical Journal C*, vol. 73, p. 2496, Jul 2013.



- 2800 [72] S. Acharya and et. al., “Multiplicity dependence of light (anti-)nuclei produc-  
2801 tion in p–pb collisions at  $\sqrt{s_{NN}}=5.02$  tev,” *Physics Letters B*, vol. 800, p. 135043,  
2802 2020.
- 2803 [73] F. Zwicky *Helvetica Physica Acta*, vol. 6, pp. 110–127, 1933.
- 2804 [74] R. L. Workman and Others, “Review of Particle Physics,” *PTEP*, vol. 2022,  
2805 p. 083C01, 2022.
- 2806 [75] T. C. Planck vol. 641, p. A6, sep 2020.
- 2807 [76] J. G. de Swart, G. Bertone, and J. van Dongen, “How dark matter came to  
2808 matter,” *Nature Astronomy*, vol. 1, mar 2017.
- 2809 [77] J. P. Ostriker, P. J. E. Peebles, and A. Yahil, “The Size and Mass of Galaxies, and  
2810 the Mass of the Universe,” , vol. 193, p. L1, Oct. 1974.
- 2811 [78] I. Ablimit, G. Zhao, C. Flynn, and S. A. Bird, “The Rotation Curve, Mass Distri-  
2812 bution and Dark Matter Content of the Milky Way from Classical Cepheids,”  
2813 *Astrophys. J.*, vol. 895, no. 1, p. L12, 2020.
- 2814 [79] Y. Sofue, “Rotation and mass in the milky way and spiral galaxies,” *Publications*  
2815 *of the Astronomical Society of Japan*, vol. 69, p. R1, dec 2016.
- 2816 [80] J.-P. Kneib and P. Natarajan, “Cluster lenses,” *The Astronomy and Astrophysics*  
2817 *Review*, vol. 19, nov 2011.
- 2818 [81] Koppelman, Helmer H. and Helmi, Amina, “Determination of the escape  
2819 velocity of the milky way using a halo sample selected based on proper motion,”  
2820 *A&A*, vol. 649, p. A136, 2021.
- 2821 [82] S. P. Martin, “A supersymmetry primer,” 1997.
- 2822 [83] H. Baer, K.-Y. Choi, J. E. Kim, and L. Roszkowski, “Dark matter production  
2823 in the early universe: Beyond the thermal wimp paradigm,” *Physics Reports*,  
2824 vol. 555, pp. 1–60, 2015. Dark matter production in the early Universe: Beyond  
2825 the thermal WIMP paradigm.
- 2826 [84] T. Padmanabhan, *Structure formation in the universe*. Cambridge Univ. Press,  
2827 1999.
- 2828 [85] R. D. Peccei and H. R. Quinn, “CP conservation in the presence of pseudopar-  
2829 ticles,” *Phys. Rev. Lett.*, vol. 38, pp. 1440–1443, Jun 1977.
- 2830 [86] S. Weinberg, “A new light boson?,” *Phys. Rev. Lett.*, vol. 40, pp. 223–226, Jan  
2831 1978.

- 2832 [87] M. Danilov, “Review of sterile neutrino searches at very short-baseline reactor  
2833 experiments,” *Physica Scripta*, vol. 97, p. 094001, aug 2022.
- 2834 [88] S. W. HAWKING, “Black hole explosions?,” *Nature*, vol. 248, pp. 30–31, Mar  
2835 1974.
- 2836 [89] M. VISSER, “ESSENTIAL AND INESSENTIAL FEATURES OF HAWKING RADI-  
2837 ATION,” *International Journal of Modern Physics D*, vol. 12, pp. 649–661, apr  
2838 2003.
- 2839 [90] E. Aprile and et.al., “Xenon1t dark matter data analysis: Signal reconstruction,  
2840 calibration, and event selection,” *Phys. Rev. D*, vol. 100, p. 052014, Sep 2019.
- 2841 [91] S. Akerib and et.al., “Extending light WIMP searches to single scintillation  
2842 photons in LUX,” *Physical Review D*, vol. 101, feb 2020.
- 2843 [92] P. A. M. Dirac, “Quantised singularities in the electromagnetic field,,” *Proceed-  
2844 ings of the Royal Society of London. Series A, Containing Papers of a Mathemat-  
2845 ical and Physical Character*, vol. 133, no. 821, pp. 60–72, 1931.
- 2846 [93] G. Collaboration, “Final results of gerda on the search for neutrinoless double-  
2847  $\beta$  decay,” *Phys. Rev. Lett.*, vol. 125, p. 252502, Dec 2020.
- 2848 [94] T. Bringmann, P. F. Depta, M. Hufnagel, and K. Schmidt-Hoberg, “Precise  
2849 dark matter relic abundance in decoupled sectors,” *Physics Letters B*, vol. 817,  
2850 p. 136341, jun 2021.
- 2851 [95] E. Aprile and et.al., “Search for new physics in electronic recoil data from  
2852 xenonnt,” *Phys. Rev. Lett.*, vol. 129, p. 161805, Oct 2022.
- 2853 [96] J. Conrad and O. Reimer, “Indirect dark matter searches in gamma and cosmic  
2854 rays,” *Nature Physics*, vol. 13, pp. 224–231, Mar 2017.
- 2855 [97] T. A. Collaboration, “The alice experiment at the cern lhc,” *Journal of Instru-  
2856 mentation*, vol. 3, p. S08002, aug 2008.
- 2857 [98] J. Alme, Y. Andres, H. Appelshäuser, S. Bablok, N. Bialas, R. Bolgen, U. Bonnes,  
2858 R. Bramm, P. Braun-Munzinger, R. Campagnolo, P. Christiansen, A. Dobrin,  
2859 C. Engster, D. Fehlker, Y. Foka, U. Frankenfeld, J. Gaardhøje, C. Garabatos,  
2860 P. Glässel, C. G. Gutierrez, P. Gros, H.-A. Gustafsson, H. Helstrup, M. Hoch,  
2861 M. Ivanov, R. Janik, A. Junique, A. Kalweit, R. Keidel, S. Kniege, M. Kowalski,  
2862 D. Larsen, Y. Lesenechal, P. Lenoir, N. Lindegaard, C. Lippmann, M. Mager,  
2863 M. Mast, A. Matyja, M. Munkejord, L. Musa, B. Nielsen, V. Nikolic, H. Oeschler,

- 2864 E. Olsen, A. Oskarsson, L. Osterman, M. Pikna, A. Rehman, G. Renault, R. Ren-  
2865 ford, S. Rossegger, D. Röhrich, K. Røed, M. Richter, G. Rueshmann, A. Rybicki,  
2866 H. Sann, H.-R. Schmidt, M. Siska, B. Sitár, C. Soegaard, H.-K. Soltveit, D. Soyk,  
2867 J. Stachel, H. Stelzer, E. Stenlund, R. Stock, P. Strmeň, I. Szarka, K. Ullaland,  
2868 D. Vranic, R. Veenhof, J. Westergaard, J. Wiechula, and B. Windelband, “The AL-  
2869 ICE TPC, a large 3-dimensional tracking device with fast readout for ultra-high  
2870 multiplicity events,” *Nuclear Instruments and Methods in Physics Research*  
2871 *Section A: Accelerators, Spectrometers, Detectors and Associated Equipment*,  
2872 vol. 622, pp. 316–367, oct 2010.
- 2873 [99] “Real-time data processing in the alice high level trigger at the lhc,” *Computer*  
2874 *Physics Communications*, vol. 242, pp. 25–48, 2019.
- 2875 [100] *ALICE Time-Of-Flight system (TOF): Technical Design Report*. Technical design  
2876 report. ALICE, Geneva: CERN, 2000.
- 2877 [101] J. Adam *et al.*, “Determination of the event collision time with the ALICE  
2878 detector at the LHC,” *Eur. Phys. J. Plus*, vol. 132, no. 2, p. 99, 2017.
- 2879 [102] K. Aamodt *et al.*, “Midrapidity antiproton-to-proton ratio in pp collisions  
2880 at  $\sqrt{s} = 0.9$  and 7 TeV measured by the ALICE experiment,” *Phys. Rev. Lett.*,  
2881 vol. 105, p. 072002, 2010.
- 2882 [103] S. Agostinelli *et al.*, “GEANT4—a simulation toolkit,” *Nucl. Instrum. Meth. A*,  
2883 vol. 506, pp. 250–303, 2003.
- 2884 [104] J. Allison *et al.*, “Recent developments in Geant4,” *Nucl. Instrum. Meth. A*,  
2885 vol. 835, pp. 186–225, 2016.
- 2886 [105] S. Acharya *et al.*, “Measurement of the low-energy antideuteron inelastic cross  
2887 section,” *Phys. Rev. Lett.*, vol. 125, no. 16, p. 162001, 2020.
- 2888 [106] V. Franco and R. J. Glauber, “High-energy deuteron cross sections,” *Phys. Rev.*,  
2889 vol. 142, pp. 1195–1214, Feb 1966.
- 2890 [107] D. Morton, Q. Wu, and G. Drake, “Nuclear charge radius for he3,” *Physical*  
2891 *Review A - PHYS REVA*, vol. 73, 03 2006.
- 2892 [108] E. Abbas and et.al., “Mid-rapidity anti-baryon to baryon ratios in pp collisions  
2893 at  $\sqrt{s} = 0.9, 2.76$  and 7 TeV measured by ALICE,” *The*  
2894 *European Physical Journal C*, vol. 73, jul 2013.
- 2895 [109] J. H. Lambert, *Photometria sive de mensura et gradibus luminis, colorum et*  
2896 *umbræ by Lambert, Johann Heinrich*. Augustae Vindelicorum : sumptibus  
2897 viduae Eberhardi Klett typis Chistophori Petri Detleffsen, 1760.

- 2898 [110] S. Acharya *et al.*, “First measurement of the absorption of  ${}^3\overline{\text{He}}$  nuclei in matter  
2899 and impact on their propagation in the galaxy,” 2022.
- 2900 [111] “Performance of the ALICE experiment at the CERN LHC,” *International Jour-*  
2901 *nal of Modern Physics A*, vol. 29, p. 1430044, sep 2014.
- 2902 [112] “Modelling of Antihelium-3 Cosmic-Ray Propagation,” 2022.
- 2903 [113] “Validation of the ALICE material budget between TPC and TOF detectors,”  
2904 2022.
- 2905 [114] R. Barlow, “Systematic errors: Facts and fictions,” in *Conference on Advanced*  
2906 *Statistical Techniques in Particle Physics*, pp. 134–144, 7 2002.
- 2907 [115] H. Hahn, E. Forsyth, H. Foelsche, M. Harrison, J. Kewisch, G. Parzen, S. Peggs,  
2908 E. Raka, A. Ruggiero, A. Stevens, S. Tepikian, P. Thieberger, D. Trbojevic, J. Wei,  
2909 E. Willen, S. Ozaki, and S. Lee, “The rhic design overview,” *Nuclear Instru-*  
2910 *ments and Methods in Physics Research Section A: Accelerators, Spectrometers,*  
2911 *Detectors and Associated Equipment*, vol. 499, pp. 245–263, 03 2003.
- 2912 [116] A. Collaboration, “Measurement of  ${}^3\overline{\text{He}}$  hadronic interaction cross-section in  
2913 pb-pb collisions,” 2021. ALICE internal Analysis note, ANA-1106.
- 2914 [117] S. Ting, “The first five years of the alpha magnetic spectrometer on the inter-  
2915 national space station.”
- 2916 [118] J. Sokol, “Sam ting’s last tease,” *Science*, vol. 356, no. 6335, pp. 240–241, 2017.
- 2917 [119] S. Lu, “Cosmic ray antideuteron search with alpha magnetic spectrometer  
2918 (ams),” *Munich Insitute for Particle and Astrophysics - Workshop on antinuclei*  
2919 *in cosmic rays 2022*, 2022.
- 2920 [120] A. W. Strong, I. V. Moskalenko, and V. S. Ptuskin, “Cosmic-Ray Propagation  
2921 and Interactions in the Galaxy,” *Annual Review of Nuclear and Particle Science*,  
2922 vol. 57, pp. 285–327, Nov. 2007.
- 2923 [121] L. Šerkšnytė *et al.*, “Reevaluation of the cosmic antideuteron flux from cosmic-  
2924 ray interactions and from exotic sources,” *Phys. Rev. D*, vol. 105, no. 8, p. 083021,  
2925 2022.
- 2926 [122] V. Poulin, P. Salati, I. Cholis, M. Kamionkowski, and J. Silk, “Where do the  
2927 ams-02 antihelium events come from?,” *Phys. Rev. D*, vol. 99, p. 023016, Jan  
2928 2019.

- 2929 [123] A. Coogan and S. Profumo, “Origin of the tentative AMS antihelium events,”  
2930 *Physical Review D*, vol. 96, oct 2017.
- 2931 [124] M. Aguilar and et. al., “Precision measurement of the boron to carbon flux  
2932 ratio in cosmic rays from 1.9 gv to 2.6 tv with the alpha magnetic spectrometer  
2933 on the international space station,” *Phys. Rev. Lett.*, vol. 117, p. 231102, Nov  
2934 2016.
- 2935 [125] D. D. Clayton, *Principles of stellar evolution and nucleosynthesis*. University of  
2936 Chicago Press, 1983.
- 2937 [126] E. M. Burbidge, G. R. Burbidge, W. A. Fowler, and F. Hoyle, “Synthesis of the  
2938 elements in stars,” *Rev. Mod. Phys.*, vol. 29, pp. 547–650, Oct 1957.
- 2939 [127] T. C. FermiLAT, “Incremental Fermi Large Area Telescope Fourth Source Cata-  
2940 log,” , vol. 260, p. 53, June 2022.
- 2941 [128] T. Bringmann and C. Weniger, “Gamma ray signals from dark matter: Concepts,  
2942 status and prospects,” *Physics of the Dark Universe*, vol. 1, no. 1, pp. 194–217,  
2943 2012. Next Decade in Dark Matter and Dark Energy.
- 2944 [129] A. Shukla, A. Datta, P. von Doetinchem, D.-M. Gomez-Coral, and C. Kanitz,  
2945 “Large-scale simulations of antihelium production in cosmic-ray interactions,”  
2946 *Physical Review D*, vol. 102, sep 2020.
- 2947 [130] D.-M. Gomez-Coral, A. M. Rocha, V. Grabski, A. Datta, P. von Doetinchem, and  
2948 A. Shukla, “Deuteron and antideuteron production simulation in cosmic-ray  
2949 interactions,” *Physical Review D*, vol. 98, jul 2018.
- 2950 [131] A. N. Diddens, W. Galbraith, E. Lillethun, G. Manning, A. G. Parham, A. E.  
2951 Taylor, T. G. Walker, and A. M. Wetherell, “Particle production in proton-proton  
2952 collisions at 19 and 24 gev/c,” *Il Nuovo Cimento (1955-1965)*, vol. 31, pp. 961–  
2953 973, Mar 1964.
- 2954 [132] V. V. Abramov *et al.*, “High  $p_T$  Deuteron and Anti-deuteron Production in  $pp$   
2955 and  $p$  a Collisions at 70-GeV,” *Sov. J. Nucl. Phys.*, vol. 45, p. 845, 1987.
- 2956 [133] W. Bozzoli, A. Bussière, G. Giacomelli, E. Lesquoy, R. Meunier, L. Moscoso,  
2957 A. Muller, F. Rimondi, and S. Zylberajch, “Production of d, t, 3he, d, t and 3he  
2958 by 200 gev protons,” *Nuclear Physics B*, vol. 144, no. 2, pp. 317–328, 1978.
- 2959 [134] J. W. Cronin, H. J. Frisch, M. J. Shochet, J. P. Boymond, P. A. Piroué, and R. L.  
2960 Sumner, “Production of hadrons at large transverse momentum at 200, 300,  
2961 and 400 gev,” *Phys. Rev. D*, vol. 11, pp. 3105–3123, Jun 1975.

- 2962 [135] A. Bussi re, G. Giacomelli, E. Lesquoy, R. Meunier, L. Moscoso, A. Muller,  
2963 F. Rimondi, S. Zucchelli, and S. Zylberajch, “Particle production and search  
2964 for long-lived particles in 200–240 gev/c proton-nucleon collisions,” *Nuclear*  
2965 *Physics B*, vol. 174, no. 1, pp. 1–15, 1980.
- 2966 [136] B. Alper, H. Bgild, P. Booth, F. Bulos, L. Carroll, G. von Dardel, G. Damgaard,  
2967 B. Duff, F. Heymann, J. Jackson, G. Jarlskog, L. Jonsson, A. Klovning, L. Leistam,  
2968 E. Lillethun, G. Lynch, G. Manning, M. Prentice, D. Quarrie, and J. Weiss, “Large  
2969 angle production of stable particles heavier than the proton and a search for  
2970 quarks at the cern intersecting storage rings,” *Physics Letters B*, vol. 46, no. 2,  
2971 pp. 265–268, 1973.
- 2972 [137] W. M. Gibson, A. Duane, H. Newman, H. Ogren, S. Henning, G. Jarlskog, R. Little,  
2973 T. Sanford, S. L. Wu, H. B ggild, B. G. Duff, K. Guettler, M. N. Prentice, S. J. Shar-  
2974 rock, and B.-S.-M. Collaboration, “Production of deuterons and antideuterons  
2975 in proton-proton collisions at the cern isr,” *Lettere al Nuovo Cimento (1971-*  
2976 *1985)*, vol. 21, pp. 189–194, Feb 1978.
- 2977 [138] M. Albrow, D. Barber, P. Benz, B. Bošnjakovi c, J. Brooks, C. Chang, A. Clegg,  
2978 F. Ern , P. Kooijman, F. Loebinger, N. McCubbin, P. Murphy, A. Rudge, J. Sens,  
2979 A. Sessoms, J. Singh, and J. Timmer, “Search for stable particles of charge 1  
2980 and mass deuteron mass,” *Nuclear Physics B*, vol. 97, no. 2, pp. 189–200, 1975.
- 2981 [139] E. Serradilla Rodr guez, *Producci n de n cleos de deuterio y antideuterio en*  
2982 *el experimento Alice del LHC*. PhD thesis, UCM, Madrid, Dept. Phys., UCM,  
2983 Madrid, Dept. Phys., 2014.
- 2984 [140] S. Acharya and et. al., “Production of deuterons, tritons, <sup>3</sup>He nuclei, and their  
2985 antinuclei in *pp* collisions at  $\sqrt{s} = 0.9, 2.76, \text{ and } 7 \text{ tev}$ ,” *Phys. Rev. C*, vol. 97,  
2986 p. 024615, Feb 2018.
- 2987 [141] T. A. Collaboration, “Production of light nuclei and anti-nuclei in *pp* and *pb-*  
2988 *pb* collisions at energies available at the cern large hadron collider,” *Phys. Rev.*  
2989 *C*, vol. 93, p. 024917, Feb 2016.
- 2990 [142] T. P schl, *Modeling of the Galactic Cosmic-Ray Antiproton Flux and Devel-*  
2991 *opment of a Multi-Purpose Active-Target Particle Telescope for Cosmic Rays*.  
2992 Dissertation, Technische Universit t M nchen, M nchen, 2022.
- 2993 [143] F. Riek, R. Rapp, Y. Oh, and T.-S. H. Lee, “Medium modifications  
2994 of themml:math xmlns:mml="http://www.w3.org/1998/math/MathML"  
2995 display="inline"mml:mrowmml:mi/mml:mi/mml:mrow/mml:mathmeson in  
2996 nuclear photoproduction,” *Physical Review C*, vol. 82, jul 2010.

- 2997 [144] M. W. Winkler and T. Linden, “Dark matter annihilation can produce a de-  
2998 tectable antihelium flux through  $\Lambda_b$  decays,” *Physical Review Letters*, vol. 126,  
2999 mar 2021.
- 3000 [145] C. Bierlich, S. Chakraborty, N. Desai, L. Gellersen, I. Helenius, P. Ilten,  
3001 L. Lönnblad, S. Mrenna, S. Prestel, C. T. Preuss, T. Sjöstrand, P. Skands,  
3002 M. Uthheim, and R. Verheyen, “A comprehensive guide to the physics and usage  
3003 of pythia 8.3,” 2022.
- 3004 [146] K. Werner, L. Karpenko, M. Bleicher, and T. Pierog, “The Physics of EPOS,” *EPJ*  
3005 *Web Conf.*, vol. 52, p. 05001, 2013.
- 3006 [147] D. J. Fixsen, “The temperature of the cosmic microwave background,” *The*  
3007 *Astrophysical Journal*, vol. 707, p. 916, nov 2009.
- 3008 [148] R. Bird and et. al., “Gaps: Searching for dark matter using antinuclei in cosmic  
3009 rays,” 2019.
- 3010 [149] A. N. Baushev, “EXTRAGALACTIC DARK MATTER AND DIRECT DETECTION  
3011 EXPERIMENTS,” *The Astrophysical Journal*, vol. 771, p. 117, jun 2013.
- 3012 [150] V. Trimble, “Existence and nature of dark matter in the universe,” *Annual*  
3013 *Review of Astronomy and Astrophysics*, vol. 25, no. 1, pp. 425–472, 1987.
- 3014 [151] P. Charlot, C. S. Jacobs, D. Gordon, S. Lambert, A. de Witt, J. Böhm, A. L. Fey,  
3015 R. Heinkelmann, E. Skurikhina, O. Titov, E. F. Arias, S. Bolotin, G. Bourda, C. Ma,  
3016 Z. Malkin, A. Nothnagel, D. Mayer, D. S. MacMillan, T. Nilsson, and R. Gaume,  
3017 “The third realization of the international celestial reference frame by very long  
3018 baseline interferometry,” *Astronomy & Astrophysics*, vol. 644, p. A159, dec  
3019 2020.
- 3020 [152] J. F. Navarro, C. S. Frenk, and S. D. M. White, “The structure of cold dark matter  
3021 halos,” *The Astrophysical Journal*, vol. 462, p. 563, may 1996.
- 3022 [153] D. Merritt, A. W. Graham, B. Moore, J. Diemand, and B. Terzić, “Empirical  
3023 models for dark matter halos. i. nonparametric construction of density profiles  
3024 and comparison with parametric models,” *The Astronomical Journal*, vol. 132,  
3025 pp. 2685–2700, jan 2006.
- 3026 [154] R. Jimenez, L. Verde, and S. P. Oh, “Dark halo properties from rotation curves,”  
3027 *Monthly Notices of the Royal Astronomical Society*, vol. 339, pp. 243–259, feb  
3028 2003.
- 3029 [155] H.-N. Lin and X. Li, “The dark matter profiles in the milky way,” *Monthly Notices*  
3030 *of the Royal Astronomical Society*, vol. 487, pp. 5679–5684, jun 2019.

- 3031 [156] F. Seiterle, “Evaluation of an extragalactic dark matter component to the galac-  
3032 tic antinuclei flux from dark matter,” 2022.
- 3033 [157] C. E. Aalseth and et. al., “DarkSide-20k: A 20 tonne two-phase LAr TPC for  
3034 direct dark matter detection at LNGS,” *The European Physical Journal Plus*,  
3035 vol. 133, mar 2018.
- 3036 [158] P. A. Zyla and et. al., “Review of Particle Physics,” *Progress of Theoretical and  
3037 Experimental Physics*, vol. 2020, 08 2020. 083C01.
- 3038 [159] I. Cholis, T. Linden, and D. Hooper, “A robust excess in the cosmic-ray antipro-  
3039 ton spectrum: Implications for annihilating dark matter,” *Phys. Rev. D*, vol. 99,  
3040 p. 103026, May 2019.
- 3041 [160] M.-Y. Cui, X. Pan, Q. Yuan, Y.-Z. Fan, and H.-S. Zong, “Revisit of cosmic ray  
3042 antiprotons from dark matter annihilation with updated constraints on the  
3043 background model from AMS-02 and collider data,” *Journal of Cosmology and  
3044 Astroparticle Physics*, vol. 2018, pp. 024–024, jun 2018.
- 3045 [161] A. Cuoco, J. Heisig, L. Klamt, M. Korsmeier, and M. Krämer, “Scrutinizing the  
3046 evidence for dark matter in cosmic-ray antiprotons,” *Physical Review D*, vol. 99,  
3047 may 2019.
- 3048 [162] A. Cuoco, J. Heisig, M. Korsmeier, and M. Krämer, “Constraining heavy dark  
3049 matter with cosmic-ray antiprotons,” *Journal of Cosmology and Astroparticle  
3050 Physics*, vol. 2018, pp. 004–004, apr 2018.
- 3051 [163] S. Hawking, “Gravitationally Collapsed Objects of Very Low Mass,” *Monthly  
3052 Notices of the Royal Astronomical Society*, vol. 152, pp. 75–78, 04 1971.
- 3053 [164] L. A. Anchordoqui, I. Antoniadis, and D. Lüst, “Dark dimension, the swamp-  
3054 land, and the dark matter fraction composed of primordial black holes,” *Phys.  
3055 Rev. D*, vol. 106, p. 086001, Oct 2022.
- 3056 [165] C. Evoli, D. Gaggero, A. Vittino, G. D. Bernardo, M. D. Mauro, A. Ligorini, P. Ullio,  
3057 and D. Grasso, “Cosmic-ray propagation with DRAGON2: I. numerical solver  
3058 and astrophysical ingredients,” *Journal of Cosmology and Astroparticle Physics*,  
3059 vol. 2017, pp. 015–015, feb 2017.
- 3060 [166] R. Kissmann, “PICARD: A novel code for the galactic cosmic ray propagation  
3061 problem,” *Astroparticle Physics*, vol. 55, pp. 37–50, mar 2014.
- 3062 [167] C. S. Jørgensen, C. Karoff, V. Senthamizh Pavai, and R. Arlt, “Christian hor-  
3063 rebow’s sunspot observations – i. life and published writings,” *Solar Physics*,  
3064 vol. 294, p. 77, Jun 2019.



- 3065 [168] M. Boschini, S. Della Torre, M. Gervasi, G. La Vacca, and P. Rancoita, “Propa-  
3066 gation of cosmic rays in heliosphere: The helmod model,” *Advances in Space*  
3067 *Research*, vol. 62, no. 10, pp. 2859–2879, 2018. Origins of Cosmic Rays.
- 3068 [169] L. J. Gleeson and W. I. Axford, “Solar Modulation of Galactic Cosmic Rays,” ,  
3069 vol. 154, p. 1011, Dec. 1968.
- 3070 [170] O. Stawicki, H. Fichtner, and R. Schlickeiser, “The Parker propagator for spher-  
3071 ical solar modulation,” , vol. 358, pp. 347–352, June 2000.
- 3072 [171] G. Gloeckler and J. Geiss, “Composition of the local interstellar medium as  
3073 diagnosed with pickup ions,” *Advances in Space Research*, vol. 34, no. 1, pp. 53–  
3074 60, 2004. To the Edge of the Solar System and Beyond.
- 3075 [172] A. W. Strong, I. V. Moskalenko, T. A. Porter, G. Jóhannesson, E. Orlando, S. W.  
3076 Digel, and A. E. Vladimirov, “Galprop version 54: Explanatory supplement,”  
3077 *Users Guide*, Sep, 2011.
- 3078 [173] M. A. et al., “Precision measurement of the proton flux in primary cosmic  
3079 rays from rigidity 1 gv to 1.8 tv with the alpha magnetic spectrometer on the  
3080 international space station,” *Physical Review Letters*, vol. 114, p. 171103, 2015.
- 3081 [174] E. Vannuccini and et. al., “Gaps, low-energy antimatter for indirect dark-matter  
3082 search,” 2018.
- 3083 [175] S. Schael, A. Atanasyan, J. Berdugo, T. Bretz, M. Czupalla, B. Dachwald, P. von  
3084 Doetinchem, M. Duranti, H. Gast, W. Karpinski, T. Kirn, K. Lübelmeyer,  
3085 C. Maña, P. Marrocchesi, P. Mertsch, I. Moskalenko, T. Schervan, M. Schluse, K.-  
3086 U. Schröder, A. Schultz von Dratzig, C. Senatore, L. Spies, S. Wakely, M. Wlochall,  
3087 D. Uglietti, and J. Zimmermann, “Ams-100: The next generation magnetic  
3088 spectrometer in space – an international science platform for physics and  
3089 astrophysics at lagrange point 2,” *Nuclear Instruments and Methods in Physics*  
3090 *Research Section A: Accelerators, Spectrometers, Detectors and Associated Equip-*  
3091 *ment*, vol. 944, p. 162561, 2019.
- 3092 [176] ALICE Collaboration, “Towards the understanding of the genuine three-body  
3093 interaction for p–p–p and p–p–,” 2022.
- 3094 [177] S. Acharya and et.al., “Production of  $4\text{he}$  and  $4\text{he}$  in pb–pb collisions at  
3095  $\sqrt{s_{\text{NN}}}=2.76\text{TeV}$  at the lhc,” *Nuclear Physics A*, vol. 971, pp. 1–20, 2018.
- 3096 [178] S. Acharya *et al.*, “Measurement of the (anti-) $^3\text{He}$  elliptic flow in Pb–Pb colli-  
3097 sions at  $\sqrt{s_{\text{NN}}} = 5.02\text{TeV}$ ,” *Phys. Lett. B*, vol. 805, p. 135414, 2020.

- 
- 3098 [179] S. Acharya *et al.*, “(Anti-)deuteron production in pp collisions at  $\sqrt{s} = 13$  TeV,”  
3099 *Eur. Phys. J. C*, vol. 80, no. 9, p. 889, 2020.
- 3100 [180] S. Acharya *et al.*, “Multiplicity dependence of (anti-)deuteron production in  
3101 pp collisions at  $\sqrt{s} = 7$  TeV,” *Phys. Lett.*, vol. B794, pp. 50–63, 2019.
- 3102 [181] S. Acharya *et al.*, “Measurement of deuteron spectra and elliptic flow in Pb-Pb  
3103 collisions at  $\sqrt{s_{NN}} = 2.76$  TeV at the LHC,” *Eur. Phys. J.*, vol. C77, no. 10, p. 658,  
3104 2017.
- 3105 [182] S. Acharya *et al.*, “Multiplicity dependence of light (anti-)nuclei production in  
3106 p-Pb collisions at  $\sqrt{s_{NN}} = 5.02$  TeV,” *Phys. Lett. B*, vol. 800, p. 135043, 2020.
- 3107 [183] A. Bianconi, E. L. Rizzini, V. Mascagna, and L. Venturelli, “Enhancement of  
3108 annihilation cross sections by electric interactions between the antineutron  
3109 and the field of a large nucleus,” *The European Physical Journal A*, vol. 50, dec  
3110 2014.
- 3111 [184] F. Becattini, “An introduction to the statistical hadronization model,” 2009.

3112 **List of Figures**

3113	1	The particles of the standard model of particle physics. There are 3 generations of quarks and leptons, which differ from previous generations only in their mass. Quarks are split into up-like quarks, with a $+\frac{2}{3}$ charge, and down-like quarks with a $+\frac{1}{3}$ charge. Leptons are split between charged leptons with charge $q = -1$ and neutrinos, which carry no electromagnetic or color charge, and are very light. There are 4 gauge bosons for the 3 fundamental forces which the standard model describes: the gluon ( $g$ ) for the strong force, the photon ( $\gamma$ ) for the electromagnetic force, and the W and Z bosons for the weak force. Additionally, there is the scalar higgs boson, which is responsible for the mechanism which gives other particles their mass. . . . .	3
3114			
3115			
3116			
3117			
3118			
3119			
3120			
3121			
3122			
3123			
3124	2	Color confinement by string fragmentation. As the antiquark-quark pair moved away from each other, more and more energy is stored in the color flux tube between them. Eventually, there is sufficient energy to create a new quark-antiquark pair, and thus truncate the flux tube. This process continues until the (anti)quarks run out of sufficient energy to create new quark-antiquark pairs. The quarks can then hadronise. The figure is taken from [8]. . . . .	4
3125			
3126			
3127			
3128			
3129			
3130			
3131	3	Timeline of the universe, starting from the Big Bang [22]. . . . .	7
3132	4	First order Feynman diagrams showing the annihilations of elementary particles. Top row: quark-antiquark annihilation through the strong (left), electromagnetic (middle) and weak (right) force. Bottom row: lepton-antilepton annihilation through the electromagnetic (left) and weak (right) force. . . . .	11
3133			
3134			
3135			
3136			
3137	5	Schematic of $p\bar{p}$ annihilation into 3 mesons, done by rearranging the valence quarks but without annihilating any quark-antiquark pair. . .	12
3138			
3139	6	Annihilation channels for antiproton-proton. The solid lines represent quarks and the dashed lines represent a gluonic string (which can then decay via string fragmentation, as shown in figure 2). Curled lines represent $\bar{q}q$ annihilations. The diagrams thus represent: a) 3 antiquark-quark annihilations; b) a single antiquark-quark annihilation into 2 mesons and a gluon string; c) corresponds to a quark-antiquark and string annihilation, with the creation of 2 quark-antiquark strings. Diagrams e) and f) can produce exotic mesons. Figure taken from [38].	14
3140			
3141			
3142			
3143			
3144			
3145			
3146			
3147	7	A comparison of antiproton-proton inelastic cross section data with the model used in Geant4 [37]. Points are experimental data as described in [40], the blue line represents the model. See text for details.	15
3148			
3149			
3150	8	Antiproton-nucleus annihilation for different materials, taken from [44].	16

3151	9	Statistical hadronisation model fits, with three different implemen-	
3152		tations, to the light flavour hadron yields in central (0-10%) Pb–Pb	
3153		collisions at $\sqrt{s_{NN}}=2.76$ TeV. The upper panel shows the fit results	
3154		together with the data, whereas the middle panel shows the differ-	
3155		ence between model and data normalised to the model value and the	
3156		lower panel the difference between model and data normalised to the	
3157		experimental uncertainties. Figure and caption taken from [48]. . . . .	18
3158	10	Production yield $dN/dy$ normalised by the spin degeneracy as a func-	
3159		tion of the mass number for inelastic pp collisions, minimum-bias	
3160		p-Pb and central Pb-Pb collisions. The empty boxes represent the	
3161		total systematic uncertainty while the statistical errors are shown by	
3162		the vertical bars. The lines represent fits with an exponential func-	
3163		tion. Figure taken from [72]. . . . .	23
3164	11	Computer simulations of the distribution of galaxies within our uni-	
3165		verse, with hot dark matter (left) and cold dark matter (right), com-	
3166		pared to the observed distribution (middle). Figure is taken from [23].	26
3167	12	Transition of dark matter from thermal equilibrium to freeze out. Both	
3168		the decoupling temperature (where dark matter stops being in ther-	
3169		mal equilibrium with luminous matter) and the freeze out tempera-	
3170		ture (when the rate of expansion has dropped the annihilation rate to	
3171		negligible amounts, so that the comoving density can be considered	
3172		constant) are indicated on the schematic. Figure is based on the figure	
3173		in [83]. . . . .	28
3174	13	Collection of candidate dark matter models over a wide mass range.	
3175		The most prominent candidates are WIMP dark matter, axion dark	
3176		matter and sterile neutrinos. Primordial black hole dark matter is not	
3177		shown on this plot. Figure taken from [83]. . . . .	29
3178	14	Thermally averaged annihilation cross section for WIMP dark matter	
3179		as a function of the dark matter mass as it is required to reproduce	
3180		the measured present-day abundance of dark matter. The left y-axis	
3181		shows the values for Dirac dark matter, while the right y-axis shows	
3182		the values for Majorana dark matter, showing the difference of a factor	
3183		2. Taken from [94]. . . . .	33
3184	15	Schematic representation of the ALICE detector and its subdetector	
3185		systems, during the Run 2 data taking period (2015-2018). . . . .	36
3186	16	A schematic of the ALICE Inner Tracking System. The three layer	
3187		groups (SPD, SSD, SDD) are marked. . . . .	38
3188	17	Left: Schematic of the field cage of the TPC detector [98]. Right:	
3189		Schematic of the reconstruction mechanism for tracks in the TPC	
3190		[99]. . . . .	39

3191	18	Specific energy loss in the TPC as a function of the rigidity $p/z$ . Due to their masses, particles can be differentiated according to equation 12. This shows the identifying power of the TPC for low momentum particles. . . . .	40
3192			
3193			
3194			
3195	19	The TOF detector of the ALICE experiment. . . . .	41
3196	20	Left: Measurement of the track velocity $\beta_{\text{TOF}}$ as a function of the reconstructed momentum of the particle associated to the track, from the TOF detector in pp collisions at $\sqrt{s} = 13$ TeV. $\beta_{\text{TOF}}$ is classically measured as length of the track divided by the time-of-flight. Right: Performance figure showing the TOF used for the identification of ${}^3\overline{\text{He}}$ nuclei. . . . .	42
3197			
3198			
3199			
3200			
3201			
3202	21	Schematic of the data structures within ALICE. The data is split by run periods, then by event, and within the event by tracks. . . . .	43
3203			
3204	22	Particle identification procedure for ${}^3\overline{\text{He}}$ (left) and ${}^3\text{He}$ (right), showing the distribution of $n\sigma_{\text{TPC}}$ for the momentum bins in the TPC only part of the analysis. The green line is the fitted signal, the red line is to fit the contamination towards negative $n\sigma_{\text{TPC}}$ . The black line shows the combined fit. . . . .	46
3205			
3206			
3207			
3208			
3209	23	Plots of the $n\sigma_{\text{TPC}}$ distribution for ${}^3\overline{\text{He}}$ (left) and ${}^3\text{He}$ (right), for the momentum bins in the TPC+TOF only part of the analysis, i.e. after a cut on $m_{\text{TOF}}^2$ is applied. The green line is the fitted signal. . . . .	47
3210			
3211			
3212	23	(Continued) Plots of the $n\sigma_{\text{TPC}}$ distribution for ${}^3\overline{\text{He}}$ (left) and ${}^3\text{He}$ (right), for the momentum bins in the TPC+TOF only part of the analysis, i.e. after a cut on $m_{\text{TOF}}^2$ is applied. The green line is the fitted signal. . . . .	48
3213			
3214			
3215			
3216	24	Particle identification procedure for ${}^3\overline{\text{H}}$ (left) and ${}^3\text{H}$ (right), showing the $n\sigma_{\text{TPC}}$ distribution for each momentum bin, after a cut on $m_{\text{TOF}}^2$ is applied. The green lines represent the fitted signal, and the black lines the fitted signal+background. . . . .	49
3217			
3218			
3219			
3220	25	(Anti)nuclei spectra for ${}^3\text{He}$ ${}^3\overline{\text{He}}$ . Blue points show ${}^3\text{He}$ while the red points show ${}^3\overline{\text{He}}$ . Statistical uncertainties are shown as errorbars while systematic uncertainties are shown as boxes. These spectra are not yet corrected for secondary particles from material spallation. . . . .	50
3221			
3222			
3223			
3224	26	Extracted primary ${}^3\text{He}$ yields in each analysis bin as a function of the value of the cut on $ \text{DCA}_z $ . Due to the variations in the first bin, an 8% uncertainty was assigned. . . . .	51
3225			
3226			
3227	27	Example $\text{DCA}_{xy}$ distributions of particles from primary and secondary particles in Monte Carlo simulations. The particle shown here is ${}^3\overline{\text{He}}$ with a $ \text{DCA}_z  < 1$ cm requirement. . . . .	52
3228			
3229			

3230	28	DCA <sub>xy</sub> distributions of <sup>3</sup> He candidates without any cut on ITS histos (left) and after a hit in one of the two first layers of the ITS is required (right). The reduction in the number of candidates is mainly in the sidebands, and therefore from secondaries. . . . .	52
3231			
3232			
3233			
3234	29	Comparison of different methods for determining the primary fraction from the template fits, shown in the second bin of the <sup>3</sup> He analysis, with a  DCA <sub>z</sub>   < 1 cm cut. (Left) Fit using the TFractionFitter. (Middle) Default templates scaled according to the weights assigned by the TFractionFitter, but without changing their shapes. (Right) Fits performed by scaling the material templates to the region outside  DCA <sub>xy</sub>   < 0.1 cm. The solid line represents the data and the histogram points are the fitted material template. See text for more details. . . . .	54
3235			
3236			
3237			
3238			
3239			
3240			
3241			
3242	30	Normalized secondary particle yields as a function of primary particles fired obtained from a toy Monte Carlo simulation of a particle beam on materials mimicking the LHC beampipe in ALICE and the beampipe + ITS support structure. The resulting secondary deuterons and <sup>3</sup> He are shown as a function of the primary particle fired, where the results are roughly scaled by the primary particles relative abundance. . . . .	55
3243			
3244			
3245			
3246			
3247			
3248	31	Cumulative material budget of the ALICE detector, as a function of radius from the beampipe, taken from [105]. The solid red line is the value for straight tracks which hit the centre of the TOF sector, while the dashed blue line is the average value over azimuthal angle. . . . .	57
3249			
3250			
3251			
3252	32	Ratio of antiprotons to protons produced at mid-rapidity as a function of beam rapidity. At LHC energies the value approaches unity, demonstrating that at such high energies antimatter and matter are produced in almost equal amounts. Figure taken from [108]. . . . .	59
3253			
3254			
3255			
3256	33	Bin by bin plots of the <sup>3</sup> He/ <sup>3</sup> He ratio as a function of the varied inelastic cross section in Monte Carlo simulations, together with the one measured in data. The fitted line is an exponential fit according to the Lambert-Beer law 15, and is used to extract the cross section scaling factor. . . . .	61
3257			
3258			
3259			
3260			
3261	34	Bin by bin plots of the <sup>3</sup> H/ <sup>3</sup> H ratio as a function of the varied inelastic cross section in Monte Carlo simulations, together with the one measured in data. The fitted line is an exponential fit according to the Lambert-Beer law 15, and is used to extract the cross section scaling factor. . . . .	62
3262			
3263			
3264			
3265			

3266	35	TPC/TOF ratio for ${}^3\overline{\text{He}}$ as a function of the varied inelastic cross section, for one momentum bin. Figure taken from [110]. The dashed green curve is the a fit of the Lambert-Beer law (equation 15) to the values of the TPC/TOF ratio obtained from MC simulations with varied inelastic cross section (black crosses). The blue datapoint is the ratio in data, and the pink point is the corresponding measurement of the inelastic cross section. . . . .	63
3267			
3268			
3269			
3270			
3271			
3272			
3273	36	Schematic representation for how the correction for the energy loss of antinuclei – and the corresponding systematic uncertainty – is applied to the measurements of the inelastic cross sections. In order to map from the scaling factor to the inelastic cross section, the default parameterization used in Geant4 is employed. . . . .	64
3274			
3275			
3276			
3277			
3278	37	Local $A$ and $Z$ values (left) and density (right) of the ALICE detector material ad mid-rapidity as a function of the radial distance from the interaction point. . . . .	65
3279			
3280			
3281	38	Uncertainty on the ALICE material budget between the TPC and TOF detectors, as found by comparing the yields in the TPC to the ones in the TOF for pions from $K_s^0$ decays (red) and protons from $\Lambda$ decays (black). The uncertainty is determined by comparing the measured ratio to ones obtained from detailed Monte Carlo simulations of the ALICE detector with varied material budgets, using Geant3 (left) and Geant4 (right). Figures taken from [113]. . . . .	67
3282			
3283			
3284			
3285			
3286			
3287			
3288	39	Evaluation of the systematic uncertainty due to track cuts, for ${}^3\overline{\text{He}}$ (left) and ${}^3\overline{\text{H}}$ (right). The same analysis was re-performed over 100 times with random permutations of "tight", "default", and "loose" cuts on each considered parameter. . . . .	69
3289			
3290			
3291			
3292	40	Uncertainty on the antiparticle-to-particle ratio introduced by varying the elastic cross sections by 30% (left) and the inelastic matter cross section by 10% (right). Since the cross section for ${}^3\overline{\text{H}}$ and ${}^3\overline{\text{He}}$ are the same in Geant4, these values are valid for both species. . . . .	70
3293			
3294			
3295			
3296	41	The antiproton inelastic cross section on the average ALICE detector material, taken from [105]. The black line and dots show the data-points, while the green and yellow bands show the 1 and 2 sigma total uncertainties ( $\text{stat}^2 + \text{syst}^2$ ). The dashed line is the parameterization for this cross section in Geant4, which is fitted to data. . . . .	71
3297			
3298			
3299			
3300			

3301	42	Ratio of the antiproton-to-proton ratios (left) and antideuteron-to-deuteron ratios (right) as a function of momentum, obtained in high multiplicity pp collisions and in pPb collisions, compared to the expected difference from the different collision energies (dashed red line). The agreement with the red line shows that this analysis technique is consistent across different collision systems, as expected. . .	72
3302			
3303			
3304			
3305			
3306			
3307	43	Template fits for determining the primary fraction of ${}^3\text{He}$ in the first 3 momentum bins (above this momentum the primary fraction goes to 1), for a $ \text{DCA}_z  < 1$ cm cut. The fits were performed using the TFractionFitter method available in ROOT. . . . .	75
3308			
3309			
3310			
3311	44	(Left) ${}^3\overline{\text{He}}/{}^3\text{He}$ measured in pp collisions at $\sqrt{s} = 13$ TeV, as a function of the particle momentum at the primary vertex. Statistical uncertainties are shown as lines, and systematic uncertainties are shown as boxes. The discontinuity at $p/Z = 1$ GeV/ $c$ is due to the additional requirement of a TOF hit, thus requiring tracks to traverse more material. (Right) $\sigma_{\text{inel}}({}^3\overline{\text{He}})$ as measured using the antiparticle-to-particle method in pp collisions at $\sqrt{s} = 13$ TeV, as a function of the antinuclei momentum at annihilation. The uncertainties include both statistical and systematic uncertainties. Open points are from the analysis using the TPC only for particle identification, while closed points require a matching hit in the TOF in addition to the TPC, which therefore has a different averaged material value. The lines show the parameterization used in Geant4. . . . .	76
3312			
3313			
3314			
3315			
3316			
3317			
3318			
3319			
3320			
3321			
3322			
3323			
3324	45	(Left) TOF-to-TPC ratio for ${}^3\overline{\text{He}}$ in Pb–Pb collisions at $\sqrt{s_{NN}} = 5.02$ TeV, as a function of the particle momentum at the primary vertex. Statistical uncertainties are shown as bars, and systematic uncertainties are shown as boxes. The colored lines are the same ratio in Monte Carlo simulations with varied $\sigma_{\text{inel}}({}^3\overline{\text{He}})$ . (Right) $\sigma_{\text{inel}}({}^3\overline{\text{He}})$ as measured using the TOF-to-TPC method in Pb–Pb collisions at $\sqrt{s_{NN}} = 5.02$ TeV, as a function of the antinuclei momentum at annihilation. The uncertainties include both statistical and systematic uncertainties. The line shows the parameterization used in Geant4. Figures taken from [110].	77
3325			
3326			
3327			
3328			
3329			
3330			
3331			
3332			
3333	46	$n\sigma_{\text{TPC}}$ vs momentum plots for tritons. A cut on the $m_{\text{TOF}}$ is applied above 2 GeV/ $c$ in all figures. (Top left) the original distribution without an additional cut on either DCA or $m_{\text{TOF}}$ . (Top right) the distribution after a cut of $ \text{DCA}_{x,y}  < 1$ mm and $ \text{DCA}_z  < 1$ mm is applied. (Bottom left) the distribution after the cut on $m_{\text{TOF}}$ is extended to momenta as low as 1 GeV/ $c$ . (Bottom right) the distribution after both the DCA and $m_{\text{TOF}}$ cuts were applied. . . . .	78
3334			
3335			
3336			
3337			
3338			
3339			



3340	47	Template fits to the DCA distribution of ${}^3\text{H}$ , to account for the contributions from secondary nuclei from spallation processes. The primary fraction is evaluated as $f_p = \int_{-0.1cm}^{0.1cm} \text{fit}_{\text{signal}} dDCA / \int_{-0.1cm}^{0.1cm} \text{data} dDCA$ . The results are shown for each momentum bin. . . . .	79
3341			
3342			
3343			
3344	48	(Left) ${}^3\bar{\text{H}} / {}^3\text{H}$ ratio as a function of momentum, with statistical uncertainties as bars and systematic uncertainties as boxes. The colored lines represent Monte Carlo simulations with varied inelastic cross sections. (Right) ${}^3\bar{\text{H}}$ TOF-to-TPC ratio as a function of momentum, with statistical uncertainties as bars and systematic uncertainties as boxes. The colored lines represent Monte Carlo simulations with varied inelastic cross sections. . . . .	80
3345			
3346			
3347			
3348			
3349			
3350			
3351	49	(Left) the resulting measurement of $\sigma_{\text{inel}}({}^3\bar{\text{H}})$ using the antibaryon-to-baryon method ( $\bar{\text{B}}/\text{B}$ ) and the TOF-to-TPC method, on the average ALICE material. The colored boxes show the total uncertainty (stat <sup>2</sup> +syst. <sup>2</sup> ). The line shows the parameterization as used in Geant4. (Right) comparison of the $\sigma_{\text{inel}}({}^3\bar{\text{He}})$ and $\sigma_{\text{inel}}({}^3\bar{\text{H}})$ measurements. . . . .	81
3352			
3353			
3354			
3355			
3356	50	Illustrated story of the journey which antinuclei undertake before being observed near earth. Red lines shown high energy cosmic ray protons, Blue lines shown ${}^3\bar{\text{He}}$ . The antinuclei get created all throughout the galaxy, and in the galactic centre antinuclei from dark matter is the most concentrated, due to the higher dark matter density. Similarly, antinuclei from high energy cosmic rays are created all over the galaxy. The created antinuclei then travel through the interstellar medium, some of them annihilating along the way. The ones which do make it to earth then are affected by the solar magnetic field, before reaching detectors near earth. All these processes need to be understood in order to be able to interpret an antinuclei signal in cosmic rays. . . . .	82
3357			
3358			
3359			
3360			
3361			
3362			
3363			
3364			
3365			
3366			
3367			
3368	51	Production cross section for antideuterons (left) and ${}^3\bar{\text{He}}$ (right), as a function of the energy of the antinucleus produced, for a range of different projectile energies, taken from Shukla et. al. The ${}^3\bar{\text{He}}$ cross section includes the effect of antitritons which are produced and subsequently decay to ${}^3\bar{\text{He}}$ . . . . .	86
3369			
3370			
3371			
3372			
3373	52	A list of experiments with measurements of (anti)deuteron production, as a function of rapidity and $\sqrt{s}$ . The compilation is taken from table 2 in [130], based on data in [131, 132, 133, 134, 135, 136, 137, 138, 139, 140, 141]. . . . .	87
3374			
3375			
3376			
3377	53	Comparison of the antideuteron (left) and ${}^3\bar{\text{He}}$ (right) spectra obtained by Shukla et. al. with ALICE data for $\sqrt{s} = 7$ TeV pp collisions. . . . .	88
3378			

3379	54	Cosmic ray particle spectra, for protons and all particles, from relevant experiments. Figure taken from [142]. . . . .	89
3380			
3381	55	The source term of antideuteron from high energy cosmic ray collisions, as a function of the incoming proton energy and the outgoing antideuteron energy. The figure is taken from [121]. . . . .	89
3382			
3383			
3384	56	A schematic of dark matter pair annihilation into standard model particles (left) and of dark matter decay into standard model particles (right) for a WIMP particle. The exact process by which this would occur is not known, and therefore currently model dependent. Note that a scattering process between a dark matter and a standard model particle would look very similar to the diagram on the left, with the space and time axes inverted (i.e. change the arrow direction of the top dark matter and bottom standard model particle). However, this scattering might happen via a very different internal process, so the two cannot be directly related in a model independent way. . . . .	90
3385			
3386			
3387			
3388			
3389			
3390			
3391			
3392			
3393			
3394	57	Antiproton (top) and antideuteron (bottom) spectra from dark matter annihilations as a function of the antinuclei kinetic energy per nucleon, normalized to a single annihilation event, for a wide variety of initial SM states. This figure is taken from [1]. . . . .	92
3395			
3396			
3397			
3398	58	Antideuteron (left) and ${}^3\overline{\text{He}}$ (right) spectra from dark matter annihilations as a function of the antinuclei kinetic energy per nucleon, normalized to a single annihilation event. Spectra for $W^+W^-$ and $b\bar{b}$ channels are taken from [4], $\overline{\Lambda}_b$ tune is taken from [144]. . . . .	93
3399			
3400			
3401			
3402	59	Rotation curve of stars in the Milky Way, as a function of distance from the galactic center. Reproduction of data reported in [78]. . . . .	94
3403			
3404	60	Dark matter density profiles used in this work, as a function of the distance to the galactic centre. The best fit values for each profile are taken from [4]. . . . .	96
3405			
3406			
3407	61	Fit of the rotation curve of the Milky Way, with a NFW profile. Figure is taken from [156], based on work in [149]. . . . .	97
3408			
3409	62	Limits from direct detection experiments on the dark matter - nucleon interaction cross section, as a function of the dark matter mass. The figure is taken from [158]. . . . .	99
3410			
3411			
3412	63	Limits on $\langle \sigma v \rangle$ based on AMS antiproton data. Figure is taken from [57]. . . . .	100
3413			
3414	64	Spectrum of produced antideuterons per second, as a function of kinetic energy per nucleon, from a primordial black hole evaporation. Data from [4], provided in private communication. . . . .	104
3415			
3416			

3417	65	Fluxes of several cosmic ray nuclei, as measured by AMS-02, compared to the predictions of the best-fit values obtained by fitting several key species. Figure taken from [63] . . . . .	106
3418			
3419			
3420	66	Comparison between the different GALPROP propagation parameters used in this work, for antideuterons from high energy cosmic ray collisions (left) and from dark matter annihilations (right). . . . .	108
3421			
3422			
3423	67	Scaled inelastic cross sections of ${}^3\overline{\text{He}}$ (top) on proton (left) and Helium-4 (right) targets and antideuterons on proton targets (bottom). The band shows the experimental uncertainty from the ALICE measurements [105, 110], plus an additional 8% uncertainty associated with the scaling from heavier targets (C, O, Al) to protons (H). The parameterization shown in the top left panel (labeled Korsmeier et al in the bottom panel) is taken from [2], and is based on scaling the total deuteron-antiproton cross section by the inelastic portion of the antiproton-proton cross section, and then scaling the obtained value by 3/2 to account for the extra nucleon in ${}^3\overline{\text{He}}$ . The cross section in the bottom panel labeled Ibarra et. al. is taken from [4], and is based on taken 2 times the antiproton-proton inelastic cross section, as parameterized by [36]. See section 1.4.4 for a more detailed discussion on calculating inelastic cross sections. . . . .	112
3424			
3425			
3426			
3427			
3428			
3429			
3430			
3431			
3432			
3433			
3434			
3435			
3436			
3437	68	Expected antideuteron fluxes for different $m_\chi$ ranging from 10 GeV to 1 TeV, and from primordial black holes (PBHs). They are compared to an expected spectrum of secondary antideuterons from high-energy cosmic-ray collisions. The results are shown for the position of the solar system. The figures on the left show the results without solar modulation, and on the right with solar modulation included by means of a force field model, as is discussed in section 5.2. The results are also shown for different possible annihilation channels of dark matter, either through $W^+W^-$ (top) or through $b\bar{b}$ (bottom). . . . .	115
3438			
3439			
3440			
3441			
3442			
3443			
3444			
3445			
3446	68	Expected antideuteron fluxes (cont.) dark matter annihilations through $\overline{\Lambda}_b \rightarrow b\bar{b}$ and light mediators (top) and from primordial black holes (PBHs) (bottom). The figures on the left show the results without solar modulation, and on the right with solar modulation included by means of a force field model, as is discussed in section 5.2. . . . .	116
3447			
3448			
3449			
3450			

3451	69	Expected ${}^3\overline{\text{He}}$ fluxes for different $m_\chi$ ranging from 1 GeV to 2 TeV. They	
3452		are compared to an expected spectrum of secondary ${}^3\overline{\text{He}}$ from high	
3453		energy cosmic ray collisions. The results are shown for the position	
3454		of the solar system. The figures on the left show the results without	
3455		solar modulation, and on the right with solar modulation included	
3456		by means of a force field model, as is discussed in section 5.2. The	
3457		results are also shown for different possible annihilation channels of	
3458		dark matter, either through $W^+W^-$ (top), through $b\bar{b}$ (bottom). . . . .	117
3459	69	Expected ${}^3\overline{\text{He}}$ fluxes (cont.) from dark matter annihilations through $\overline{\Lambda}_b$	
3460		decays. They are compared to an expected spectrum of secondary ${}^3\overline{\text{He}}$	
3461		from high energy cosmic ray collisions. The results are shown for the	
3462		position of the solar system. The figures on the left show the results	
3463		without solar modulation, and on the right with solar modulation	
3464		included by means of a force field model, as is discussed in section 5.2.	118
3465	70	Antideuteron fluxes for different dark matter profiles (left) and the	
3466		corresponding transparencies (right), for antideuterons from dark	
3467		matter annihilation through the $b\bar{b}$ channel. . . . .	118
3468	71	Plot of the rigidity resolution of AMS for comparing ${}^3\overline{\text{He}}$ and ${}^3\text{He}$ sig-	
3469		nals. 9 possible ${}^3\overline{\text{He}}$ events are shown. These findings have not yet	
3470		been published and this figure is taken from a talk [119]. . . . .	123
3471	72	(Left) GAPS antiparticle detection method: antiparticles slow down	
3472		and stop in the Si(Li) target, forming an exotic atom. Atomic X-rays	
3473		will be emitted as it de-excites, followed by the pion (and proton) emis-	
3474		sion from nuclear annihilation. $\bar{d}/\bar{p}$ identification is based on (1) the	
3475		stopping range, (2) the pion and proton multiplicity, (3) the atomic X-	
3476		rays energies. Figure and caption taken from [174]. (Right) The GAPS	
3477		detector, the central tracker (C) is surrounded by the inner (“cube”, B)	
3478		and outer (“umbrella”, A) TOF layers. The readout electronics, flight	
3479		computer, ballast and other support infrastructure are located under-	
3480		neath the tracker (D). Solar panels, cooling systems, antennae and	
3481		thermal insulation are not shown for clarity. Figure and description	
3482		taken from [148]. . . . .	124
3483	73	The inelastic cross section measurements for the antinuclei from $A$	
3484		$= 1$ to $A = 3$ , as measured by ALICE in [105, 110] and in an upcoming	
3485		publication on ${}^3\overline{\text{H}}$ . . . . .	127

3486 **List of Tables**

3487	1	Constant values for determining the fit parameter $R_A$ used in the	
3488		Geant4 Glauber approximation for antinucleus-nucleus collisions	
3489		[44]. . . . .	17
3490	2	Values for the average atomic mass number of the ALICE detector	
3491		material $\langle A \rangle$ , for different analysis methods. They are evaluated	
3492		according to equation 16. . . . .	65
3493	3	Individual axisymmetric parts of the Milky Way used for fitting rota-	
3494		tion curves. The distinction is made in order to simplify the fit, rather	
3495		than a hard distinction within the actual galaxy. Non-axisymmetric	
3496		components are neglected for rotation curves, based on the assump-	
3497		tion that any effects would cancel out when averaged over the full	
3498		rotation. The values for the total mass were taken from [79]. The	
3499		extent column is approximate and given in order to help the reader	
3500		visualise the distributions. Due to the distributions being exponential,	
3501		they only asymptotically approach 0. . . . .	95
3502	4	Two of the parameters for the tuning of Galprop, which show the	
3503		degeneracy between them. . . . .	109
3504	5	A list of the sizes of uncertainties involved in making predictions for	
3505		antinuclei fluxes. The second and third column are describing the size	
3506		of the effect on antinuclei from high energy cosmic ray collisions and	
3507		from potential dark matter annihilations, respectively. . . . .	119